Mutation and/or inactivation of actin regulatory genes relevant for infection using the CRISPR/Cas system in tissue culturedcells

Von der Fakultätfür Lebenswissenschaften
der Technischen Universität Carolo-Wilhelmina zu Braunschweig
zur Erlangung des Grades einer
Doktorin der Naturwissenschaften
(Dr. rer. nat.)
genehmigte

DISSERTATION

von **Jana Kollasser**
aus Senftenberg

1. Referentin: Prof. Dr. Stradal
2. Referent: Prof. Dr. Köster

eingereicht am: 01.04.2019
mündliche Prüfung (Disputation) am: 23.05.2019
Druckjahr: 2019

Vorveröffentlichungen

Teilergebnisse aus dieser Arbeit wurden mit Genehmigung der Fakultät für Lebenswissenschaften, vertreten durch die Mentorin der Arbeit, in folgenden Beiträgen vorab veröffentlicht:

Publikationen

Kollasser J, Stahnke S, Kirchenwitz M, Otto A, Rottner K, Stradal TE. WHAMM- and Arp2/3-complex driven endomembrane trafficking during infection. (2016) Mol. Biol. Cell 27, 3947 [Abstract #P984 (Poster)]

Tagungsbeiträge

Kollasser J, Stahnke S, Kirchenwitz M, Otto A, Steffen A, Rottner K, Stradal TE. Mutation and/or inactivation of actin regulatory genes relevant for infection using the CRISPR-Cas system in tissue cultured cells. Vortrag. 7^{th} Annual Retreat GS-Fire, Goslar-Hahnenklee (2017).

Posterbeiträge

Kollasser J, Stahnke S, Brakebusch CH, Stradal TE. WHAMM- and Arp2/3-complex-driven endomembrane trafficking during infection. Poster P27. 10^{th} Annual PhD Symposium GS-Fire, HZI Braunschweig (2017).

Kollasser J, Gröbe L, Schweitzberger D, Stahnke S, Stradal TE. Mutation and/or inactivation of actin regulatory genes relevant for infection using the CRISPR-Cas system in tissue cultured cells. Poster P17. 6^{th} Annual Retreat GS-Fire, Goslar-Hahnenklee (2016).

Kollasser J, Gröbe L, Stradal TE. Mutation and/or inactivation of actin regulatory genes relevant for infection using the CRISPR-Cas system in tissue cultured cells. Poster P24. 6^{th} Annual Retreat GS-Fire, Brunsviga Braunschweig (2015).

Kollasser J, Gröbe L, Stradal TE. Mutation and/or inactivation of actin regulatory genes relevant for infection using the CRISPR-Cas system in tissue cultured cells. Poster P42. 8^{th} Annual PhD Symposium GS-Fire, HZI Braunschweig (2015).

Für mein Herz Skippy.

To my heart Skippy.

Contents

List of Figures

List of Tables

List of Abbreviations

ADP	adenosine diphosphate
Amp	Ampicillin
Arp2/3	actin-related protein-2/3
ATG	autophagy-related
ATP	adenosine triphosphate
BafA1	Bafilomycin A1
BFA	Brefeldin A
CC	coiled-coil
cDNA	complementary DNA
cGAS	cyclic GMP-AMP synthase
Cm	Chloramphenicol
CMA	Chaperone-mediated autophagy
CRISPR	Clustered Regularly Interspaced Short Palindromic Repeats
crRNA	CRISPR RNA
DMSO	Dimethylsulfoxide
DNA	deoxyribonucleic acid
dNTP	Deoxyribonucleotide triphosphate
DTT	Dithiothreitol
ECM	extracellular matrix
E. coli	*Escherichia coli*
EGFP	enhanced green fluorescent protein
ER	endoplasmic reticulum
ERGIC	ER-Golgi intermediate compartment

FBS	Fetal bovine serum
Gm	Gentamycin
GMS	Galloway-Mowat syndrome
GST	Glutathione S-transferase
HBSS	Hank´s Balanced Salt Solution
HDR	homology directed repair
hpi	hours post infection
HRP	Horseradish peroxidase
HSV-1	Herpes simplex virus type 1
indel	*insertion or deletion*
ITGA	integrin alpha subunits
ITS-G	Insulin-Transferrin-Selenium-G
JMY	junction-mediating and regulatory protein
Kana	Kanamycin
KO	knockout
LAMP2A	lysosome-associated membrane protein 2A
LB	Lysogeny broth
LIR	LC3-interacting region
MAP1LC3	microtubule associated protein 1 light-chain 3
MOI	multiplicity of infection
mRNA	messenger RNA
mTORC1	mammalian target of rapamycin complex 1
NHEJ	non-homologous end joining
NPF	nucleation promoting factor

OD	optical density
PAM	protospacer adjacent motif
PBS	Phosphate buffered saline
PFA	paraformaldehyde
PFU	Plaque forming units
PE	phosphatidylethanolamine
PtdIns3K	phosphatidylinositol 3-kinase
PI3P	phosphatidylinositol 3-phosphate
PP	proline-rich region
PRR	pattern recognition receptor
PVDF	Polyvinylidene difluoride
qPCR	quantitative polymerase chain reaction
RNA	ribonucleic acid
SDS-PAGE	SDS-Polyacrylamide gel electrophoresis
sgRNA	Single guided ribonucleic acid
SHRC	WASH regulatory complex
siRNA	Short interfering RNA
SV40	Simian virus 40
TAE	Tris-acetate EDTA
TBS-T	Tris-buffered saline with Tween
TGN	trans-Golgi network
TLR	toll-like receptor
ROCK	Rho-associated protein kinase
rpm	rounds per minute

RSV	Respiratory syncytial virus
ULK1/2	Unc-51-like kinase family
VAP-A	vesicle-associated membrane protein-associated protein-A
VSV	Vesicular stomatitis virus
WASH	WASp and Scar homolog
WASp	Wiskott–Aldrich Syndrome protein
WHAMM	WASp homolog associated with actin, membranes and microtubules
WHD	WASH homology domain
WMD	WHAMM membrane interaction domain
WT	wild type

List of Symbols and (SI) Units

bp	Basepair
°C	Degree Celsius
Δ	Delta (indicates gene deletion)
g	Gram
kb	Kilobase pair
kDa	Kilodalton
L	Liter
μg	Microgram
μL	Microliter
mg	Milligram
mL	Milliliter
mM	Millimolar
M	Molar mass
ng	Nanogram
V	Volt
xg	Multiple of acceleration of gravity

1 Summary

Bacterial and viral pathogens have evolved a wide range of strategies to invade their unwilling hosts. Many of them rely on actin-based motility to penetrate and survive within the host cells, yet in many cases it is not fully understood how and where exactly they manipulate actin dynamics. Arp2/3-mediated nucleation and branching of actin depends on nucleation promoting factors that locally recruit and activate the Arp2/3 complex. In particular, Arp2/3 activation and function is regulated by a class of proteins termed type I nucleation promoting factors, which comprise the WAS-superfamily including the well-known WASp and WAVE proteins as well as WASH, WHAMM, and JMY that operate in endomembrane traffic.

The aim of this study was to elucidate the connection between actin polymerization on internal membranes and the intracellular lifecycle of pathogenic invaders by systematically inactivating the respective nucleation promoting factor genes using the CRISPR/Cas9 technology. Aside from specific functions in host-pathogen interaction, this approach was expected to help shedding new light on the cellular functions of these Arp2/3-activators. Upon somatic gene knockout of actin regulators, I examined a broad set of cellular and infection processes in murine fibroblasts and human cancer cells.

To this end, I have generated several independent clones of mouse embryonic fibroblasts (NIH/3T3) as well as human osteosarcoma cells (U-2 OS) by disrupting their genes of WASH, WHAMM, and JMY, respectively. All cell lines were probed for the absence of the respective proteins by western blotting. Additionally, NIH/3T3 knockouts were genomically sequenced for targeted loci of clones lacking protein expression. The cellular phenotypes of obtained NIH/3T3 WHAMM knockout cell lines have been characterized with special emphasis on ER- and Golgi morphology as well as on autophagy. Moreover, I performed transcriptional profiling to identify pathways, which are differentially regulated dependent on the respective phenotype, followed by exemplary evaluation of the affected pathways.

WHAMM knockout significantly alters NIH/3T3 morphology. In particular, WHAMM-deficient cells exhibited enlarged cell size and nuclear area and displayed higher granularity. In addition, knockout of WHAMM significantly affects integrity of the Golgi apparatus. Microarray analyses revealed a deregulation of genes encoding for enzymes involved in autophagy, cholesterol biosynthesis as well as of genes crucial for integring-

mediated adhesion in WHAMM knockout clones. Notably, examination of autophagy uncovers increased numbers of LC3-, p62-, and LAMP-1-positive vesicles as well as revealed enlarged omegasomes, autophagosomes, and lysosomes in WHAMM knockout cells. Lastly, it could be shown that WHAMM ablation decreases the infection rate of Vesicular stomatitis virus and Herpes simplex virus type 1, suggesting that loss of WHAMM is involved in viral infection processes.
Preliminary data of NIH/3T3 JMY knockout cells revealed also enlarged cell nuclei as well as showed a strong increase of LC3- and p62-positive vesicles under nonstarved conditions. Moreover, JMY knockout cells exhibited a clear inhibition of Vesicular stomatitis virus release, indicating that JMY is also likely involved in Vesicular stomatitis virus infection.

Current experiments are designed to unravel specific functions of WHAMM and its relatives in autophagy as well as during Vesicular stomatitis virus and/or Herpes simplex virus type 1 infection in more detail and to explore membrane alterations of for instance omegasomes by both super-resolution and electron microscopy in WHAMM KO cells.

2 Introduction

Shaping, locomotion and internal organization of eukaryotic cells are generated and maintained by a structure called the cytoskeleton, a network of filaments or fibers. It is composed of three distinct elements that differ in size and protein composition.
Microtubules are the largest type of filaments. These long hollow tubes consist of 13 columns of tubulin dimers. Microtubules mainly function in maintenance of cell shape and a variety of cell migration events such as intracellular organelle transport and chromosome movements in cell division.
The second cytoskeletal subtype are intermediate filaments. These rope-like fibers are constructed from a number of different fibrous proteins depending on the cell type. Indeed, intermediate filaments are not directly involved in cell movements, but possess a structural role by providing mechanical strength to cells and tissues (e.g. in epithelial tissue) [1].
The machinery that powers locomotion of eukaryotic cells is built from the actin cytoskeleton. Cell locomotion is a fundamental event of multi-cellular life and formation of dynamic membrane protrusions occurs as lamellipodia, membrane ruffles or filopodia [2]. Actin exists as globular monomers termed G-actin, which can polymerize to filamentous actin (F-actin) [3]. In addition to cell locomotion, actin is the major cytoskeletal filament exploited by pathogens. Actin rearrangements are a common feature of most pathogenic internalization events enabling bacteria or viruses to move around within the cytoplasm or to support cell-to cell spread [4]. The next chapters will focus on the regulation of actin polymerization by nucleation promoting factors (NPFs), the potential impact of these proteins on a mechanism termed autophagy and will describe how pathogens use the host actin cytoskeleton for their own purposes.

2.1 The actin cytoskeleton

Actin, also referred to as microfilament system, is the most abundant intracellular protein observed in eukaryotes [5]. It is a highly conserved ATPase and participates in diverse processes, including cell migration, endocytosis, vesicle trafficking and cytokinesis. As mentioned above, actin is found both as monomeric G-actin, and as a polymeric linear chain of G-actin subunits termed F-actin. F-actin is formed by reversible non-covalent self-association of monomeric G-actin [3]. The transition between these two states involves adenosine triphosphate (ATP) hydrolysis and the binding of adenosine diphosphate (ADP) to actin. G-actin binds ATP via a central grove, a prerequisite to allow polymerization to F-actin that is constantly occurring within living cells [6].

In vitro experiments such as viscometry, sedimentation, and fluorescence spectroscopy monitored the polymerization process showing that actin polymerization proceeds in three sequential phases (Figure 2.1). In the initial step G-actin aggregates into short, unstable oligomers. However, the formation of new actin filaments in cells is kinetically unfavorable because of the instability of these polymerization intermediates. Once the oligomer reaches a length of three or four subunits it can form stable complexes of actin (nuclei). In the second phase, the nuclei rapidly elongate into filaments by the addition of actin monomers to both ends of the filament. In the third phase (steady state) G-actin monomers exchange with subunits at the filament ends but there is no net change in the total mass of filaments [7].

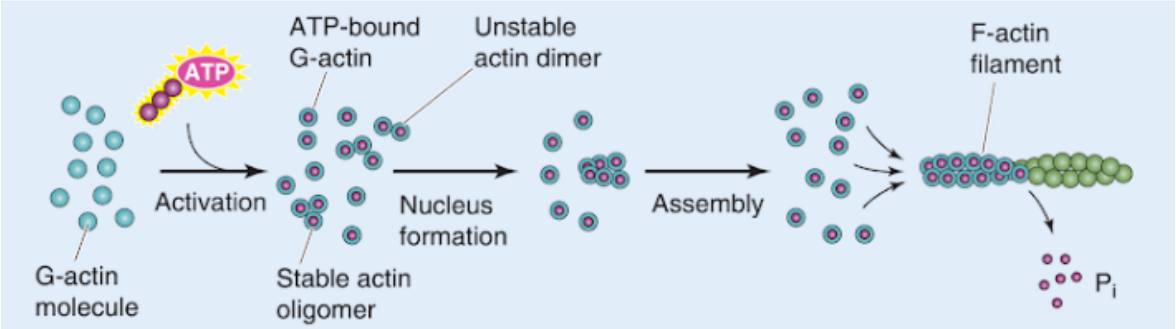

Figure 2.1: Formation of F-actin. G-actin forms the basic unit for actin filaments. Generally, actin polymerization proceeds over three stages: A nucleation phase, an elongation phase and a steady state phase. A G-actin monomer binds to ATP and interacts with other ATP-bound G-actin molecules. The formation of a stable trimer (nucleus) occurs that usually consists of three or four actin monomers. Nucleus formation is essential for the assembly of F-actin. In the third phase, both ends of the filament are in a steady state with monomeric ATP-G-actin. Shortly after its integration into a filament, subunits hydrolyze ATP to ADP and inorganic phosphate (P_i) is released [8].

F-actin is a double-helical filament, which arranges head-to-tail to give the filament a molecular intrinsic polarity (Figure 2.2). Filamentous actin structures have a fast growing plus end (barbed end) and a slowly growing minus end (pointed end). The barbed end displays a cleft where ATP-actin monomers are preferentially incorporated, while the opposite end possesses an actin subunit with an exposed ATP binding site. The cycle of actin polymerization and depolymerization is termed actin treadmilling mechanism by which ADP exchange for ATP enhances the addition of G-actin monomers to the barbed end [9]. However, even cells contain a large pool of actin monomers, spontaneous actin assembly is prohibited *in vivo*. Actin monomer-binding proteins such as profilin suppress spontaneous nucleation of new filaments and the cell requires nucleation factors to catalyze the *de novo* assembly of filaments (Chapter 2.2) [10].

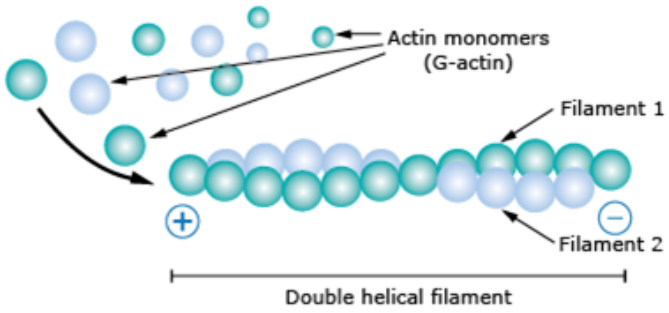

Figure 2.2: .
F-actin appears as a double-helical filament. A F-actin filament grown from the polymerization of G-actin monomers. Plus = barbed end, minus = pointed end (https://www.hypermol.com/index.php?cat=c91_FAQs-FAQs.html)(13.09.2018)

2.2 Actin nucleators

The dynamic assembly and disassembly of actin filaments and the formation of larger scale filament structures are controlled by a vast number of regulatory proteins, which bind to and modify both G- and F-actin [3, 11]. Some of these factors bind to actin monomers (e.g. thymosin $\beta 4$ and profilin), thereby suppressing spontaneous actin polymerization. Therefore the initial step, known as nucleation (Figure 2.1), represents the rate-limiting step in *de novo* filament formation. Once nucleated, filaments elongate at their barbed ends at a rate proportional to the concentration of available actin monomers [12]. To overcome this kinetic hurdle to filament polymerization, cells express actin nucleators that can accelerate or bypass this step [3]. These proteins contain actin-binding sites and either mimic or stabilize the spontaneous formation of dimeric and then trimeric actin intermediates. A variety of actin nucleators have been found to date, which include the actin-related protein-2/3 (Arp2/3) complex, the formins and Spire (Figure 2.3).
The first physiologically relevant actin nucleation factor identified was the Arp2/3 complex [11]. It is a seven-subunit protein complex containing Arp2 and Arp3, and five unique polypeptides [3]. Arp2 and Arp3 are closely related to G-actin, which allows the formation of a "cryptic dimer" similar to an actin dimer that can act as a stable nucleus for actin polymerization [13]. The Arp2/3 complex alone does not stimulate actin filament assembly as it possesses little biochemical activity. Rather, it is activated by NPF proteins to catalyze the formation of a new (daughter) filament from the side of an pre-existing (mother) filament in a y-branch configuration at a 70° angle [3]. This process is known as dendritic nucleation and is utilized to assemble actin struc-

tures such as *Listeria* comet tails, lamellipodia, and focal adhesions. The best studied Arp2/3 complex activators are the Wiskott–Aldrich Syndrome protein (WASp)/WAVE family proteins, which enhance conformational changes to enable the Arp2/3 complex to nucleate actin (Chapter 2.3) [12, 13].

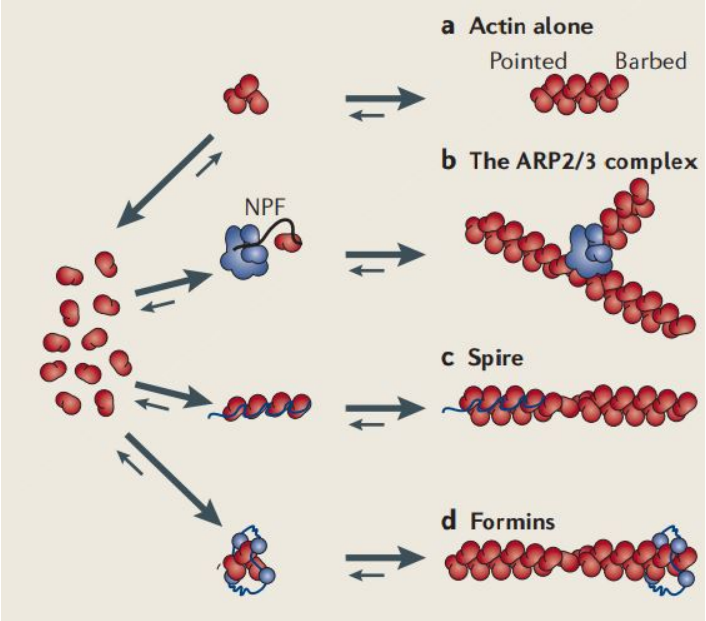

Figure 2.3: Paths to actin nucleation. (a) The initial step in actin-filament assembly requires the formation of a stable, trimeric complex (nucleus), a process called nucleation. However, spontaneous nucleation is kinetically unfavourable due to the instability of actin dimer intermediates. To overcome the kinetic hurdle for nucleation and to promote the initiation of new filament assembly, cells utilize factors that directly nucleate actin (b-d). (b) Arp2/3 complex is activated by binding to NPFs. It mimics actin dimer or trimer and functions in the initiation of a new actin (daughter) filament, forming y-branched networks. (c) Another class of proteins called tandem-monomer-binding nucleators (e.g. Spire) use actin-monomer-binding WH2 domains to nucleate and polymerize into long stretches of linear microfilaments. (d) Formins generate actin polymerization nuclei by stabilizing actin dimer or trimer through their FH2 domains. In contrast to Arp2/3 complex and Spire, formins remain processively attached to the growing barbed ends of actin filaments [3].

The second major class of actin nucleators identified are the formin proteins, which generate linear (unbranched) actin filaments *in vitro* independently of the Arp2/3 complex and NPFs [11]. They are large, dimeric multi-domain proteins and characterized by the C-terminal FH1 and FH2 domains [14]. The FH1 domain harbors polyproline stretches for profilin recruitment and to mediate interactions with domain proteins such as SH3. The FH2 motif associates with the barbed end and is required for dimerization as well as actin nucleation [15]. Formins assemble diverse actin structures, including stress fibers, filopodia and lamellipodia, cytokinetic actin rings, and actin cables *in*

vivo [12,14]. More recently, it was shown that FMNL2 and FMNL3 contribute to the velocity of lamellipodium protrusion *in vitro*, and loss of these proteins reduces lamellipodial width, actin filament density and -bundling [16].
The third class of nucleators discovered are known as tandem-monomer-binding nucleators. This group comprises proteins such as Spire, Cordon bleu (Cobl), and Leiomodin (Lmod) [11,12]. Each member possesses tandem repeats of G-actin binding motifs (typically WH2 domains) [11], which function in nucleation by recruiting actin monomers to form the polymerization nucleus [17].

2.3 Regulation of Arp2/3 complex by NPFs

The Arp2/3 complex promotes actin nucleation weakly, but it can be activated by a class of proteins termed NPFs. Most mammalian NPFs are members of the (Class I) WASp/WAVE family, which comprises ten proteins. WASp was identified as the product of the gene mutated in human patients with Wiskott–Aldrich Syndrome and is restricted to haematopoietic cells. Its closest homolog N-WASp and the more distant relatives WAVE1-3 (also known as SCAR proteins) are ubiquitously expressed in other cells and tissues. In the last years, further NPFs called WASp and Scar homolog (WASH) (also known as WASHC1), WASp homolog associated with actin, membranes and microtubules (WHAMM) and junction-mediating and regulatory protein (JMY) have been identified, but little is known about their biochemical regulation and cellular function [18]. Moreover, evolutionary investigation of WASp family members in other organisms has revealed three other families of WASp proteins known as WHAMY, WAML (WASp and MIM-like) and WAWH (WASp without WHI domain) [19]. All members of this family are diverse in their overall domain organization but share a WCA (WH2 domain, connector region, acidic region) catalytic module at the C-terminal region, required for potent activation of Arp2/3-mediated actin nucleation (Figure 2.4) [3, 20]. The WH2 domain is an actin monomer-binding motif and enables actin polymerization onto the barbed end, whereas the connector and acidic region mediate binding to Arp2/3. This interaction faciliates a conformational change of the Arp2/3 complex, which brings Arp2 and Arp3 into proximity. Subsequently, the WH2 domain presents an actin monomer to Arp2/3, thereby enhancing the formation of a nucleus required for polymerization of a new actin filament [3].
A second class of NPFs (Class II) binds actin filaments instead of actin monomers and are best represented by Src kinase substrate cortactin [20].

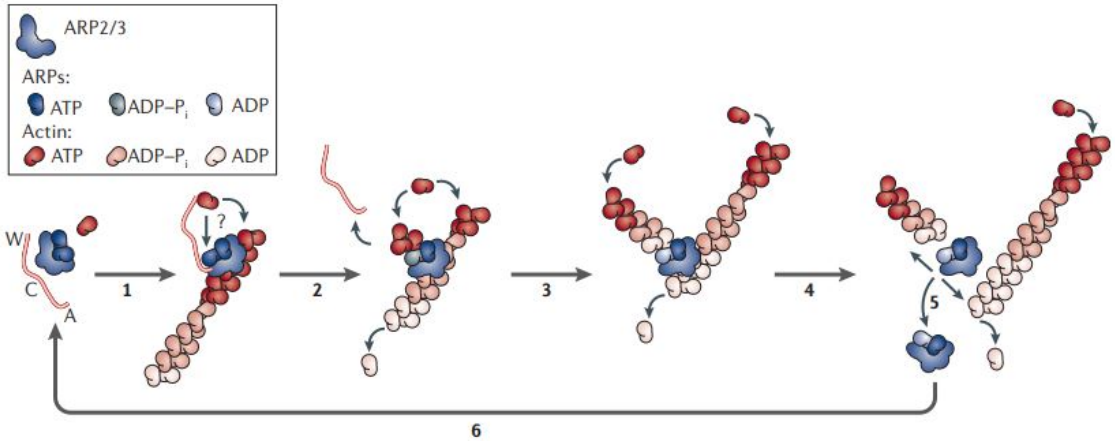

Figure 2.4: Scheme of Arp2/3 complex activation and recycling. Overview of branching nucleation depicting the required reaction components (Arp2/3 complex in blue, actin in red, NPFs indicated with WCA). The Arp2/3 starts in an inactive state. (Step 1) Binding of two WCA domain facilitates a conformational change in the Arp2/3 complex that leads to complex activation. WCA motif presents an ATP–actin monomer to the complex and/or possibly to the fast growing (barbed) end of the pre-existing actin filament. (Step 2) ATP hydrolysis occurs on Arp2 concomitant with or shortly after nucleation of the new (daughter) filament and the WCA domain dissociates from the complex. (Step 3) Phosphate is released from Arp2 and mother as well as daughter filaments elongate. (Step 4) The interactions between Arp2/3 complex and the daughter and/or the mother filament are weaken (Step 5) leading to branch disassembly and release of the Arp2/3 complex. (Step 6) Nucleotide exchange on Arp2 occurs and the cycle restarts from step 1 [3].

2.3.1 WASH

The gene encoding for WASH was discovered as one of several subtelomeric genes in humans [21] and is conserved from simple eukaryotes such as *Dictyostelium* to humans. The modular organization of WASH includes N-terminal localization domains WASH homology domain (WHD) 1 and tubulin-binding WDH2 followed by a proline-rich region (PP) and the C-terminal WCA unit [18] (Figure 2.5). WASH is intrinsically inactive and functions in a heteropentameric complex (WASH regulatory complex (SHRC)) containing strumpellin, FAM21A, KIAA1033, and CCDC53, which show sequence homology to components of the WAVE complex [22]. Moreover, both complexes share similarities in shape and size as determined by electron microscopy [19].

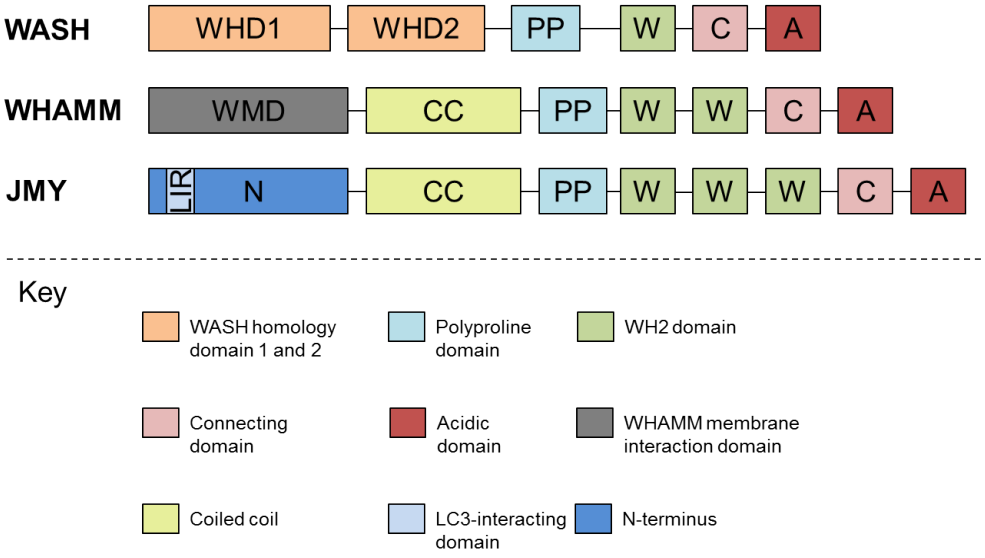

Figure 2.5: Domain organization of WASH, WHAMM and JMY. The C-terminus of each NPF is characterized by Arp2/3-binding CA-modules linked N-terminally to different numbers of actin monomer-binding sites (WH2 domains). The divergent N-termini mediate subcellular targeting. [19].

Initial mutation experiments of WASH in *Drosophila* showed an impairment of oogenesis and larval development [21, 23] and deletion of WASH in mice led to early embryonic lethality [24, 25]. In contrast to the these data, a recent report shows that homozygous *wash* mutant flies are viable and fertile [26]. Mutations in the genes of individual subunits (e.g. strumpellin and KIAA1033) have been linked to intellectual disability syndromes [27, 28], and separate mutations in strumpellin caused hereditary spastic paraplegia [29].

A number of subcellular and ribonucleic acid (RNA) interference studies in mammalian cells revealed that WASH associates with endosomes regulating sorting and maturation steps of endocytic vesicles. WASH inactivation induced endosome tubulation [30, 31], a collapse of the endolysosomal system [24], and studies in *Drosophila* exhibited a role for WASH in integrin receptor recycling and lysosome acidification [26].

Experimemts performed in *Dictyostelium* showed that WASH drives the retrieval of the vacuolar ATPase from post-lysosomal compartments [32], and regulates the recycling of membrane components from macropinosomes and phagosomes [33]. Furthermore, it was demonstrated that WASH is recruited to retromer-enriched endosomal subdomains via an interaction of FAM21 with the retromer subunit VPS35 [34]. A mutation in VPS35 displayed a reduced interaction of the SHRC with VSP35 and impaired vesicular trafficking from the late endosomes [35, 36]. WASH and the Arp2/3 complex regulate endosome shape and trafficking by actin polymerization [31], however, vesicle scission at WASH-containing endosomes requires also the coordinated action of

microtubules and the endoplasmic reticulum (ER) [37–40]. Other essential but controversial roles of WASH have been recently described in autophagy (Chapter 4.2.2). These aspects will be further discussed in Chapter 2.5.2.

2.3.2 WHAMM

WHAMM is another actin-binding protein that is expressed in virtually all human and mouse tissues [18]. It localizes to the *cis*-Golgi apparatus as well as tubulo-vesicular membrane transport intermediates and has been described to drive vesicle traffic between the ER and the Golgi (ER-Golgi intermediate compartment (ERGIC)). The modular organization of WHAMM includes an N-terminal WHAMM membrane interaction domain (WMD), a coiled-coil (CC) microtubule-binding domain, a PP sequence, and a C-terminal WWCA motif involved in regulating actin nucleation (Figure 2.5). WHAMM is <20% similar to other Class I NPFs, but is roughly 35% identical and 50% similar to JMY, another NPF that controls p53-mediated apoptosis (Chapter 2.3.3) [20]. Recent studies have been shown that G-proteins have the ability to interact with WHAMM. The first report displayed that WHAMM acts downstream of RhoD and is required for RhoD-dependent actin reorganization [41]. The second study demonstrated that the G-protein Rab1 inhibits WHAMM-mediated actin assembly *in vitro*. Active Rab1 recruited WHAMM to tubulovesicular structures through an interaction with the WMD [42].
Cryoelectron microscopy unveiled that WHAMM binds to the outer surface of microtubule protofilaments through an interaction between its CC region and tubulin heterodimers. Upon microtubule binding, the N-terminal WMD was exposed at the microtubules periphery, thereby recruiting vesicles, which are remodelled into tubular structures. In contrast, microtubule binding masked the C-terminal WWCA domain, thus preventing actin polymerization [43]. Furthermore, recent findings have identified that WHAMM is another NPF involved in autophagy [44, 45] (Chapter 2.5.2).

2.3.3 JMY

The last NPF interesting for this study is the multifunctional actin nucleator called JMY that is most closely related to WHAMM [18]. It was shown that JMY localizes to lamellipodia in migrating cells, and its loss slowed motility while its overexpression enhanced cell migration [46]. Moreover, recent data showed that JMY localizes to vesiculo-tubular structures throughout the cytoplasm and partially interacts with vesicle-associated membrane protein-associated protein-A (VAP-A), a protein implicated in ER/Golgi vesicle transport [47]. JMY was initially discovered as a p300

cofactor that facilitates the p53 response by augmenting p53-dependent transcription and apoptosis [48]. It was found to carry a WCA domain containing a series of WH2 motifs (WWWCA) that promotes *in vitro* actin nucleation. Moreover, it possesses a PP and a CC sequence at its N-terminus (Figure 2.5). JMY is a dual function protein as it nucleates actin filaments in the presence and absence of Arp2/3 complex [18]. It directly nucleates unbranched actin filaments but also cooperates and activates the Arp2/3 complex to polymerize branched actin filaments [46, 49]. Under basal, non-stressed conditions, JMY localizes at the leading edge of a cell, but in response to deoxyribonucleic acid (DNA) damage it accumulates in the nucleus and promotes p53-dependent apoptosis [46, 50]. This subcellular localization is controlled by a nuclear localization sequence, which has been found within the tandem WH2 domains [50]. Overexpression experiments exhibited that JMY affects integrity of the Golgi network by loss from the trans-site and impaired Vesicular stomatitis virus (VSV)-G transport in HeLa cells [47].
As WASH and WHAMM, recent publications link JMY to autophagy. It enhances the formation of autophagosomes based on its function as Arp2/3 regulator (Chapter 2.5.2).

2.4 Actin cytoskeleton manipulation by microbial pathogens

Bacteria and viruses comprise a group of highly infectious human pathogens. They possess unique adaptations that support intracellular lifestyles and have evolved numerous ways to subvert the host molecular signaling machinery. Microbial pathogens utilize mechanisms that support key infection events including invasion, replication, immune evasion, and dissemination [51]. To accomplish this, they hijack the cytoskeleton and modulate actin dynamics at the plasma membrane or in the cytosol [52].
One example for the stimulation of actin assembly is the manipulation of pathways governed by Rho-family GTPases [52]. Rac1 and Cdc42 are best known for Arp2/3 complex activation through proteins of the WASp/WAVE family [53]. Microorganisms modify eukaryotic GTPases, thereby manipulating various cellular pathways to favor microbial colonization and/or proliferation, which finally results in parasitizing and even killing the host cell [54].
Upon contact, pathogens such as *Salmonella* and *Shigella* express specialized virulence proteins known as effector proteins, which can be delivered into the host cell cytoplasm. These proteins help the bacteria to invade the host through directly or indirectly targeting the Arp2/3 complex by either mimicking NPFs or cellular upstream regulators of actin polymerization [52, 55]. The delivery of effector proteins from *Salmonella*

or *Shigella* into eukaryotic cells is a key feature of virulence and is conferred by a type III secretion system. This complex macromolecular machine transfers effector toxins directly from the bacterium into the host cell cytosol [56]. *Salmonella* is one prominent example that comprises several effector proteins. These toxins directly or indirectly manipulate actin or regulators of the actin polymerization machinery such as SipA, which promotes actin filament polymerization as well as prevents depolymerization [52, 57]. Other bacteria (e.g. *Listeria* or *Yersinia*) do not secrete virulence factors to stimulate their uptake but instead induce host-cell receptors or employ receptors at the sites of bacterial attachment and invasion [52]. However, *Listeria monocytogenes* and *Shigella flexneri* possess proteins that activate the Arp2/3 complex (i.e. act as NPFs) to promote intracellular motility, cell-to-cell spread, and rapid dissemination in the infected host [55]. In contrast to intracellular bacteria, pathogenic *E. coli* and *Helicobacter pylori* subvert actin polymerization from outside to facilitate adherence (actin pedestal formation). Extracellular pathogens such as enterohemorrhagic *E. coli* and enteropathogenic *E. coli* manipulate the actin cytoskeleton by their translocated intimin receptor, which mainly supports the bacteria to bind to the epithelial cell surface [58].

A second major type of pathogenic organisms are viruses, which can convert the normal functions of a cell to optimize its own replication as well as production. They are capable to reconfigure and reorganize the host actin cytoskeleton, thereby affecting every stage of the viral life cycle: Entry, assembly, and egress [59]. The first links between viral infection and changes of the actin cytoskeleton were described in the early 1970s [60–62]. Amongst others, cell lines exhibited diminished microfilaments and disrupted stress fibres, which involves actin remodelling mediated by Rho proteins and Rho-associated protein kinases (ROCKs) [59]. Actin is routinely engaged and exploited by infective viruses such as Respiratory syncytial virus (RSV), Simian virus 40 (SV40) and Herpes simplex virus type 1 (HSV-1). Current data suggest that F-actin is crucial for RSV assembly and budding [63]. The SV40 small tumor antigen induced disorganization of the actin cytoskeleton and loss of tight junctions in epithelial cells [64]. Moreover, it is known that early events (e.g. cell surface attachment) in the herpesvirus life cycle trigger cytoskeletal rearrangements that promote efficient virus entry. HSV-1 virus particles utilize a “phagocytosis-like” entry pathway and attachment to fibroblasts activated Cdc42 and RhoA, resulting to filopodium-like protrusions from the cell membrane. It was further shown that HSV-1 virus particles preferentially associated with these protrusions and treatment with actin-depolymerizing drugs blocked HSV-1 internalization [65].

2.5 Autophagy

Autophagy literally means "self-eating" and is a self-degradative process that happens inside all eukaryotic cells. It is crucial for balancing intracellular energy stores at critical times in development and in response to nutrient stress such as amino acid and fatty acid starvation. Autophagy also plays a prominent role in removing misfolded, ubiquitylated proteins, clearing damaged organelles (e.g. mitochondria, ER, and peroxisomes) as well as in eliminating intracellular pathogens such as bacteria [66]. Moreover, autophagy malfunction is associated with a variety of diseases, including cancer, certain neurodegenerative disorders, infectious diseases, and metabolic diseases such as diabetes [67, 68]. There are three main types of autophagy in mammalian cells: macroautophagy, microautophagy, and Chaperone-mediated autophagy (CMA) (only occurs in mammalian cells)(Figure 2.6), all of which facilitate proteolytic degradation of cytosolic components at the lysosome [66, 69]. Microautophagy is characterized by direct lysosomal engulfment of the cytoplasmic cargo by invagination or protrusion/septation of the lysosomal limiting membrane. CMA involves selective degradation of cytosolic proteins that contain a pentapeptide motif. This motif is recognized specifically by the chaperone Hsc70, which transfers protein substrates to the lysosomal membrane. Protein substrates bind to the receptor lysosome-associated membrane protein 2A (LAMP2A) and translocate into the lysosomal lumen for degradation.
In this work, I will focus on macroautophagy (referred to here as autophagy) that in contrast to microautophagy and CMA involves sequestration of a cargo and, finally, fusion with the lysosome. During this process, cells form a double-membrane sequestering compartment (phagophore), which matures into a double-membraned vacuole, known as autophagosome. The autophagosome ultimately fuses with the lysosome to form autolysosomes, which supply acid hydrolases resulting in degradation of the cargo [67–70].

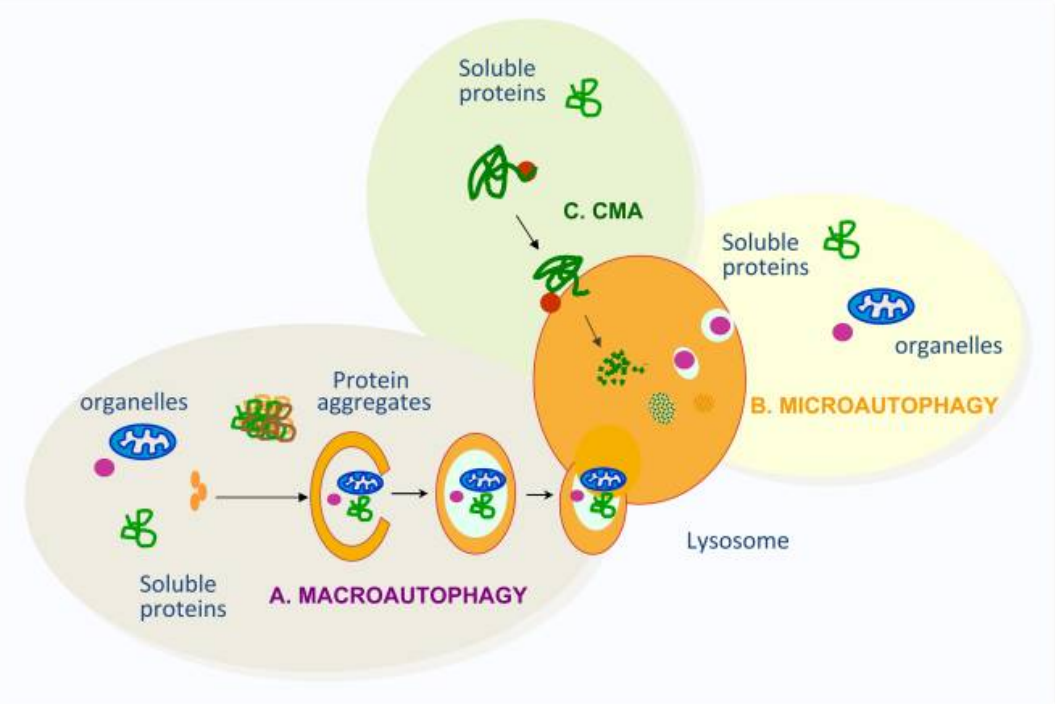

Figure 2.6: Schematic depiction of the three main types of autophagy. Macroautophagy degrades soluble proteins, damaged organelles, and protein aggregates upon their sequestration into a *de novo*-formed double membrane vesicle (termed autophagosome) that fuses with the lysosome to form a structure known as autolysosome. (B) Microautophagy also degrades soluble proteins and damaged organelles by direct lysosomal engulfment in small vesicles that are formed from invaginations or protrusion/septation of the lysosomal membrane. (C) CMA contributes to the selective degradation of soluble proteins, which are targeted to lysosomes without any type of membrane deformity [71].

2.5.1 Molecular regulation of autophagy in mammalian cells

Autophagy is an evolutionarily conserved pathway and genetic screens in *Saccharomyces cerevisiae* set the basis for studies in mammalian cells. They also led to the identification of more than 30 autophagy-related (ATG) genes, many of which have known orthologs in higher eukaryotes [69, 70].
Autophagy starts with the formation of a double membrane structure termed phagophore or isolation membrane (Figure 2.7). Various studies have implicated several membrane sources that make up the phagophore such as ER, mitochondria, the Golgi apparatus, and the plasma membrane [72].

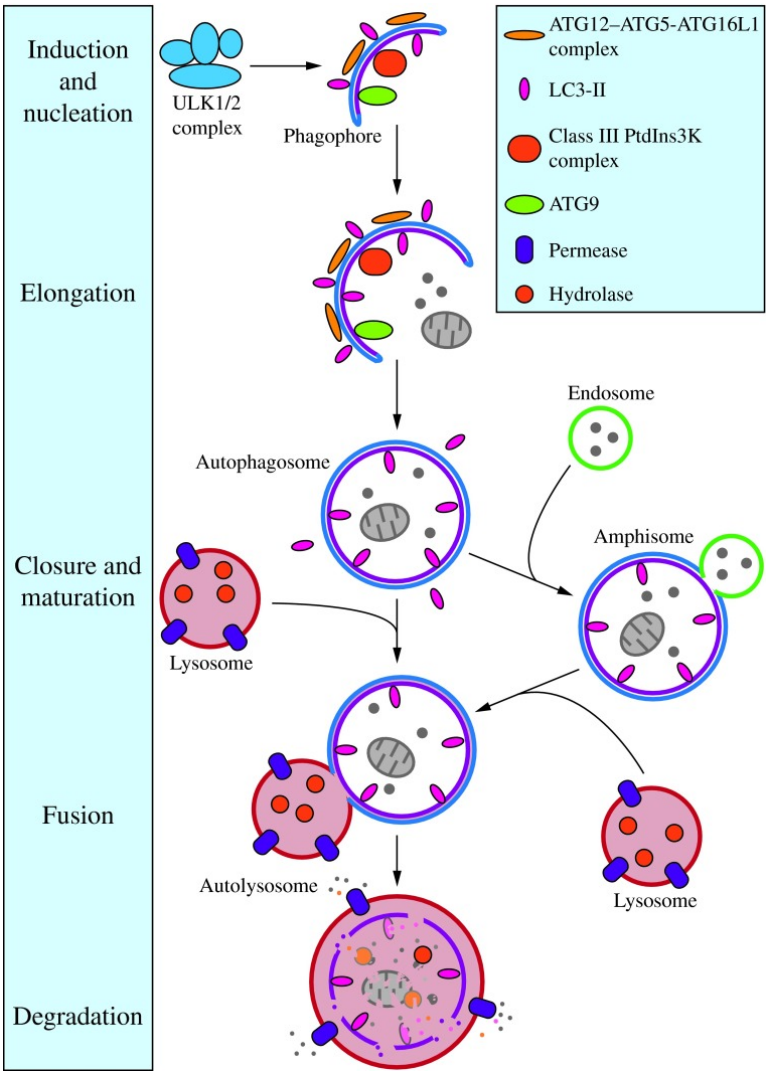

Figure 2.7: The process of autophagy in mammalian cells. During starvation, autophagy is initiated by the Unc-51-like kinase family (ULK1/2) complex and nucleation of the phagophore occurs. This double membrane structure elongates with the help of the ATG12–ATG5-ATG16L1 complex, the class III phosphatidylinositol 3-kinase (PtdIns3K) complex, LC3-II, and ATG9. The expanding phagophore closes around its substrate to form an autophagosome and LC3-II is cleaved from the outer membrane. The autophagosome then fuses with a lysosome to form an autolysosome. The inner membrane of the autophagosome, along with engulfed compounds, are degraded by acid hydrolases and exported back into the cytoplasm for reuse by the cell. In some cases, the autophagosome receives input from the endocytic pathway and may fuse with an endosome. The resulting amphisome fuses with the lysosome [68].

In yeast, initiation of autophagy begins at a single perivacuolar site termed phagophore assembly site, whereas in mammalian systems the initiation takes place at multiple sites througout the cytoplasm [68, 72]. It was shown that ER-subdomains enriched in phosphatidylinositol 3-phosphate (PI3P), called omegasomes, are a major initia-

tion site in mammalian cells [70, 73, 74]. Following the induction of autophagy, the phagophore begins to expand and then closes to an autophagosome [68, 70]. Its diameter ranges from 0.4 to 0.9 µm in yeast and 0.5 to 1.5 µm in mammals [68]. The outer membrane of these double-membrane vesicles will fuse with lysosomes to release their cargo into the acidic and hydrolytic lumen of these organelles. Exposed to the acidic environment, the autophagosome inner membrane as well as the autophagic content (e.g. proteins, lipids, nucleic acids) are degraded and exported back into the cytoplasm through lysosomal permeases and transporters, where they can be reused in biosynthetic processes or to generate energy [68, 75]. In mammals, the autophagic pathway intersects with the endocytic pathway when autophagosomes fuse with early or late endosomes forming amphisomes, which then fuse with lysosomes to generate autolysosomes [68]. Important to highlight is that all these events such as autophagosome maturation, intracellular transport, and fusion with lysosomes and endosomes involves actin- and microtubule-mediated motility [76]. There are four steps in the autophagic process: induction, nucleation, expansion, and maturation (see the following).

Induction. Induction of autophagosome formation in mammals is regulated by the ULK1/2 complex, which consists of ULK1/2-ATG13-RB1CC1/FIP200 [68]. Directly bound to ATG13 is C12orf44/ATG101 that protects ATG13 from proteasomal degradation [77]. Under nutrient-rich conditions, the key upstream negative regulator of autophagy termed mammalian target of rapamycin complex 1 (mTORC1) associates with the complex and inactivates ULK1/2 and ATG13 by phosphorylation. Upon nutrient starvation, mTORC1 is released from the complex, resulting in partial dephosphorylation of its substrates and induction of autophagy [68, 78].

Nucleation. The next step following the initiation of autophagy is the recruitment of the ATG14-containing class III PtdIns3K complex that phosphorylates phosphatidylinositol to generate PI3P, a phospholipid central for membrane trafficking processes [68, 79]. The formation of phagophores requires the class III PtdIns3K complex, which consists of PIK3C3/VPS34, PIK3R4/p150, and Beclin 1. The complex either functions in autophagy or in the endocytic pathway by interacting with UVRAG. The UVRAG-associated PtdIns3K complex was shown to play an essential role in autophagosome formation, but also in later stages of autophagosome development [68].

Elongation. Phagophore expansion requires ubiquitin-like proteins, which are part of two distinct conjugation systems. The first system involves formation of the ATG5, ATG12 and ATG16L1 complex that associates with the phagophore membrane, but dissociates from fully formed autophagosome [68]. The second ubiquitin-like system crucial for phagophore expansion is the Atg8/microtubule associated protein 1 light-chain

3 (MAP1LC3) system (hereafter referred to as LC3) that is associated with closure, hemi-fusion, or transport of the autophagosome during its maturation [80]. Atg8/LC3 is processed by the protease ATG4(B) to expose a C-terminal glycine residue. The cleaved form of LC3 is referred to as LC3-I and is then phosphatidylethanolamine (PE)-conjugated by sequential activation of Atg7 (E1-like enzyme), Atg3 (E2-like enzyme), and the Atg12 complex. The lipid-modified form of LC3 is called LC3-II, and can be degraded during autophagy. LC3 itself is a widely used marker to monitor autophagic flux [68, 80]. Although there is only one Atg4 and one Atg8 protein in yeast, there are four isoforms of ATG4 and several Atg8-like proteins in mammals. The latter are classified into the MAP1LC3-A/-B/-C, GABARAP, and GABARAP-L1/-L2 subgroups, however the functional characterization has mostly been focused on LC3 [80]. Another ATG protein that is required for phagophore elongation is the multi-spanning transmembrane protein ATG9. It has a key role in directing membrane sources from donor organelles such as ER or Golgi for autophagosome formation [81]. Under nutrient-rich conditions, ATG9 travels to the trans-Golgi network (TGN) and the endosomal system. Upon nutrient starvation, ATG9 localizes with autophagosomal marker (e.g. LC3) [68, 82].

Autophagosome completion and fusion. Once the phagophore is fully expanded, it is sealed to form an autophagosome, which traffics to and fuses either directly with a lysosome or with components of the endocytic pathway, such as endosomes or multivesicular bodies [76].

2.5.2 NPFs and their role during autophagy

It was demonstrated that the actin cytoskeleton is necessary during early events of autophagsome formation and reports on WASH, WHAMM, and JMY confirmed a link between the Arp2/3 complex and mammalian autophagy [19, 83].

The pentameric WASH complex colocalizes with autophagic markers such as Atg5, LC3-II and p62, and data revealed a role of WASH in the early stages of autophagy [76]. However, its role in autophagy appears controversial. In the first report, WASH-complex deficiency causes early embryonic lethality at embryonic day 7.5 and mutant mice exhibited extensive autophagy. WASH suppressed Beclin 1 ubiquitination by Ambra1, an event required for the activation of VPS34 [25]. A follow-up study identified that the E3 ligase RNF2 associates with AMBRA1 leading to its ubiquitination and degradation with the help of WASH [84]. A more recent report showed that loss of WASH function in *Drosophila* also leads to a dramatic increase of autophagy [26]. Interestingly, another study revealed that WASH functions to promote autophagy.

Short interfering RNA (siRNA)-mediated silencing of WASH causes an accumulation of ATG9A at the Golgi apparatus and a mild, but statistically significant decrease of LC3-positive structures in nutrient-starved cells, indicating an impaired ATG9A trafficking, which is required for autophagosome biogenesis [36]. Future investigations should clarify whether WASH is a positive or negative regulator of autophagy.
The two related NPFs, WHAMM and JMY, were also described in autophagosome biogenesis [44,85]. WHAMM colocalizes with autophagy markers (i.e. LC3, DFCP1, and p62) and additionally to Arp2/3 complex-enriched actin comet tails. Gene silencing of WHAMM resulted in fewer actin comet tails, and reduced the number of autophagosomes. Deleting the first 169 amino acids impaired autophagosome localization and led to the assumption that WHAMM interacts with the phagophore membrane through its N-terminal region [44]. Recently, WHAMM has also been implicated in an inherited disorder called Galloway-Mowat syndrome (GMS). Patient cells harbor mutations in the *wdr73* as well as the closely linked *whamm* gene and exhibit cytoskeletal irregularities and defects in autophagosome biogenesis. Reexpression of wild type (WT) WHAMM restored defects in autophagy in patient cells. In addition, the study showed that WHAMM is recruited to nascent autophagosomes by binding to PI3P, a key player in membrane dynamics and trafficking regulation [45,86].
JMY was shown to enhance the formation of elongated membranes containing LC3, suggesting a participation in the autophagy maturation process. As observed for WHAMM, removal of the first amino acids (119) of JMY caused a loss of autophagosome localization. It has been discovered that JMY harbors an LC3-interacting region (LIR) within its N-terminus, which targets the protein to LC3-containing autophagosome. Mutation of the LIR resulted in lack of autophagosomal localization of JMY and prevented its colocalization with foci of F-actin. Gene silencing by siRNA or mutations that abrogate JMY´s ability to activate Arp2/3 resulted in decreased LC3-II levels and reduced the number of autophagosomes [85].

2.6 CRISPR/Cas9 gene editing

The Clustered Regularly Interspaced Short Palindromic Repeats (CRISPR)/Cas9 was originally discovered in bacteria and archaea as an adaptive immune system as a way of protecting against viruses and plasmid DNA. It uses RNA-guided nucleases to cleave these foreign genetic elements. Short DNA sequences from invaders are incorporated at CRISPR loci within the bacterial genome and serve as "memory" of previous infection (Figure 2.8). Re-infection triggers the complementary mature CRISPR RNA (crRNA) to find a matching sequence, providing RNA-guided Cas nuclease the specificity to form a double-strand break at specific foreign nucleic acids [87].

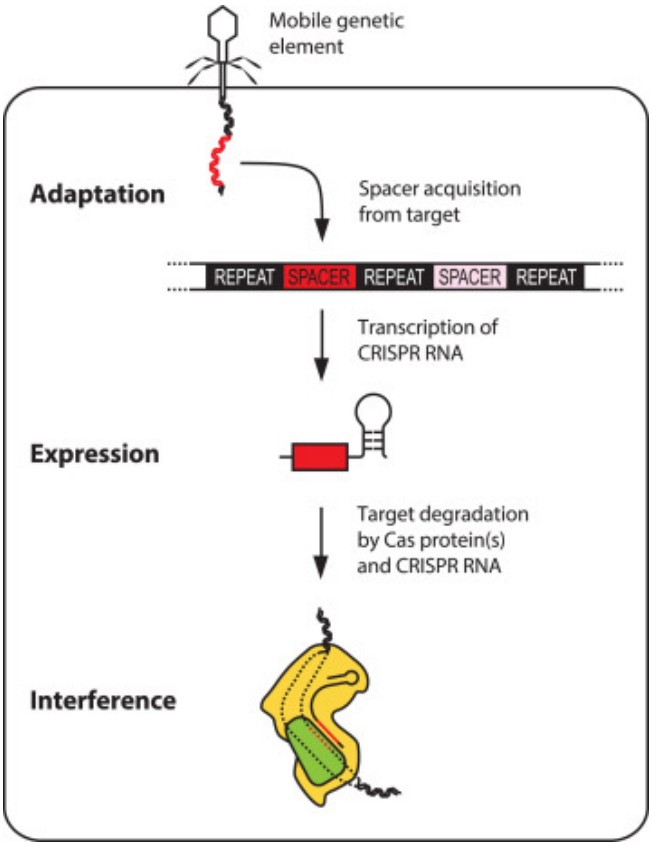

Figure 2.8: The three major phases of CRISPR/Cas immune systems. The key steps of CRISPR/Cas immunity comprise adaptation, expression and interference. 1.) Adaptation: Cas proteins excise the new spacer derived from foreign DNA and insert it into the CRISPR locus. 2.) Expression: The CRISPR sequence is transcribed and processed into multiple short crRNA molecules, each harboring a single spacer sequence and part of the adjoining repeat sequence. 3.) Interference: The crRNAs are assembled and associate with and guide bacterial molecular machinery to a matching target sequence of either invading element or their transcripts. The molecular machinery cuts up and destroys the invading DNA [87,88].

Three types (I-III) of CRISPR have been identified in bacterial and archaea hosts, wherein each system comprises a cluster of Cas genes, noncoding RNAs and direct repeats (repetitive elements). These repeats are interspaced by short variable sequences (protospacer) derived from exogenous DNA targets, and together they constitute the crRNA array. Within the DNA target, each protospacer is associated with a protospacer adjacent motif (PAM), which varies depending on the specific CRISPR system. Through this PAM sequence, the Cas9 select its target sites directly 3´of the target sequence. The CRISPR/Cas9 technology facilitates targeted DNA double strand breaks at specific loci of interest and stimulates genome editing via non-homologous end joining (NHEJ) or homology directed repair (HDR). NHEJ leaves scars in form of *insertion or deletion* (*indel*) mutations that might occur within a coding exon lead-

ing to frameshift mutations and premature stop codons. HDR is an alternative major DNA repair pathway and can be leveraged to generate precise, defined modifications at a target locus [89].

2.7 Project aims

The actin cytoskeleton is a critical target of many bacteria and viruses at multiple stages of infection. A large number of pathogens utilize actin-based motility to spread within and between mammalian host cells. This is frequently associated with hijacking of the Arp2/3 complex, but requires Arp2/3 complex activators, namely NPFs. Finally, actin cytoskeleton dynamics also appear to play essential roles in autophagy. Autophagy, however, can act as anti-pathogen defense or be utilized by selected pathogens to promote infection.

Hence, I wanted to elucidate the functional roles of the three most recently identified Arp2/3 complex activators (NPFs), which have all been implicated in endomembrane traffic and/or autophagy. Genetic inactivation of these proteins was approached by generating somatic knockouts (KOs) in tissue cultured cells using the CRISPR/Cas9 technology. On basis of preliminary phenotypic observations and expression profiling, I finally selected subprojects to uncover the relevance of selected actin regulators during homeostasis, autophagy, and infection with selected pathogens.
Together, this thesis had the following aims:

1. Establish CRISPR/Cas9 technology-mediated gene inactivation of the NPFs WASH, WHAMM, and JMY in murine NIH/3T3 fibroblasts as well as in human U-2 OS cells.

2. Characterize cellular phenotypes of obtained KO cell lines with special emphasis on ER- and Golgi morphology as well as on autophagy.

3. Perform transcription profiling to identify pathways, which are differentially regulated dependent on the respective genotypes.

4. Perform infection assays with selected viruses in WT *versus* KO cells and identify provisional alterations of the viral life cycle in the host.

3 Materials and Methods

3.1 Chemicals and buffers

3.1.1 Chemicals and reagents

Chemicals, reagents, and solvents were purchased from AppliChem, Invitrogen, J.T. Baker, Biochrom, Calbiochem, Merck Millipore, New England Biolabs, Promega, Qiagen, Roche, Roth, Serva, Sigma-Aldrich and Thermo Fisher Scientific. The analytical purity was *per analysis*. Special equipment, consumables, and chemicals are listed in the corresponding paragraphs.

3.1.2 Buffers

All buffers were prepared with deionized water and, if suitable, autoclaved prior to use. Deionized water was purified by a Milli-Q-System (Merck Millipore). Heat-sensitive components were sterile-filtered and added to the autoclaved medium. Buffers not listed below (Table 3.1), are listed in the corresponding method description.

Table 3.1: Buffers

Name	Components
Amplex lysis buffer I	50 mM Tris 2 mM $CaCl_2$ 80 mM NaCl 1% (v/v) Triton X-100
Amplex lysis buffer II	100 mM Tris 2 mM $CaCl_2$ 100 mM NaCl 1% (v/v) NP-40
Buffer A, pH 7.5	50 mM Tris 150 mM NaCl

	5 mM $MgCl_2$ 1 mM DTT
Elution buffer	50 mM Tris, pH 8.0 10 mM reduced glutathione
Flow cytometry buffer	Phosphate buffered saline (PBS), 1x 2% (v/v) FBS 2 mM EDTA
DNA lysis buffer	100 mM Tris, pH 8.5 5 mM EDTA, pH 8 0.2% (w/v) SDS 200 mM NaCl
NP-40 lysis buffer	50 mM Tris-HCl, pH 8 100 mM NaCl 2 mM MgCl 1% (v/v) Nonidet P-40 100 mM NaF 1 mM Na_3VO_4 1x Protease inhibitor cocktail 10% (v/v) Glycerol
PBS, 1x, pH 7.4	137.9 mM NaCl 2.7 mM KCl 8 mM Na_2HPO_4 1.5 mM KH_2PO_4

Resolving buffer	1.5 M Tris, pH 8.8 0.4% (w/v) SDS
SDS loading buffer, 8x	1.5 M Tris-HCl, pH 6.8 16% (w/v) SDS 0.5% (w/v) Bromophenol blue 33% (v/v) ß -Mercaptoethanol
SDS running buffer, 1x	25 mM Tris, pH 6.8 192 mM Glycine 0.1% (w/v) SDS
Stacking buffer	0.5 M Tris, pH 6.8 0.5% (w/v) SDS
Tris-acetate EDTA (TAE) buffer, 1x	40 mM Tris base 20 mM Acetate 1 mM EDTA
Tris-buffered saline with Tween (TBS-T)-20 1x	20 mM Tris-HCl, pH 7.6 137 mM NaCl 0.1% (v/v) Tween-20
Tris lysis buffer	50 mM Tris, pH 7.5 150 mM NaCl 1 mM EDTA 1% (v/v) Triton X-100

3.2 Bacterial culture

3.2.1 Bacterial strains

The following bacterial strains were used in this study (Table 3.2). Liquid bacterial cultures were grown in Lysogeny broth (LB) medium at 37°C with agitation (Infors).

Table 3.2: Bacterial strains

Bacterial strain	Source	Application
Escherichia coli (E. coli) DH5α	Melanie Brinkmann HZI, Braunschweig	Transformation
E. coli TOP10	Ingo Schmitz HZI, Braunschweig	Transformation
E. coli BL21 (DE3)	Susanne Häußler HZI, Braunschweig	Transformation Protein purification
E. coli Rosetta (Chloramphenicol (Cm) resistance)	Novagen	Protein purification

3.2.2 Bacterial media and antibiotics

All media were prepared with deionized water and autoclaved prior to use. Respective antibiotics were added from sterile filtered stock solutions after the medium had cooled down below 50°C.

Table 3.3: Bacterial media and antibiotics

Name	Concentration/Component
LB medium	10 g/L bacto-tryptone 5 g/L bacto-yeast extract 10 g/L NaCl
LB agar plates	0.4% (w/v) agar in LB medium

Ampicillin (Amp)	100 µg/mL
Kanamycin (Kana)	50 µg/mL
Cm	25 µg/mL
Gentamycin (Gm)	10 µg/mL

3.3 Molecular biological methods

Molecular biological standard methods were performed according to Maniatis *et al.* [90], if not stated otherwise. (Restriction) Enzymes and the appropriated buffer were obtained from Epicentre, New England Biolabs, Promega, Roche and Thermo Fisher Scientific.

3.3.1 Oligonucleotides

All oligonucleotides used in this study were purchased from Eurogentec. Oligonucleotides were diluted in deionized water and stored as 100 µM stock solutions at -20°C. Single guided ribonucleic acid (sgRNA) molecules were designed with the help of the online tools crispr.mit.edu and crispr.cos.uni-heidelberg.de to target the gene of interest (Table 3.4).

Table 3.4: sgRNAs applied for gene editing

Target	Organism	Exon	Sequence
WASH	Mouse	2	*top* GCGACGAGAGGAGGCAATCC *bottom* GGATTGCCTCCTCTCGTCGC
WHAMM	Mouse	1	*top* GTGGCTGGGTTCCGCTGCGTG *bottom* CACGCAGCGGAACCCAGCCAC
JMY	Mouse	1	*top* GGAGACACTCGAGTCCGACT *bottom* AGTCGGACTCGAGTGTCTCC

WASH	Human	4	*top* TCTTCACGGGCGCCCAGGAC *bottom* GTCCTGGGCGCCCGTGAAGA
		5	*top* GTGTGCGTGAGCACCAAGCC *bottom* GGCTTGGTGCTCACGCACAC
WHAMM	Human	2	*top* AGAGGAAGATGAAGCATACC *bottom* GGTATGCTTCATCTTCCTCT
		3	*top* GGATGACCTAGGTCCTAGAA *bottom* TTCTAGGACCTAGGTCATCC
JMY	Human	2	*top* GCTTCTGGACTTGTATCAGA *bottom* TCTGATACAAGTCCAGAAGC
		4	*top* GAAATTTGGTAAAGCATCAT *bottom* ATGATGCTTTACCAAATTTC

Moreover, oligonucleotides were designed flanking the region of interest in order to verify gene modifications (Table 3.5).
Primer used in quantitative polymerase chain reaction (qPCR) are listed in Table 3.6.

Table 3.5: Primer sequences for sgRNA validation

Target	**Organism**	**Sequence**	**Product size**
WASH	Mouse	*fw* ATAGGCAGAGGGGTGAGTGT *rv* ACACTGGGCATTAGTTGGGT	330 bp
WHAMM	Mouse	*fw* TAACCAACTCCAGACAGCCTC *rv* TCGTGACAGGTGACGGCGAA	272 bp
JMY	Mouse	*fw* GAACCGCTCCTCTGTCTCTG *rv* ATTGTCTCTTCTGAGAGCCGC	330 bp

WASH	Human	*fw* GTTCTCCAGTGCCAAGTACC *rv* GGTTCTCGGTGGTGTTGAAG	281 bp
WHAMM	Human	*fw* GCTGCGCCAGGTTATTCAAG *rv* CAACCTGGGAATTGCTGTGG	409 bp
JMY	Human	*fw* TGACCGAGCAGGAAATCGAC *rv* CTCATGTCTCGGAATGGCTG	343 bp
		fw GAAGATGCTGATTGGCAGCG *rv* GTGCATGTTTCCGCTGTTCC	255 bp

Table 3.6: Primer sequences applied in qPCR

Target	**Organism**	**Sequence**
DHCR7	Mouse	*fw* GTACCACCCTGTGCAGCTC *rv* GGTCCTTCTGATGGTTGGTCAT
SOAT-1	Mouse	*fw* TTATGAAGGAAGTTGGGTGCCA *rv* AATGGAGAAGGTTGTGAGTGCA

3.3.2 Plasmid constructs

Plasmids used in this thesis are shown in Table 3.7.

Table 3.7: Plasmid constructs

Vector	**Resistance**	**Characteristics**	**Reference**
pSpCas9(BB)-2A-GFP (pX458)	Amp	Cas9 from *S. pyogenes* with 2A-enhanced green fluorescent protein (EGFP)	Addgene

		Cloning backbone for sgRNA	
pGEX-6P-3	Amp	Provides Glutathione S-transferase (GST) fusion	Pharmacia
pX458-WASH-2-Mouse	Amp	Encodes sequence for KO of murine WASH, Exon2 (see Table 3.4)	This dissertation
pX458-WASH-4-Human	Amp	Encodes sequence for KO of human WASH, Exon4 (see Table 3.4)	This dissertation
pX458-WASH-5-Human	Amp	Encodes sequence for KO of human WASH, Exon5 (see Table 3.4)	This dissertation
pX458-WHAMM-1-Mouse	Amp	Encodes sequence for KO of murine WHAMM, Exon1 (see Table 3.4)	This dissertation
pX458-WHAMM-2-Human	Amp	Encodes sequence for KO of human WHAMM, Exon2 (see Table 3.4)	This dissertation
pX458-WHAMM-3-Human	Amp	Encodes sequence for KO of human WHAMM, Exon3 (see Table 3.4)	This dissertation

pX458-JMY-1-Mouse	Amp	Encodes sequence for KO of murine JMY, Exon1 (see Table 3.4)	This dissertation
pX458-JMY-2-Human	Amp	Encodes sequence for KO of human JMY, Exon2 (see Table 3.4)	This dissertation
pX458-JMY-4-Human	Amp	Encodes sequence for KO of human JMY, Exon4 (see Table 3.4)	This dissertation
pGEX-6P-3-WHAMM$_{AA696-809}$	Amp	Encodes GFP-fused human WHAMM	This dissertation
pGEX-6P-1-JMY$_{AA824-983}$	Kana	Encodes GFP-fused VVVCA domain of murine JMY	Jan Hänisch, HZI
pEGFP-C2-DFCP1	Kana	Encodes GFP-fused DFCP1	Axe, Babraham Institute [91]
EGFP-C1-ERGIC53	Kana	Encodes GFP-fused ERGIC	Ben-Tekaya [92]
EGFP-C1-VAP-A	Kana	Encodes GFP-fused VAP-A	Kai Schlüter, University Münster

3.3.3 Experimental design of sgRNAs and cloning into pX458

Genome editing of murine NIH/3T3 fibroblasts and human U2-OS cells was performed with the CRISPR/Cas9 technology. Selected DNA target sequences were provided to a CRISPR design tool (CRISPR.mit.edu or CCTop). These online softwares offer the sequences necessary for designing the sgRNA constructs (20 bp), assay target

modification efficiency and assess cleavage at potential off-target sites [89]. To generate pX458(sgRNA), a pair of annealed oligonucleotides (Table 3.4) was cloned into the expression plasmid pX458. This plasmid allows the simultanous expression of sgRNA, SpCas9 and contains EGFP as a selection marker.

First, the top and bottom strands of oligonucleotides of the different sgRNAs were phosphorylated and annealed according to the following protocol:

100 µM sgRNA top
100 µM sgRNA bottom
1 μL T4 ligation buffer, 10x
1 µL T4 Polynucleotide kinase (10,000 U/mL)
ad 10 µL ddH_2O

The reaction mixture was incubated in a thermocycler (Biometra, TGradient) using the following parameters:

37°C for 30 min
95°C for 5 min
Ramp down to 25°C at 5°C/min

Phosphorylated and annealed oligonuleotides were diluted 1:200 and cloned into pX458:

100 ng pX458
2 µL diluted oligo duplex
2 µL Tango buffer, 10x
1 µL Dithiothreitol (DTT), 10 mM
1 µL ATP, 10 mM
1 µL FastDigest *BbsI*
0.5 µL T4 DNA ligase (400,000 U/mL)
ad 20 µL ddH_2O

The reaction mixture was incubated in a thermocycler using the following parameters:

Cycles 1-6, 37°C for 5 min, 21°C for 5 min

The ligation reaction was then treated with PlasmidSafe to digest any residual linearized DNA:

11 µL Ligation reaction
1.5 µL PlasmidSafe buffer, 10x
1.5 µL ATP, 10 mM
1 µL PlasmidSafe exonuclease (10,000 U/mL)
ad 15 µL ddH_2O

PlasmidSafe reaction was incubated at 37°C for 30 min, followed by 70°C for 30 min and stored at -20°C, if necessary.
In order to verify successful cloning from sgRNA into pX458, a double digestion with FastDigest restriction enzymes *BbsI* and *EcoRV* was performed for 20 min at 37°C and checked by agarose gel electrophoresis (Chapter 3.3.4).

1 μg DNA
2 µL FastDigest buffer, 10x
0.5 µL FastDigest *BbsI*
1 µL FastDigest *EcoRV*
ad 20 µL ddH_2O

3.3.4 Agarose gel electrophoresis

DNA samples were analyzed via agarose gel electrophoresis. The samples were loaded into pre-cast wells in the gel and a voltage of 120 V was applied (Biorad PowerPac Basic Electrophoresis Power Supply). Due to its negatively charged phosphate backbone, DNA migrates to the positively charged anode. Depending on the fragment size, 1-2% (w/v) agarose was dissolved in 1x TAE buffer using a microwave. After cooling down to approximately 50°C, the gel was supplemented with Midori Green, which binds to DNA, but less aggressively than ethidium bromide. The DNA sample was mixed with 6x Orange DNA loading dye. Quick-Load® 100 bp and/or 1 kb DNA ladder were loaded as molecular weight standards to estimate fragment sizes. The detection was carried out under UV light using Intas GelJet Imager.

3.3.5 Cloning of *egfp-whamm* into the pGEX-6P-3 vector

In order to produce high levels of WHAMM, EGFP-WHAMM$_{AA696-809}$ was cloned into pGEX-6P-3, a bacterial vector expressing GST fusion proteins. In the first step, *egfp-whamm* was digested with two restriction enzymes for 1 h at 37°C:

5 µg DNA
2 µL FastDigest buffer, 10x
1 µL FastDigest *Eco72I*
1 µL FastDigest *NotI*
ad 20 µL ddH_2O

The reaction was stopped by heat inactivation for 5 min at 80°C and obtained *whamm* fragment was analyzed on 2% agarose (Chapter 3.3.4). DNA was cleaned from the agarose gel with NucleoSpin® Gel kit (Table 3.12) as recommended by the manufacturer.
Furthermore, pGEX-6P-3 was digested with *SmaI* for 1 h at 25°C and *NotI* for 1 h at 37°C:

1 µg DNA
2 µL FastDigest buffer, 10x
1 µL FastDigest *SmaI*
1 µL FastDigest *NotI*
ad 30 µL ddH_2O

The reaction was stopped by heat inactivation for 5 min at 80°C. To avoid undesired religation of the linearized vector, desphosphorylation was applied for 15 min at 37°C:

30 µL DNA
10 µL Antarctic phosphatase reaction buffer, 10x
1 µL Antarctic phosphatase (5,000 U/mL)
ad 100 µL ddH_2O

The reaction was stopped by heat inactivation for 5 min at 70°C and linearized pGEX-6P-3 was analyzed on a 1% (w/v) agarose gel (Chapter 3.3.4). DNA was cleaned as previously described.
Subsequently, $WHAMM_{AA696-809}$ was ligated into linearized pGEX-6P-3 resulting in pGEX-6P-3-$WHAMM_{AA696-809}$. Ligations were performed overnight at 14°C according to the following protocol:

0.3 µg plasmid DNA
0.9 µg insert DNA
1 µL Ligation buffer, 10x
1 µL T4 DNA ligase (400,000 U/mL)
ad 20 µL ddH_2O

pGEX-6P-3-WHAMM$_{AA696-809}$ was transformed into competent *E. coli* to allow protein expression as described in chapter 3.5.3.

3.3.6 Transformation of plasmid DNA into *E. coli*

Chemically competent *E. coli* strains (DH5α, TOP10 or BL21 (DE3)) were thawed on ice and mixed with 100 ng DNA. The suspension was incubated on ice for 10 min to allow DNA attachment followed by a heat shock at 42°C for 1 min (Thermomixer, Eppendorf®Model 5436) to induce DNA uptake. Transformed bacteria were incubated on ice as previously and supplemented with 1 mL LB medium. The cell suspension was incubated at 37°C for 1 h while shaking in order to develop antibiotic resistance. Afterwards, bacteria were spun down for 10 s at (Heraeus Biofuge pico), an appropriate amount of LB medium was removed and the bacterial pellet was resuspended in the remaining medium. Bacteria were transferred onto pre-warmed LB agar plates with the appropriate antibiotic for selection and were incubated overnight at 37°C (Incubator Heraeus instruments).
TOPO® Cloning ligation reaction was transformed into electrocompetent *E. coli* DH5α. Bacteria were thawed on ice, ligation reaction was added and the suspension was incubated for 2 min. Bacteria were given into a 0.2 cm GenePulser electroporation cuvette (Biorad) followed by electroporation with GenePulser® II (Biorad). Default setting applied for electroporation was: 25 µF, R = Ω and V = 2.3 kV. Immediately after the electrical pulse, 1 mL LB medium was added and the cell suspension was incubated at 37°C for 1 h while shaking. Bacteria were spun down and 900 µL of LB medium were removed. The pellet was resuspended in the remaining 100 µL, spread on LB agar plates containing kana and incubated overnight at 37°C.

3.3.7 Isolation of plasmid DNA from *E. coli*

Plasmid DNA was isolated using a kit from Macherey & Nagel (Table 3.12) following the manufacturer´s instructions. DNA concentration and purity was determined by DeNovix Spectrophotometer.

3.3.8 Genomic DNA isolation

Single colony-derived strains were expanded and cultivated to 90% confluency. Standard trypsinization was performed and cells were lysed adding 200 µL DNA lysis buffer containing 0.5 mg /mL proteinase K (20 mg/mL). Samples were incubated overnight at 55°C with agitation. Nucleic acid extraction was performed by a standard ethanol

precipitation procedure. 700 µL 100% ice-cold ethanol were added and samples were centrifuged at 16,000 xg at 4°C for 30 min (Thermo Fisher Scientific, Fresco 21). The supernatant was removed and samples were washed with 400 µL 70% ice-cold ethanol. Samples were dried at 45°C for 20 min. Subsequently, 100 µL deionized water were added and DNA was dissolved at 4°C overnight. Next day, DNA concentration and purity was determined as previously.

3.3.9 PCR

Amplification of murine genes by PCR

Isolated genomic DNA from NIH/3T3 KO cells was used as template in a PCR. PCR reactions were carried out in 50 µL volume in PCR strips (Kisker, G003-SF) and reaction cycles were performed in a thermocycler (PeqStar). Amplification of DNA was performed using GoTaq G2 flexi DNA polymerase. Primer employed in PCR reactions are listed in Table 3.5. Reaction set ups and temperature programs for murine genes are listed in Table 3.8 and Table 3.9, respectively. Taq DNA polymerase exhibits 5´-3´ exonuclease activity and allows an DNA extension of 1 kb/60 s. To overcome amplification failure and low DNA yield, the PCR-enhancing agent Dimethylsulfoxide (DMSO) was applied. It is used as an additive to aid PCR amplification of GC rich targets. PCR products were analyzed via agarose gel electrophoresis (Chapter 3.3.4). To avoid any residual enzyme activity, appropriate PCR products were either purified from reaction mixtures with PCR clean-up kit or from agarose gels (Table 3.12) as previously described following the manufacturer´s recommendations.
To screen and identify gene mutations in the DNA of potential NIH/3T3 KO cells, purified PCR products were cloned into a sticky end TOPO vector for 5 min at room temperature according to the following protocol:

2 µL DNA
1 µL salt
0.5 µL pCR™4-TOPO® vector
2.5 µL ddH_2O

DNA was finally transformed into electrocompetent bacteria as described in chapter 3.3.6.

Table 3.8: PCR reaction mixtures of murine WASH, WHAMM and JMY

Component	Final concentration
DNA template	1 ng/µL
5x Colorless GoTaq® Reaction Buffer	1x
Forward primer, 10 µM	0.2 µM
Reverse primer, 10 µM	0.2 µM
$MgCl_2$, 25 mM	2 mM
Deoxyribonucleotide triphosphates (dNTPs), 10 mM	0.2 mM
DMSO	3%
Polymerase, 5 U/µL	0.05 U/µL
Sterile deionized H_2O	ad 50 µL

Table 3.9: PCR cycling program of murine [1]WASH, [2]WHAMM and [3]JMY

Step	Purpose	Condition
1	Initial denaturation	95°C for 120 s
2	Denaturation	95°C for 30 s
3	Primer annealing	[1]60.7°C for 30 s [2]65.7°C for 30 s [3]67°C for 30 s
4	DNA elongation	[1,3]72°C for 40 s [2]68°C for 40 s
5	Repetion steps 2-4	35x
6	Final DNA elongation	[1,3]72°C for 5 min [2]68°C for 5 min
7	Stop of reaction	4°C (Hold)

Amplification of human genes by PCR

Inspection of human U-2 OS cells was performed with complementary DNA (cDNA) as template in a PCR. Therefore, RNA was isolated and used to generate cDNA by a reverse transcription PCR (Chapter 3.3.10). PCR reactions were carried out as previously described. Primer employed in PCR reactions are listed in Table 3.5. Reaction set ups and temperature programs for human genes are listed in Table 3.10 and Table 3.11, respectively.

Table 3.10: PCR reaction mixtures of human WASH, WHAMM and JMY

Component	Final concentration
cDNA template	1 ng/µL
5x Colorless GoTaq® Reaction Buffer	1x
Forward primer, 10 µM	0.2 µM
Reverse primer, 10 µM	0.2 µM
dNTPs, 10 mM	0.2 mM
Polymerase, 5 U/µL	0.05 U/µL
Sterile deionized H_2O	ad 50 µL

Table 3.11: PCR cycling program of human [1]WASH, [2]WHAMM and [3]JMY

Step	Purpose	Condition
1	Initial denaturation	95°C for 120 s
2	Denaturation	95°C for 30 s
3	Primer annealing	[1,2,3]62°C for 30 s
4	DNA elongation	72°C for 40 s
5	Repetion steps 2-4	35x
6	Final DNA elongation	72°C for 5 min
7	Stop of reaction	4°C (Hold)

3.3.10 RNA extraction, cDNA synthesis and qPCR

For successful validation of human KOs by conventional PCR, 5x10^5 cells were seeded onto 6-well plates and grown for 24 h. RNA was isolated using RNeasy Mini kit (Table 3.12) according to the manufacturer´s recommended protocol. RNA was applied as template in a reverse transcription reaction to synthesize cDNA using transcriptor first strand cDNA synthesis kit (Table 3.12) following the manufacturer´s instructions. cDNA served as template in a PCR reaction (Chapter 3.3.9). RNA isolation, cDNA synthesis, and PCR were performed with the help of Annette Otto (HZI, Braunschweig).
For qPCR, cells were seeded and total RNA was isolated using NucleoSpin RNA Plus kit (Table 3.12) according to the manufacturer´s recommended protocol. cDNA synthesis and qPCR were performed simultaneously using SensiFAST™ SYBR® No-ROX One-Step Kit (Table 3.12) according to the manufacturer´s recommended protocol. Reactions were carried out in a Rotor-Gene Q lightcycler (Qiagen). RNA isolation, cDNA synthesis, and qPCR were performed with the help of Silvia Prettin.

3.3.11 DNA sequencing

Sequence validation was accomplished by Eurofins MWG Operon. Screening of pX458(sgRNA) was performed using crCHECK1 primer (GCACCGACTCGGTGCCAC) to identify positive clones. DNA samples from TOPO cloning reactions were analyzed using M13 forward primer (GTAAAACGACGGCCAG). Result analysis was performed with SnapGene® Viewer software 2.6.2.

3.3.12 DNA microarray hybridization and analysis

Microarray analyses using AffymetrixTM genechips were performed by Robert Geffers (HZI, Braunschweig). 3x10^6 cells were seeded onto 6-well plates and grown for 24 h. RNA isolation was performed using RNeasy Mini kit (Table 3.12) according to the manufacturer´s recommended protocol. Quality and integrity of total RNA isolated from NIH/3T3 WT and KO cells was controlled on Agilent 2100 Bioanalyzer (Agilent Technologies). 500 ng of total RNA was used for biotin labeling according to the 3´ IVT Express Kit (Affymetrix). 7.5 µg of biotinylated cRNA was fragmented and placed in a hybridization cocktail containing four biotinylated hybridization controls (BioB, BioC, BioD, and Cre). Samples were hybridized to an identical lot of Affymetrix GeneChip MOE 430 2.0 for murine samples for 16 h at 45°C. Steps for washing and SA-PE staining were processed on the fluidics station 450 using the mini euk2v3 FS450 protocol (Affymetrix). Image analysis was performed on a GCS3000 Scanner equipped with GCOS1.2 Software Suite (Affymetrix).

3.3.13 Kits

Kits used in this thesis are shown in Table 3.12.

Table 3.12: Kits

Product	Supplier
NucleoSpin® Plasmid Quick Pure	Macherey & Nagel
NucleoSpin® Gel	Macherey & Nagel
PCR clean-up	Macherey & Nagel
TOPO® TA Cloning®	Invitrogen
RNeasy Mini	Qiagen
NucleoSpin RNA Plus	Macherey & Nagel
Transcriptor first strand cDNA synthesis kit	Roche
SensiFAST™ SYBR® No-ROX One-Step Kit	Bioline
Pierce BCA Protein Assay Kit	Thermo Fisher Scientic
Amplex™ Red Cholesterol Assay Kit	Thermo Fisher Scientic

3.4 Cell culture

3.4.1 Reagents and plasticware

Cell culture media and additives were purchased from Corning, Thermo Fisher Scientic, Sigma and PAA, if not stated otherwise. Hank´s Balanced Salt Solution (HBSS) starvation medium was purchased from Biochrom. Fetal bovine serum (FBS) (Lot: 054M3396) was sterile filtered using bottel top filters and stored at 4°C. Plasticware was from Corning.

3.4.2 Cell lines and culture conditions

Mouse embryonic fibroblast cells (NIH/3T3, ATCC CRL-1658) and human osteosarcoma cells (U2-OS cells, DSMZ ACC 785) were maintained on sterile 10 cm cell culture

dishes in DMEM (4.5 g/L glucose) supplemented with 10% (v/v) FBS, 1 mM sodium pyruvate, 1x non-essential amino acids and 2 mM L-glutamine at 37°C in a humidified 7.5% CO_2-atmosphere. For starvation and autophagic flux analyses, cells were incubated in complete culture medium for 24 h and either starved in HBSS or starved in HBSS and treated with 100 nm Bafilomycin A1 (BafA1)(Cayman Chemical) for the indicated time points. To assess cholesterol levels, cells were incubated in complete culture medium or serum free culture medium supplemented with 1% (v/v) Insulin-Transferrin-Selenium-G (ITS-G) for 24 h.
For passaging, cultures were washed once with PBS and incubated in trypsin/EDTA solution at 37°C until cell detachment. The reaction was stopped by adding complete culture medium and cells were subcultured at dilutions suitable for further cultivation.

3.4.3 Cell thawing and freezing

For recultivation, cells were rapidly thawed in a 37°C water bath, slowly transferred to a 5 mL tube containing complete culture medium and centrifuged at 115 xg for 5 min at 4°C (Eppendorf 5804R). The supernatant was discarded and cells were resuspended in complete culture medium and plated onto 10 cm cell culture dishes.
For longterm storage, cells were trypsinized and centrifuged as previously. Cell pellets were resuspended in chilled freezing medium (70% DMEM (4.5 g/L glucose) containing 20% (v/v) FBS and 10% (v/v) DMSO) and transferred into cryogenic storage vials. Cells were frozen overnight at -70°C in a cell freezing container (Biocision) and stored in liquid nitrogen.

3.4.4 Transfection and generation of mutant eukaryotic cells

Transfections were performed using X-tremeGENE^{TM}9 following the manufacturer´s recommended protocol. For transfection of cells in 10 cm dishes, the mixture was scaled up accordingly. Opti-MEM I Reduced Serum Medium was used as transfection reagent. The protocol given below was performed to transfect cells grown in 6-well plates.

1 µg DNA
100 µL Opti-MEM
3 µL X-tremeGENE^{TM} 9

The transfection mixture was incubated for 30 min at room temperature and finally added to the cells. Transfection efficiency was monitored with EVOS® FL Cell Imaging System 24 h post-transfection. Cells were grown to confluence and subsequently

inspected by flow cytometry in order to sort single, GFP-positive cells. Therefore, cells were dissociated and spun down at 115 xg for 5 min at room temperature. The medium was aspirated and cells were resuspended in 500 µL PBS. Flow cytometry was carried out by Lothar Gröbe (HZI, Braunschweig) and performed with Aria II instrument (BD Biosciences) using FACSDiva (Version 6.1). Non-transfected WT NIH/3T3 fibroblasts and U-2 OS cells, respectively, served as negative controls. Afterwards, sorted cells were maintained in cell culture medium supplemented with 30% conditioned medium and 10 µM Y-27632 ROCK inhibitor (Biosciences). A second approach to isolate single cells from a cell population was serial dilution since cell types vary in their response to flow cytometry and do not survive the process itself or the subsequent outgrowth.

3.4.5 Flow cytometry

To analyze cell size and cell granularity of NIH/3T3 WHAMM KOs, subconfluent cells were harvested and fixed with ice-cold 70% (v/v) ethanol at 4°C for 30 min. Cells were spun down at 115 xg for 5 min, washed with PBS and centrifuged as previously. Cell pellet was washed again with PBS and centrifuged as previously. Supernatant was discarded and cells were collected in PBS containing 50 µg/mL RNase (Qiagen) and 20 µg/mL propidium iodide (Biolegend) and incubated at 37°C for 15 min. Subsequently, cells were analyzed by flow cytometry using a LSR-II SORP flow cytometer (BD Biosciences) operated by FACSDiva software (Version 6.1) carried out by Stephanie Stahnke (HZI, Braunschweig). Forward and side-scatter profiles were obtained and at least 10,000 events were recorded per sample. Data was analyzed using FlowJo® software (Version 10).

Moreover, flow cytometry has been used to assess autophagic flux in NIH/3T3 WT as well as WHAMM KO cells by measuring LC3 and LAMP1 signal. $8x10^3$ cells were seeded in a 96-well plate (round bottom) and grown for 24 h. Cells were starved for the indicated time points with HBSS, harvested and washed with flow cytometry buffer. Subsequently, cells were centrifuged at 259 xg for 5 min, supernatant was discarded and live/dead staining solution (1:1000, Thermo Fisher Scientific) was added for 20 min at 4°C. Cells were washed and centrifuged, supernatant was discarded and cells were fixed in 4% (w/v) paraformaldehyde (PFA) in PBS for 20 min at room temperature. Cells were washed with flow cytometry buffer, centrifuged, and stained with the respective primary antibody (Table 3.14) diluted in flow cytometry buffer containing 0.1% (w/v) saponin for 20 min at room temperature. Note that usage of saponin is highly recommended as it selectively extracts cytosolic LC3-I, while lipidated LC3-II is membrane-bound and insoluble. Otherwise, one can barely discriminate between

nonautophagosome-associated LC3-I and autophagosome-associated LC3-II [93]. Afterwards, cells were washed, centrifuged, and stained with the apropriate secondary antibody (Table 3.15) diluted in flow cytometry buffer containing 0.1% (w/v) saponin. Cells were washed and centrifuged as previously. Subsequently, samples were resuspended in flow cytometry buffer and flow cytometry was carried out as described. At least 1,000 events were recorded per sample.

3.5 Protein biochemistry

3.5.1 SDS-PAGE

SDS-Polyacrylamide gel electrophoresis (SDS-PAGE) was used to separate protein samples according to their molecular weight as described by Laemmli *et al.* (1970).

Standard preparation of protein extracts from cultured cells
Confluent adherent tissue culture cells were incubated on ice for 10 min, washed three times with ice-cold PBS followed by addition of NP-40 lysis buffer. Cells were scratched, transferred into pre-chilled Eppendorf tubes and kept on ice for 20 min. Next, cells were centrifuged at 18,800 xg for 15 min at 4°C. The supernatant was transferred and protein concentration was determined with Pierce™ BCA Protein Assay kit (Table 3.12) following the manufacturer´s instructions. Lysate samples with equal amounts of total protein were mixed with appropriate amounts of 8x SDS sample buffer and boiled for 5 min at 95°C.

Preparation of protein extracts from cultured cells to assess autophagy
To analyze autophagy in established NIH/3T3 KO cells, 2.2x10^5 cells were plated in a 6 cm dish and grown for 24 h. Next day, cells were washed once with HBSS and incubated with HBSS for the indicated time points. Samples were placed on ice, washed three times with ice-cold PBS and Tris lysis buffer was added. Cells were harvested, centrifuged and protein concentration was determined as previously described.

After preparation of protein extracts, samples were separated on SDS-PAGE, which consists of a top layer (stacking gel) and a bottom layer (resolving gel) (Formula Table 3.13). To determine the protein size, a mixture of proteins having defined molecular weights was loaded along the samples (PageRuler™ Prestained Protein Ladder, BioLabs Broad Range Color Prestained Protein Standard or Spectra Multicolor Broad Range Protein Ladder). Electrophoresis was carried out at constant voltage (80 V) at room temperature. After electrophoresis was completed, proteins were transferred from the gel onto a Polyvinylidene difluoride (PVDF) membrane (Merck Millipore) (Chapter 3.6.4).

Preparation of protein extracts from cultured cells to determine cholesterol levels

To quantify cholesterol in established NIH/3T3 WHAMM KO cells, 2x10^5 cells were plated in a 6-well plate and grown for 24 h in complete culture medium or in serum free culture medium supplemented with ITS-G. Next day, cells were incubated on ice for 5 min, washed two times with ice-cold PBS and lysed in Amplex lysis buffer I and II, respectively. Subsequently, protein samples were snap frozen two times in liquid nitrogen and used in Amplex® Red Cholesterol Assay kit (Table 3.12) following the manufacturer´s instructions. Fluorescence was detected using Tecan infinite 200 Pro microplate reader (excitation/emission of 530/590 nm).

Table 3.13: Formula of stacking and resolving gel

Component	Stacking gel	Resolving gel			
		7.5%	10%	12.5%	15%
H_2O	4 mL	7.8 mL	6.6 mL	5.24 mL	3.9 mL
1.5 M Tris/0.4% SDS pH 8.8	-	4 mL			
0.5 M Tris/0.4% SDS pH 6.8	0.9 mL	-			
*Acrylamide solution	0.9 mL	4 mL	5.34 mL	6.66 mL	8 mL
TEMED	8 µL	16 µL			
25% APS	32 µL	64 µL			

*30% Acryalamide/0.8% N,N´-Methylenbisacrylamide

3.5.2 Coomassie blue and Ponceau S staining

Coomassie blue was used to visualize proteins on polyacrylamide gels. The gel was incubated with Coomassie stain and heated in a microwave on 50% power for 10 to 30 s (until the Coomassie solution boils). Afterwards, the gel was incubated with the Coomassie stain for 5 to 10 min on a rocking table. Destaining of the gel was performed by replacing Coomassie stain with distilled water followed by microwave heating for 10 to 30 s.

To check for successful protein transfer, the PVDF membrane was stained with Ponceau S. Therefore, the membrane was washed with distilled water and incubated with

Ponceau S for 5 min. Destaining of the membrane was done by washing extensively in water until the protein bands were well-defined.

Coomassie solution
0.1% Coomassie brilliant blue G-250
10% Ethanol
5% Aluminium sulfate
2% Phosphoric acid
ddH_2O

Ponceau S
0.5% Ponceau S
1% Acetic acid
ddH_2O

3.5.3 Expression of recombinant proteins in *E. coli*

In order to express recombinant WHAMM or JMY, pGEX-6P-3-WHAMM$_{AA696-809}$ and pGEX-6P-1-JMY$_{AA824-983}$ were transformed into *E. coli* BL21 (DE3) and *E. coli* Rosetta, respectively (Chapter 3.3.6). Both pGEX-6P-3 and pGEX-6P-1 provide GST fusion. *E. coli* cells harbouring the recombinant plasmid were inoculated into 100 mL LB medium containing the appropriate antibiotic(s) (Table 3.2 and Table 3.7) and cultured overnight at 37°C with agitation. Starter cultures were diluted 1:10 in 1 L fresh medium containing the appropriate antibiotic(s) and were grown at 37°C until an optical density (OD) value of 0.8 at 600 nm was reached. Isopropyl-beta-D-thiogalactopyranoside was added to a final concentration of 1 mM and cultures were further grown for 4 h (BL21 (DE3)) or 3 h (Rosetta) at 37°C with agitation. Cells were harvested by centrifugation (6,000 rounds per minute (rpm) for 15 min at 4°C in an Avanti™ J-25 Beckman centrifuge with JA10 rotor). The pellet was washed with ice-cold buffer A containing 1 mM DTT and centrifuged as previously. Cells were resuspended in cold buffer A containing 1 mM DTT, 1 µL Benzonase for degradation of DNA, 1 pill Mini-complete protease inhibitor cocktail to inhibit protease activity and a tip of a spatula of lysozyme. Cells were disrupted on ice by gentle sonication (3 cycles, 45 s, Branson Sonifier 250) and centrifuged (16,500 rpm for 30 min at 4°C). Glutathione Sepharose® 4B slurry (GE Healthcare) was equilibrated with buffer A containing 1 mM DTT and 1 mL was mixed with the supernatant for 1 h at 4°C on a rotary wheel. pGEX-6P-3-WHAMM$_{AA696-809}$ and pGEX-6P-1-JMY$_{AA824-983}$ were

purified using a PD10 plastic column cartidge (sepharose column from Amersham Biosciences). Beads were washed ten times with buffer A containing 1 mM DTT and the GST tagged proteins were eluted with elution buffer (0.5 mL elution buffer/1 mL Glutathione Sepharose® 4B slurry). The total protein amount was quantified photometrically by measuring the OD at 280 nm. The expression and purity of the protein was assessed by SDS-PAGE applying samples from every step of the procedure.

3.6 Immunological methods

3.6.1 Primary antibodies

Primary antibodies applied for immunoblotting (WB), immunofluorescence (IF), or flow cytometry (FC) are listed in Table 3.14.

Table 3.14: Primary antibodies

Target	mc/pc	Species	Application	Source
Actin	pc	rabbit	WB 1:1,000	Sigma, A2066
ATG9A	mc	rabbit	WB 1:1,000 IF 1:100	Abcam, 108338
Calnexin	pc	rabbit	IF 1:100	Abcam, 75801
EEA1	mc	rabbit	IF 1:100	Cell Signaling, C45B10
GAPDH	mc	mouse	WB 1:10,000	CalBiochem, 1001
Giantin	pc	rabbit	IF 1:500	BioLegend®, PRB-114C
JMY	pc	rabbit	WB 1:500	This dissertation
LAMP1	mc	rat	*IF 1:200 FC 1:500	Abcam, 25245
LC3A/B	pc	rabbit	WB 1:2,000	Cell Signaling, 4108
LC3B	pc	rabbit	*IF 1:500 FC 1:1,000	Novus, 600-1384

mTOR	mc	rabbit	WB 1:1,000	Abcam, 7c10
Paxillin	mc	rabbit	WB 1:500 IF 1:100	Abcam, Y113
p62	mc	mouse	WB 1:5,000 *IF 1:500	Abcam, 56416
p-mTOR	mc	rabbit	WB 1:1,000	Abcam , D9C2
Tubulin YL 1/2	mc	rat	WB 1:10,000	J. Wehland, HZI, Braunschweig
Tubulin	mc	mouse	IF 1:500	Sigma, T 6793
Ubiquitin	mc	mouse	WB 1:2,000	Cell Signaling, 3936
Vinculin	mc	mouse	WB 1:5,000 IF 1:250	Sigma, V-9131
WASH	pc	rabbit	WB 1:800	A. Gautreau, Ecole Polytechnique Paris, France
WHAMM	pc	rabbit	WB 1:500	Abcam, 122572

mc = monoclonal, pc = polyclonal, *Fixative: Methanol

3.6.2 Secondary antibodies

Secondary antibodies applied for immunoblotting (WB), immunofluorescence (IF) or flow cytometry (FC) are listed in Table 3.15. All secondary antibodies listed in Table 3.15 are specific for both heavy and light chains of IgG. Phalloidin conjugates used in immunofluorescence are listed in Table 3.15.

Table 3.15: Secondary antibodies and phalloidin conjugates.

Name	Description	Coupled to	Application	Source
A4C	goat anti-mouse IgG	Horseradish	WB 1:5,000	Dianova

		peroxidase (HRP)		
B4C	goat anti-rabbit IgG	HRP	WB 1:5,000	Dianova
C4C	goat anti-rat IgG	HRP	WB 1:5,000	Dianova
A12C	goat anti-mouse IgG	Alexa Fluor™ 488	IF 1:400	Invitrogen
A13C	goat anti-mouse IgG	Alexa Fluor™ 594	IF 1:400	Invitrogen
B12C	goat anti-rabbit IgG	Alexa Fluor™ 488	IF 1:400	Invitrogen
B13C	goat anti-rabbit IgG	Alexa Fluor™ 594	IF 1:400 FC 1:1,000	Invitrogen
C12C	goat anti-rat IgG	Alexa Fluor™ 488	IF 1:400 FC 1:1,000	Invitrogen
PH12	-	Alexa Fluor™ 488	IF 1:200	Invitrogen
PH13	-	Alexa Fluor™ 594	IF 1:200	Invitrogen
PH20	-	ATTO 594	IF 1:200	ATTO TEC

3.6.3 Generation of polyclonal WHAMM and JMY antibodies

For generation of WHAMM and JMY antibodies, $WHAMM_{AA696-809}$ and $JMY_{AA824-983}$ were expressed in *E. coli* BL21 (DE3) and Rosetta, respectively (Chapter 3.5.3). Generation of antisera against the proteins was carried out by Prof. Jan Faix (MHH, Hanover).

3.6.4 Western blotting

After protein separation via SDS-PAGE (Chapter 3.5.1), Western blotting was applied to detect specific proteins in cell lysate samples. Proteins were transferred with Pierce G2 Fast Blotter (Thermo Fisher Scientific) employing the semi-dry technique. The PVDF membrane was activated by soaking in pure methanol and afterwards equilibrated in Pierce 1-Step transfer buffer. Whatman filter paper and SDS gels were incubated in transfer buffer for 10 min. The activated and washed PVDF membrane was placed beneath the gel for transferring the proteins. Both sides were surrounded

with Whatman filter paper and western blotting was performed. Depending on the molecular weight, proteins <100 kDa were transferred up to 15 min, whereas larger proteins (>100 kDa) up to 20 min. Protein transfer was performed at a maximum of 25 V and at a constant current of 2.5 A. Subsequently, the membrane was incubated in methanol and completely dried before blocking. Successful protein transfer was investigated by Ponceau S staining (Chapter 3.5.2). To prevent nonspecific binding of the antibody, the membrane was incubated in blocking solution for 1 h on a shaker at room temperature.

Blocking solution I (applied for LC3 and p62 antibodies)
5% (w/v) Skim milk powder in 1x TBS-T

Blocking solution II
10% (v/v) FBS in 1x TBS-T

Next, the membrane was incubated with the primary antibody diluted in the respective blocking solution at 4°C overnight on a shaker. The membrane was washed three times in 1x TBS-T for 20 min and incubated with a HRP coupled secondary antibody diluted in the respective blocking solution for 1 h at room temperature. Afterwards, the membrane was washed as previously and protein detection was conducted using Lumi-Light Western blotting substrate (Roche). Protein bands were visualized via a chemiluminescence reaction, which results from the oxidation of luminol by the peroxidase linked to the secondary antibody. Resulting luminescence was detected with Intas ECL Chemocam Imager at different exposure times.

3.6.5 Immunofluorescence

Preparation of coverslips
Coverslips (12 mm or 15 mm Ø from Thermo Fisher Scientic; 18 mm Ø from Marienfeld) were washed in a solution of 60% (v/v) ethanol and 40% (v/v) HCl for 30 min on a shaker. Washing solution was removed and coverslips were rinsed extensively with distilled water. Afterwards, coverslips were air dried separately on Whatman filter paper and finally sterilized by autoclavation (121°C, 30 min).

Coating of coverslips
Before cell seeding, coverslips were coated with 25 µg/mL fibronectin (Roche) in PBS for 1 h at room temperature. Fibronectin is a excellular matrix protein, which im-

proves cell adhesion on the glass surface. Coating solution was removed by washing three times with PBS followed by cell seeding. Fibronectin was stored as 1 mg/mL solution in 2 M urea.

Fixation and staining of samples

In general, 22.5x10^3 cells were plated onto coated coverslips and cultured for 24 h followed by fixation.

For Brefeldin A (BFA) treatment, 3x10^4 cells were seeded into 12-well plates and grown for 24 h. BFA (2.5 µg/mL) was added and cells were incubated at 37°C for 35 min. For regeneration studies, cells were removed from the treatment medium and washed free of BFA with fresh culture medium for time points as indicated in the figure.

To compare and quantifiy F-actin intensities between NIH/3T3 WT and WHAMM KO cells, 4x10^4 cells were seeded into 12-well plates and grown for 24 h. Media was discarded and either WT or WHAMM KO cells were incubated with 7.5 µM/mL CellTracker™ Green CMFDA (Thermo Fisher Scientific) in Opti-MEM at 37°C for 30 min. Half of the WT and the respective KO clone plate was seeded onto coated coverslips and fixation was performed after cell detachment.

To study autophagy, cells were either starved with HBSS or starved with HBSS and treated with BafA1 prior to fixation.

In this study, both PFA and methanol fixation procedures were performed. Therefore, cells were placed on a styrofoam and cell culture medium was discarded. Next, cells were fixed with prewarmed 4% (w/v) PFA in PBS for 20 min at room temperature in order to cross-link proteins. For vinculin stainings, cells were pre-extracted with 0.3% (v/v) Triton X-100 in 4% (w/v) PFA in PBS for 1 min and fixed as previously. Cells were washed thrice with PBS and permeabilized with 0.2% (v/v) Triton X-100 in PBS for 1 min at room temperature to become permeable for larger structures. Cells were washed as previously.

In case of methanol fixation, cells were placed on a styrofoam and cell culture medium was removed. Ice-cold 100% methanol was added for 5 min at room temperature and finally washed out with PBS by slowly decreasing the methanol concentration. As methanol is a permeabilization agent, no treatment with 0.2% (v/v) Triton X-100 in PBS was required.

To avoid nonspecific binding of the antibody, cells were incubated in blocking solution (5% (v/v) horse serum in 1% (w/v) BSA in PBS) for 1 h at room temperature with the cell side down in a humidified chamber. Cells were then stained with the primary

antibody diluted in the blocking solution and added to the cells as previously. Afterwards, cells were washed five times in PBS and incubated with the secondary antibody diluted in the blocking solution for 1 h at room temperature. If required, the secondary antibody solution was supplemented with phalloidin (Table 3.15) and/or DAPI (1:500, Sigma). Phalloidin is a phallotoxin that binds to F-actin, thereby preventing its depolymerization. DAPI staining was performed to visualize cell nuclei. Cells were washed two times in PBS and one time in deionized water to remove any salts. Coverslips were overturned on a microscope slide covered with ProLong Antifade mounting medium (Thermo Fisher Scientific) and stored in the dark at 4°C.

For filipin staining, cells were PFA-fixated as described, washed thrice with PBS and incubated with 1 mL of 1.5 mg/mL (w/v) glycine in PBS for 10 min at room temperature. Cells were stained with 0.25 mg/mL Filipin (Sigma) in 10% (v/v) FBS in PBS for 2 h at room temperature. Cells were washed and mounted as previously described.

3.7 Microscopical methods

3.7.1 Epifluorescence microscopy

To localize a certain protein in cells, it can be coupled to fluorochromes as described by Mies *et al.* A fluorophore is a fluorescent chemical compound that can be excited allowing the visualization of biological molecules and structures. For this purpose, samples were prepared as described in chapter 3.6.5 and imaging was conducted with the following tools (Tables 3.16 and 3.17).

Table 3.16: Hardware used for immunofluorescence analyses

Microscope	**Axiovert 135TV** Carl Zeiss Microscopy	**Spinning Disk** **Perkin Elmer** Nikon Ti Eclipse
Light source	Mercury lamp HXP120	Intensilight Nikon C-HGFIE Modular laser system 2.0
Objective	Plan Apo 100x/1.4 NA Plan Apo 63x/1.4 NA	Plan Apo 60x/1.4 NA Plan Apo 100x/1.4 NA
Camera	Coolsnap HQ2 (Photometrics)	Orca R2 EM-CCD (Hamamatsu)
Acquisition	Visi View	Volocity
Immersion oil	Carl Zeiss or Nikon (Refraction index: 1.518)	

Table 3.17: Hardware used for immunofluorescence analyses

Microscope	**SIM-E Nikon**	**Ti2 Nikon**
	Nikon Ti Eclipse	
Light source	Intensilight Nikon C-HGFIE	CoolLED pE-4000
Objective	Plan Fluor 60x/1.4 SR Apo TIRF 100x/1.49 NA	Plan Apo 60x/1.4 NA Plan TIRF 100x/1.49 NA
Camera	Orca Flash LT (Hamamatsu)	PCOedge (PCO)
Acquisition software	NIS-Elements	
Immersion oil	Carl Zeiss or Nikon (Refraction index: 1.518)	

Particle analysis using ImageJ

Images acquired by fluorescence microscopy have been analyzed for their number, size and/or intensity of the respective, stained target. To do so, two different approaches have been utilized in order to make an appropriate particle analysis. Counting LC3 and p62 spots has been performed by manual thresholding. The monochrome images were most simply thresholded via the menu command *Image-Adjust-Threshold*. Finally, the command *Analyze-Analyze particles* provided me with information about each single particle in the image. This procedure turned out to work properly for p62-detection (Figure 3.1, A). However, the tool illustrated difficulties in the selection of LC3 particles, especially due to non-uniform lighting images (Figure 3.1, B). Moreover, some LC3 spots could not reliably selected since there was partly a strong nucleus staining throughout the samples. Examples shown in Figure 3.1, B) were either not taken into considerations or, depending on the signal intensity, the image has been cropped and calculations were performed gradually.

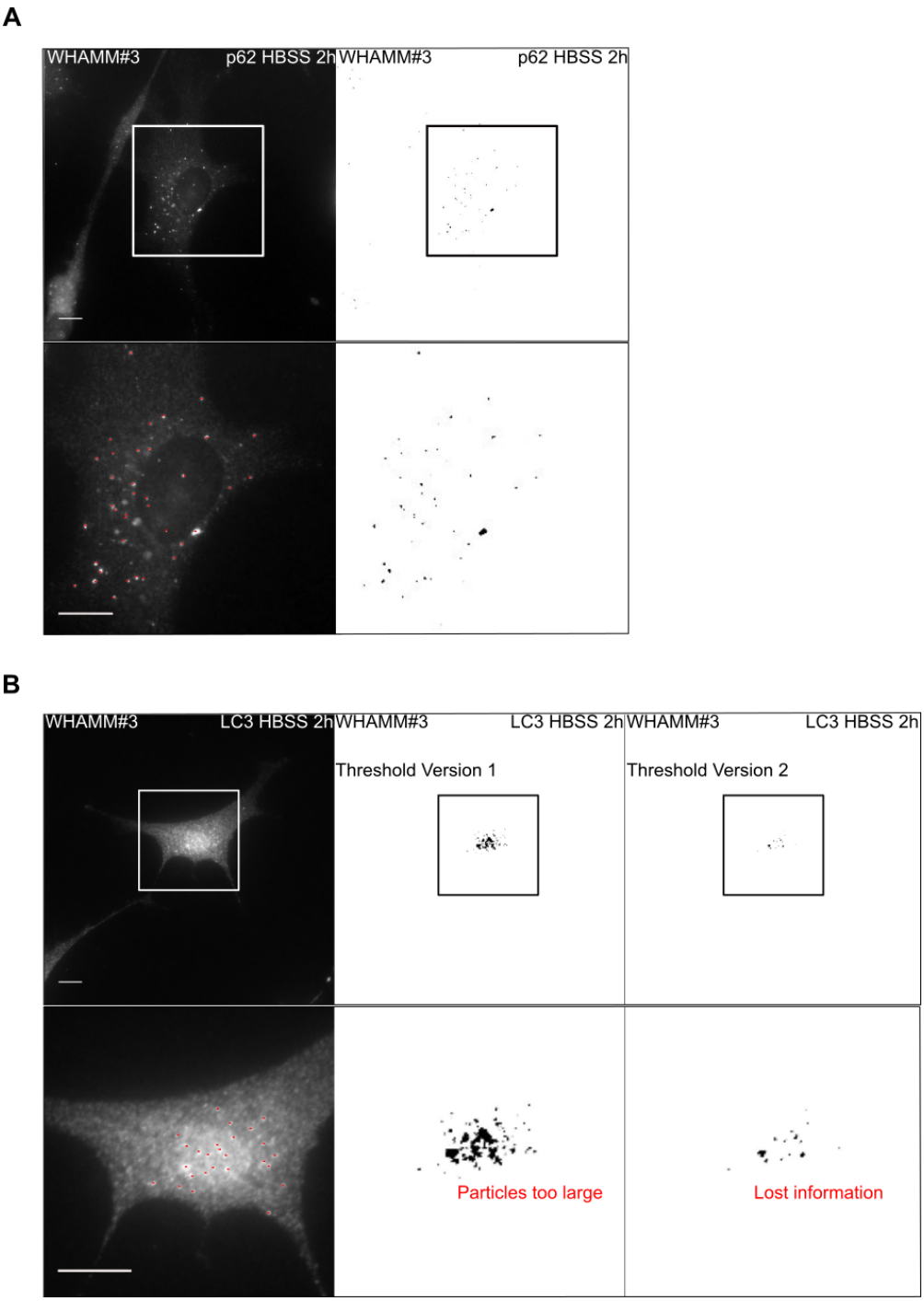

Figure 3.1: Threshold selection of p62-positive as well as LC3-positive particles. Autophagy was induced by HBSS treatment and was studied with autophagy markers p62 (A) and LC3 (B). ImageJ thresholding was used to perform particle analysis of both proteins. (A) Individual p62-positive structures were precisely detected by the threshold function. (B) Depending on the image, LC3 particles could not reliably selected due to non-uniform lighting of the sample. Red dots indicate p62-positive or LC3-positive structures. Scale bar: 10 µm.

In order to analyze the Golgi apparatus with/without BFA treatment, the number of ATG9-positive and LAMP1-spots as well as the number of focal adhesions, I applied automatic particle counting using an ImageJ plugin named MosaicSuite. Note that background subtraction seetings were equal for all measured particles (Remove background: Yes; Rolling ball window size: 10).

For Golgi analysis the settings were chosen as follows:

Table 3.18: MosaicSuite analysis of Golgi fragments

Settings	**Value**
Segmentation parameters	
Regularization (>0) ch1	0.010
Regularization (>0) ch2	0.050
Minimum object intensity channel 1 (0 to 1)	0.150
Minimum object intensity channel 2 (0 to 1)	0.90
Subpixel segmentation	No
Exclude Z edge	Yes
PSF model (Gaussian approximation)	
Standard deviation xy (in pixels)	0.91
Standard deviation z (in pixels)	0.69
Region filter	
Remove region with intensities <	0
Remove region with size <	0 pixels

For ATG9 and LAMP1-particle analysis the settings were chosen as follows:

Table 3.19: MosaicSuite analysis of ATG9-containing particles as well as LAMP1 spots

Settings	**Value**
Segmentation parameters	
Regularization (>0) ch1	0.010
Regularization (>0) ch2	0.050
Minimum object intensity channel 1 (0 to 1)	0.150
Minimum object intensity channel 2 (0 to 1)	0.150
Subpixel segmentation	No
Exclude Z edge	Yes
PSF model (Gaussian approximation)	
Standard deviation xy (in pixels)	1.21
Standard deviation z (in pixels)	0.69
Region filter	
Remove region with intensities <	0
Remove region with size <	2 pixels

For Vinculin and paxillin analyses the settings were chosen as follows:

Table 3.20: MosaicSuite analysis of vinculin- and paxillin-positive spots

Settings	Value
Segmentation parameters	
Regularization (>0) ch1	0.010
Regularization (>0) ch2	0.050
Minimum object intensity channel 1 (0 to 1)	0.150
Minimum object intensity channel 2 (0 to 1)	0.68
Subpixel segmentation	No
Exclude Z edge	Yes
PSF model (Gaussian approximation)	
Standard deviation xy (in pixels)	0.71
Standard deviation z (in pixels)	0.69
Region filter	
Remove region with intensities <	0
Remove region with size <	15 pixels

Even though the majority of particles has been properly detected, the MosaicSuite tool also displayed inaccuracies, independent from the particle of interest. Examples are shown for the Golgi apparatus (Figure 3.2), ATG9 detection (Figure 3.3), LAMP1 staining (Figure 3.4), Vinculin staining (Figure 3.5), and Paxillin staining (Figure 3.6), where some particles were falsely detected (e.g. brighter regions were falsely recognized as positive structures), other were not recognized at all as well as some structures were incorrectly recognized (e.g. counting three spots instead of two). Since these errors appeared in both genotypes, they were considered tolerable (for Vinculin see Results, Figure 4.28).

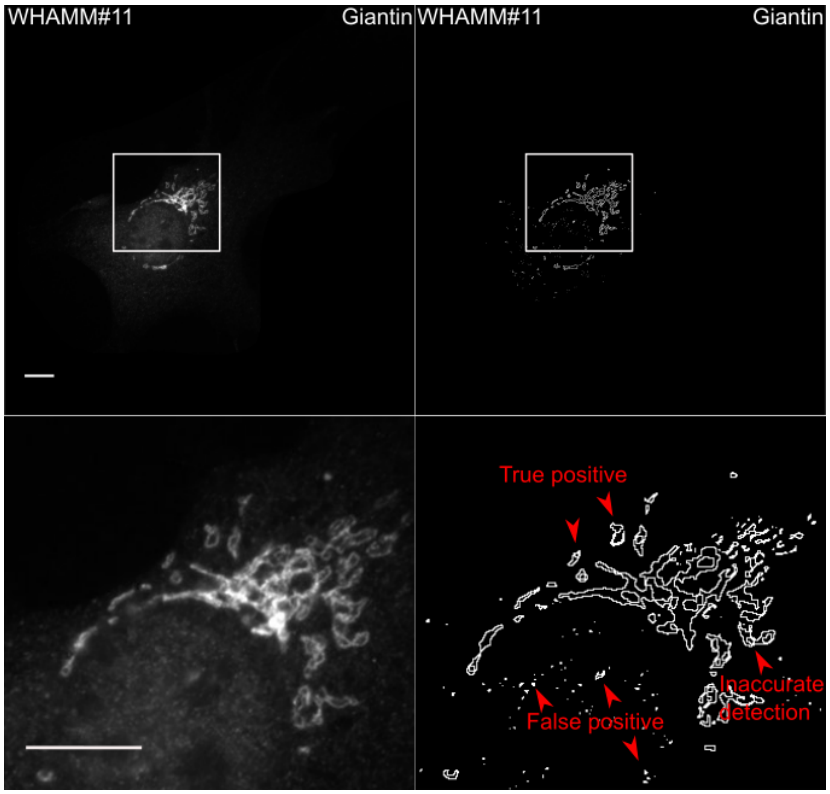

Figure 3.2: Counting Golgi fragment by MosaicSuite. The Golgi apparatus was investigated in both NIH/3T3 WT and WHAMM KO cells. One example is shown for WHAMM#11. Giantin staining was used to label the position of Golgi. The MosaicSuite tool was applied to count the number of fragments. Scale bar: 10 µm.

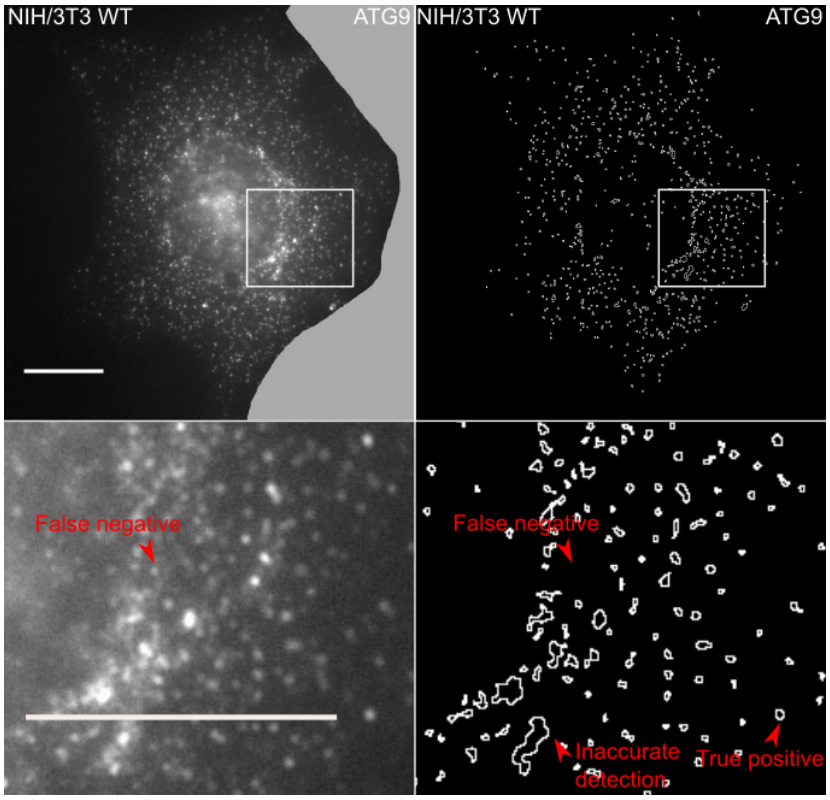

Figure 3.3: Counting ATG9 dots by MosaicSuite. Number and distribution of ATG9 particles were investigated in both NIH/3T3 WT and WHAMM KO cells. One example is shown for NIH/3T3 WT fibroblasts. ATG9 staining was used to label small single membrane-vesicles. The MosaicSuite tool was applied to count the number of ATG9-containing spots. Note that the monochromatic image (upper left) depicts a cropped version. Scale bar: 10 µm.

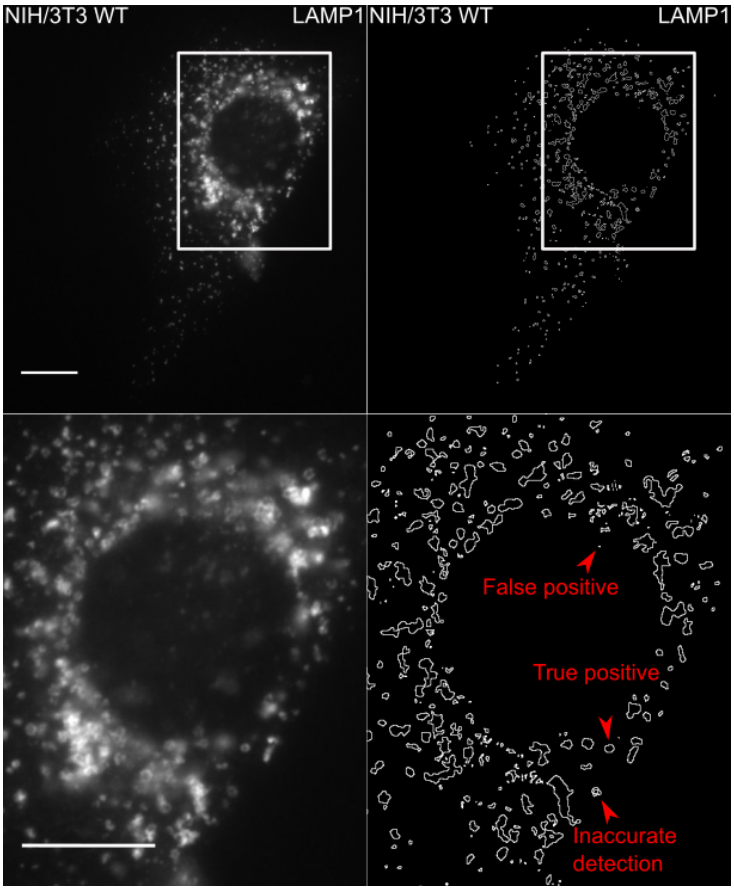

Figure 3.4: Counting lysosomal structures by MosaicSuite. Number and size of lysosomes were investigated in both NIH/3T3 WT and WHAMM KO cells. One example is shown for NIH/3T3 WT fibroblasts. LAMP1 staining was used to label the position of lysosomes. The MosaicSuite tool was applied to count the number of lysosomes. Note that the monochromatic image (upper left) depicts a cropped version. Scale bar: 10 µm.

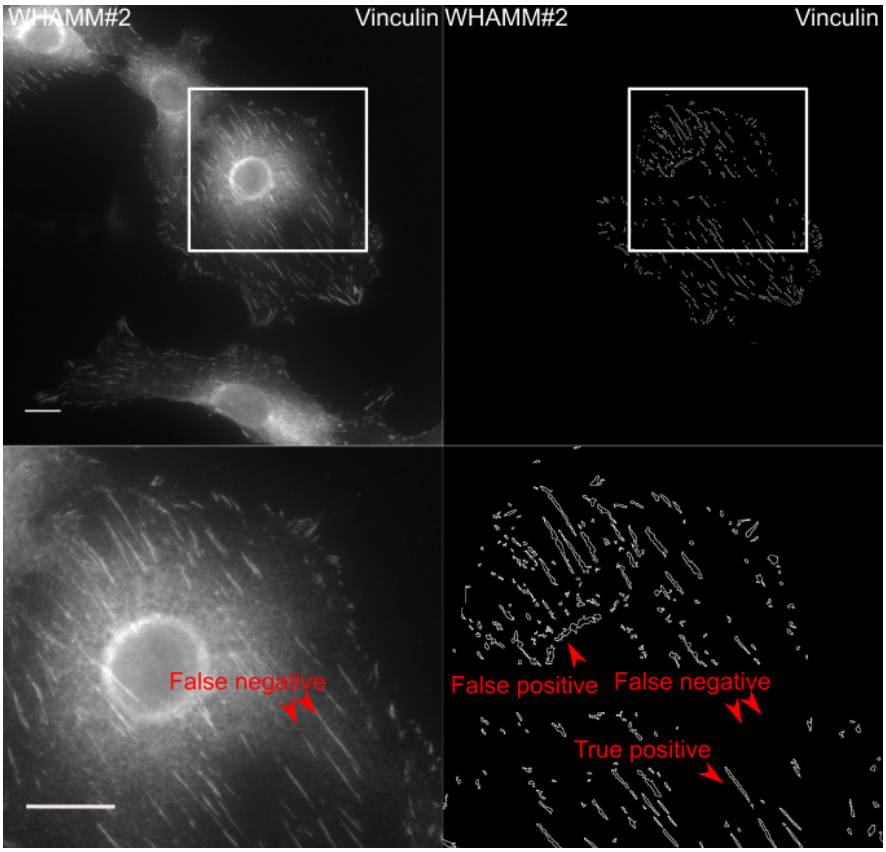

Figure 3.5: Counting vinculin-containing focal adhesions by MosaicSuite. Number, length, and intensity of focal adhesions were investigated in both NIH/3T3 WT and WHAMM KO cells. One example is shown for WHAMM#2. Vinculin staining was used to visualize focal adhesions. The MosaicSuite tool was applied to count the number of focal adhesions. Note that the monochromatic image (upper left) depicts a cropped version. Scale bar: 10 µm.

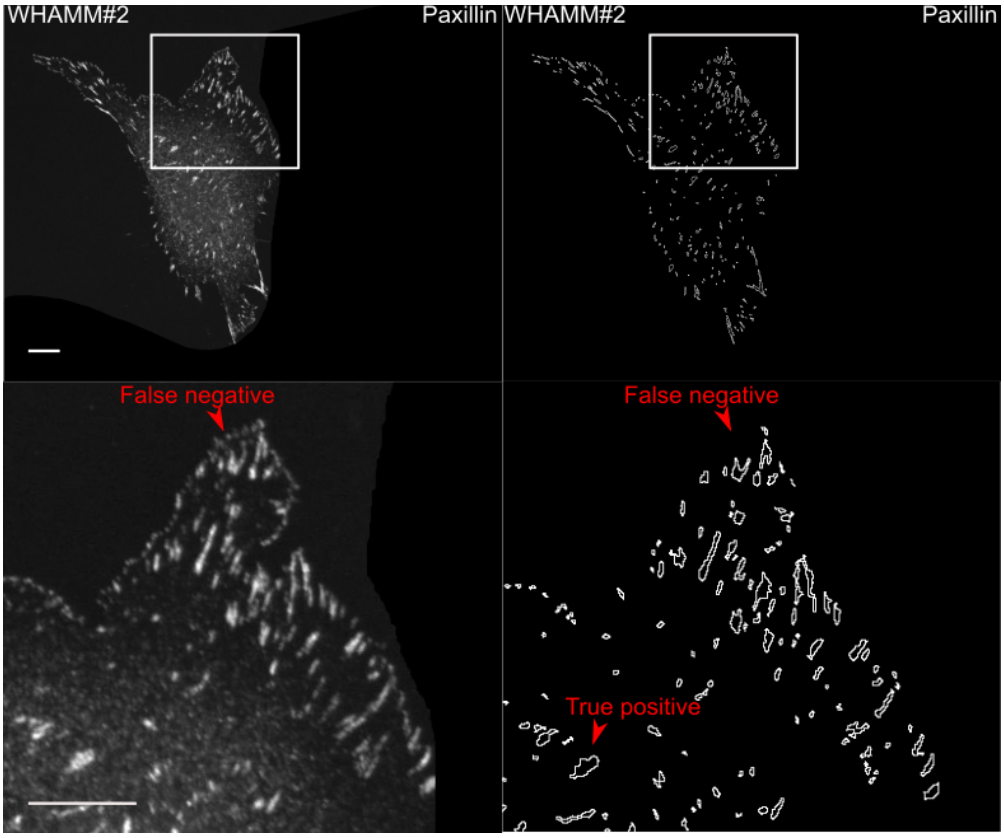

Figure 3.6: Counting paxillin-containing focal adhesions by MosaicSuite. Number, length, and intensity of focal adhesions were investigated in both NIH/3T3 WT and WHAMM KO cells. One example is shown for WHAMM#2. Paxillin staining was used to visualize focal adhesions. The MosaicSuite tool was applied to count the number of focal adhesions. Note that the monochromatic image (upper left) depicts a cropped version. Scale bar: 10 µm.

3.7.2 Live cell imaging

To monitor life cell imaging of EGFP-DFCP1, cells were plated onto 12-well plates and transiently transfected according to the protocol in chapter 3.4.4. The next day the transfected cells were transferred onto 35-mm glas bottom dishes (Ibidi) and on the third day the cells were starved with HBSS for 1, 2, and 4 h. Microscopy was performed with SIM-E Nikon (Table 3.17). Cells were maintained at 37°C and 7.5 % CO_2 using an OKO Labs full enclosure incubation system. Technical equipment and software were analogous to the description in chapter 3.7.1.

3.7.3 Superresolution microscopy

For 3D-structured illumination microscopy of EGFP-DFCP1, cells were seeded and transfected as described in chapter 3.4.4. Data as well as corresponding movies were acquired on Nikon SIM-E superresolution microscope (Chapter 3.7.1). Reconstructions were performed with the stack reconstruction tool (Nikon, NIS-Elements).

3.8 Viral infection studies of NIH/3T3 WHAMM and JMY KO cells

3.8.1 Analysis of virus-infected cells by flow cytometry

The absolute infection rate of VSV and HSV-1 was determined by flow cytometry. 1.8x10^5 NIH/3T3 WT and NIH/3T3 KO cells were seeded onto 24-well plates and grown for 24 h in complete culture medium. Next day, cells were either infected with VSV-eGFP or HSV-1-eGFP (Kalinke, Twincore) at a multiplicity of infection (MOI) of 5.5 for 1 h at 37°C. The supernatant was removed and cells were cultured in complete culture medium for 6 h or 12 h. After the indicated time points, medium was discarded and cells were detached with 1 mM EDTA in PBS up to 30 min at 4°C. Cells were carefully removed by pipetting up and down and placed in flow cytometry tubes. Cell suspension was washed with flow cytometry buffer at 300 xg for 6 min, supernatant was discarded and fixation was applied with 3% (w/v) PFA in PBS. Analysis was performed by flow cytometry using a LSR II flow cytometer (BD bioscience) operated by DIVA software (Version V8.0.1) carried out by Luca Ghita (Twincore). At least 10,000 events were recorded per sample. Data was analyzed using FlowJo® software (Version 1).

3.8.2 Plaque assay

The approximate virus titer after infection was determined by plaque assays. 1.8x10^5 NIH/3T3 WT and NIH/3T3 KO cells were seeded onto 24-well plates and grown for 24 h in complete culture medium. Next day, cells were either infected with VSV or HSV-1 (Kalinke, Twincore) at a MOI of 10 for 24 h at 37°C. Furthermore, 2x10^5 Vero cells (Kalinke, Twincore) were seeded onto 24-well plate and grown for 24 h. Supernatant of infected NIH/3T3 cells was taken off and used to prepare serial dilutions from 10^{-3} to 10^{-8}. Vero cells were infected by transferring 50 µL to the subsequent dilution for 1 h at 37°C. Afterwards, the media was discarded and infected cells were overlayed with pre-warmed 1% (w/v) methyl cellulose (Sigma) in distilled water. In case of VSV infection, the overlay was discarded after 24 h and samples were stained with 0.1% crystal violet for 30 min at room temperature. HSV-1 infected samples were incubated with the overlay for 72 h and stained as previously described. Plates were carefully washed with distilled water, dried and plaques were counted (Plaque forming units (PFU)).

3.8.3 Live cell imaging of EGFP-VSV

For real-time visualization of virus movement, cells were seeded onto 35-mm glas bottom dishes and grown for 24 h. Next day, cells were infected with VSV-eGFP in

RPMI containing 30 mM HEPES for 1 h at a MOI of 5.5. The dish was placed in a closed chamber maintained at 37°C and 5% CO2. Infection medium was replaced with complete culture medium and live cell imaging was performed for 8 hours post infection (hpi) using the Leica SP8 microscope fitted with a 63× lens. For time-lapse recording of the same sets of cells, images were collected every 30 s for 6 h.

3.9 Data processing and statistical analyses

Brightness and contrast levels were adjusted using ImageJ software (Version: 1.48). Figures were further processed and assembled with both ImageJ and Inkscape (Version: 0.92.3). For statistical analysis of western blot quantification, protein levels were quantitated by densitometry and normalized to the control group. One-Way ANOVA was used as statistical test for flow cytometry analyses, whereas all other experiments were analyzed using Two-tailed Student´s t-test (if not stated otherwise). Expression results of microarray analysis were displayed as binary logarithm. KO values were normalized to WT results. For statistical analyses, Microsoft Excel 2010, SigmaPlot Version 14, and GraphPad Prism 5 or 8 were employed.

4 Results

4.1 Generation of clonal cell lines lacking WASH, WHAMM or JMY

The CRISPR/Cas technology offers unprecedented genome editing capability and was applied in this thesis to elucidate and study the functional roles of WASH, WHAMM, and JMY. These NPFs are distinct catalytic activators of the Arp2/3 complex, which is unique in its ability to polymerize branched actin networks in the cell [3]. Interestingly, pathogenic microbes have evolved molecular mechanisms to manipulate Arp2/3-mediated actin polymerization in order to subvert actin-based motility for their own purposes (e.g. adhesion to, spreading within, and immune evasion from the host) [4,94]. However, little is known about the role of these actin regulators during infection with invasive pathogens. Additionally, recent publications link the mammalian NPFs WASH, WHAMM, and JMY to autophagy, an intracellular bulk degradation system used to remove misfolded, ubiquitylated proteins, damaged organelles as well as intracellular pathogens such as bacteria [25, 44, 84, 85]. Indeed, Bacteria have developed multiple mechanisms to avoid, inhibit or subvert the autophagy machinery [95].

To delineate the cellular role of the selected NPFs in these processes, I created somatic KOs in mouse embryonic fibroblasts (NIH/3T3) and human osteosarcoma cells (U-2 OS). I first determined an appropriate targeting sequence in WASH, WHAMM, and JMY using a bioinformatic database (ensembl.org) and focused on the coding region of the respective exon (Table 3.4). sgRNAs were designed with the help of two target online predictors (crispr.mit.edu and crispr.cos.uni-heidelberg.de). I have chosen a sgRNA binding in close proximity to the "ATG" start codon and best provided off-target score to specifically disrupt the protein-coding region. Gene editing by the CRISPR/Cas9 system was performed by transient transfections of NIH/3T3 and U-2 OS WT cells. Cells were transfected with pSpCas9(BB)-2A-GFP carrying a certain sgRNA targeting WASH, WHAMM, and JMY. Isolation of clonal cell lines bearing a KO in the respective locus was achieved by flow cytometry of single GFP-positive cells into 96-well plates or by single cell dilution.

The generation of the different KO cells yielded at least three clones in NIH/3T3 cells bearing either homozygous or heterozygous mutations (Table 4.1). Note that positions of premature stop codons are depicted in Figures 4.3 and 6.5.

Table 4.1: Established NIH/3T3 KO cells (+ = insertion, Δ = deletion)

Clone	Allele 1	Allele 2	Premature stop codon
WASH#19	+T	+A	No
WASH#20	+A	ΔCGACGAG	No
WASH#22	+A	ΔA, +T	No
WHAMM#2	+C	Identical to allele 1	Yes
WHAMM#3	+C	ΔC	Yes
WHAMM#7	+C	ΔGTGAGGAC	Yes
WHAMM#11	+C	Identical to allele 1	Yes
JMY#2	ΔCG	ΔAGTCCGACTGGGTG	Yes
JMY#5	ΔAC	ΔCG	Yes
JMY#10	+G	ΔC, ΔGAC	No

All clones were examined for gene editing by PCR amplification of the targeted locus of genomic DNA followed by sequencing (Figure 4.1, Supplementary data, Figures 6.1 − 6.3). At least nine clonal amplicons from each KO cell line were analyzed. Sequencing data revealed *indel* mutations (+ = insertion, Δ = deletion) in the WASH, WHAMM, and JMY loci (Table 4.1). Consequence of these gene modifications in WHAMM and two JMY KO cell lines was a frameshift mutation generating a premature stop codon resulting in the termination of protein synthesis (Figure 4.3, Supplementary data, Figure 6.5). In the case of WASH and JMY#10, CRISPR/Cas9 did not introduce an early stop codon, but resulted in extensive alterations of a certain number of amino acids that likely led to a misfolding and hence protein degradation (Supplementary data, Figures 6.4 and 6.5). Sequencing results of WASH#22 and JMY#10 displayed three different alleles which might indicate a mixture of clones or the presence of more than two alleles. Moreover, all NIH/3T3 KO clones were probed for protein expression by western blotting and showed a complete lack of the respective protein as compared to the non-edited control (Figure 4.2 A-C).

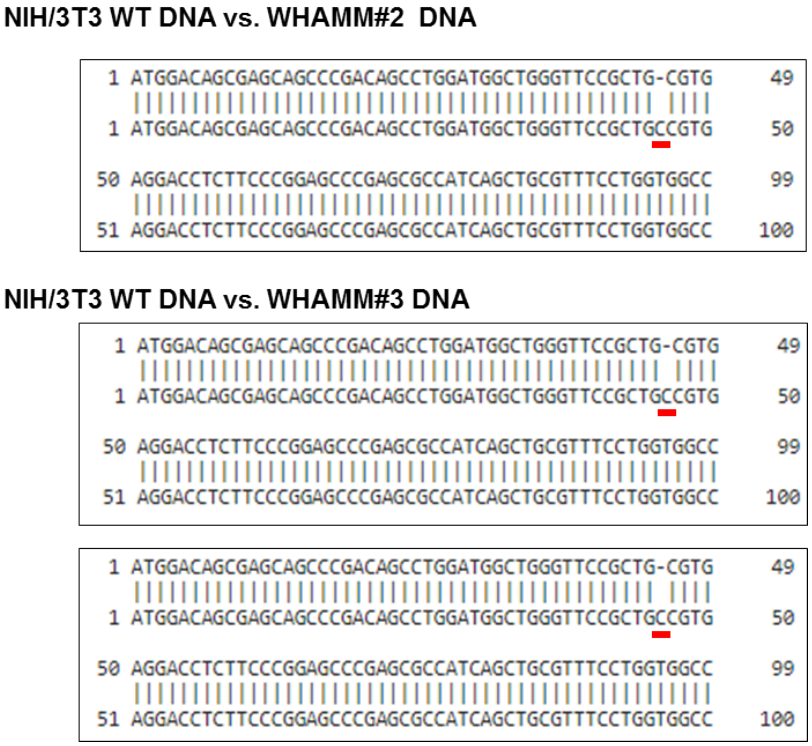

Figure 4.1: Representative DNA alignments of NIH/3T3 WT and WHAMM KO cells. WHAMM#2 displayed the same two alleles (homozygous mutation), whereas WHAMM#3 bears two different alleles (heterozygous mutation). Sequencing gaps (underlined in red) in the WHAMM locus indicate *indels* (pair-wise alignments were done in Clustal Omega (https://www.ebi.ac.uk/Tools/msa/clustalo)). Upper lane = WT sequence, lower lane = KO sequence.

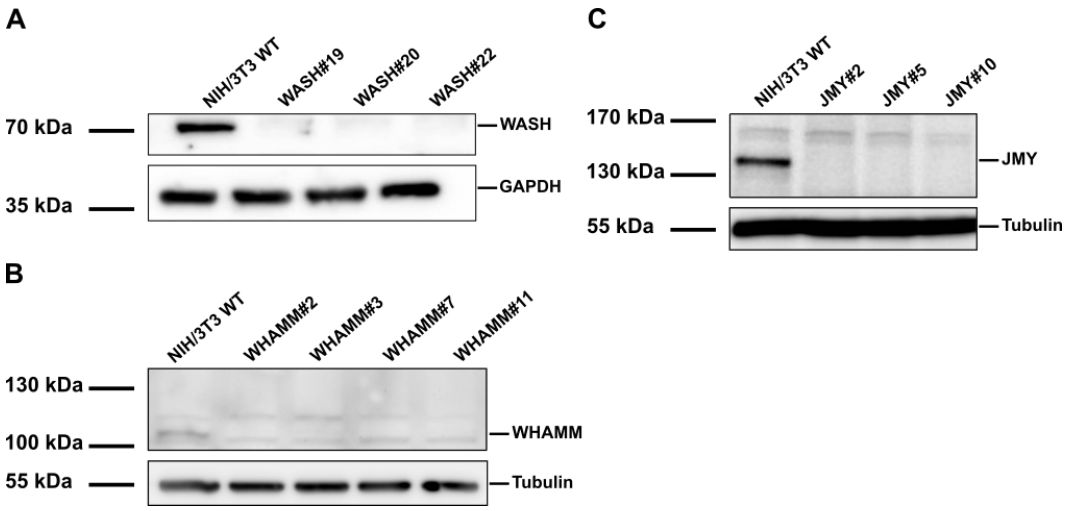

Figure 4.2: Western blot analyses show absence of expression of WASH, WHAMM or JMY in NIH/3T3 clones. NIH/3T3 WT cells were transfected with pSpCas9(BB)-2A-GFP containing a sgRNA targeting the respective NPF. Single clonal strains were obtained by flow cytometry or serial dilution and were sent for sequencing after cell expansion. Cell lysates were harvested and protein expression was checked by western blotting. GAPDH or Tubulin was used as loading control. (A-C) Representative images of western blots. Western blot analysis revealed efficient loss of WASH (A), WHAMM (B) or JMY (C) proteins in murine fibroblasts. Data are representative of three independent experiments. Individual clones are designated by numbers.

Protein sequence of murine WHAMM WT (**black**) or mutation-derived (red)	GB Acc and Clone numbers
MDSEQPDSLDGWVPLREDLFPEPERHQLRFLVAWNAAKGQFAVTCHDRT AQRRRRERREAGDGGCSWAGVLSPAGFRGAHRQLAALWPALEPCFPPL PPELDAASGAGWGLGRGLWALLWPLLWPAPADPGDSALQELCRQLEHYL GLAAEGCGGATVRDVLFPAPGDSADCEGLSEFRERTLRARL....	Murine WHAMM (793AA) NP_001004185
MDSEQPDSLDGWVPLP*	#2 Mutant allele 1/2
MDSEQPDSLDGWVPLP* MDSEQPDSLDGWVPLVRTSSRSPSAISCVSWWPGTPRRASSPSPVTTAR RSGGGASGGRPATGDVAGPGCCRPPGSAARTGSWRRCGRPWSPASRR CRPSWTRRAARAGAWDAGCGPSCGRSCGRRLRTLATRRCRSCAGSWS TTWAWRPKDAAAPPCATCSSRPRVTRQTARA*	#3 Mutant allele 1 #3 Mutant allele 2
MDSEQPDSLDGWVPLPLPGARAPSAAFPGGLERREGPVRRHLSRPHGA AAAARAAGGRRRGM* MDSEQPDSLDGWVPLP*	#7 Mutant allele 1 #7 Mutant allele 2
MDSEQPDSLDGWVPLP*	#11 Mutant allele 1/2

Figure 4.3: Protein alignments of NIH/3T3 WT and WHAMM KO cells. In this study, I established NIH/3T3 cells deficient in *whamm*. Four clonal cell lines were generated by using one sgRNA targeting the coding region of *whamm*, which produced *indels* that abolished WHAMM protein expression. Amino acids labeled in red indicate positions that differ from the WT sequence. Protein sequence alignments show positions of premature stop codons (designated by stars) due to the introduced frameshifts.

Targeting NPF genes in human cells proved to be more complicated. First, I performed the experiments with one sgRNA per candidate in MDA-MB-231 and A549 cells (data not shown). However, western blotting still exhibited protein expression for the respective protein and sequencing data also displayed unsuccessful gene editing (data not shown). In order to improve CRISPR/Cas efficiency in human cell systems, I targeted two different exons of the respective gene in U-2 OS cells (Table 3.4). The generation of at least one clone per genotype was achieved by CRISPR/Cas. Western blot analysis confirmed loss of protein expression (Figure 4.4), however, sequencing data of the individual genes failed (data not shown). Although standard PCR did yield the desired amplicon of WHAMM and JMY, DNA sequencing resulted in poor results. Amplification of human WASH failed and needs to be optimized.
Collectively, these findings confirm the generation of different murine cell lines carrying either early abortive mutations on the coding sequence or sequence alterations that led to misfolding and therefore protein degradation induced by the CRISPR/Cas method. Gene KOs in human U-2 OS cells have been validated by western blotting indicating a loss of targeted NPFs in a human cell system.

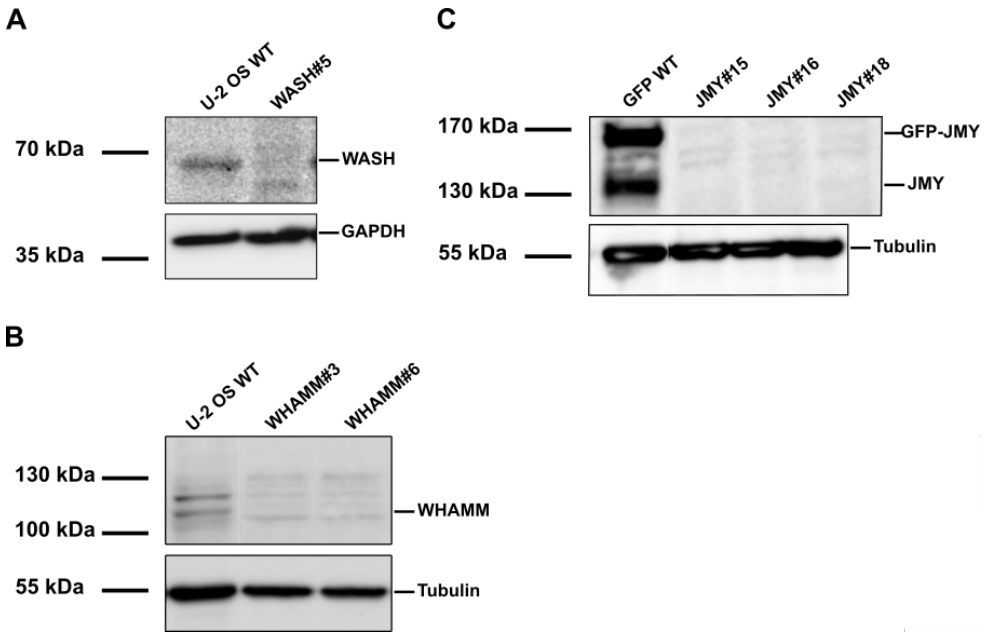

Figure 4.4: Western blot analyses show absence of expression of WASH, WHAMM or JMY in human U-2 OS clones. U-2 OS WT cells were transfected with pSpCas9(BB)-2A-GFP containing a sgRNA targeting the respective NPF (each protein was targeted with two sgRNAs). Single clonal strains were obtained by flow cytometry or serial dilution and were sent for sequencing after cell expansion. Cell lysates were harvested and protein expression was checked by western blotting. GAPDH or Tubulin was used as loading control. (A-C) Representative images of western blots. Western blot analysis revealed efficient loss of WASH, WHAMM or JMY proteins in human osteosarcoma cells. Data are representative of at least two independent experiments. Individual clones are designated by numbers.

4.2 Cellular characterization of NIH/3T3 WHAMM KO cells

4.2.1 Morphology of WHAMM KO cells

Established NIH/3T3 WHAMM KO cells were utilized for further investigation ("Clones pooled" comprised all four WHAMM KO cell lines). Therefore, clones were first analyzed for morphological parameters, including cell area, cell volume, and cell granularity. It was noted that on average WHAMM deficient cells appeared larger and I asked whether this may be due to an overall increased cell size or due to increased cell spreading. Thus, I investigated the cell and nuclear area. As anticipated, WHAMM deficiency caused an increase of the cell area and the nuclear area in fixed, spread cells (Figure 4.5, A-C, Supplementary data, Figure 6.6).

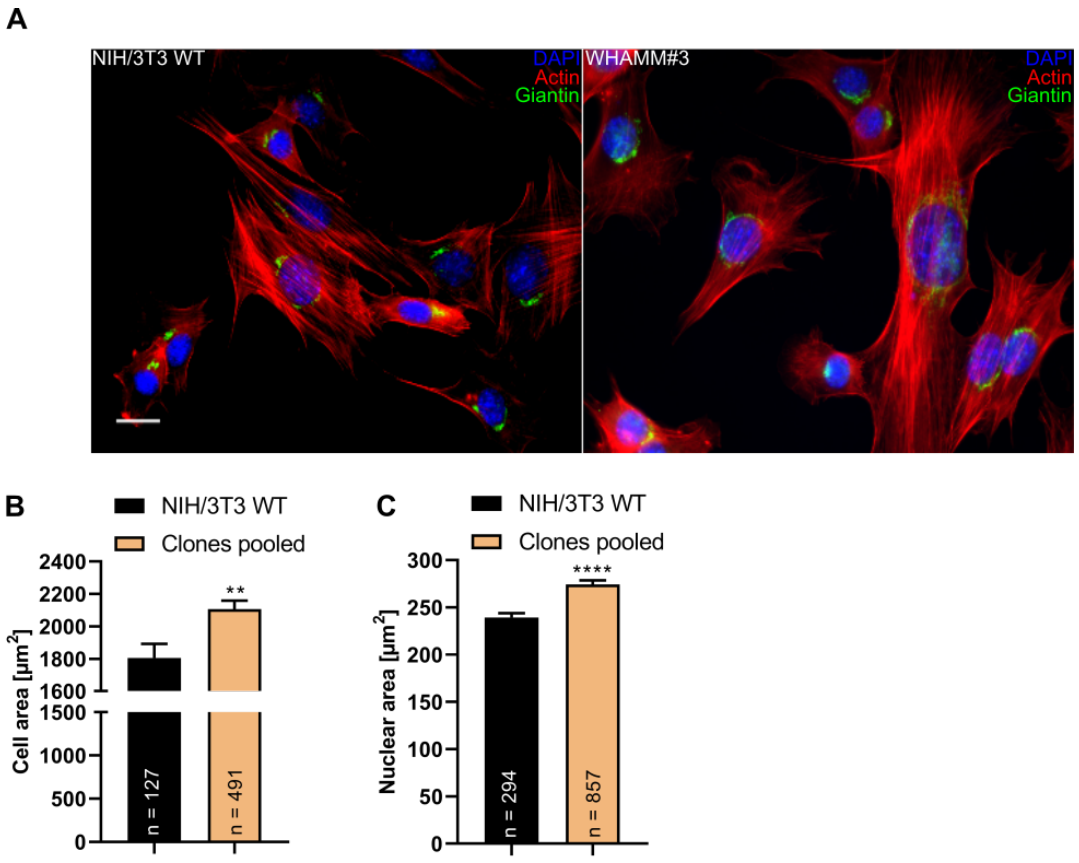

Figure 4.5: Cells deficient in *whamm* are larger in size and display larger cell nuclei. (A) Representative immunofluorescence images of WT cells and WHAMM KO clone #3. Cells deficient in *whamm* show an increase in cell size and larger cell nuclei. Giantin staining (green) was used to label the position of Golgi. DAPI staining (blue) was used as a cellular nucleus marker. F-actin (red) was stained by fluorescent phalloidin. Scale bar: 20 µm. (B-C) Quantitative analysis of WT cells *versus* WHAMM KO clones confirms significantly larger cells and larger cell nuclei in KO cells. Data are representative of three independent experiments. n = number of cells analyzed. **P $\leq$ 0.01, ****P$\leq$ 0.0001, Two-tailed Student's t-test. Error bars represent SEM.

I also analyzed the cells by flow cytometry with the help of Stephanie Stahnke (HZI, Braunschweig) to assess their cellular volume. Cells were grouped into four categories, depending on cell size and cell granularity. For this measurement, sideward scatter SSC and forward scatter FSC are plotted and gates are set to WT parameters (Figure 4.6, A). The results clearly exhibited that WHAMM deficiency results in a shift from smaller to larger granular cells (Figure 4.6, B). Moreover, it became evident that WHAMM KO cells display a significant increase in granularity (Figure 4.6, C), indicative of an accumulation of light scattering material in the cell, such as protein aggregates or vesicles.

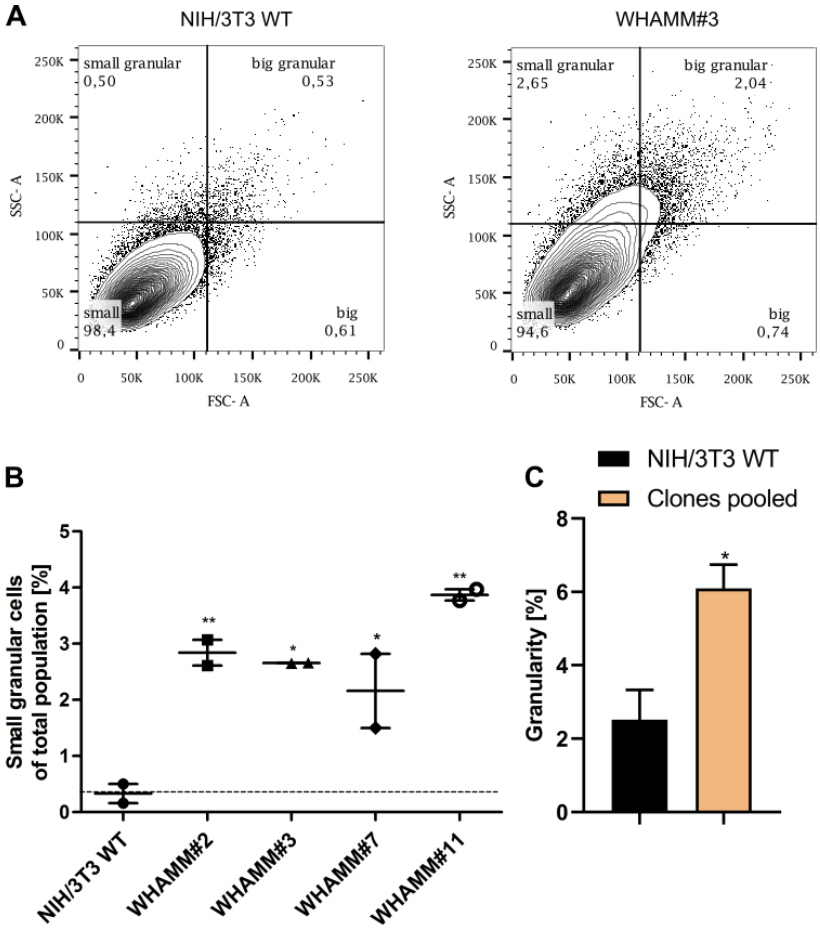

Figure 4.6: Effect of WHAMM KO on cell size and granularity. (A) Cell size and cell granularity were analyzed by flow cytometry. Quadrant gates split the population into four adjacent, discrete subpopulations. (B-C) Quantitative analysis of WT cells *versus* WHAMM KO clones confirms a shift in cell population from smaller to large cells in KO cells as well as to higher granularity. Data are representative of two independent experiments. (B) *P $\leq$ 0.05, **P $\leq$ 0.005, ***P $\leq$ 0.0001, One-way ANOVA, (C) *P $\leq$ 0.05, Two-tailed Student's t-test. Error bars represent SEM.

WHAMM is known to promote ERGIC-membrane tubulation in an actin- and microtubule dependent fashion [20]. Therefore, I investigated with the help of Frieda Kage (TU Braunschweig) whether WHAMM-deficiency impairs the general cytoskeletal organization or ER appearance. WT and KO cells were stained with probes to F-actin, ER, and ERGIC. To this end, I found no effects on stress fiber formation (Supplementary data, Figure 6.6), differing from previous observations upon siRNA treatments in BJ/SV40 T fibroblasts [41]. F-actin bundles were organized into conventional stress fibers in both WT and KO cells. Total protein levels of actin were assessed via western blotting and results exhibited similar expression levels in WT and WHAMM KO cells (Figure 4.7, A). Next, CellTracker and phalloidin stainings were performed to mea-

sure F-actin intensity in both WT and WHAMM KO cells. Quantification analysis displayed that intensity levels of WHAMM KO cells are similar to control levels measured in WT cells (Figure 4.7, B). These data imply that loss of WHAMM did not affect actin expression and stress fiber formation.

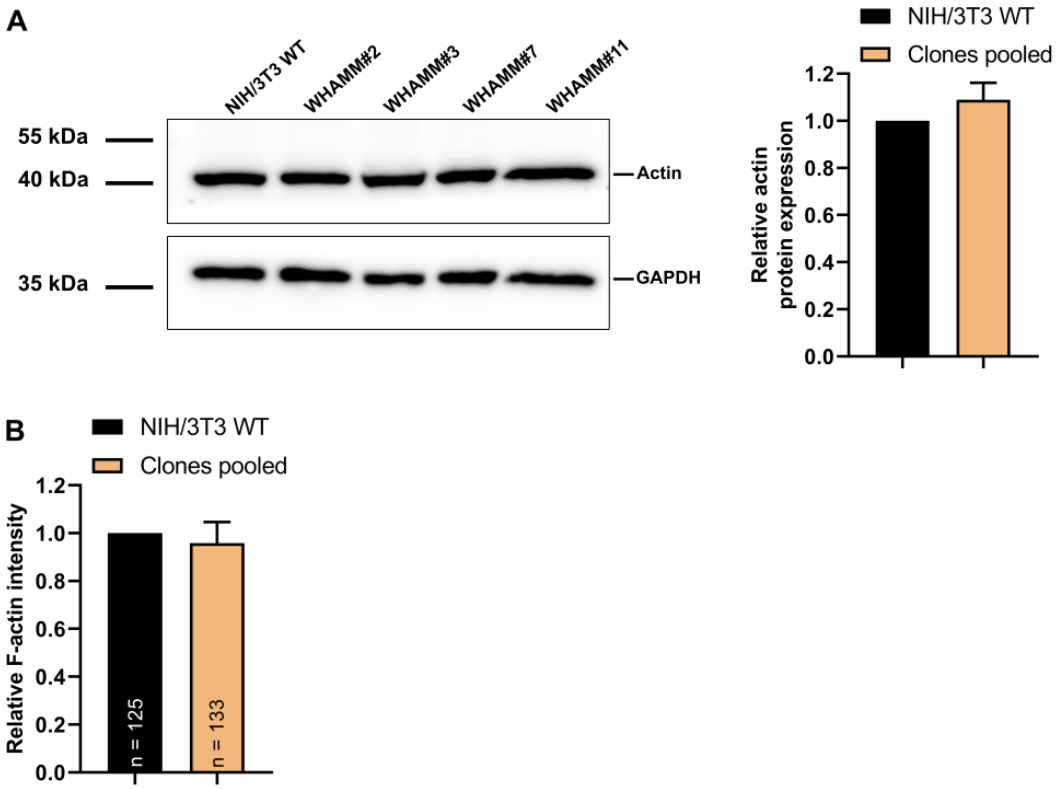

Figure 4.7: Total actin and F-actin intensity levels in WHAMM KO cells. (A) Representative image of western blots. Lysates of WT and WHAMM KO cells were separated on a SDS gel. Membrane was blotted for actin and GAPDH was used as loading control. Total actin protein expression levels were quantified by densitometry analysis of western blot bands. Data were normalized to WT protein levels. Data are representative of two independent experiments. (B) F-actin intensities of WHAMM KO cells in comparison to WT cells were analyzed via CellTracker and phalloidin stainings. Intensities were measured with ImageJ software and normalized to WT values. n = number of cells analyzed. Data are representative of two independent experiments. Error bars represent SEM.

In addition, the ER and ERGIC region were also unaffected concerning general distribution and network structure (Supplementary data, Figures 6.8 and 6.9), which also contradicts current data [45]. Since it has been described that WHAMM interacts with microtubules [20], WT and WHAMM KO cells were stained with an anti-tubulin antibody. The microtubule pattern of KO cells was unaltered and virtually identical to WT cells (Figure 4.8).

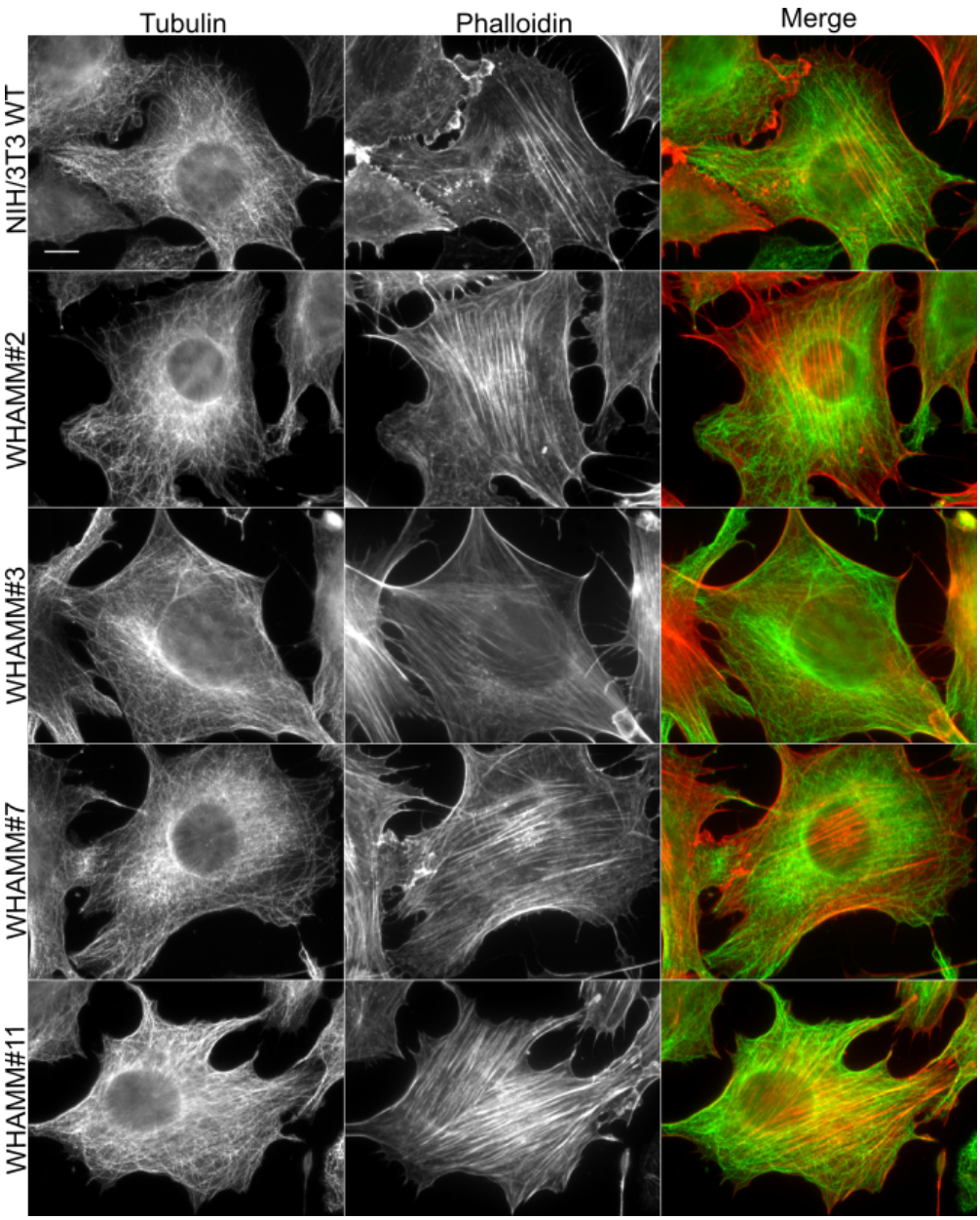

Figure 4.8: Microtubules in WHAMM KO fibroblasts are unaltered. Tubulin staining (green) was used to label the position of microtubules. F-actin (red) was stained by fluorescent phalloidin. Scale bar: 10 µm. Data are derived from one experiment.

WHAMM was described to facilitate and regulate vesicle transport between ER and Golgi as well as to contribute to the maintenance of Golgi integrity and morphology [20]. Therefore, I probed whether deletion of WHAMM might cause alterations of the Golgi complex. To do so, I stained Giantin, a cis-Golgi matrix protein in WT and WHAMM KO cells (Figure 4.9, A, Supplementary data, Figure 6.10). KO of WHAMM resulted in noticeable scattering of the Golgi apparatus and an increase of detectable Golgi fragments in all four clones (Figure 4.9, B-C), whereas WT cells

expressing WHAMM showed a predominant compact Golgi pattern. While 70% of WT cells showed a compact Golgi phenotype, only 30% of WHAMM KO cells exhibited a normally compact Golgi structure. These data support a model, in which WHAMM impacts on *cis*-Golgi integrity and organization.

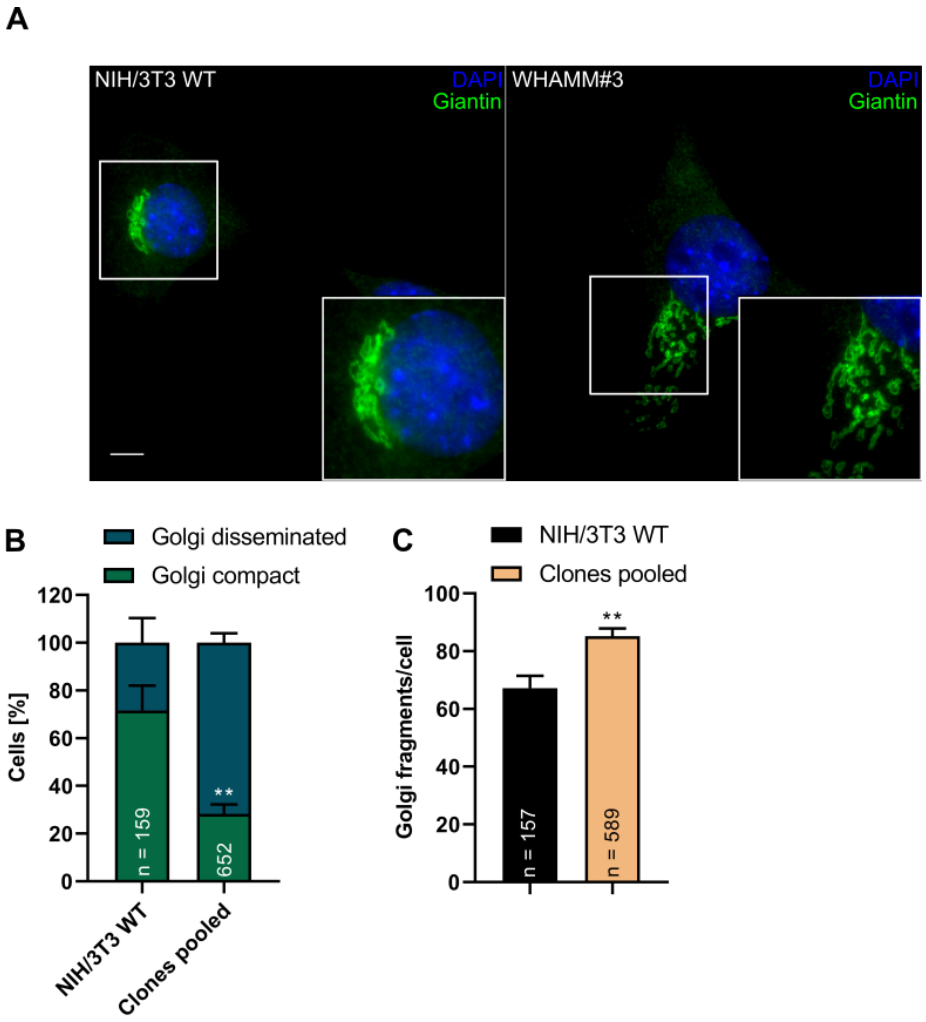

Figure 4.9: Effect of WHAMM KO on Golgi apparatus in NIH/3T3 cells. (A) Representative immunofluorescence images of WT cells and WHAMM KO clone #3. The majority of cells deficient for WHAMM show a disseminated Golgi complex. Giantin staining (green) was used to label the position of Golgi. DAPI staining (blue) was used as a cellular nucleus marker. Scale bar: 10 µm. (B-C) Quantitative analysis of WT cells *versus* WHAMM KO clones confirms a significant dispersion of Golgi apparatus in KO cells. Golgi structures were categorized as compact or disseminated. Number of particles has been assessed using the MosaicSuite tool. n = number of cells analyzed. Data are representative of three independent experiments. **P $\leq$ 0.01, Two-tailed Student's t-test. Error bars represent SEM.

Due to the known involvement of WHAMM in vesicular trafficking [20], I aimed at analyzing the dynamics of Golgi disassembly and assembly further. To do so, I conducted a BFA washout assay in WT and KO cells examining the reassembly of the Golgi complex. BFA is a fungal metabolite that causes disassembly of the Golgi compartment within 30 min of application [96]. To explore potential defects in Golgi reassembly in WHAMM KO cells, BFA was washed out for various time points followed by Giantin staining. BFA treatment caused a similar Golgi phenotype in both genotypes, with the Golgi appearing disseminated (Figure 4.10, A). The number of Golgi fragments is significantly increased in WHAMM KO cells, as already observed earlier (Figure 4.9). Interestingly, in both WT and KO cells the Golgi apparatus reassembled to the state before BFA treatment with comparable kinetics (Figure 4.10, B) indicating that WHAMM is not involved in Golgi reassembly from ER membranes upon BFA washout.

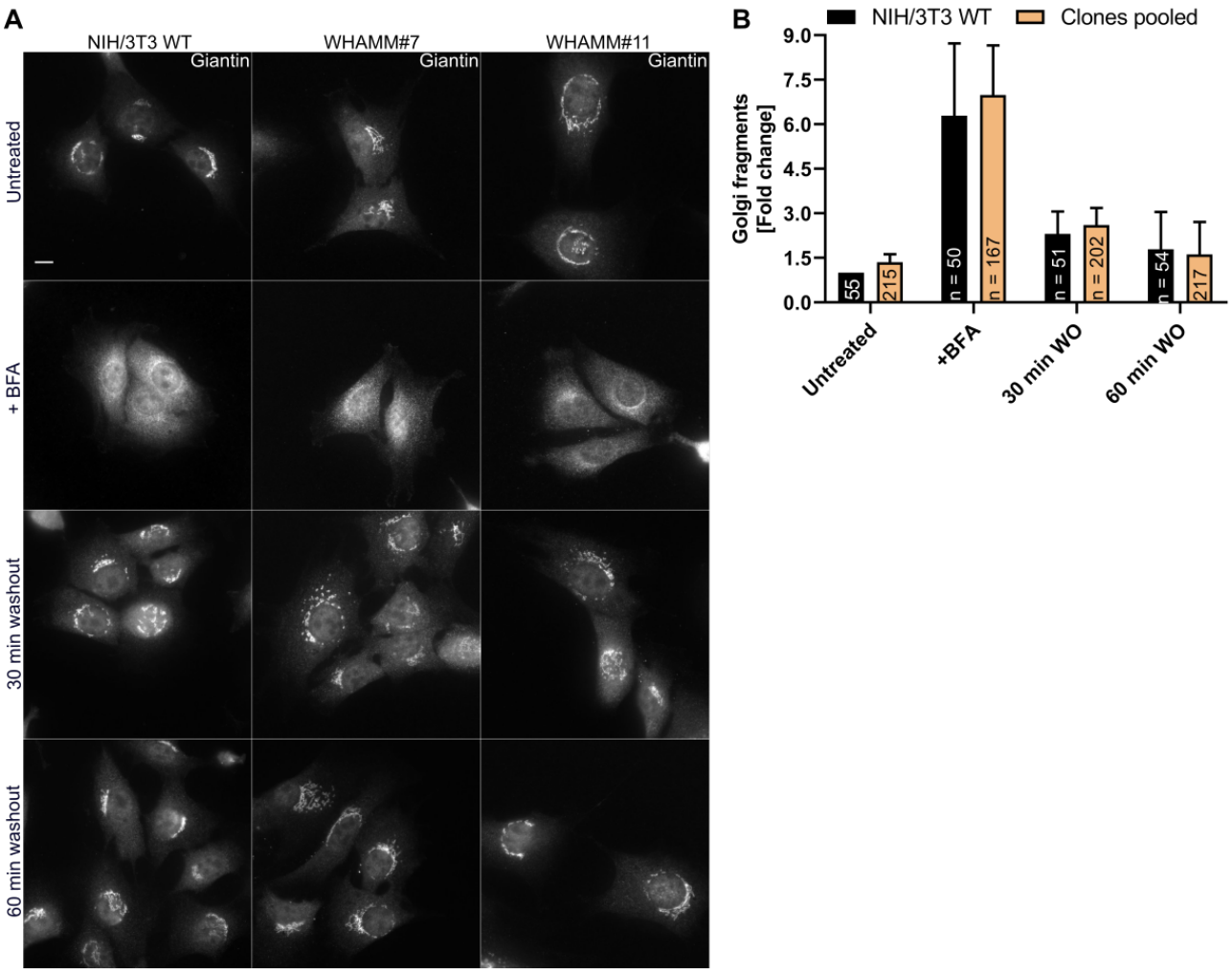

Figure 4.10: Loss of WHAMM leads to a more pronounced Golgi fragmentation but does not affect Golgi reassembly. (A) Representative immunofluorescence images of WT cells and two WHAMM KO clones untreated or treated with 2.5 µg/mL BFA (+ BFA) for 35 min, followed by replacement of BFA-containing medium with complete culture medium (WO = washout) for the times indicated. Giantin staining was used to label the position of Golgi. Note that untreated KO cells display a less organized and less compact Golgi apparatus as compared to control cells, consistent with previous experiments (Figure 4.9). Scale bar: 10 µm. (B) Quantitative analysis of average number of Golgi fragments in WT cells and WHAMM KO clones. KO clones were normalized to the average number of Golgi fragments in control cells (Untreated). Both cell lines showed complete recovery from BFA-treatment. Number of particles has been assessed using the MosaicSuite tool. n = number of cells analyzed. Data are representative of two independent experiments. Error bars represent SEM.

4.2.2 The contribution of WHAMM to autophagy

KO cells displayed a significant increase in granularity, indicative of an accumulation of granular particles (e.g. protein aggregates or vesicles) (Figure 4.6, C). WHAMM has previously been reported to be an important regulator of endomembranes, acting not only in the ERGIC region but also at the ER during autophagy [20, 44]. Moreover, it has been shown that WHAMM is involved in autophagosome biogenesis through an actin-comet tail motility mechanism [44]. An important facet of autophagy is the production of autophagic vacuoles [97], which may explain increased intracellular granularity observed in WHAMM KOs. Thus, I aimed at further investigation of the role of WHAMM during autophagy and examined this process in established WHAMM KO cells. To explore the function of WHAMM in autophagosome assembly, I compared WT and KO cells grown under nutrient-rich (fed or basal) *versus* starvation conditions, the latter is a well-known inducer of autophagy via the mTOR pathway [68, 78]). I investigated the mTOR pathway by western blotting and visualized the formation of omegasomes, autophagosomes, and lysosomes by staining for the distribution of different autophagy markers, including DFCP1, ATG9, LC3, p62, and LAMP1.
As mTOR is a prominent inhibitor of autophagy, I first examined expression of mTOR and p-mTOR via western blotting. Interestingly, protein expression levels of mTOR under basal conditions were significantly reduced by about 20 % in WHAMM KO cells (Figure 4.11, A), but surprisingly displayed a clear upregulation of p-mTOR (Figure 4.11, B). This phenotype suggests that the absence of WHAMM increases active mTOR levels together with a downregulation of total mTOR protein levels to counterbalance overactivation.

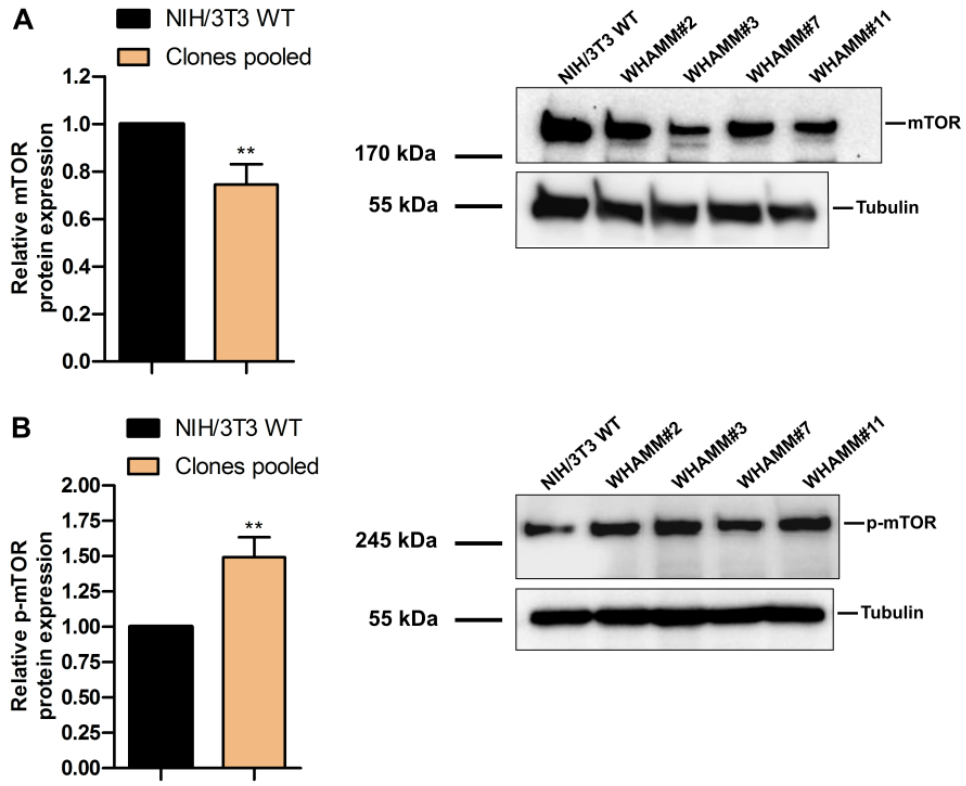

Figure 4.11: WHAMM KO cells exhibit lower expression of mTOR, but increased mTOR phosphorylation. (A) Total mTOR protein expression levels were quantified by densitometry analysis of western blot bands. Lysates of WT and WHAMM KO cells were separated on a SDS gel. Membrane was blotted for mTOR and Tubulin was used as loading control. Data were normalized to WT protein levels. (B) Total p-mTOR protein expression levels were quantified by densitometry analysis of western blot bands. Lysates of WT and WHAMM KO cells were separated on a SDS gel. Membrane was blotted for p-mTOR and Tubulin was used as loading control. Data were normalized to WT protein levels. (A-B) One representative blot is shown of three independent experiments. **P $\leq$ 0.01, Two-tailed One-Sample t-test. Error bars represent SEM.

Another interesting aspect with regard to autophagy was to investigate the number and distribution of ATG9-positive vesicles, which are important membrane sources during early steps of autophagy [81]. ATG9 mainly resides in the Golgi apparatus but under starvation conditions, it partially colocalizes with markers of early endosomes and recycling endosomes [98]. Since it is known that WHAMM associates with Golgi membranes [20], I asked whether WHAMM might facilitate ATG9 transport. If so, I expected an accumulation of ATG9 vesicles in WHAMM KO cells. So far, preliminary analysis of immunofluorescence images displayed small ATG9-containing structures in WT cells under basal conditions, which were distributed in a normal fashion throughout the cytoplasm, whereas WHAMM KO cells showed larger ATG9 clusters (Figure 4.12, A). Moreover, the majority of ATG9 spots in WHAMM KO cells was positioned in the perinuclear region (Figure 4.12, A) and their number was clearly reduced as compared to WT cells (Figure 4.12, B).

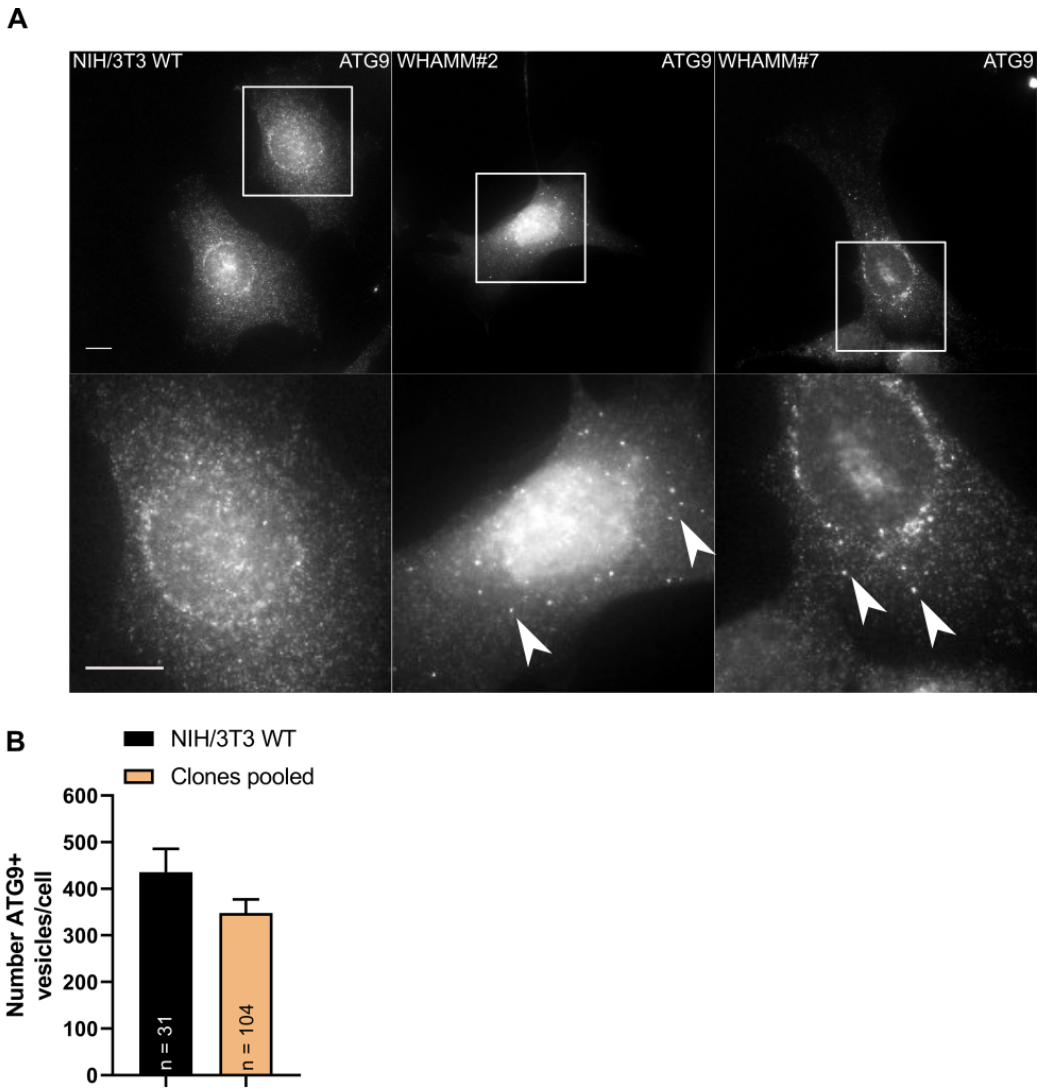

Figure 4.12: ATG9 distribution in WHAMM KO cells. (A) Representative immunofluorescence images of WT and WHAMM KO cells. ATG9 was used to label ATG9-containing structures (single-membrane vesicles). The majority of ATG9-positive structures accumulated in the juxtaperinuclear region under fed conditions. Arrowheads indicate enlarged ATG9 dots in KO cells. Scale bar: 10 µm. (B) Quantitative analysis of WT cells *versus* WHAMM KO clones confirms a decreased number of ATG9 puncta per cell in WHAMM-deficient cells under fed conditions. Number of particles has been assessed using the MosaicSuite tool. n = number of cells analyzed. Data are derived from one experiment. Error bars represent SEM.

Total ATG9 protein expression levels were tested by western blotting under both fed and starvation conditions with the help of Silvia Prettin (HZI, Braunschweig). However, preliminary data uncovered strikingly different protein expression levels of ATG9 among WHAMM KO clones (data not shown). To probe for RNA levels, I examined the expression profiles of various ATG genes including ATG9 from GeneChip Arrays with the help of Robert Geffers (HZI, Braunschweig), which are shown in Figure 6.19 (Supplementary data), however, with no significant result.

I also inspected the localization of DFCP1, an early autophagy marker found on omegasomes, by transfecting fibroblasts with EGFP-tagged DFCP1. EGFP-DFCP1-coated omegasomes were formed in both genotypes. However, WHAMM depletion resulted in a marked accumulation of enlarged EGFP-DFCP1-positive structures (Figure 4.13, A, Supplementary data, Figure 6.11) under fed conditions. Strikingly, omegasomes tended to accumulate in clusters in WHAMM KO cells, whereas singular structures predominantly appeared in WT cells. Clustering of omegasomes was also confirmed with superresolution microscopy (data not shown). I quantified the number and size of clustered DFCP1 structures affirming a distinct increase in both parameters in WHAMM KOs (Figure 4.13, B-C). These data suggest a defect in early autophagy upon ablation of WHAMM. Omegasome formation was also visualized with live cell imaging to investigate whether DFCP1 spots in KO cells display alterated kinetics. Preliminary data of EGFP-DFCP1 structures revealed no difference in DFCP1 puncta formation in fed and starvation medium (data not shown). Omegasomes in both WT and WHAMM KO cells appeared mobile and dynamic.

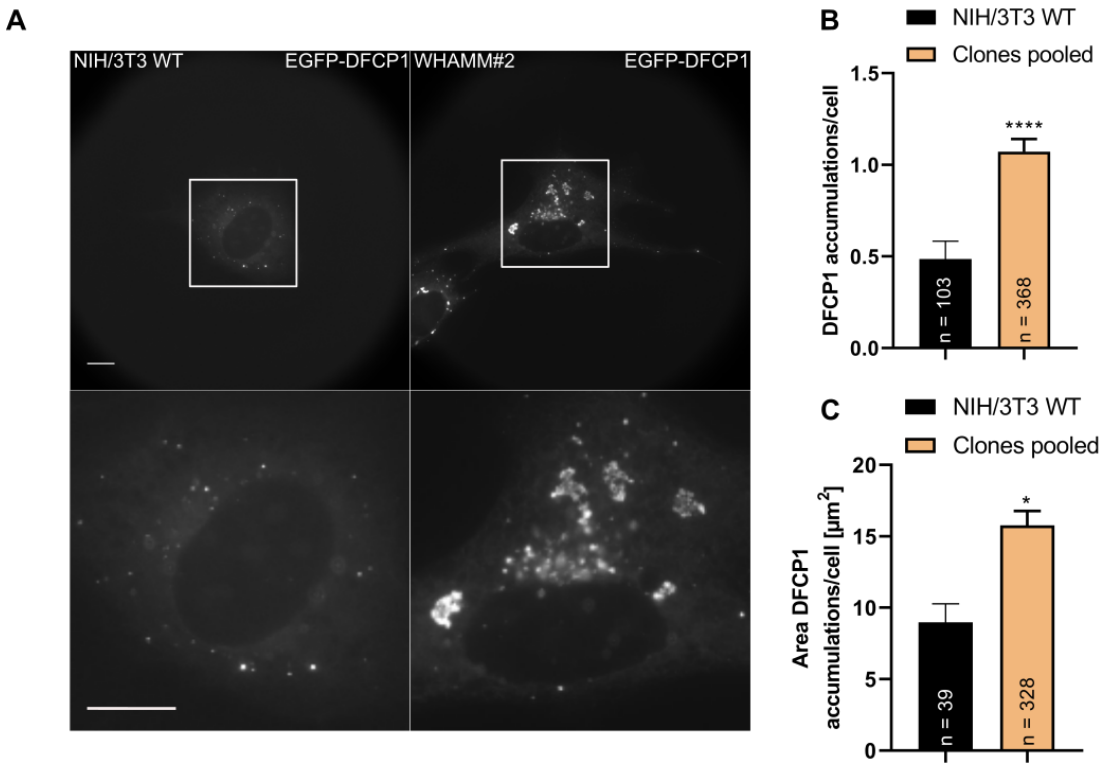

Figure 4.13: WHAMM KO leads to an accumulation of omegasomes. (A) Representative immunofluorescence images of WT cells and WHAMM KO clone #2. EGFP-DFCP1 was used to label the position of omegasomes. WHAMM KOs in general exhibited an accumulation of DFCP1-positive structures under fed conditions. Scale bar: 10 µm. (B) Accumulated DFCP1 structures are increased in WHAMM KO cells under fed conditions. (C) WHAMM KO cells contain enlarged DFCP1 structures under fed conditions. (B-C) n = number of cells analyzed. Data are representative of three independent experiments. *P $\leq$ 0.05, ****P $\leq$ 0.0001, Two-tailed Student's t-test. Error bars represent SEM.

Next, I determined whether WHAMM KO has an effect on autophagosome maturation. Therefore, I investigated the lipidated form of LC3, LC3-II, under fed and starved conditions in WT *versus* KO cells by western blotting. However, results only showed either a diffused or weak antibody staining, especially for LC3-I detection, which could not be quantified (Supplementary data, Figure 6.12). To circumvent this, I performed immunofluorescence staining for LC3 (Figure 4.14, A). Interestingly, initial localization analysis showed that autophagic vesicles in WHAMM KO cells are more frequently found in the perinuclear region of the cell as compared to WT cells (Figure 4.14, B-C).

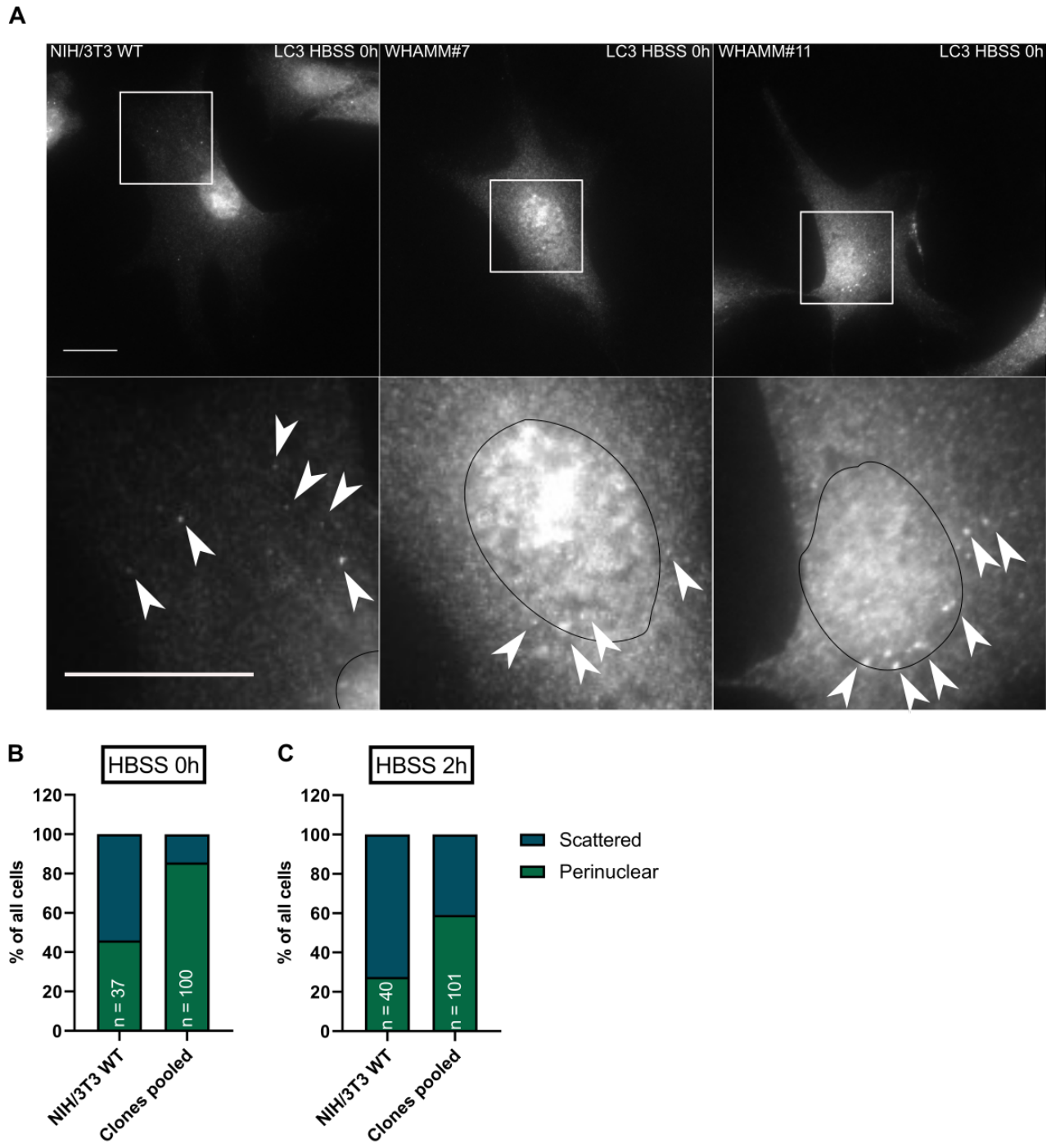

Figure 4.14: WHAMM KO affects distribution of autophagosomes. (A) Representative immunofluorescence images of WT cells and two WHAMM KO clones. LC3 was used to label the position of autophagosomes. WHAMM KOs in general exhibited a perinuclear localization of LC3-positive structures under fed conditions (indicated by arrow heads). Drawn circles indicate cell nuclei. Scale bar: 20 µm. (B) Preliminary analysis of WT cells *versus* WHAMM KO clones indicates a perinuclear distribution of LC3 puncta in WHAMM-deficient cells under fed conditions. (C) Preliminary analysis of WT cells *versus* WHAMM KO clones show a perinuclear distribution of LC3 puncta in WHAMM-deficient cells under starvation conditions. (B-C) n = number of cells analyzed. Data are derived from one experiment.

Analysis of the total number of LC3 puncta per cell showed that the quantity of LC3 vesicles was similar in both WT and KO cells during fed conditions (Figures 4.15, A and 4.18, A), but decreases upon prolonged starvation in WT cells, indicative for increased autophagic degradation of LC3-II-labeled structures. Whereas the basal level of LC3-positive structures was almost identical in both genotypes, the number of LC3 puncta per cell in KO cells was markedly higher upon starvation than that in WT cells (Figure 4.15, A, Supplementary data, Figures 6.13 and 6.14), leading to a drastic difference in the number of LC3-vesicles between WT and KO cells. In fact, KO cells on average showed a 50% - 75% increase of LC3 vesicles per cell in comparison to WT cells. The increase of LC3 dots in WT cells upon starvation was very moderate in comparison to that in KO cells, indicative of an accumulation of autophagosomes in WHAMM KO cells due to impaired degradation during autophagic flux. Also note that the ratio between untreated and starved NIH/3T3 WT cells was not remarkably altered, indicating that shorter starvation time points might be necessary to assess increased autophagy due to amino acid deprivation. Moreover, the total area of autophagosomes per cell was significantly elevated in comparison to WT cells upon starvation (Figure 4.15, B, Supplementary data, Figures 6.13 and 6.14), suggesting a defect in vesicle fusion or fission. In order to better understand the autophagic flux in WT and KO cells, I chose additional approaches to assess LC3 turnover.

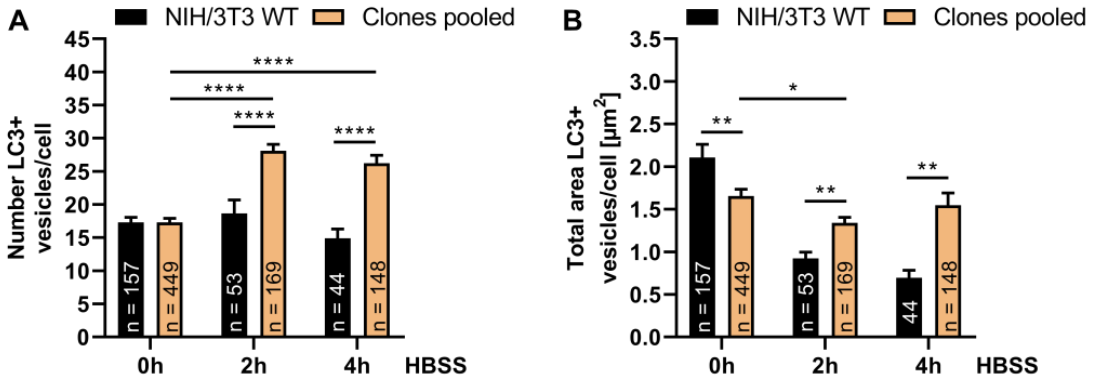

Figure 4.15: WHAMM KO affects number and total area of autophagosomes. (A) Quantitative analysis of WT cells *versus* WHAMM KO clones confirms an increased number of LC3 puncta per cell in WHAMM-deficient cells under starvation conditions. (B) Quantitative analysis of WT cells *versus* WHAMM KO clones shows no differences in the total area occupied by LC3-positive vesicles under fed conditions, whereas starvation leads to larger LC3-positive vesicles in WHAMM-deficient cells. (A-B) Particle analysis has been performed with the Threshold function (see Materials and Methods). n = number of cells analyzed. Data are representative of at least two independent experiments. *P≤ 0.01, **P≤ 0.01, ****P≤ 0.0001, Two-tailed Student's t-test. Error bars represent SEM.

Thus, autophagic activity in WHAMM KO cells was also measured by flow cytometry. This methodology is based on the fact that LC3 serves as a potential autophagic substrate for degradation. Therefore, changes in total intracellular LC3 fluorescence intensity were used as an indicator of cellular autophagic activity in WT and KO cells. Representative plots of untreated cells are shown in Figure 6.17 A (Supplementary data). As expected, WHAMM KO cells showed a higher fluorescence intensity compared to WT cells (Supplementary data, Figure 6.17, B) supporting my previous notion that autophagic material preferentially accumulates in WHAMM KO cells, indicative of dysregulated autophagy.

Another assay to monitor autophagic flux is the inhibition of autophagosome degradation. Therefore, cells were kept under starvation conditions and/or treated with BafA1. This inhibitor is known to block the acidification inside the lysosome as well as autophagosome-lysosome fusion, thereby preventing LC3-II degradation [99]. Accordingly, differences in the amount of LC3-II in the presence and absence of a lysosomal inhibitor represent the amount of LC3 that is delivered to lysosomes for degradation (i.e. autophagic flux). Fed conditions with BafA1 resulted in no significant difference in the number and size of LC3 puncta in both WT and WHAMM KO cells (Figures 4.16, A-B and 4.19, A). However, KO cells showed a clear increase of autophagic vacuoles after starvation and BafA1 treatment compared to WT cells (Figure 4.16, A and Supplementary data, Figures 6.15 and 6.16). In fact, data displayed more than 70 LC3-positive dots in KO cells, while WT fibroblasts carried less than 40 LC3 vesicles per cell. Furthermore, these particles were again increased in size (Figure 4.16, B). However, NIH/3T3 WT and KO fibroblasts in general displayed a somewhat untypical nucleus staining for LC3 making it partially challenging to monitor endogenous LC3 by immunofluoresence (see discussion). Nonetheless, autophagosomes strikingly appeared to accumulate in WHAMM KO cells under starvation and BafA1 treatment, exemplified by significant differences between WT and WHAMM KO cells. Moreover, an accumulation of LC3-positive spots upon starvation plus BafA1 treatment corresponds to the expected dynamics, indicative of impaired autophagic flux and thereby confirming previous assumptions. In summary, these data suggest that WHAMM deficiency leads to a stronger increase of autophagosomes under amino acid deprivation and lysosomal block conditions.

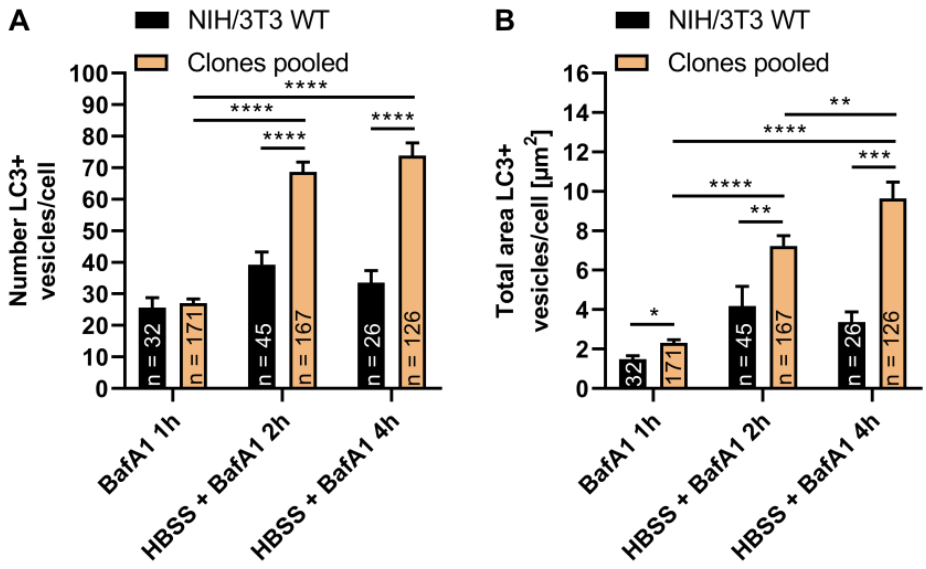

Figure 4.16: Effect of WHAMM KO on autophagic flux. (A) Analysis of WT cells *versus* WHAMM KO clones confirms an increased number of LC3 puncta per cell in WHAMM-deficient cells under starvation and/or BafA1 treatment. (B) Analysis of WT cells *versus* WHAMM KO clones leads to larger LC3-positive vesicles in WHAMM-deficient cells under starvation and/or BafA1 treatment. (A-B) Particle analysis has been performed with the Threshold function (see Materials and Methods). n = number of cells analyzed. Data are representative of two independent experiments. *P$\leq$ 0.05, **P$\leq$ 0.01, ***P$\leq$ 0.001, ****P$\leq$ 0.0001, Two-tailed Student's t-test. Error bars represent SEM.

To clarify observed effects of WHAMM KO on autophagy, I also examined the p62 level by both western blotting and immunofluorescence. p62 is a carrier protein selectively incorporated into autophagosomes through direct binding to LC3. Induction of autophagy leads to its degradation [99, 100], which can be utilized as readout. In fact, the steady-state p62 level is widely used as a marker of autophagy degradation activity.

Strikingly, p62 protein expression levels in WHAMM KO cells were strongly increased under both fed and starvation conditions compared to WT fibroblasts (Figure 4.17, B). Loss of WHAMM resulted in a 2.5-fold increase of p62 under nutrient rich conditions compared to WT cells. During prolonged starvation, protein expression levels of p62 were slightly increased (early starvation time points), but not significantly changed in WT cells. In contrast, p62 was more abundant in KOs than in WT cells. In fact, a significantly higher amount of p62 was detected in WHAMM KOs upon starvation, which initially increased and then dropped below starting levels. This result suggests once more that material which is dedicated to autophagic degradation accumulates faster and to a greater extent in WHAMM KO cells.

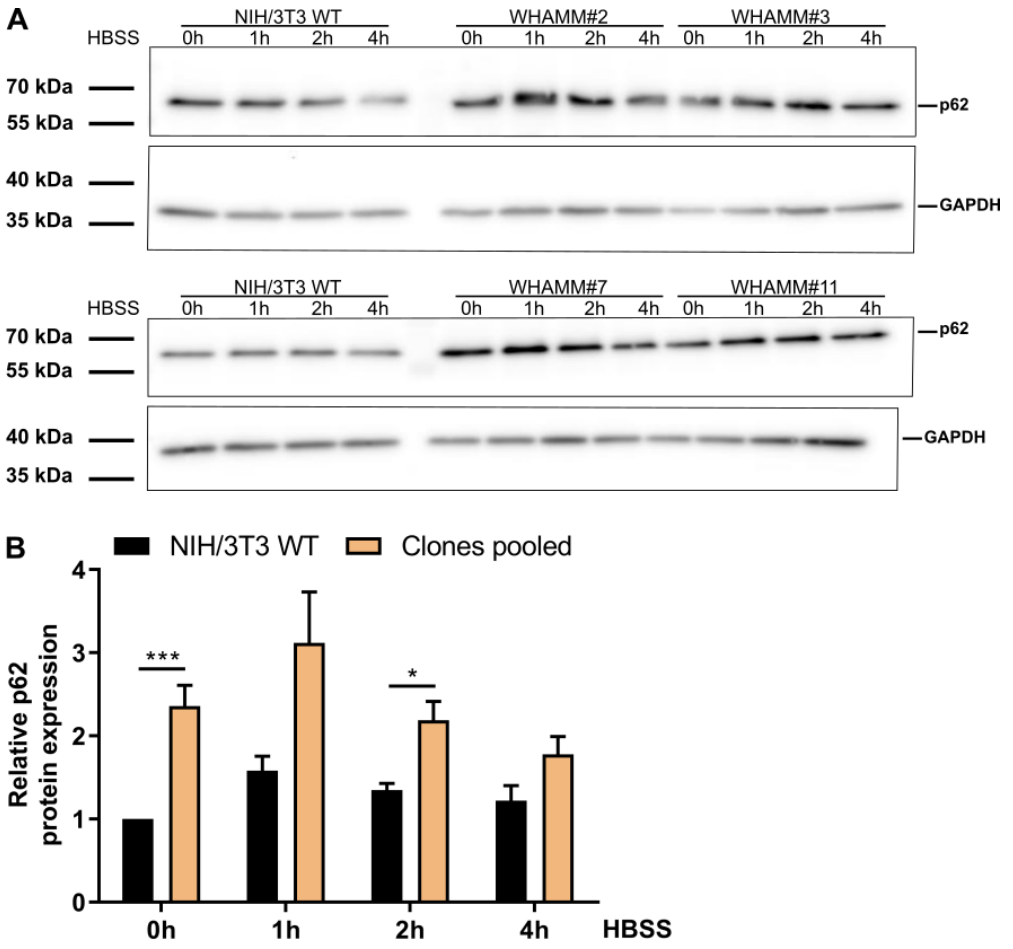

Figure 4.17: Quantification of p62 levels after HBSS treatment. (A) Representative image of western blots. Cells were seeded and starved with HBSS for the indicated time points. Lysates of WT and WHAMM KO cells were separated on a SDS gel. Membrane was blotted for p62 and GAPDH was used as loading control. Data are representative of three independent experiments. (B) Total p62 protein expression levels were quantified by densitometry analysis of western blot bands. Data were normalized to untreated WT protein levels. Data are representative of three independent experiments. *P$\leq$ 0.05, ***P$\leq$ 0.001, Two-tailed Student's t-test. Error bars represent SEM.

Western blot data were additionally verified by staining endogenous p62 by immunofluorescence. Microscopic analyses showed a clear difference of p62 spots per cell between WT and KO cells during fed conditions (Figure 4.18, A-B). Moreover, a significant increase of p62 puncta per cell was detected in both genotypes upon starvation, followed by a reduction during prolonged starvation, most likely reflecting degradation (Figure 4.18, B, Supplementary data Figures 6.13 and 6.14). However, also in this assay the number of p62-positive structures was significantly higher in WHAMM KO cells, suggesting that loss of WHAMM impairs the autophagic process. The total area of p62-positive structures per cell seemed to be not significantly different between the genotypes and tended to decrease upon starvation (Figure 4.18, C, Supplementary data, Figures 6.13 and 6.14).

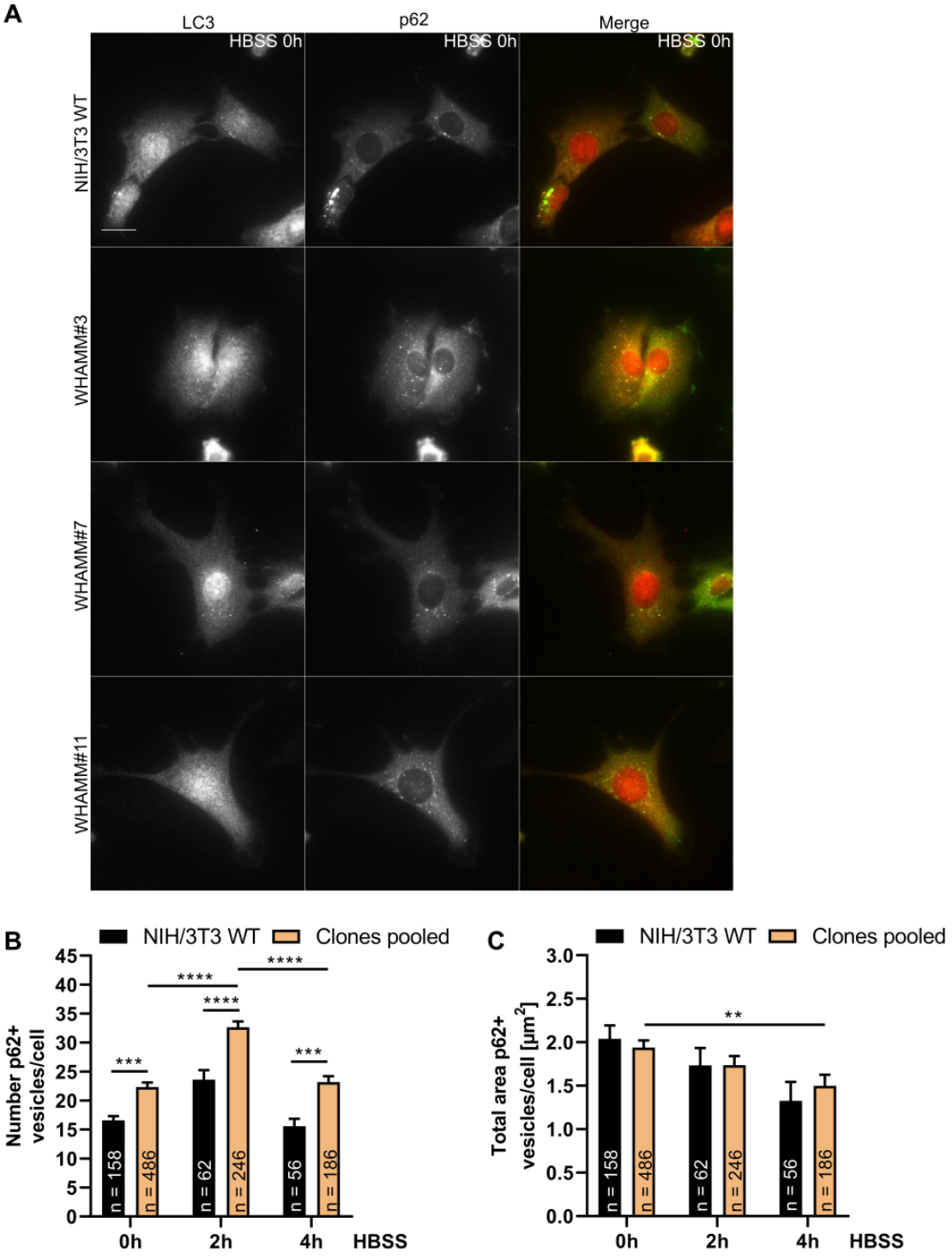

Figure 4.18: WHAMM KO affects number of p62-positive spots. (A) Representative immunofluorescence images of WT cells and WHAMM KO clones. Basal level of autophagy was studied with autophagy markers LC3 (red) and p62 (green). Scale bar: 20 µm. (B) Quantitative analysis of WT cells *versus* WHAMM KO clones confirms an increased number of p62 puncta per cell in WHAMM-deficient cells under fed and starvation conditions. (C) Quantitative analysis of WT cells *versus* WHAMM KO clones shows no differences in the total area occupied by p62-positive vesicles under fed and starvation conditions. (B-C) Particle analysis has been performed with the Threshold function (see Materials and Methods). n = number of cells analyzed. Data are representative of at least two independent experiments. **P≤ 0.01, ***P≤ 0.001, ****P≤ 0.0001, Two-tailed Student's t-test. Error bars represent SEM.

Finally, additional treatment with BafA1 resulted in further accumulations of p62 puncta in both genotypes, which was again more pronounced in WHAMM KO cells (Figure 4.19, A). The number of p62-particles slowly decreased during prolonged starvation in WT fibroblasts, whereas p62-accumulation in WHAMM KOs did not fade and instead cells showed persistent p62-levels upon starvation. In addition, these accumulated p62 punctae were significantly larger than those of WT cells (Figure 4.19, B).

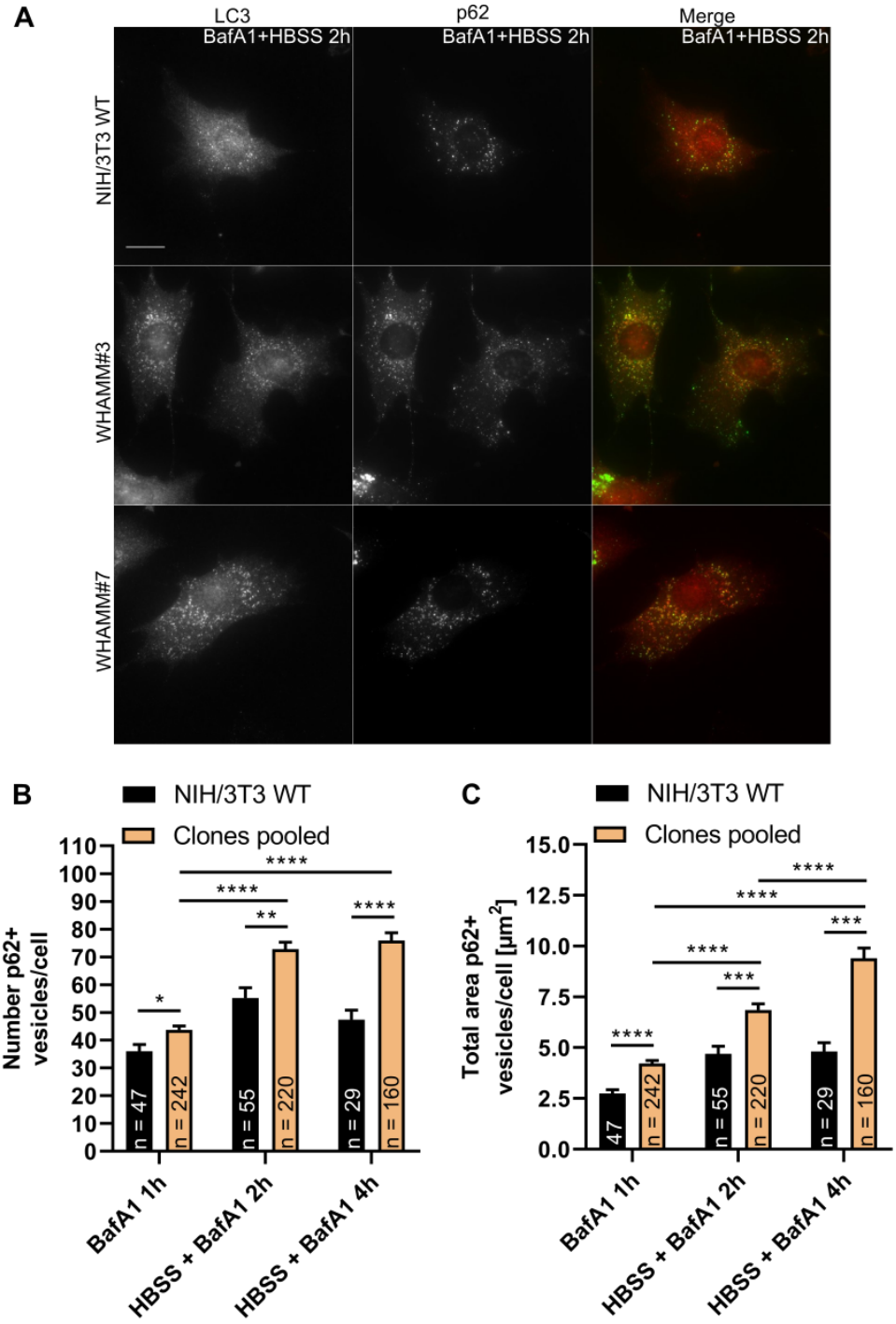

Figure 4.19: Effect of WHAMM KO on autophagic flux. (A) The autophagic flux was further investigated by HBSS treatment in the presence of BafA1 and studied with autophagy markers LC3 (red) and p62 (green). (B) Analysis of WT cells *versus* WHAMM KO clones confirms an increased number of p62 puncta per cell in WHAMM-deficient cells under starvation and/or BafA1 treatment. (C) Analysis of WT cells *versus* WHAMM KO clones confirms a larger area occupied by p62-positive vesicles in WHAMM-deficient cells under starvation and/or BafA1 treatment. (B-C) Particle analysis has been performed with the Threshold function (see Materials and Methods). n = number of cells analyzed. Data are derived from one experiment. *P≤ 0.05, **P≤ 0.01, ***P≤ 0.001, ****P≤ 0.0001, Two-tailed Student's t-test. Error bars represent SEM.

p62 has a dual role in intracellular proteolysis: It can not only interact with ubiquitinated proteins via its C-terminal ubiquitin-associated domain, but also binds directly to LC3 and GABARAP family proteins via its LIR motif. Consequently, p62 shuttles ubiquitinated proteins to the autophagic machinery enabling their degradation in the lysosome [101, 102]. Additionally, it is known that p62 is involved in ubiquitin-dependent proteasomal degradation [103, 104]. Hence, an accumulation of p62 observed in Figures 4.17, 4.18 and 4.19 might not only result from hindered autophagy but also from an inhibition of the ubiquitin-proteasome pathway due to the introduced gene KO. To analyze whether WHAMM KO affects proteasomal degradation of poly-ubiquitinated proteins, I performed western blotting of whole cell lysates of WT and KO cells and probed for the abundance of poly-ubiquitinated proteins. Results did not show any significant difference in the pattern of poly-ubiquitinated proteins (Figure 4.20) indicating that WHAMM KO more likely and more strongly affects the autophagic machinery than the ubiquitin-proteasome pathway.

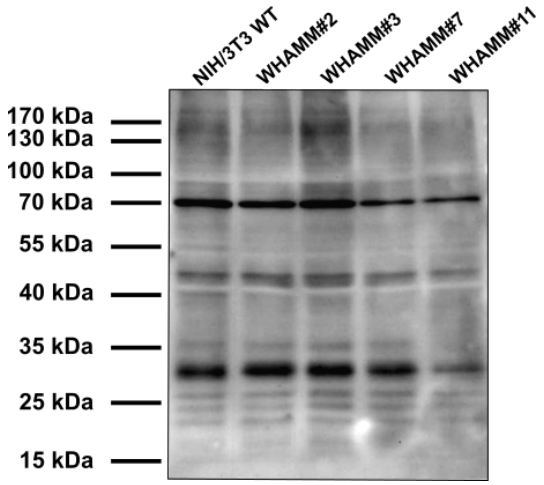

Figure 4.20: Western blot analysis of total ubiquitin-bound protein levels in WHAMM KO cells. Representative image of western blots. Lysates of WT and WHAMM KO cells were separated on a SDS gel. Membrane was blotted for ubiquitin. Data are representative of two independent experiments.

Lysosomes are the final destination of the autophagic pathway [105]. Impaired autophagy (see Figures 4.15 and 4.18) might be a result of lysosomal dysfunction induced by the deletion of *whamm*. Although earlier work has implied WHAMM in early autophagosome biogenesis [44], I aimed at formally excluding additional defects in later steps of autophagy, such as autophagosome-lysosome fusion. An accumulation of lysosomes might indicate impaired autophagosome-lysosome fusion and a block of the autophagic flux. Therefore, I visualized lysosomes with LAMP1 staining under

basal and starvation conditions. Results revealed that the number of LAMP1 spots in WHAMM KO cells is increased in comparison to WT cells (Figure 4.21, A). Moreover, the number gradually increased in KO cells, whereas WT cells revealed similar amounts of LAMP1 spots upon both fed and starvation conditions. I also found that WHAMM KO cells contain a larger portion of bigger structures as compared to WT cells under both basal and starvation conditions (Figure 4.21, B). Culturing both genotypes under fed conditions resulted in virtually 50% more of enlarged LAMP1-spots in WHAMM KOs as compared to WT cells. This effect slowly faded upon starvation but WHAMM KO cells contained still higher numbers of bigger lysosomes per cell in comparison to WT cells. This data uncover that WHAMM ablation also results in enlarged lysosomes (Figure 4.21, C) supporting the assumption of possible defects in vesicle fusion or fission.

Collectively, the data on DFCP1, LC3, p62, and LAMP1 support the notion that autophagosome formation and maturation as well as later fusion events are affected due to the absence of WHAMM pointing to a defect in membrane fission and/or fusion. This might lead to an inhibited autophagic flux and finally to a congestion of autophagic material destined for degradation.

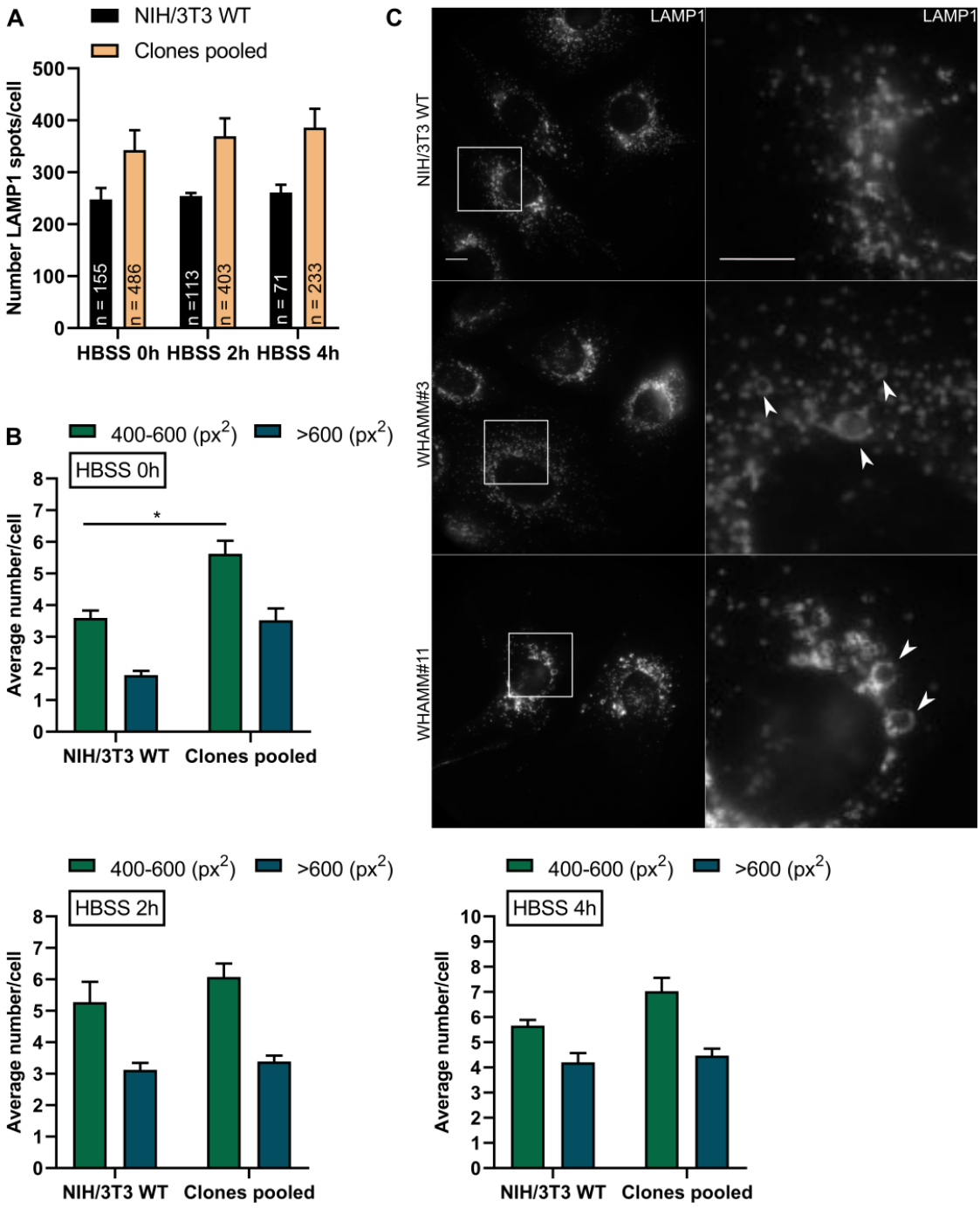

Figure 4.21: WHAMM KO affects number and size of LAMP1 spots. (A) Quantitative analysis of WT cells *versus* WHAMM KO clones confirms an increased number of LAMP1 spots per cell in WHAMM-deficient cells under fed and starvation conditions. (B) Quantitative analysis of WT cells *versus* WHAMM KO clones shows differences in the number of larger lysosomes per cell in WHAMM-deficient cells under fed and starvation conditions. (A-B) Data are representative of at least two independent experiments. *P$\leq$ 0.05, Two-tailed Student's t-test. Error bars represent SEM. (C) Representative immunofluorescence images of WT cells and two WHAMM clones under fed conditions. Cells deficient in *whamm* show enlarged lysosomal structures. Scale bar: 10 µm.

The quantitative power of flow cytometry has also been used for a deeper LAMP1 analysis (Supplementary data, Figure 6.17). As performed for LC3, non-starved and starved cells were analyzed for changes in their fluorescence intensity. Preliminary results exhibited an increase in fluorescence in WHAMM KO cells (Supplementary data, Figure 6.18). This data is consistent with previous data (see Figure 4.21) and indicates once more that loss of WHAMM leads to an accumulation of lysosomes.

4.2.3 Gene regulation and cholesterol homeostasis in WHAMM KO cells

To get a deeper insight into WHAMM KO imposed cellular changes and the alterations in autophagy described above, I performed cDNA microarray analyses of WT and WHAMM KO cells with the help of Robert Geffers (HZI, Braunschweig). Two different WT samples (ran in duplicates) served as controls and were compared to WHAMM KO clones #2, #3, #7, and #11. Heatmaps in Figure 4.22 display the differential expression of the top 500 (A) as well as top 50 genes (B). WHAMM KO cells revealed a distinct gene expression pattern compared to WT cells. All KO clones clustered and deviated from WT samples, suggesting that loss of WHAMM has an impact on the expression profile. Interestingly, WT samples were more similar to each other than KO samples, which might indicate that gene disruption of WHAMM posses a significant pressure on the surviving of cell clones. I searched for the top 50 genes (done by Robert Geffers) and data analyses revealed two major gene clusters (indicated by red and green boxes) (Figure 4.22, B). I analyzed both clusters and identified differentially expressed genes between WT and KO cells, such as *acly* and *tm7sf2* or *lrrk2*. The formers are known to be involved in lipid synthesis, whereas Lrrk2 is a positive regulator of autophagy (Supplementary data, Table 6.1). Moreover, other interesting genes differentially expressed in WHAMM KOs are involved in the budding of vesicles from the Golgi apparatus (i.e. *ap3s1 ps1/ps2*), play a role in maintaining normal plasma cholesterol levels (i.e. *pdzk1ip1*) or have been associated with remodeling of the actin cytoskeleton (i.e. *gmpr*). Interestingly, WHAMM functions in ER to *cis*--Golgi transport [20] and it was also connected to drive autophagy through a mechanism dependent on actin assembly [44]. Therefore, a comparison between new data shown by this and previous chapters as well as published studies indicates a direct link between WHAMM, efficient vesicle fission and/or fusion, and autophagy.

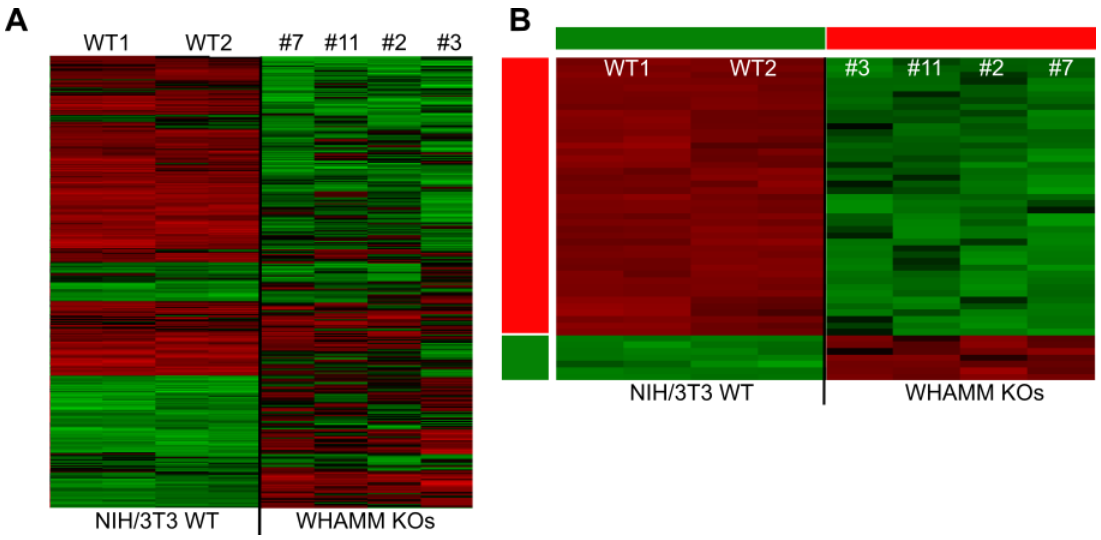

Figure 4.22: Heat maps of gene expression in WHAMM KO cells. Heatmaps depicting differential expression of top 500 (A) as well as top 50 genes showing two major clusters of genes (indicated by red and green boxes) (B) between control and KO conditions. Each horizontal line displays one of the top regulated genes. Red indicates higher expression and green indicates lower expression. Microarray analysis was performed with the help of Robert Geffers (HZI, Braunschweig). Data are derived from one experiment measuring WT control samples in duplicates and four WHAMM KO cell lines.

I next examined whether WHAMM KO impairs the expression of WASH or JMY genes. Indeed, WASH messenger RNA (mRNA) levels were decreased in cells lacking WHAMM, whereas no changes in JMY mRNA levels were detected (Figure 4.23, A-B). However, an additional analysis by western blotting revealed that neither WASH protein levels nor JMY protein levels were altered in comparison to WT cells (Figure 4.23, C-D), indicating that loss of WHAMM does not affect abundance of WASH or JMY.

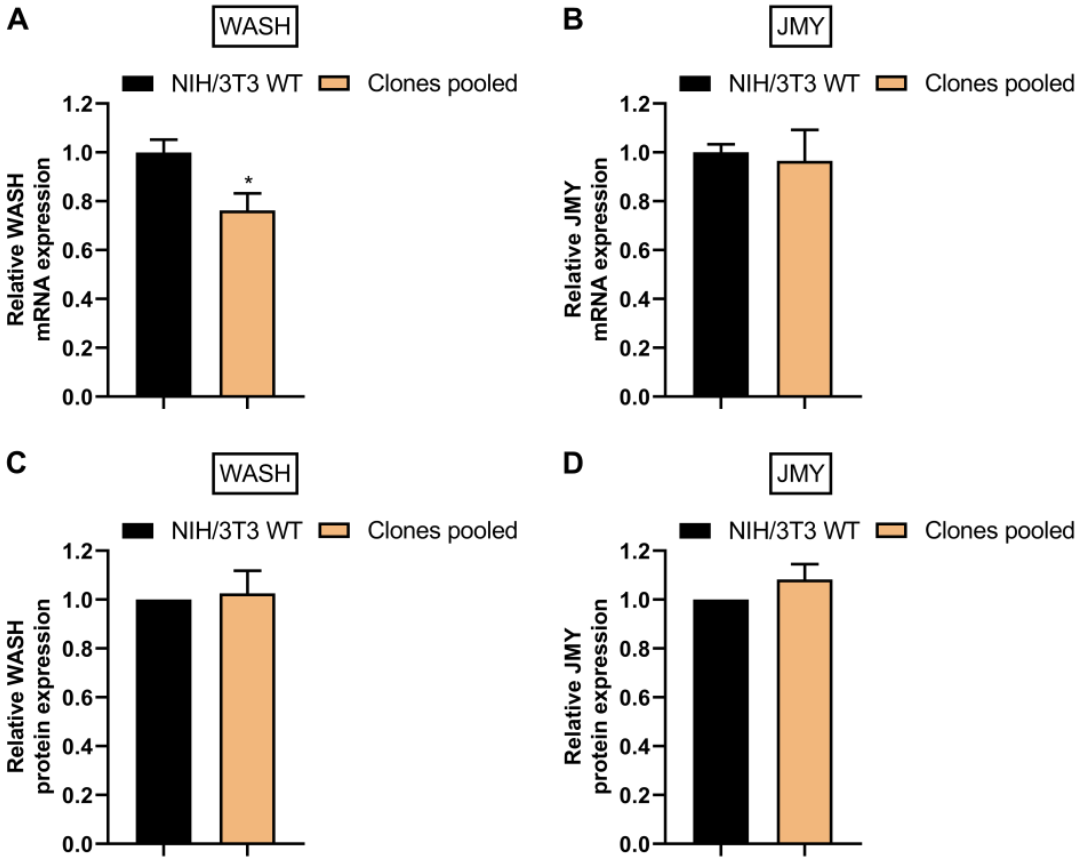

Figure 4.23: WASH and JMY mRNA and protein levels in WHAMM KO cells. (A-B) Relative mRNA expression of WASH and JMY in WHAMM KO cells. Gene expression was assessed by microarray analysis and normalized to WT levels. Data are derived from one experiment. (C-D) Total WASH and JMY protein expression levels were quantified by densitometry analysis of western blots bands. Data were normalized to WT protein levels. Data are representative of two independent experiments. (A-D) *P $\leq$ 0.05, Two-tailed Student's t-test. Error bars represent SEM.

The observations described in Chapter 4.2.2 suggest that autophagy is affected due to WHAMM deletion in NIH/3T3 cells. Therefore, expression pattern of several autophagy markers were analyzed and are depicted in Figures 4.24 and 6.19. mRNA Expression of DFCP1 and LC3B were significantly downregulated in WHAMM KO cells (Figure 4.24, A-B), whereas expression levels of p62 was unaltered (Figure 4.24, C). Data also revealed that LAMP1 mRNA expression tends to be decreased compared to WT levels (Figure 4.24, D). These results are suggestive of a compensatory restriction/reduction of DFCP1 and LC3 transcription to counteract protein accumulation, which might be due to an impeded autophagic flux.

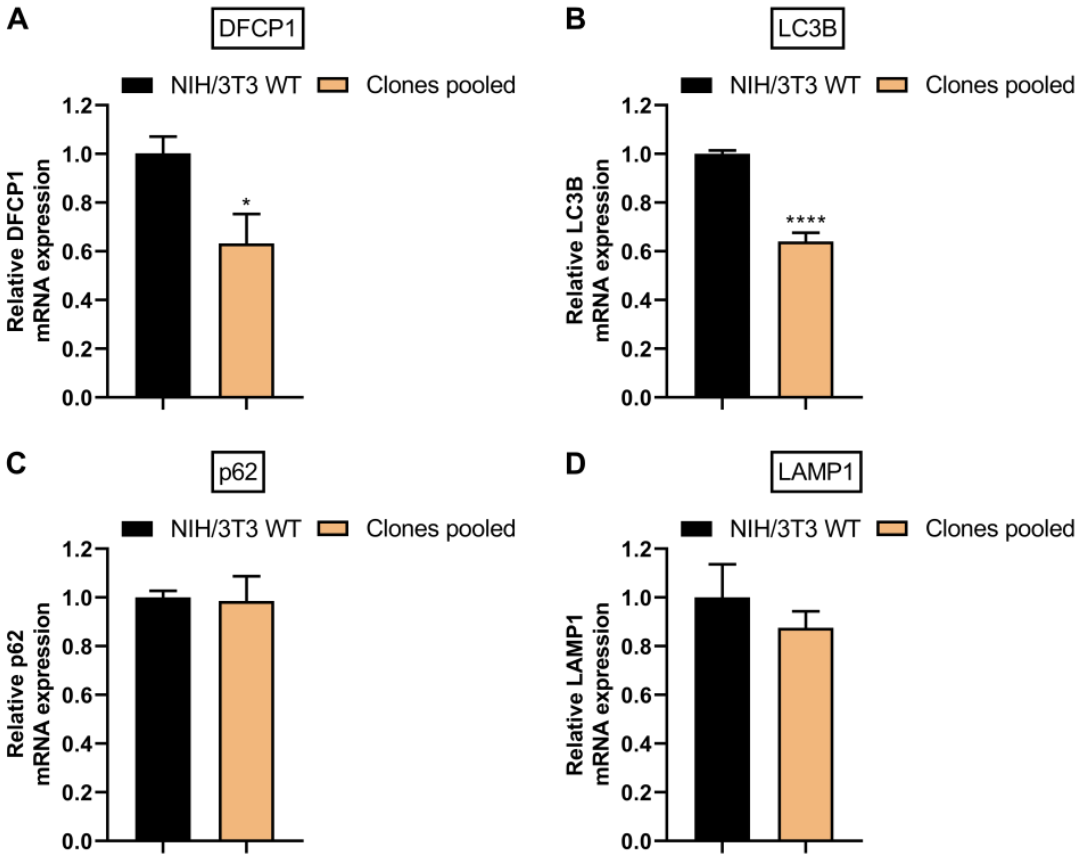

Figure 4.24: mRNA levels of important autophagy markers. Relative mRNA expression of DFCP1 (A), LC3B (B), p62 (C), and LAMP1(D) in WT and WHAMM KO cells. Gene expression was assessed by microarray analysis and normalized to WT levels. Data are derived from one experiment. *P $\leq$ 0.05, ****P $\leq$ 0.0001, Two-tailed Student's t-test. Error bars represent SEM.

Interestingly, expression cluster analysis of microarray data revealed a down- and up-regulation of genes involved in cholesterol biosynthesis, such as DHCR7 and SOAT1 (Figure 4.25, A-C, Supplementary data, Figure 6.21), as well as an impact on genes involved in adhesion signaling (Supplementary data, Figure 6.22). In order to validate microarray data, qPCR was performed to assess gene expression levels of DHCR7 and SOAT1. However, results depicted in Figure 6.20 (Supplementary data) showed discrepancies in transcript levels determined by qPCR.

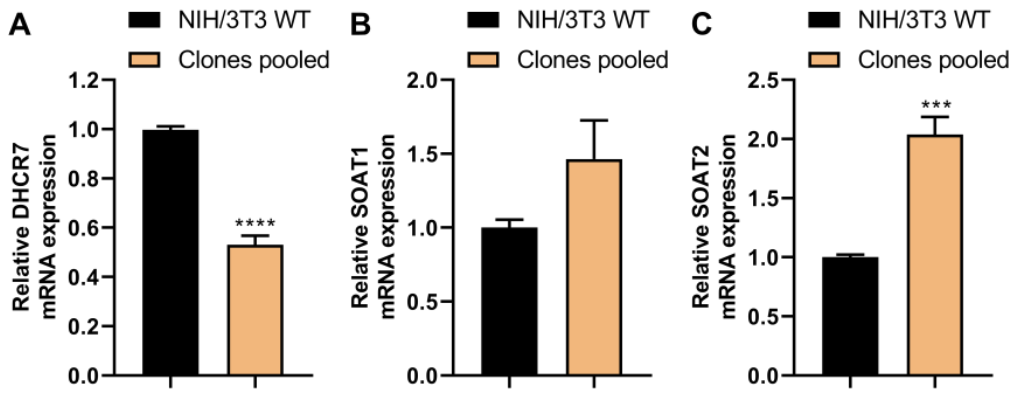

Figure 4.25: Gene regulation in WHAMM KO cells. (A-C) Relative mRNA expression of DHCR7 and SOAT1/2 in WHAMM KO cells. Gene expression was assessed by microarray analysis and normalized to WT levels. Data are derived from one experiment. ***P $\leq$ 0.0005, ****P$\leq$ 0.0001, Two-tailed Student's t-test. Error bars represent SEM.

Aside from this data, an intimate relationship between cholesterol content and integrin adhesion has been described in detail [106, 107]. Lipids also regulate lysosome function and autophagy [108]. They stimulate covalent modification of proteins to ensure proper membrane targeting to initiate isolation membrane elongation and autophagosome closure. Finally, lipids directly affect lipid bilayers by controlling their physicochemical properties [109]. For instance, cholesterol contributes to membrane fluidity and is crucial in membrane trafficking as well as transmembrane signaling processes. *De novo* cholesterol biosynthesis takes place in the smooth ER [110]. It was shown that depletion of cholesterol activates autophagy in human fibroblasts [111], whereas an overload in total cellular cholesterol may affect autophagosome clearance [112, 113].
As shown by microarray analysis, cholesterol biosynthesis might be altered in WHAMM KO cells. To test if this is also mirrored by cholesterol content or cholesterol distribution in WHAMM KO cells, I employed filipin labeling (Figure 4.26, A). Filipin is a naturally fluorescent polyene antibiotic and a widely used tool for detection of free cholesterol *in vitro* [114].

It should be noted, that cells cultured in regular FBS containing medium are constantly exposed to a number of steroids as FBS itself carries large amounts of cholesterol. Therefore, culturing under serum starvation condition was necessary. Cell culture medium was supplemented with ITS-G to still enable optimal growth conditions for fibroblasts. However, both WT and WHAMM KO cells showed similar filipin staining intensities per cell (Figure 4.26, B). Furthermore, the localization pattern of filipin spots was also unchanged between WT and WHAMM KO clones (Figure 4.26, C).

However, WT cells showed a spotted staining and clearly outlined vesicular structures, whereas WHAMM-deficient cells prevalently displayed a less defined staining of filipin spots (Figure 4.26, A).

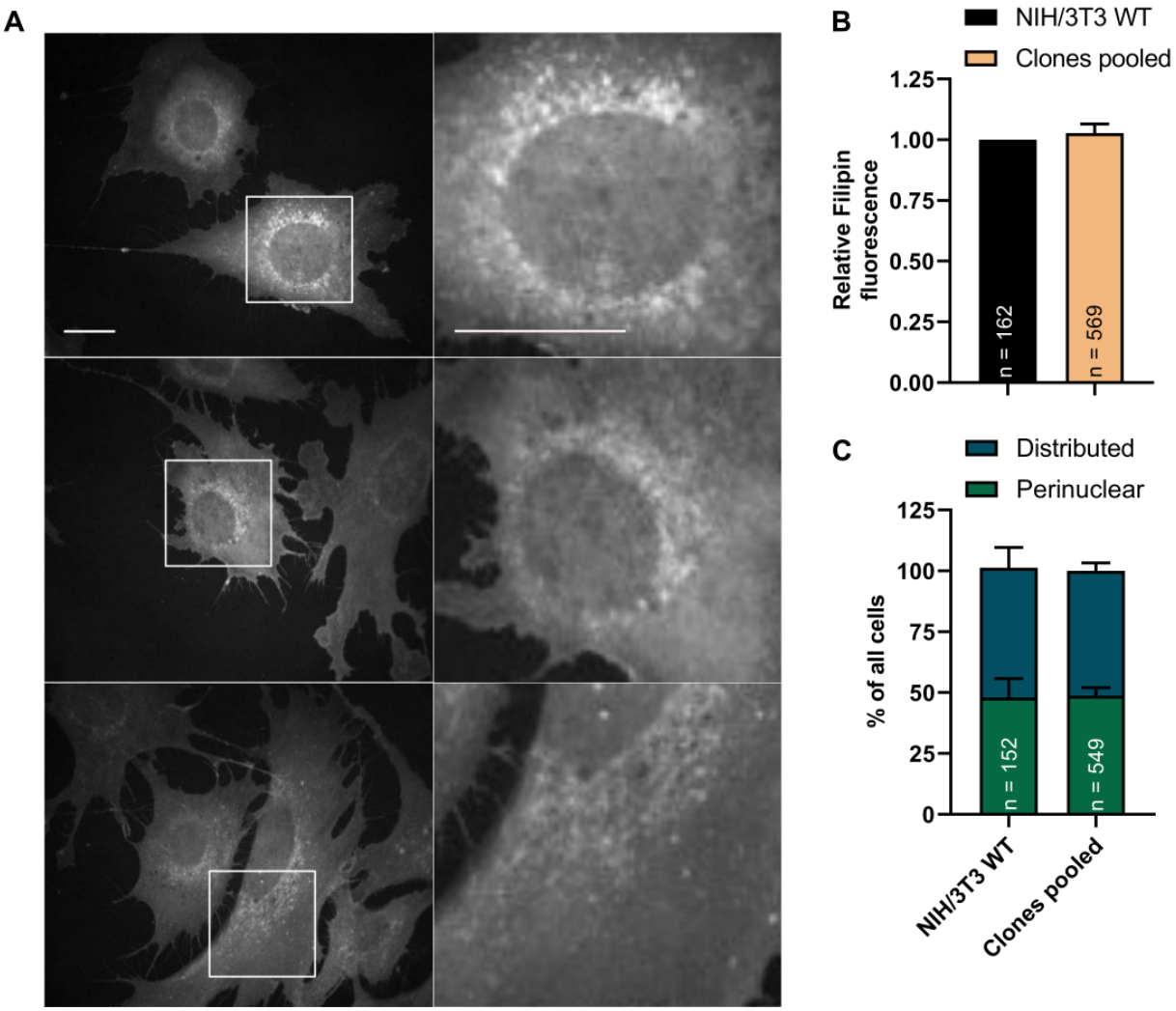

Figure 4.26: Cholesterol analysis in WHAMM KO cells. (A) Representative immunofluorescence images of WT cells and WHAMM KO clones. Filipin staining was used to label unesterified cholesterol. Scale bar: 20 µm. (B) Intensities were measured with ImageJ software and normalized to WT values. (C) Localization of filipin spots in WT and WHAMM KO cells. (B-C) n = number of cells analyzed. Data are representative of three independent experiments. Error bars represent SEM.

I additionally analyzed the cholesterol levels in whole cell extracts using a commercial Amplex® Red Cholesterol Assay Kit. Two different lysis buffers were applied, but the data obtained exhibited no significant changes between WT and WHAMM KO cells (Figure 4.27, A-B) suggesting that the cholesterol content was unaffected by WHAMM KO.

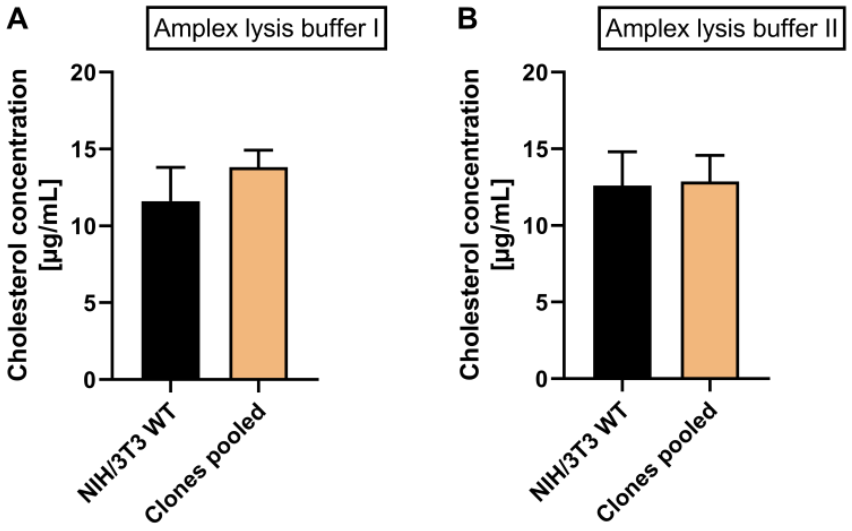

Figure 4.27: Cholesterol concentration in WHAMM KO cells. (A-B) WT and WHAMM KO cells were lysed with Amplex lysis buffer I or Amplex lysis buffer II and cellular cholesterol content was measured using Amplex^{TM} Red Cholesterol Assay Kit. Data are representative of two independent experiments. Error bars represent SEM.

Microarray analyses revealed that WHAMM KO impairs extracellular matrix (ECM) and integrin alpha subunits (ITGA) signaling (Supplementary data, Figure 6.22), in particular *spp1* (encoding secreted phosphoprotein 1), *itga10* (encoding integrin-α10), and *adamts4* (encoding a disintegrin and metalloproteinase) gene expression was downregulated in WHAMM KO cells. Thus, I decided to analyze the adhesion pattern of mutated fibroblasts. WT and WHAMM KO cells were stained for the focal adhesion-associated proteins vinculin and paxillin.

Important to note is that immunoflurescence images displayed partly a high background staining as well as KO cells tended to depict a strong perinuclear signal after vinculin staining. Both remarks made it challenging for the automated detection by MosaicSuite to distinguish between positive and negative particles (i.e. to detect actual focal adhesions). Therefore, I double-checked the quantification procedure and recognized that numerous false positive structures have been detected but I also false negative structures that have not been considered (Figure 4.28, see Materials and Methods, Figure 3.5).

So far, immunofluorescence stainings of vinculin revealed that loss of WHAMM resulted in similar numbers numbers of focal adhesions compared to WT cells, while the length and the average intensity were significantly decreased in WHAMM KOs (Figure 4.29, A-B). Further analyses showed that neither vinculin transcript (Figure 4.29, C) nor protein expression levels (Figure 4.29, D) were significantly up- or downregulated in WHAMM KO cells.

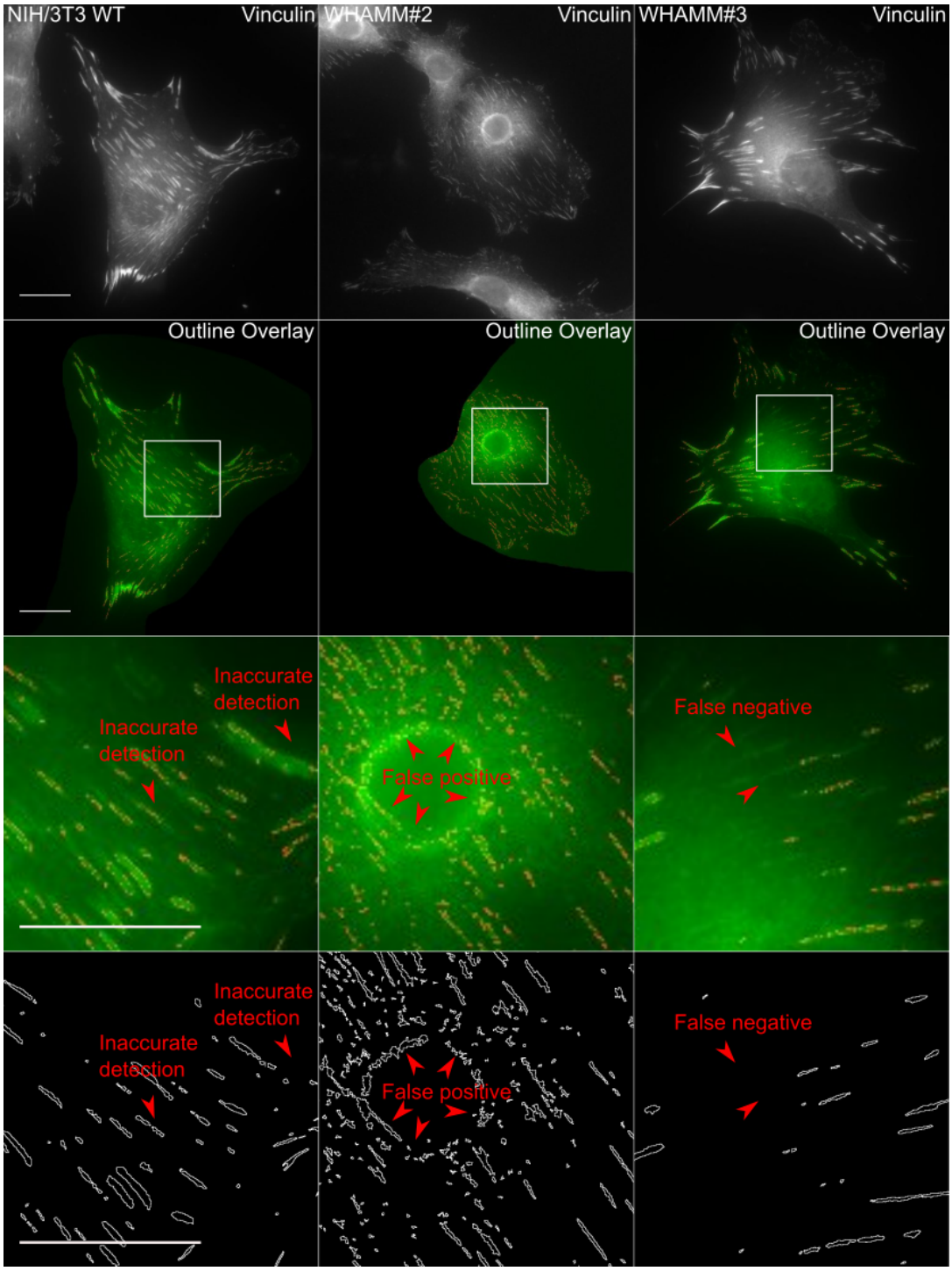

Figure 4.28: Analysis of vinculin-containing focal adhesions by MosaicSuite. Representative immunofluorescence images of WT cells and two WHAMM KO clones. Vinculin was used to label the position of focal adhesions. Number, length, and intensity of focal adhesions were investigated in both NIH/3T3 WT and WHAMM KO cells. The MosaicSuite tool was applied to analyze focal adhesions. Note that the second panel depicts a cropped image version. Scale bar: 20 µm.

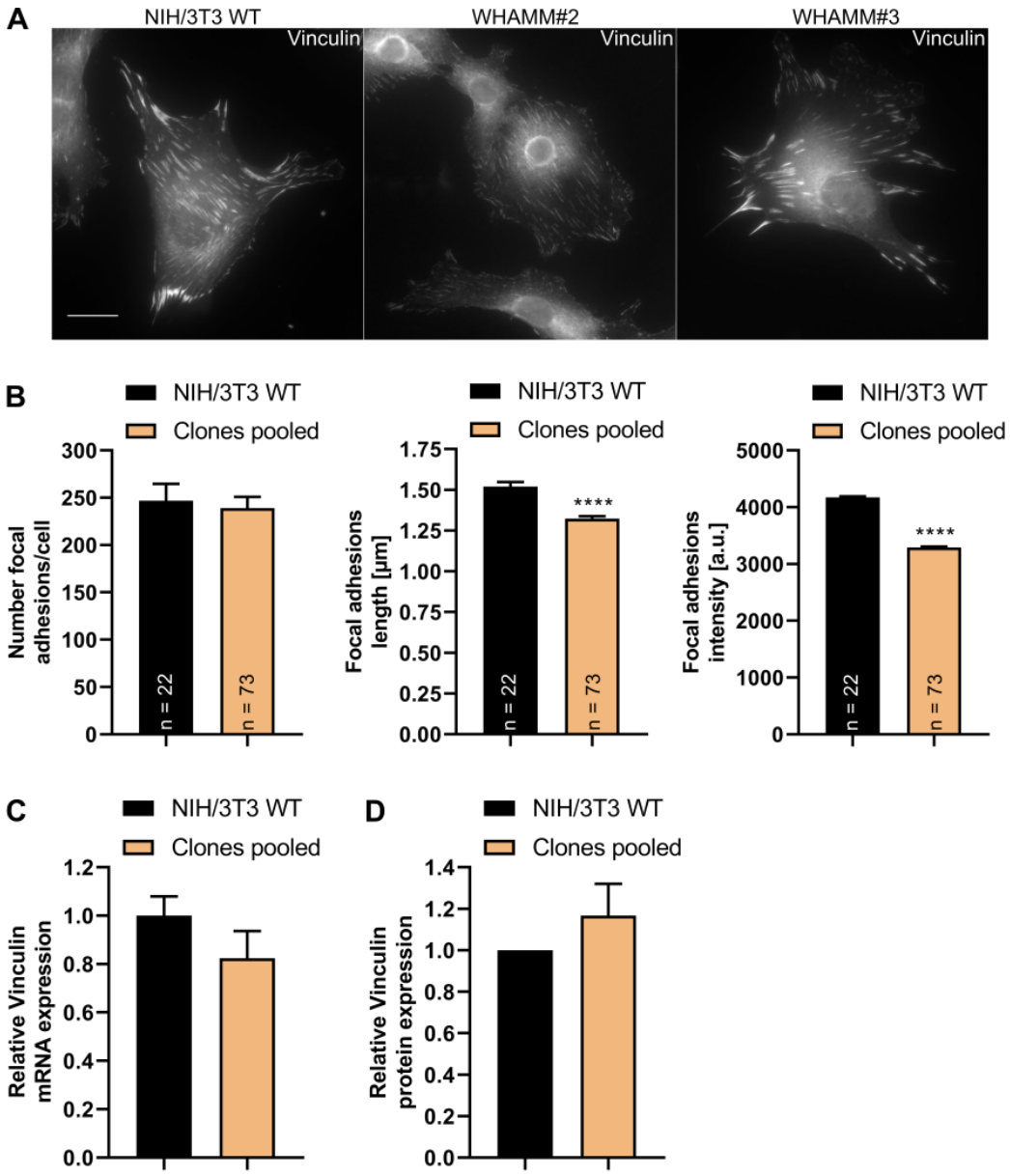

Figure 4.29: Analysis of vinculin-containing focal adhesions in WHAMM KO cells. (A) Representative immunofluorescence images of WT cells and two WHAMM KO clones. Vinculin was used to label the position of focal adhesions. Focal adhesions in WHAMM KOs appeared smaller compared to WT cells. Scale bar: 20 µm. (B) Preliminary analysis of WT cells *versus* WHAMM KO clones revealed that both genotypes exhibited similar numbers of focal adhesions per cell. In addition, length, and average focal adhesion intensity were decreased in KO cells. Number of focal adhesions has been assessed using the MosaicSuite tool. n = number of cells analyzed. Data are representative of two independent experiments. ****P$\leq$ 0.0001, Two-tailed Student's t-test. Error bars represent SEM. (C) Relative mRNA expression of Vinculin in WHAMM KO cells. Gene expression was assessed by microarray analysis and normalized to WT levels. Data are derived from one experiment. Error bars represent SEM. (D) Total Vinculin protein expression level was quantified by densitometry analysis of western blots bands. Data were normalized to WT protein levels. Data are representative of three independent experiments. Error bars represent SEM.

Immunofluorescence, stainings were repeated with paxillin, a protein that also localizes to focal adhesions. Preliminary experiments revealed a slight increase of focal adhesions per cell in WHAMM KO cells (Figure 4.30, A-B). Consistent with previous vinculin stainings, KO cells showed a significant reduction in focal adhesions length as well as intensity (Figure 4.30, B). Paxillin mRNA expression levels in WHAMM KO cells were roughly equal to those in WT cells, but protein expression results showed a slight decrease (Figure 4.30, C-D). Overall, these data suggest that genetic removal of *whamm* leads to smaller adhesion sites that exhibit less intensity, but future work is necessary in order to confirm these assumptions.

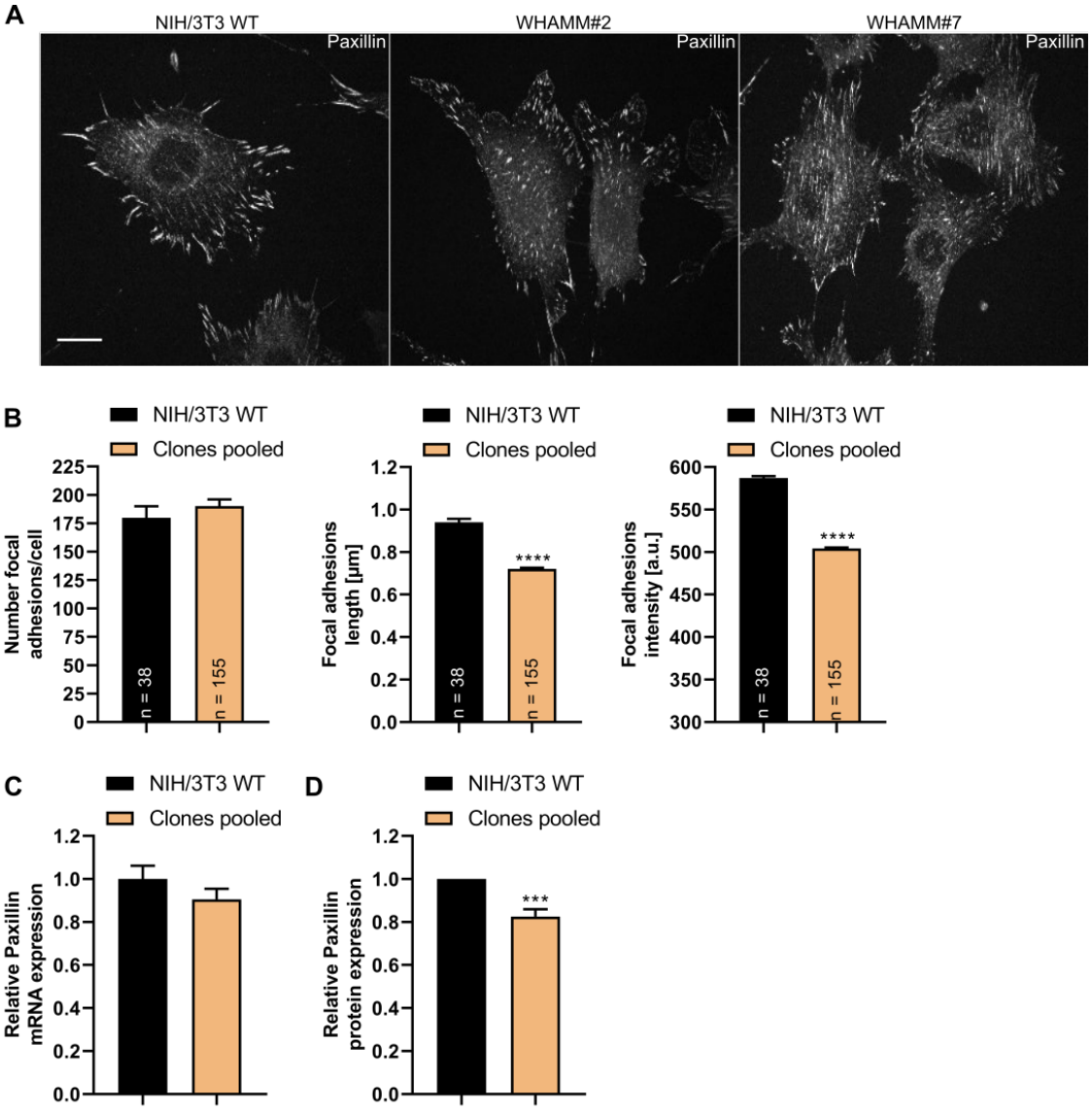

Figure 4.30: Analysis of paxillin-containing focal adhesions in WHAMM KO cells. (A) Representative immunofluorescence images of WT cells and two WHAMM KO clones. Paxillin was used to label the position of focal adhesions. Focal adhesions in WHAMM KOs appeared smaller, but cells exhibit an increased number compared to WT cells. Scale bar: 20 µm. (B) Preliminary analysis of WT cells *versus* WHAMM KO clones revealed increased adhesion numbers per cell. In addition, length, and average focal adhesion intensity were decreased in KO cells. Number of focal adhesions has been assessed using the MosaicSuite tool. n = number of cells analyzed. Data are representative of two independent experiments. ****P$\leq$ 0.0001, Two-tailed Student's t-test. Error bars represent SEM. (C) Relative mRNA expression of Paxillin in WHAMM KO cells. Gene expression was assessed by microarray analysis and normalized to WT levels. Data are derived from one experiment. Error bars represent SEM. (D) Total Paxillin protein expression level was quantified by densitometry analysis of western blots bands. Data were normalized to WT protein levels. Data are representative of two independent experiments. ***P$\leq$ 0.001, Two-tailed One-Sample t-test. Error bars represent SEM.

4.2.4 Viral infection studies in WHAMM KO cells

WHAMM is known to allow Arp2/3 complex activation, which in turn forms actin filament branches on endomembranes [3], which are utilized by viruses for their propagation. Viruses have evolved highly varied strategies for manipulating the actin cytoskeleton, critical for viral replication at many stages of the viral life cycle such as binding, entry, and trafficking [115]. A study from 2009 showed that VSV-containing vesicles depend on actin for their internalization [116]. A crucial role for actin was also reported for entry of HSV-1. Virus particles attached to human corneal fibroblasts and nectin-1-expressing CHO cells, activated both Cdc42 and RhoA, resulting in filopodium-like protrusions. HSV-1 particles preferentially associated with these protrusions and treating cells with actin-depolymerizing drugs such as Cyto D and Lat B blocked HSV-1 internalization [65].

I asked whether altered endomembrane trafficking in WHAMM KO cells also affects virus propagation. Thus, the following experiments were meant to preliminarily test if virus infections are suited to learn more about *whamm* deficiency in cells. I conducted infection experiments with VSV and HSV-1 in cooperation with Mario Schelhaas (University Münster) and Ulrich Kalinke (Twincore, Hanover), respectively. In the first experiment, I assessed the efficacy of infection by quantifying the number of infected cells of all genotypes by flow cytometry. A GFP reporter was used to provide information about uninfected and infected cells. Cells were mock infected or infected with EGFP-VSV or EGFP-HSV-1 at a MOI of 5.5. The experiment revealed that WHAMM KO cells tend to be less susceptible to both VSV and HSV-1 compared to WT cells (Figure 4.31, Supplementary data, Figures 6.23 and 6.24). In the case of HSV-1, WHAMM#3 even showed 50% less GFP-positive cells in comparison to WT cells, indicating that WHAMM might be an interesting protein important for viral infection processes.

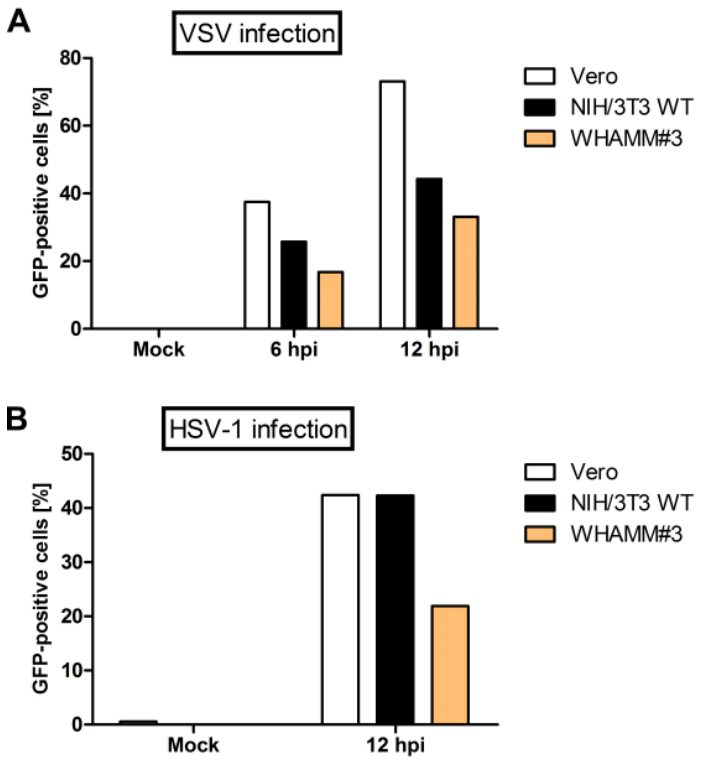

Figure 4.31: VSV and HSV-1 infection in WHAMM KO cells. (A) GFP-positive cells after VSV infection. Cells were seeded, infected with VSV and inspected after 6 hpi and 12 hpi, respectively. WHAMM#3 exhibited reduced VSV infection. (B) GFP-positive cells after HSV-1 infection. Cells were seeded, infected with HSV-1 and inspected after 12 hpi, respectively. WHAMM#3 exhibited reduced HSV-1 infection. (A-B) Mock infection was used as negative control. Vero cell line was utilized as infection control. Data are derived from one experiment.

VSV and HSV-1 infection in WHAMM KO cells was additionally investigated using a plaque assay. I already observed in preliminary experiments that WHAMM KO cells showed less entry of VSV and HSV-1 compared to WT cells (data not shown). The plaque assay was performed once with three WHAMM KO clones. However, the total virus titer (PFU) of VSV was only diminished in two WHAMM KO cell lines (data not shown). Infection with HSV-1 also resulted in opposite findings (data not shown). Based on these observations, the entry mechanism of VSV and HSV-1 into WHAMM-deficient cells might be affected but further experiments are necessary in order to revise contradictory data.

Finally, I visualized the dynamics of infection using live cell imaging of EGFP-tagged VSV particles (EGFP-VSV) in WT and KO cells. Preliminary data revealed that increased green fluorescent dot formations, indicative of virus production, were detectable as early as 120 min after infection and became numerous by 5-6 hpi (data not shown).

Time-lapse imaging showed that virus particle were mobile within the cytoplasm, moving toward the cell periphery. In both genotypes the virus could spread from cell to cell indicating that the infection is progressing without obvious defects.

4.3 Preliminary data of NIH/3T3 JMY KO cells

WHAMM and JMY are two NPFs with similar domain architecture, which show similar localization [44]. As previously described in this thesis, WHAMM binds microtubules and is involved in ER to *cis*-Golgi transport [20]. Unlike WHAMM, JMY plays a role in cytoskeleton remodelling and *trans*-Golgi transport [47]. Despite the different preferred localizations, the strong similarity between WHAMM and JMY suggest that both NPFs might have partially overlapping functions. To gain deeper insights into the distinct functions of JMY, I conducted preliminary experiments with JMY KO cells, which are described below.

JMY is not only found in the cytosol, but also in the nucleus [44]. Therefore, I investigated the nuclei in JMY KO cells. In fact, JMY deficiency resulted in a substantially increased nuclear area (Figure 4.32). Moreover, KO cells appeared much larger compared to WT cells as described above for WHAMM KO cells (data not shown). These data suggest that JMY might affect both nuclear area and cell size. Future measurements, for instance by flow cytometry, are required to uncover whether this phenotype is due to excessive cell spreading or whether it reflects an increase in cell size.

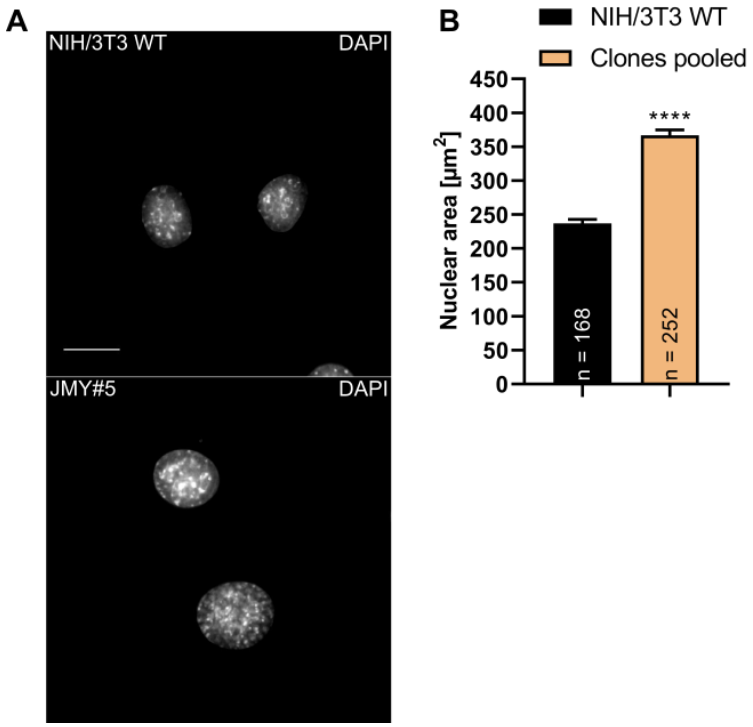

Figure 4.32: Cells deficient in *jmy* display larger cell nuclei. (A) Representative immunofluorescence images of WT and JMY KO clone #5. DAPI staining was used as a cellular nucleus marker. Scale bar: 20 µm. (B) Quantitative analysis of WT cells *versus* JMY KO clones confirms significantly larger cell nuclei in KO cells. Data are representative of three independent experiments (Note that data from JMY#2 and JMY#10 are from one experiment.) n = number of cells analyzed. ****P≤ 0.0001, Two-tailed Student's t-test. Error bars represent SEM.

A report from 2015 showed that JMY plays a role in autophagy through its nucleation activity. They identified a N-terminal LIR motif, which is necessary to target JMY to the autophagsome [85]. In addition, a recent study demonstrated that LC3 and a regulator of JMY called STRAP regulate JMY´s actin activities in trans during autophagy [117]. To learn more about the potential participation of JMY in autophagy, I examined in preliminary experiments endogenous expression of LC3 and p62 under basal conditions in WT and JMY KO cells (Figure 4.33). KO cells showed elevated levels of both LC3 and p62-positive vesicles as well as a significant increase in the total area occupied by LC3 and p62 spots (Figure 4.34). These data contradict previous depletion studies by siRNA, where a reduction in both the autophagosome number and the total autophagosome area has been observed [85].

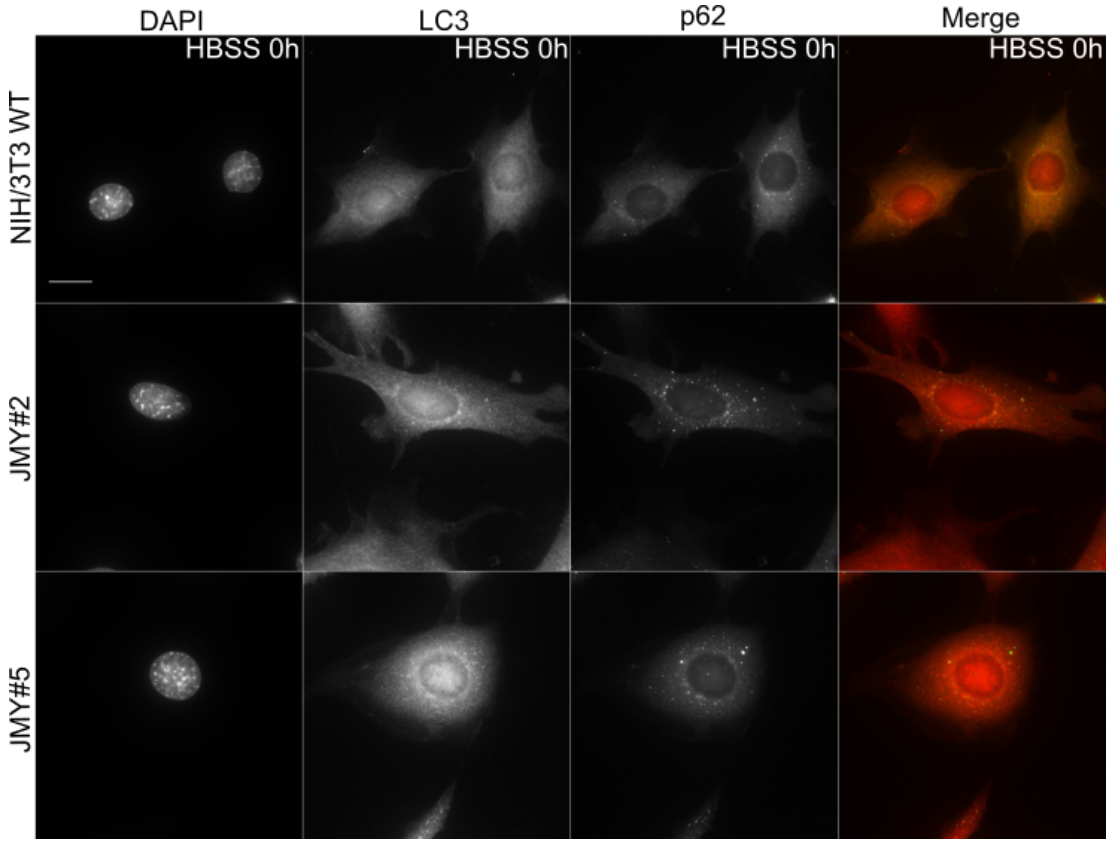

Figure 4.33: Loss of JMY affects autophagy. DAPI staining was used as a cellular nucleus marker. Basal level of autophagy was studied with autophagy markers LC3 (red) and p62 (green). Scale bar: 20 µm.

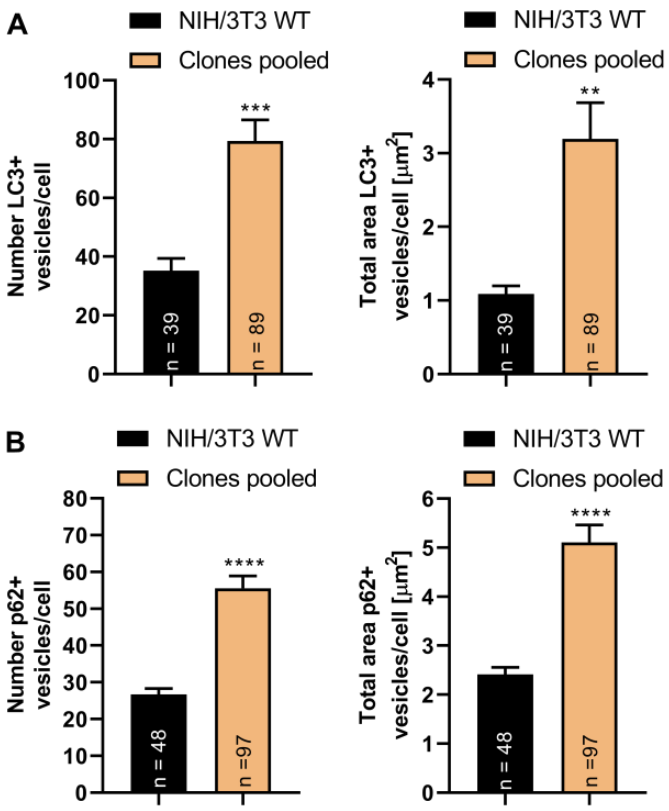

Figure 4.34: JMY KO affects number and total area of autophagosomes and p62-positive spots. (A) Quantitative analysis of WT cells *versus* JMY KO clones confirms an increased number of LC3-positive vesicles per cell in JMY-deficient cells under fed conditions. The total area occupied by LC3-positive vesicles was significantly increased. (B) Quantitative analysis of WT cells *versus* JMY KO clones confirms an increased number of p62-positive vesicles per cell in JMY-deficient cells under fed conditions. The total area occupied by p62-positive vesicles was significantly increased. (A-B) n = number of cells analyzed. Data are derived from one experiment. **P≤ 0.01, ***P≤ 0.001, ****P≤ 0.0001, Two-tailed Student's t-test. Error bars represent SEM.

Flow cytometry analysis as well as *in vivo* monitoring of EGFP-VSV was also conducted with NIH/3T3 JMY KO clones. First, I assessed the number of infected cells by flow cytometry. Data revealed that JMY KO reduced the viral infection by 65% (Figure 4.35, A). Next, I performed time-lapse videomicroscopy to gather additional information on the altered infection dynamics in JMY KO cells. The results clearly show that both infected WT and KO cells produced viruses as they became more and more green 4.35, B). Interestingly, WT cells released the virus at some point, leading to infection of neighbouring cells. This was rarely observed in JMY KO cells, suggesting that trafficking of the virions to the cell periphery or virus egress may be altered.

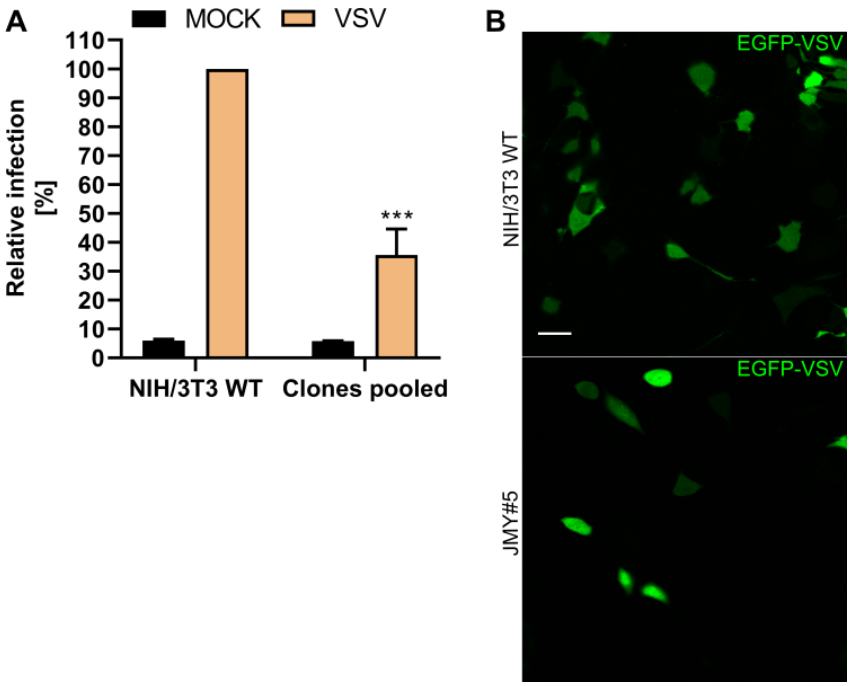

Figure 4.35: VSV infection in JMY KO cells. (A) Quantitative flow cytometry analysis of JMY KO cells after VSV infection. Cells were seeded, infected with VSV and inspected after 6 hpi. GFP fluorescence provided a sensitive and accurate measure of the proportions of infected cells. Mock infection was used as negative control. Data are derived from one experiment. ***P$\leq$ 0.001, Two-tailed Student's t-test. Error bars represent SEM. (B) WT and JMY KO clone #5 were infected with EGFP-VSV at a MOI of 5.5 and maintained at 37°C with 5% humidified CO2. Images were taken 8 hpi. Scale bar: 40 µm.

5 Discussion and Outlook

5.1 CRISPR/Cas9-mediated gene KO of WASH, WHAMM and JMY

Targeted genome modification based on the CRISPR-associated RNA-guided endonuclease Cas9 is a leading genome engineering technique. The simplicity of this tool to modify specific targets resulted in multiple applications, such as deleting, silencing, enhancing, or targeting genomic loci in mammalian cell lines and several species, including monkeys, mice, and rats [89].

In this study, the CRISPR/Cas9 technology was used to generate KO cell lines of the three NPFs WASH, WHAMM, and JMY in order to dissect their roles during various processes. The conducted methodology offers a simple and broadly applicable framework for generating KO cell lines. The workflow has been adapted from previously published methods [89] and can be divided into four steps: 1) sgRNA design and construction, 2) sgRNA screening, 3) clone isolation, and 4) clone screening and validation. This approach could be applied to any cell culture model that easily receives foreign DNA by transfection and tolerates flow cytometry.

As mice and humans share many genetic similarities, I established both murine NIH/3T3 fibroblasts and human osteosarcoma cells (U-2 OS) lacking the respective NPF (see Figures 4.2 and 4.4). These two different cell systems will aid to gain insights and information that can be used to better understand how the selected genes may cause or contribute to biological mechanisms, as well as may provide information about species/cell-specific differences in the utilization of these NPFs. Importantly, both cell lines are commonly used to study many aspects of cell biology and are widely applied in biomedical research.

The results in Chapter 4.1 demonstrate the capability of a CRISPR/Cas9-based approach to rapid targeted gene KO in cultured NIH/3T3 as well as U-2 OS cells. Customizable sgRNAs programmed to an exon of the *wash*, *whamm*, and *jmy* gene triggered sequence-specific Cas9-mediated NHEJ and resulted in the ablation of WASH, WHAMM and JMY protein expression, respectively.

sgRNAs were sufficient to lead to homozygous or heterozygous gene mutations in NIH/3T3 cells after a single transient CRISPR/Cas9 treatment (see Table 4.1). In my experience, this straightforward approach can be used to generate gene-edited NIH/3T3 clones within a matter of weeks. CRISPR/Cas9 also provides a distinct advantage, since it permits the study of endogenous genes that are embryonically lethal when knocked out *in vivo*, such as *wash* [24, 25].

Gene editing in human cell systems has emerged to be much more challenging than the application of murine cells. Targeting the gene of interest with a single sgRNA did not allow robust and efficient gene KO. Functional disruption of *wash*, *whamm*, and *jmy* required disruptive *indels* in all (or most) alleles of the gene. Since U-2 OS cells are known to be polyploid [118], it is likely that *indels* occured at one or more alleles but were not sufficient to disrupt the gene of interest to the desired extent. To overcome this limitation, two sgRNAs that target different regions of the gene of interest were designed. For future considerations, it should be noted that human *wash* was discovered within subtelomeric regions, which are duplication-rich, structurally variable regions situated near chromosome ends [21]. They are typically composed of various repeated elements, pseudogenes, and retrotransposons and provide low efficiency of target site cleavage by Cas9 [119]. Subtelomeric regions are also enriched in epigenetic marks that are characteristic for heterochromatin [120], that can negatively affect Cas9 binding and functioning [121]. A second important limitation of the CRISPR/Cas9 system which might explain initial issues in human cells, is the generation of off-target cleavage sites as a result of complexing of the sgRNA with mismatched complementary target DNA within the genome [122]. To date, efforts to improve the Cas9 enzyme have been performed to increase specificity and reduce off-target cleavage. Mali *et al.* engineered a sgRNA:Cas9 system by tethering transcriptional activation domains to either a nuclease-null Cas9 or to sgRNAs mitigating the effects of off-target sgRNA:Cas9 activity [123]. Furthermore, a study from 2014 also described an improved DNA cleavage specificity by fusion of FokI nuclease to an inactive Cas9 (fCas9) [124]. They showed that fCas9 modified target DNA sites with >140-fold higher specificity than WT Cas9 and with an efficiency similar to that of paired Cas9 nickase. Another strategy to minimize off-target effects is to increase the PAM length [122]. Cas9 orthologs from bacterial species show differences in their PAM repertoire. For instance, the CRISPR/Cas9 system derived from *Neisseria meningitidis* represents a safer alternative for precision genome engineering in human cells. It recognizes an 8-mer PAM sequence that can improve target specificity and reduce potential off-target cleavage [125]. Another approach to specifically target NPFs in human cell systems could be the CRISPR nickase system. It utilizes a single Cas9 nickase to ensure precise base editing up to 53 bp from the nicking site. Intriguingly, this technology showed no off-target editing and provides a versatile and powerful technology for rapid, site-specific, and precise base editing in eukaryotes [126].

To validate gene editing of potential WASH, WHAMM, and JMY KO clones, I performed both western blotting and DNA sequencing. KOs for WASH and JMY in

NIH/3T3 and U-2 OS cells could easily be determined. In the case of WHAMM, I was facing protein detection issues regardless of the applied cell line (see Figures 4.2 and 4.4). WHAMM is known to be expressed at very low levels in NIH/3T3 cells [47]. Even loading more protein per lane and including protease inhibitors in the lysis buffer did not improve WHAMM detection. Furthermore, I also tried to generate an own WHAMM antibody in cooperation with Jan Faix (MHH, Hanover). Yet it appeared that the produced antibody nonspecifically interacted in both murine and human cells indicating a cross reactivity against homologous epitopes (data not shown).
Furthermore, in human cells introduced KOs could not be confirmed by sequencing analysis because of poor sequencing data. Since WHAMM mutation in NIH/3T3 KO cells produced a distinct phenotype, it would be interesting whether similar findings will appear in an alternative cell system such as U-2 OS. To assess whether these observations are not off-target related phenotypes, recovery experiments will be valuable for validation of CRISPR/Cas9 KO gene activity in human cells. Design of a HDR strategy for genomic tagging or generation of constructs for ectopic re-expression of the targeted gene may additionally contribute to efficient validation of the phenotype. An alternative approach would be to transiently transfect WASH, WHAMM, and JMY into human KO cells and compare transfected KO cell lines to WT controls.
So far, *indels* in human KO cells were difficult to detect by Sanger sequencing. A simple procedure for quantifying point mutations and *indels* is the Surveyor nuclease assay, which detects genome editing in a cell pool without the need for clonal expansion prior to analysis [127–129]. The Surveyor nuclease is a DNA endonuclease, which cleaves with high specificity at the 3´ side of any mismatch side in both DNA strands [130]. Finally, deep sequencing of human KO cells would be a comprehensive gold standard to guide study interpretation. It seems advisable to pursue such characterization in U-2 OS cells as edited cells are difficult to sequence by Sanger sequencing.

5.2 WHAMM KO significantly alters NIH/3T3 morphology

WHAMM, a protein uniquely expressed in vertebrates, was identified to be a canonical Arp2/3 activator that interacts with both the actin and the microtubule cytoskeleton [20, 43]. It localizes to the *cis*-Golgi and ERGIC making it an interesting example for the coordination of vesicle traffic between ER and Golgi [20].
The cellular studies presented here highlight the importance of WHAMM in regulating cell and nucleus size, as well as for the organization of the Golgi apparatus. I observed significant increases of both cell size and nucleus size in WHAMM KO cells (see Figure 4.5). There are conflicting reports regarding the factors that determine nuclear size.

On the one hand, there is evidence that the DNA content influences the volume of the nucleus, which in turn has an impact on the cell size [131, 132]. In contrast, investigations of yeast showed that a 16-fold increase in nuclear DNA content did not affect nuclear size [133]. Even though NIH/3T3 cells generally exhibit higher aneuploidy levels [134], propidium iodide staining to estimate nuclear DNA content did not confirm differences between WT and KO cells (data not shown). On the other hand, previous studies support the notion that nuclear size is determined by cytoplasmic volume rather than DNA content. A cytoplasmic factor that might determine nuclear size is an intact ER. *In vitro* data of mammalian cells uncovered an interaction between the ER and nuclear envelope formation and expansion [135]. However, results showed a normal ER distribution as well as network structure in both WT and WHAMM KO cells (see Appendix, Figure 6.8). Consequently, increased nucleus size is presumably not ER-associated.

WHAMM is a classically cytosolic protein, but other NPFs such as WASH and JMY have been described to localize in the nucleus [136, 137], which has not yet determined for the WHAMM protein. It was shown that WASH interacts with B-type lamin and functions in the nucleus to modulate global nuclear organization [136]. According to this, enlarged nuclei in WHAMM KO cells might occur due to a loss of nuclear structural integrity, such as by disrupting lamins or nuclear actin. Lamins belong to the intermediate filament protein family and represent the main components of the nuclear lamina. Nuclear actin may exist in conformations distinct from actin filaments in the cytoplasm [138]. It is tempting to speculate that WHAMM may be involved in the regulation of nucleoskeletal structures and may contribute to maintenance of the nuclear shape.

Another interesting notion to explain increased nucleus size in WHAMM KO cells is the involvement of mTOR signaling. The mTOR pathway has been considered to be a molecular regulator of cell size [139]. Moreover, there is growing evidence that mTOR localizes to the nucleus, where it directly regulates gene expression [140]. Since active mTOR levels are increased in WHAMM KO cells (see Figure 4.11), future investigations will include a potential role of mTOR in nucleus size regulation in these cells.

Compared to WT cells, WHAMM mutant cells also exhibited increased cell size (see Figure 4.5). This phenotype may also be associated with the mTOR pathway. I reported that active mTOR protein expression is increased in WHAMM KO cells (see Figure 4.11). mTOR is known to stimulate cell growth, thereby increasing cell size [139]. In particular, mTORC1 activity promotes cell size upon activation in mammalian cells [141]. Of great interest would be to dissect the role of mTOR during cell

size regulation in WHAMM KO cells and if mTOR-dependent downstream signaling pathways are involved in cell size control. First insights into whether mTOR is involved in cell size regulation in WHAMM KO cells may come from rapamycin treatments. It primarily inhibits mTORC1, but long-term exposure also inhibits mTORC2 [142]. Moreover, I would also hypothesize that dysfunctional autophagy and cell size are connected. This degradation pathway might be critical for increased cell size of WHAMM KO cells. I observed a clear accumulation of autophagy markers such as p62 and LAMP1 during fed conditions (see Figures 4.18 and 4.21). Therefore, I would propose that WHAMM KO disturbs the clearance of (abnormal) proteins, which in turn might also result in an enlargement of cell size.

Changes in WHAMM KO cells size may additionally be caused by altered adhesion and spreading patterns. Cell adhesion was not investigated during this study but a previous report showed that knockdown of WHAMM did not affect cell attachment [41]. WHAMM KO cells spreaded smoothly on coated plastic surfaces. However, microarray data generated in this thesis identified impaired signaling of the ECM and ITGA (see Appendix, Figure 6.22) (i.e. downregulation of *spp1*, *itga10*, and *adamts*4), indicating that focal adhesion formation or more specifically adhesion turnover may be affected (see discussion below).

In this study, I have not tested yet whether also altered cell spreading plays a role in increased cell size of WHAMM KO cells. Cell spreading requires an interaction between membrane-based integrins with their corresponding ECM proteins and the engagement of the cytoskeleton, which initiates a complex cascade of signaling events. When cells are plated onto artificial surfaces coated e.g. with fibronectin or gelatin, they first attach, then flatten, and spread [143]. It is known that binding of integrins to specific ECM epitopes leads to the recruitment of anchor proteins to the adhesion site and ultimately induces the assembly of focal complexes and focal adhesions and the associated cytoskeleton [144]. Focal adhesions are dynamic actin–integrin links that lie at the convergence of integrin adhesion, signaling, and the actin cytoskeleton [145, 146]. WHAMM KO cells exhibited smaller focal adhesions compared to WT cells (see Figures 4.29 and 4.30), which points to changes in cell attachment. Studies showed that focal adhesion disassembly was impaired in autophagy-deficient cells leading to abnormally large focal adhesions as well as impairment in autophagy-driven focal adhesions turnover [147]. Interestingly, WHAMM KO cells exhibited dysregulated autophagy, in particular I could observe an increase of autophagic markers under basal conditions (e.g. p62 or LAMP1; see Figures 4.18 and 4.21). Even though my results revealed smaller focal adhesions in the absence of WHAMM, it still would be interesting whether there is a relationship between defective autophagy and focal adhesion number/length in KO cells.

Ablation of WHAMM also resulted in increased cell granularity as inspected by flow cytometry (see Figure 4.6). This phenotypic change may implicate a higher number of protein aggregates or vesicles. Interestingly, WHAMM KO cells exhibit an increase of autophagy markers (see Figures 4.18 and 4.21, see discussion below), which would correspond to the observed phenotype. Increased cell granularity is indeed often associated with enhancement of autophagy, since one important facet of this process is the production of autophagic vacuoles [97]. A report from 2009 showed that senescent keratinocytes die as a result of high autophagic activity and also revealed higher granularity [148]. Additionally, WHAMM KO cells showed an increased number of lysosomes upon fed and starved conditions (see Figure 4.21). It was shown in several cancer cells that accumulation of lysosomes presumably contributed to higher granularity [149], which is a considerable overlap with my results and would also explain increased cell granularity in KO cells.

WHAMM ablation is additionally associated with a genetic disorder named the GMS. It is characterized by various developmental and physical abnormalities, including microcephaly, developmental delay, and nephrotic syndrome. Patient harbor homozygous mutations in *wdr73* as well as the closely linked *whamm* gene. Patient cells showed abnormal stress fibers organization and an enlarged ERGIC morphology [45]. Interestingly, findings in WHAMM KO fibroblasts contradict these observations. Cultured KO cells displayed normal, prominent bundles of F-actin as found in WT cells (see Figures 4.5 and 6.6), which is not consistent with previous data [41, 45]. Although WHAMM facilitates membrane tubulation and trafficking on the ER, *cis*-Golgi, and ERGIC [45], ablation of WHAMM did not alter ER or ERGIC appearance (see Appendix, Figures 6.8 and 6.9). In contrast, Mathiowetz *et al.* claimed that the ERGIC appeared larger in patient fibroblasts [45]. This specific phenotype may result through the coincident *wdr73* mutation in these patients. Moreover, there might be differences in the gene expression profiles between primary and immortalized cell culture systems and utilizing mouse cells instead of human cells also might explain these disparities. On the other hand, four WHAMM KO cell lines have been included in this study, each arosen from a single cell in order to get reliable results and exclude clonal variance. All subclones showed low clonal variation with high consistency in growth, transcript levels and phenotypic observations, indicating that *whamm* deletion might cause the described phenotype.
In accordance with a previous study, WHAMM KO cells displayed a disseminated Golgi apparatus (see Figures 4.9 and 6.10). WHAMM is crucial for controlling a compact

and stacked Golgi structure and VSV-G transport assays stated that it functions in membrane trafficking from the ER to the Golgi [20]. The Golgi complex receives proteins and lipids from the ER, where they are further processed and sorted for their final destinations through the secretory pathway. Proteins are sorted in and bud from the TGN and eventually deliver their content to various cellular locations, including plasma membrane, lysosomes, and for secretion [150]. This anterograde traffic is balanced by a transport pathway, known as retrograde traffic that runs in the opposite direction. Cargo proteins or lipids are transported from endosomes to secretory compartments such as TGN or *cis*-Golgi [151]. Scattered membrane structures in the Golgi apparatus observed for WHAMM KO cells might affect intracellular transport mechanisms. Previous depletion experiments showed that VSV-G progression from the ER to the Golgi, and the amount of VSV-G reaching the cell surface was diminished suggesting that WHAMM is important for anterograde transport [20]. It is also likely that in the absence of WCA-Arp2/3-mediated tubulation events or F-actin networks near the Golgi, proteins in general are transported more rapidly via small tubular transport intermediates rather than large tubular structures [152].
To explore the role of WHAMM in Golgi function and transport mechanisms in more detail, I conducted a BFA washout assay (see Figure 4.10), constituting a standard assay for examining the assembly of the Golgi apparatus. BFA is a fungal metabolite that induces a redistribution of Golgi enzymes to the ER compartment [153]. It shuts down anterograde transport, whereas retrograde transport of Golgi components to the ER still takes place. Based on BFA washout results, WHAMM is not involved in reformation of Golgi stacks from ER membranes and does not affect retrograde transport.

5.3 WHAMM impairs autophagy

Autophagy involves highly dynamic membrane organization as well as vesicular trafficking from different subcellular compartments to the forming autophagosome [154, 155]. Such trafficking must be tightly regulated by various intra- and extracellular signals [44, 45]. Membrane shaping and remodeling events are mediated by lipid modifying enzymes, membrane sculpting and remodeling proteins, lipid-binding effector proteins, protein kinases, and phosphatases [156]. WHAMM has been implicated in mammalian autophagy, in particular it connects actin assembly via the Arp2/3 complex at sites of autophagosome formation [44, 45]. Indeed, several studies revealed a colocalization of actin filaments with autophagic markers, demonstrating a link between actin assembly and autophagy [83, 157]. In addition, it has been suggested that

mouse knockout of Atg7 prevents autophagosome formation but also revealed disorganized F-actin fibers as well as a loose F-actin net. The authors suggest a link between impaired autophagy and morphological changes in F-actin in Atg7-deficient primary cells [158]. However, established WHAMM KO cells did not show changes in stress fiber formation or organization as previously observed in primary cells [45]. However, the Golgi apparatus was clearly dispersed in the absence of WHAMM (see Figure 4.9 and 6.10) and it is known that ER-Golgi membrane transport and autophagy constitute intersecting trafficking pathways [159].

Aligning the findings of this study with the literature, I suggest dysregulated autophagy in response to WHAMM ablation. KO cells clearly revealed increased levels of autophagy markers such as LC3, p62, and LAMP1 upon starvation (see Figures 4.15, 4.18 and 4.21. These results imply that WHAMM likely plays a role in early stages of autophagy (i.e. autophagosomal biogenesis) in addition to maturation of autophagosomes (see discussion below).

Total protein levels of mTOR, a known regulator of autophagy under-nutrient rich conditions [68, 78], were downregulated by about 20% in WHAMM KO cells (see Figure 4.11). However, its activated form, p-mTOR, displayed a clear upregulation in KO cells (see Figure 4.11). Typically, mTOR activity is high under fed conditions which in turn leads to the phosphorylation of the ULK1 complex and accordingly to an inhibition of autophagy [160]. In response to starvation, reduced mTOR activity results in an activation of the ULK1 complex and finally in an activation of autophagy [161]. Future work will be needed to further determine the levels of mTOR and p-mTOR, for instance by immunofluorescence stainings or qPCR.

In previous studies, WHAMM has been detected adjacent to LC3-positive vesicles as well as omegasomes, PI3P-enriched structures that form at sites of the ER [44, 45, 91]. Omegasomes are cup–shaped structures marked by the protein DFCP1, which associate with actin filaments upon starvation [45, 91]. Dynamic localization studies of EGFP-DFCP1 in WHAMM KOs revealed a strong defect in omegasome formation which is inconsistent with the normal ERGIC morphology (see Appendix, Figure 6.9). This compartment is required for membrane recruitment of DFCP1 and finally for omegasome generation [162]. WHAMM KO actually induced clustering of DFCP1-positive omegasomes around the nucleus (see Figure 4.13). I therefore propose that the progression of omegasome to autophagosome maturation partially depends on the presence of WHAMM. Hence, it would be interesting to visualize DFCP1-structures upon starvation to gain information, whether there is a delay in phagophore formation due to the accumulated omegasomes. Thus far, I can also not exclude the possibil-

ity that the scattered Golgi influences this phenotype, even though DFCP1-positive omegasomes normally appear to localize near the connected mitochondria-associated ER [163]. Disruption of the Golgi architecture with e.g. BFA followed by a visualization of omegasomes would clarify the possibility of Golgi contribution. Another interesting future aspect is to evaluate the morphological membrane properties of omegasomes in KO cells by electron microscopy. Identifying the structural features (e.g. thickness, topology of the isolation membrane) may provide important insights into the characteristics of these clustered structures.

Phagophore elongation and closure is a dynamic process that is regulated in a cargo-specific manner. A protein, that functions in phagophore assembly, is the multi-spanning integral membrane protein ATG9. It possibly participates in the formation of phagophore curvature since induction of autophagy results in a distribution of ATG9 from the Golgi into tubo-vesicular compartments [156], where it co-localizes with LC3 [164]. Since WHAMM regulates the Golgi structure, its absence might affect trafficking of ATG9-containing vesicles which again is indicative of an involvement of the Golgi complex in the autophagic pathway. More precisely, the observed ATG9 accumulation at the perinuclear region (see Figure 4.12) suggests a defect in the transport of ATG9-containing membranes for expansion of the phagophore membrane. Colocalization studies of both ATG9 and the phagophore membrane marker such as ULK1 would help to shed light on this question. Interestingly, altered distribution of ATG9 did not affect autophagosome development in WHAMM KO cells. However, a study from 2009 showed that fibroblasts deficient in ATG9 did not properly induce autophagosome formation and exhibited impaired degradation of long-lived proteins as well as p62 [165]. The latter would be consistent with my observations since WHAMM KO cells displayed a clear increase of p62 vesicles upon fed and starvation conditions (see Figure 4.18).

LC3 is a model substrate essential for autophagosome biogenesis/maturation. After translation, its preform is cleaved by ATG4 family proteases to form cytosolic LC3-I. Subsequently, LC3-I is conjugated to PE to become LC3-II, which localizes to isolation membranes and autophagosomes. The amounts of LC3-I and LC3-II and their ratio under different conditions and/or over time are therefore indicative of autophagosome formation, but turned out to be technically too demanding. Generally, the number of autophagosomes increases during nutrient starvation such as HBSS treatment and accordingly the amount of LC3-II increases [166]. Unfortunately, immunoblotting of LC3

was problematic in both WT and WHAMM KO cells. A band for LC3-I could not be detected at all or was very faint (see Appendix, Figure 6.12). A known issue regarding the detection of the ratio of LC3-I to LC3-II conversion is the different immunoreactivity of the antibody, which preferentially binds LC3-II [167]. In general, LC3-I tends to be less sensitive to detection [168], especially when performing semi-try transfer of proteins as I applied in my studies. Moreover, it was reported that the signal ratio between LC3-I and LC3-II may not always reliably reflect the actual ratio of cytosolic and membrane-bound LC3 [166], thus it is recommended for future experiments to compare the amount of LC3-II among samples [167].
Autophagic activity may also be measured by immunofluorescence (see Figures 4.18 and 4.19 as well as Appendix, Figures 6.13 – 6.16). This method provides information about the number as well as size of LC3-positive puncta. Knockdown of WHAMM was proposed to reduce autophagosomal size and movement, and a WHAMM point mutation that should have a reduced affinity for Arp2/3 also decreased the number of LC3-positive structures [44]. Measuring LC3 vesicles under fed conditions revealed that both genotypes showed similar amounts of autophagosomes (see Figure 4.15, A), but differed in the total area of LC3 puncta per cell (see Figure 4.15, B). Accordingly, WHAMM KO does not affect the number of autophagosomes under basal conditions, but strikingly led to higher levels of LC3-positive structures upon starvation (see Figure 4.15), indicative for an accumulation of autophagosomes. This accumulation may be caused by impaired degradation of autophagy substrates, which in turn could be explained by defective lysosomal fusion with autophagosomes. WHAMM KO cells showed enlarged lysosomes (see Figure 4.21, see discussion below), which might result in defects in autophagosome-lysosome fusion and consequently to the observed phenotype in WHAMM KO cells upon nutrient deprivation. In order to prove obtained results as well as the idea of affected autophagosome-lysosome fusion events, I recommend visualizing autophagic structures in an alternative cell system, such as U-2 OS WHAMM KO cells. Studying another biological system will provide evidence of the reproducibility of dysregulated autophagy due to the absence of WHAMM. However, counting the amount of autophagosomes remained challenging in both WT and WHAMM KO as the applied threshold function of ImageJ software (see Material and Methods) was not easy to adapt to the need of the approach. Especially the high background and in particular the high background in nuclei made it somewhat complicated to ensure reliable LC3 detection in both WT and WHAMM KO cells. Recently however, in the course of two independent Master´s Theses, LC3 stainings were further optimized. It may be worth to repeat the stainings shown here with an optimized staining procedure, which

includes the addition of low concentrations of a permeabilizing agent such as Triton X-100. Another quantification strategy might also be considered in order to measure LC3 vesicles in WT and KO cells more reliably. For instance, the threshold function may be replaced by a tool called MosaicSuite which tracks single particles in 2D and 3D and has already been utilized in this study for different sets of experiments (see Materials and Methods) [169,170].
p62 was an alternative marker to monitor autophagic activity because it directly binds to LC3, thereby serving as a selective substrate of autophagy [166, 167]. Most interestingly, p62 levels appeared significantly higher in WHAMM KOs upon fed and starvation conditions as compared to WT cells (see Figures 4.17 and 4.18). Upon 4 h starvation, the amount of p62 decreased in both genotypes (see Figure 4.18), suggesting that p62 degradation occurs in response to starvation. Together, these data indicate an inhibition of the autophagic flux in WHAMM KO cells. Generally, activation of autophagy results in a decrease of p62 expression due to faster degradation of the protein and, contrarily, an accumulation of p62-positive structures reflects a decline in the autophagic flux [171]. Interestingly, elevated p62 levels after starvation (early time points) have also been observed in WT cells (see Figures 4.17 and 4.18). Thus, it might be that p62 transcriptional levels in these cells are upregulated upon 1 h and 2 h starvation resulting in higher protein expression. Nonetheless, the speed of autophagic degradation appears decreased in WHAMM KO cells, which is in line with my hypothesis that autophagy is delayed or inhibited in WHAMM KO cells.

In order to determine the lysosome-dependent degradation of autophagic vessels, it was important to measure the amount of LC-II and p62 with the concomitant use of a compound that blocks autophagy (e.g. BafA1). The difference in the amount of LC3-II or p62 in the presence and absence of such a selective inhibitor is indicative of the autophagic flux [166]. BafA1 is a vacuolar-type ATPase inhibitor, which blocks the fusion between autophagosome and lysosome, and leads to a block in lysosomal degradation [168]. Usually, the number of LC3-positive structures increases upon BafA1 treatment, indicating that lysosomal degradation of LC3 is inhibited. I expected a pronounced accumulation of LC3-positive vesicles in non-starved plus BafA1 treatment conditions compared to control cells. This has indeed been observed for both WT and WHAMM KO cells (see Figures 4.15 and 4.16). Furthermore, WHAMM KO cells showed significantly increased levels of LC3 upon 2 h and 4 h starvation in the presence of BafA1 compared to WT cells (see Figure 4.16). This confirms once more that LC3-positive particles accumulate due to the loss of WHAMM. In fact, WHAMM

deletion presumably leads to a defect in autophagosome formation and/or degradation and I would propose that WHAMM KO rather delays than fully abrogates autophagy. This study also demonstrated that WHAMM KO cells showed a marked increase in the amount of p62 upon BafA1 treatment for all tested time points and/or treatment conditions (see Figure 4.19). Interestingly, KO cells treated either with HBSS alone or with HBSS and BafA1 (see Figures 4.15 *versus* 4.16 and 4.18 *versus* 4.19) exhibited similar trends in the amount of LC3 and p62 dots, respectively. Both treatment of KO cells with HBSS or HBSS plus BafA1 succeeded to observe a clear difference compared to WT cells by revealing a strong accumulation of LC3-vesicles and p62 particles. Together, these data confirm dysregulated autophagy due to WHAMM deficiency and strengthen the assumption of a degradation defect in WHAMM KO cells.
Apart from the potential structural function of WHAMM during autophagy, it is also likely that it plays a specific role during mTOR signaling. Steady state levels of p62 measured by western blotting were increased in KO cells (see Figure 4.17) and most likely resulted in the higher number of p62 vesicles upon fed conditions observed during immunofluoresence stainings (see Figure 4.18). p62 has been previously linked to the mTOR pathway, where Duran *et al.* uncovered an interaction between both proteins and showed that p62 is required for mTORC1 activation [172]. Since active mTOR levels are increased upon WHAMM KO (see Figure 4.11), it is tempting to speculate whether WHAMM is involved in mTOR signaling by increasing p62 levels.

Another direct method to measure autophagic flux and to assess any changes between WT and KO cells was flow cytometry. Preliminary measurement of endogenous LC3 indicated an increase in WHAMM KO cells upon both fed and starvation conditions (see Appendix, Figure 6.17), which is consistent with the previous assumption that loss of WHAMM leads to an accumulation of LC3 due to dysregulated autophagy (see Figure 4.15). Future work will include flow cytometry in combination with inhibitors of degradation (e.g. BafA1), which will additionally provide information about changes in the autophagic flux of the system.
Moreover, a second approach to measure autophagic activity in cultured cells will be based on the fluorescent probe GFP-LC3-RFP-LC3ΔG [166]. This fusion protein is cleaved by endogenous ATG4 proteases generating equimolar numbers of GFP-LC3 and RFP-LC3ΔG in the cytosol. When autophagy is induced, GFP-LC3 is PE-conjugated and localizes to the autophagosomes followed by degradation within autolysosomes, while RFP-LC3ΔG remains in the cytosol. Finally, the autophagic flux is estimated by calculating the GFP/RFP ratio, which precisely determines the cumulative GFP-LC3 degradation [166, 173]. Using this probe may circumvent LC3 detection problems I faced in NIH/3T3 fibroblast.

The last stage of autophagy comprises the fusion of the autophagosome with the lysosome, when the cargo is released into the acidic and hydrolytic lumen of these organelles [174]. Lysosome size is regulated by a balance between lysosomal membrane fusion and fission [175]. This study provides evidence that WHAMM KO leads to changes in lysosomal size and number (see Figure 4.21). Functional lysosomes are critical for the maturation process of autophagosomes and for the degradation of the cytoplasmic material [105]. First, I suspected that WHAMM KO affects a process called lipophagy because of the analysis of regulated pathways upon GeneChip Arrays (see discussion below). It literally is the degradation of lipids via autophagy, which is particularly relevant in the context of genetic lysosomal storage disorders. Perturbations of the autophagic flux, which I could observe for WHAMM KO cells, have been suggested to contribute to the disease aetiology [176]. However, with two methods I could not detect any defect in cholesterol amount or distribution in WHAMM KO cells (see Figures 4.26 and 4.27). Therefore, I assumed that the observed lysosomal phenotype might be more likely caused by the dispersed Golgi apparatus. Vesicle size is normally regulated by the rate of fusion *versus* the rate of fission [175], indicating that inhibited lysosomal fusion/fission may explain the increased number and size of lysosomes observed in WHAMM KO cells (see Figure 4.21). Moreover, the formation of enlarged lysosomes might be connected to the accumulation of autophagosomes as well as p62-positive structures. An interesting future aspect will be to test the degradative capacity of lysosomes in WHAMM KOs. Impaired hydrolytic function might impair the degradation of LC3- and p62-positive vesicles in WHAMM KOs. Future work will also focus on the determination of the kinetics of fusion and fission of vesicles, but also on a deeper analysis of lysosomal structures using super-resolution microscopy.
Studying the SNARE syntaxin 17 will also be considered since it is crucial for the last maturation step of autophagosomes [177]. This protein is required for the fusion of autophagosomes with lysosomes to form autolysosomes [178] and it would be interesting to examine whether its expression or turnover is impaired due to loss of WHAMM. Another important future aspect, that has not yet been tested in this study, is to investigate the mechanism underlying WHAMM's normal function during autophagy. Thus, localization of endogenous WHAMM as well as its dynamics during autophagy would be of great interest. However, WHAMM is a low abundant protein and reagents available at present are not suited to detect it by immunofluoresence. GFP-tagged WHAMM, which easily induces overexpression artefacts, could be a helpful tool when optimizing the experimental conditions.
In summary, WHAMM KO leads to an accumulation of LC3 and p62 as well as enlarged lysosomal structures, implying dysregulated autophagy due to its loss.

5.4 Gene regulation in WHAMM KO cells

The study of gene expression profiling of cells has become a major tool in biology and allows for simultaneous assessment of the expression level of thousands of genes [179, 180]. cDNA microarray analysis was performed to determine which genes are transcriptionally influenced by the absence of WHAMM to gain information about its cellular role in general and its function in autophagic and infectious processes in particular. So far, gene expression profiles of cells lacking WHAMM protein have not been published. This thesis now reports on specific genes, which play important roles in biological processes to be significantly regulated upon WHAMM KO. Heat maps clearly demonstrated the differential gene expression pattern in WT and WHAMM KO cells (see Figure 4.22). Transcriptom analysis revealed that ablation of WHAMM slightly decreases WASH mRNA expression, whereas JMY levels appeared unaltered (see Figure 4.23). However, analysis of protein quantity via western blotting showed that the expression levels of both NPFs were unchanged in WHAMM KO cells (see Figure 4.23). KO of WHAMM represents a genetic perturbation, which is apparently not functionally compensated by WASH or JMY. Genetic compensation in response to a KO is a widespread phenomenon, in particular of related genes, whereby the loss of one gene may be compensated by another with overlapping functions [181]. WHAMM and JMY share a similar domain architecture and it was shown that both colocalize and comigrate with LC3 and the ER-resident protein VAP-A pointing to some degree of overlap [44]. However, whether WHAMM and JMY perform similar or overlapping roles is not substantiated by this study.

In addition, microarray analysis has been used to potentially identify altered genes associated with autophagy (see Figure 4.24). Interestingly, the amount of DFCP1 mRNA was significantly downregulated upon WHAMM KO (see Figure 4.24, A). However, WHAMM KO cells showed an increase of accumulated DFCP1-positive structures under basal conditions (Figures 4.13 and 6.11). Moreover, previous data (see discussion above) demonstrated a strong increase of diverse autophagic markers and I already proposed a degradation defect in WHAMM KO cells. Thus, microarray data might implicate a cell-specific regulation of DFCP1 mRNA levels due to defects in lysosomal degradation. Since omegasomes are still formed, it might be worth to inspect DFCP1 protein expression levels by western blotting.
WHAMM has been closely linked to autophagy and its inactivation inhibited LC3 lipidation as well as clearance of ubiquitinated protein aggregates [44,45]. LC3 is a suitable marker for detecting autophagic structures, in particular, it reflects the number of au-

tophagosomes and autophagy-related structures [166]. As observed for DFCP1, mRNA analysis of LC3 showed less LC3 mRNA expression in WHAMM KO cells (see Figure 4.24, B). On the other hand, KO cells exhibited a higher amount of LC3-positive particles under starved conditions compared to WT cells (see Figure 4.15), indicative of again slower protein turnover. Thus, WHAMM KO cells might try to compensate the degradation defect of LC3-positive vesicles by downregulating mRNA levels. In mammalian cells, 30-40% of the variation in protein concentration may be explained by mRNA abundance [182]. Apart from other factors such as (post-)translational modifications and measurement errors [182, 183], the most common reason in regulating protein stability is by protecting it from or driving it into degradation. The relationships between the rates of the processes producing and degrading the participating molecules determine the abundances of mRNA and proteins.
Finally, with the help of Robert Geffers (HZI, Braunschweig), I performed meta expression analysis to understand if the regulated genes in WHAMM KO *versus* WT belong into distinct pathways. KEGG pathway analysis implicated a deregulation of enzymes involved in cholesterol biosynthesis, in particular, it showed a downregulation of DHCR7 and an upregulation of SOAT1 and SOAT2, respectively (see Figures 4.25 and 6.21). Since lipid synthesis/degradation is also associated with autophagy [108, 109], the cholesterol content in WT and WHAMM KO cells was investigated. However, analysis of cholesterol content via filipin staining or Amplex assay did not confirm that absence of WHAMM affects cholesterol levels (see Figures 4.26 and 4.27). Thus, a direct validation of gene expression of DHCR7 and SOAT1 has been determined by qPCR (see Appendix, Figure 6.20). In contrast to microarray analysis, qPCR results actually showed unchanged mRNA expression levels in WHAMM KO compared to WT cells. These findings highlight that microarray results might vary considerably and need to be validated by further methods.

5.5 WHAMM KO impairs VSV and HSV-1 infection in NIH/3T3 cells

Viral infections hijack normal functions of a cell, including reconfiguration and reorganization of cellular actin. The extent and degree of cytoskeletal rearrangement varies among different viruses [59]. The Arp2/3 complex, a know actin nucleator, has weak actin nucleation activity, which in turn requires an activation by NPFs leading to robust actin nucleation. Both bacteria and viruses developed sophisticated strategies to exploit the power of Arp2/3-mediated actin polymerization to promote cell-to-cell

spread [184]. Reorganization of the actin cytoskeleton accompanies all stages of the viral life cycle (i.e. entry, replication, assembly, and egress) [185]. Viruses such as VSV require the actin system for their uptake (clathrin-mediated actin-assisted endocytosis) and also take advantage of the actin cytoskeleton for intracellular nucleocapsid mobility [186, 187]. HIV-1, as another example, exploits and modulates the actin cytoskeleton to facilitate its entry into, transport within, and egress from host cells [188]. To this end, I investigated virus infection in WHAMM KO cells and found distinct defects in VSV and HSV-1 infections (see Figure 4.31). Flow cytometric analysis of virus infection was aimed at the measurement of EGFP-VSV and EGFP-HSV-1, respectively, in order to identify infected cells (see Appendix, Figures 6.23 and 6.24). Interestingly, the infection rate decreased for both viruses (i.e. by about 20% for VSV and 50% for HSV-1) in WHAMM KO compared to WT cells, implying an impact on both viruses due to loss of WHAMM. On the basis of these results, I cannot clearly conclude which stages of the viral life cycle (i.e. entry, replication, assembly, and/or egress) are impaired. However, I could observe that entry of VSV was not completely blocked by WHAMM KO. Flow cytometry data showed a GFP signal in cells deficient in *whamm* (see Appendix, Figure 6.23), thereby reflecting that cells still got infected. Hence, I would suggest that viruses were obviously internalized despite the lack of WHAMM. Indeed, a possible consequene of absence of WHAMM could be that VSV replication and/or assembly are affected. Growth inhibition of VSV by BFA revealed that interference with membrane traffic leads to the inhibition of viral protein glycosylation and also blocks virus genome replication [189]. WHAMM is known to function in ER to Golgi transport and WHAMM KO cells exhibit a dispersed Golgi phenotype (see Figures 4.9 and 6.10). Thus, it is tempting to speculate that inhibition of viral progression/maturation is connected to alterations of this cellular compartment and that the Golgi is actively involved in VSV assembly in WHAMM KO cells. A similar connection between Golgi and virus assembly was found in studies performed with vaccinia virus. Data revealed that the intracellular mature virus becomes enwrapped by a cellular cisterna to form first the intracellular enveloped virus and finally the extracellular enveloped virus. The origin of this wrapping cisterna is derived from the TGN [190]. Another report dealing with hepatitis C virus showed by transmission electron microscopy as well as confocal microscopy that viral proteins appeared located in the Golgi complex and ER, underlining the supposed involvement of these compartments in viral assembly and morphogenesis [191]. Moreover, transport and release of newly-assembled japanese encephalititis virus particles utilize the host membrane transport systems, including the ER to the classic secretory pathway (via the

Golgi apparatus), by using viral structural proteins [192]. In order to visualize ER-to-Golgi transport in the future, fluorescently tagged viral glycoprotein VSV-G could be applied [20]. Cells harboring siRNA to WHAMM showed that VSV-G transport to the Golgi was reduced by 40% as compared to control cells and also exhibited a 50% reduction in plasma membrane localization of VSV-G. These data would support the notion of impaired virus assembly due to the absence of WHAMM.

In comparison, a previous report identified a role for the WASH complex in *Salmonella* entry [193]. In particular, it accumulated at sites of *Salmonella* entry in fibroblasts and RNA interference studies revealed an impaired pathogen uptake [193]. Furthermore, the WASH complex has been described to accumulate on phagosomes and macropinosomes in *Dictyostelium*, where it has an important role in protein recycling to the plasma membrane [33]. It remains to be determined with the help of established WASH KO cell lines whether WASH has a similar function during virus uptake or whether it plays a distinct role in actin-dependent virus entry.

Interestingly, autophagy has not only been described in cellular homeostasis, cellular stress responses, and immune pathways, but also to be involved in pathogenesis of virus infections. It either plays a pro-viral or anti-viral role, depending on the virus, the cell type, and the cellular environment. During cell infection, viral proteins are initially targeted for degradation via autophagy. However, many viruses are able to escape autophagy-induced lysosomal degradation. Indeed, certain viruses even utilize the autophagy machinery by replicating themselves in autophagosome-like structures, well protected from the overall immune response and other intracellular degradation pathways [194]. On the other side and noteworthy for my studies is that invasion of host cells by DNA viruses activates autophagy, illustrated for instance by Herpesviruses [195]. HSV-1 is a member of the human Herpesviridae family [196] with a double-stranded DNA genome protected by a capsid and a proteinaceous tegument [195]. Early HSV-1 infection has been associated with autophagic changes in the host cell, specifically it induces an interaction of the cyclic GMP-AMP synthase (cGAS) with the autophagy protein Beclin 1. During robust immune responses, cGAS acts as an intracellular pattern recognition receptor (PRR) sensing cytosolic pathogen DNAs, producing the second messenger cGAMP to initiate the STING pathway and subsequently interferon production [197]. During HSV-1 infection, the above mentioned interaction between cGAS and Beclin 1 inhibits the production of cGAMP, allowing the activation of PtdIns3K, thereby increasing autophagy and targeting viral DNA for degradation [195, 197]. In

myeloid cells, autophagy is activated already upon viral entry, thus independent of viral gene expression [198]. Apart from cytosolic PRR, surface receptors such as toll-like receptor (TLR)2 and TLR4 are also able to interact with viruses and induce autophagy. They can interact with multiple viral components, for instance with the VSV-G viral glycoprotein for TLR2 or HSV glycoproteins gH/gL/gB for TLR2 [195]. However, WHAMM-deficient cells showed a clear defect in the autophagic process, more precisely loss of WHAMM resulted in an accumulation of autophagic markers such LC3 or p62 (see Figures 4.15 and 4.18), likely inhibiting this process. From those data I would assume that decreased autophagy should likely lead to higher levels of HSV-1 infection. However, loss of WHAMM in NIH/3T3 cells lead to reduced GFP-positive cells, thus to lower levels of HSV-1 infection (see Figure 4.31, B).
On the other side, it has been shown that autophagy can have different effects on HSV-1 infection depending on the cell type [199]. For instance, it has been reported that autophagy is critical for viral control in primary neurons, whereas being dispensable in mouse embryonic fibroblasts [200, 201]. In my study it is well possible that reduced HSV-1 infection in KOs results from a defect in transport, not directly related to autophagy. It is known that cytoplasmic envelopment of HSV-1 virions is followed by their vesicular transport to the cell surface and secretion by fusion of the vesicle membrane with the plasma membrane [202]. I hypothesize that the dispersed Golgi phenotype might lead to dysfunctional trafficking of viral components or virions budding from this compartment. Future analyses must focus on the efficiency of virus entry, capsid transport to the nucleus, as well as virus assembly and egress in the absence of WHAMM, preferably using GFP-HSV-1 and super-resolution microscopy.

5.6 Characterization of NIH/3T3 JMY KO cells

JMY was initially discovered as a p300 cofactor that facilitates the p53 response by augmenting p53-dependent transcription and apoptosis [48]. It is a dual function protein as it nucleates actin filaments in the presence and absence of Arp2/3 complex [18]. Interestingly, domain organization and sequence alignments showed that JMY is roughly 35% identical and 50% similar to WHAMM. Moreover, both NPFs have been linked to autophagy [44, 45, 85, 117]. Aside from its ability to regulate actin filament assembly, JMY is capable of translocation to the nucleus in response to DNA damage, where it promotes transcription by p53 and enhances apoptosis [50].
As I could clearly show for WHAMM KO cells (see Figure 4.5), JMY KO cell lines also exhibited an increase in the nuclear area (see Figure 4.32). JMY´s WH2 domain harbors a bipartite nuclear localization signal motif that controls JMY´s subcellular

localization. Decreases in the concentration of monomeric actin in the cytoplasm induced JMY to accumulate in the nucleus [50]. Moreover, knockdown of JMY by siRNA decreased the cytoplasmic concentration of filamentous actin [46]. Interestingly, actin itself has also been found to translocate to the nucleus. Unlike cytoskeletal actin, nuclear actin does not polymerize into persistent filaments. Instead, it exists as monomers and probably as highly dynamic polymers and has been implicated in a variety of processes such as regulation of transcription factors, the nuclear lamina, and as a crucial component of multiple chromatin remodeling complexes [203]. JMY KO in NIH/3T3 cells might cause a disruption of cytoskeletal attachments to linkers of the nucleoskeleton to the cytoskeleton at the nuclear envelope. These complexes physically connect the nucleus to the endomembrane and the cytoskeletal system. They are required to maintain nuclear size and shape in mammalian cells as well as to maintain structure and integrity of the nuclear envelope. However, no formal evidence is provided here to support these notions and further experiments are required.

In general, NPFs have been linked to autophagy [25, 44, 45, 117]. It was previously demonstrated that JMY localizes to autophagosomes and influences their formation. Furthermore, JMY has been described to induce actin assembly needed for the expansion of the phagophore membrane [76] and to increase autophagosome number and size [85, 204]. Interestingly, JMY contains a LIR motif, which is required to target it to the autophagosome, where it might contribute to autophagosome formation [85]. A novel study showed that JMY partially coincides and comigrates with DFCP1 and ATG9. Most interestingly, JMY can be enforced to lysosomal compartments when endo-lysosomal fusion is blocked with BafA1 [117]. In addition, JMY has been shown to partially localize to the ER, a compartment linked to the formation of early autophagic structures [46, 47, 70, 74].
siRNA studies performed in human U-2 OS exhibited that downregulation of JMY affected autophagosome number and size upon drug treatment [85]. However, preliminary assessment of LC3 and p62 particle number and size under fed conditions revealed that loss of JMY led to a strong increase of these two parameters (see Figure 4.34). It would be interesting to address the autophagic flux under nutrient deprivation, however, the dramatic increase of LC3 and p62 vesicles at steady state may point to a higher activity level of the autophagic machinery in JMY KO cells. Since JMY localizes to the ER and the TGN where it functions in vesicle trafficking [47], JMY KO in NIH/3T3 cells might also lead to decreased autophagosome motility and consequently to an accumulation of autophagic markers such as LC3 and p62. There-

fore, further experiments such as starvation and/or BafA1 treatment are necessary to obtain a better understanding of the contribution of JMY in autophagy regulation in cultured cells. Super-resolution imaging of early and late autophagic structures will also be interesting, as well as live-cell imaging applications in order to uncover JMY´s role during autophagy.

As mentioned above, cytoplasmic JMY localizes to the ER and the TGN and has been shown to influence cell motility and invasion [46,47,205]. Further, it was described that its overexpression affects both Golgi integrity and VSV-G transport to the plasma membrane [47]. Interestingly, JMY KO cells described here were less susceptible to VSV infection and displayed a clear defect in virus release (see Figure 4.35), indicating an involvement of JMY in the life cycle of VSV. One current idea is to investigate transport mechanisms via the secretory pathway. Studies of the trafficking of viral integral membrane proteins such as RSV-F protein may lead to a better understanding of intracellular transport mechanisms in JMY KO cells. RSV-F traffics through the secretory pathway and has an ER signal sequence. Moreover, it is responsible for viral fusion with the host cell membrane as well as for the induction of the characteristic syncytia produced in RSV infections [206]. I anticipate that JMY KO might lead to aberrant localization of RSV-F. Another future experiment would be to quantify virus infection via a plaque assay. Plaques result from the infection of a cell layer by virions followed by the virus replication and the death of the infected cells. This assay may be used as a complementary method to flow cytometry and video microscopy in order to confirm previous results.

In this work presented here, I report a simple and rapid approach that used programmable CRISPR/Cas9 nucleases to generate specific KO cell lines. I could generate four individual WHAMM KO clones by this method, among others. Recent evidence indicates an intriguing relationship between WHAMM, vesicle trafficking, and autophagy. In-depth analysis showed a distributed Golgi apparatus in all WHAMM KO clones. Furthermore, WHAMM KO led to abnormal accumulation of autophagic markers such as DFCP1, LC3, and p62 that can be associated with impaired autophagosome maturation as well as lysosomal fusion dysfunction. In addition, this study shows for the first time the relevance of key molecular players (e.g. WHAMM or JMY) involved in VSV and/or HSV-1 infection processes. These novel data will provide a further piece of understanding of the viral infection route and will improve our idea by which mammalian cells are harnessed by VSV or HSV-1 and thereby how to protect the host against these potential invaders.

6 Appendix

6.1 Supplementary data

6.1.1 Sequencing alignments of NIH/3T3 cells deficient in WASH, WHAMM or JMY

DNA from generated NIH/3T3 KO cell lines was isolated and sent for sequencing. Reads were aligned to NIH/3T3 WT cells using Clustal Omega and are shown in Figures 6.1 – 6.3. Sequencing gaps indicate *indels* and are underlined in red. Sequencing results revealed both homozygous and heterozygous gene mutations depending on the targeted gene. Respective amino acid translations of NIH/3T3 WASH and JMY KO cells are depicted in Figures 6.4 – 6.5. Amino acids labeled in red indicate positions that differ from the WT sequence. Protein sequence alignments of JMY also show positions of premature stop codons (designated by stars) due to the introduced frameshifts.

NIH/3T3 WT DNA vs. WASH#19 DNA

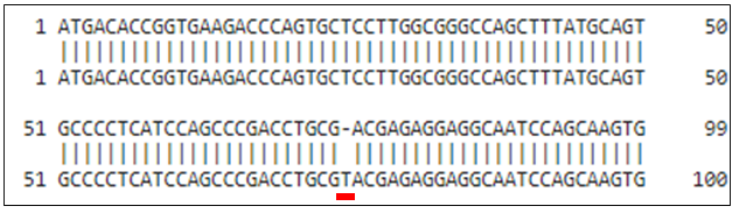

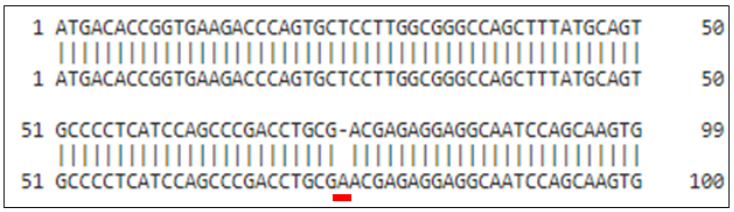

NIH/3T3 WT DNA vs. WASH#20 DNA

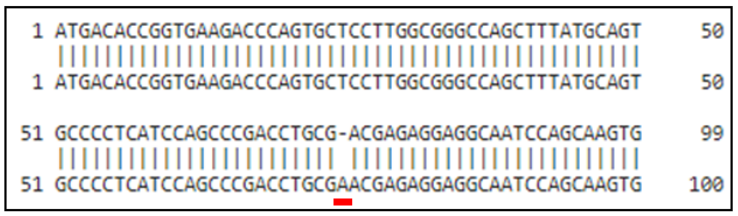

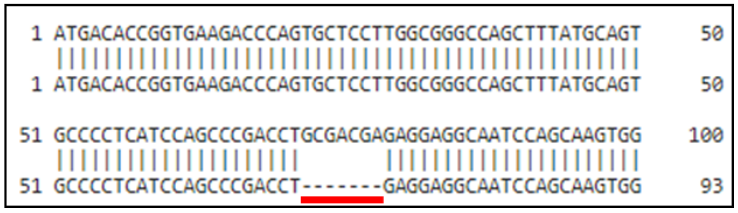

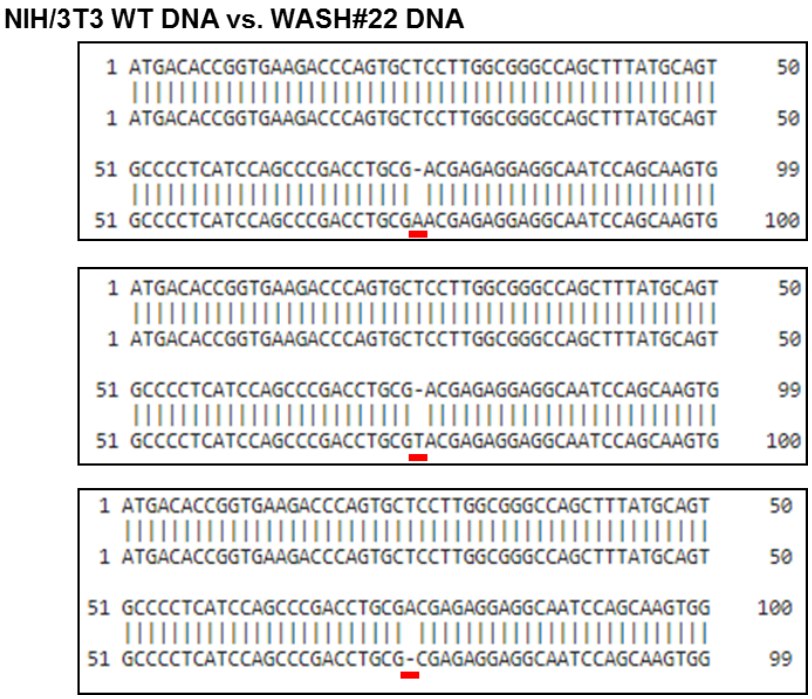

Figure 6.1: DNA alignments of NIH/3T3 WT and WASH KO cells. All WASH KO clones exhibit heterozygous gene mutations (indicated by two different alleles). WASH#22 displays three different alleles which might indicate a mixture of clones. Sequencing gaps (underlined in red) in the WASH locus implicate *indels*. Upper lane = WT sequence, lower lane = KO sequence.

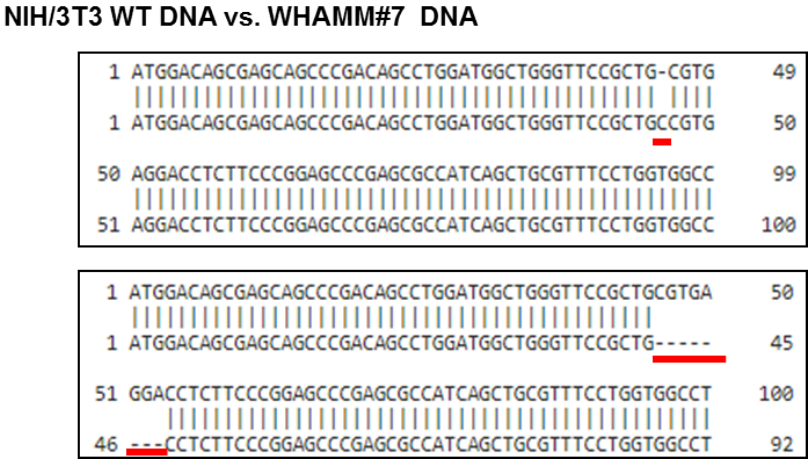

NIH/3T3 WT DNA vs. WHAMM#11 DNA

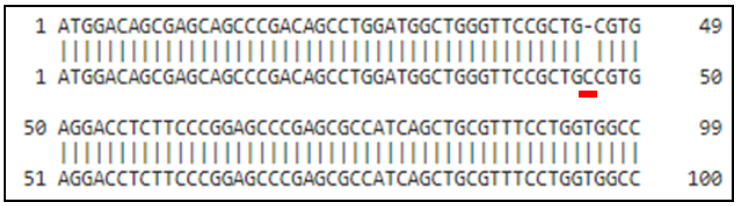

Figure 6.2: DNA alignments of NIH/3T3 WT and WHAMM KO cells. WHAMM#7 bears two different alleles (heterozygous mutation), whereas WHAMM#11 has exactly the same two alleles (homozygous mutation). Sequencing gaps (underlined in red) in the WHAMM locus implicate *indels*. Upper lane = WT sequence, lower lane = KO sequence.

NIH/3T3 WT vs. JMY#2

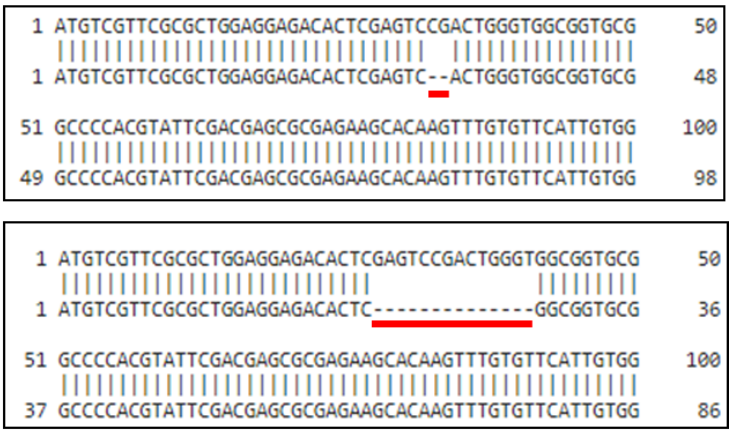

NIH/3T3 WT vs. JMY#5

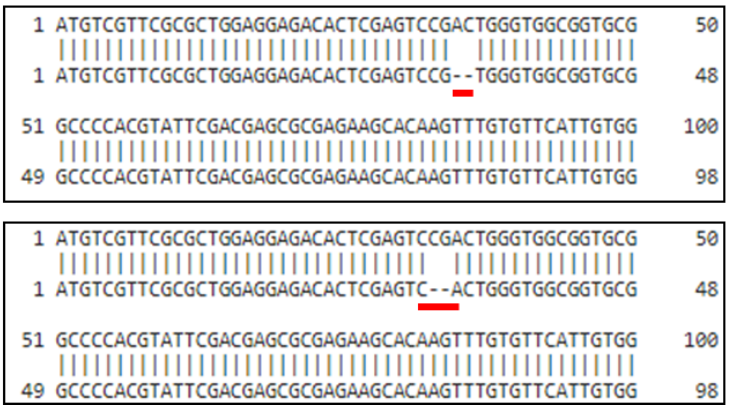

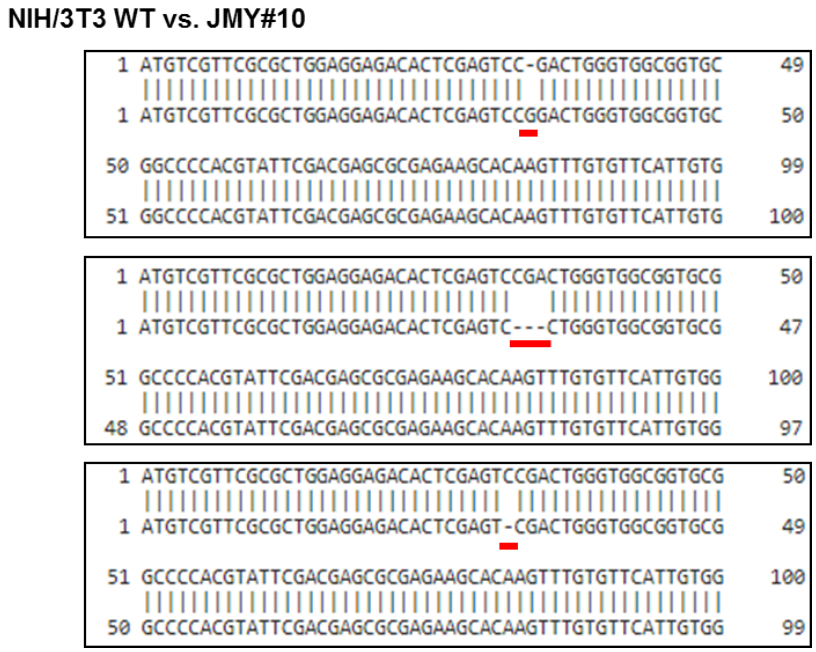

Figure 6.3: DNA alignments of NIH/3T3 WT and JMY KO cells. All JMY KO clones exhibit heterozygous gene mutations (indicated by two different alleles). JMY#10 displays three different alleles which might indicate a mixture of clones. Sequencing gaps (underlined in red) in the JMY locus implicate *indels*. Upper lane = WT sequence, lower lane = KO sequence.

Protein sequence of murine WASH WT (**black**) or mutation-derived (red)	GB Acc and Clone numbers
MTPVKTQCSLAGQLYAVPLIQPDLRREEAIQQVADALQYLQNISGDIFSRIS RRVELSRRQLQAISERVSLAQAKIEKIKGSKKAIKVFSSAKYPAPEHLQEYG SIFTGALDPGLQRRPRYRIQSKHRPLDERALQEKLKYFPVCVNTKSEPED EAEEGLGGLPSNISSISSLLLFNTTENLYKKYVFLDPLAGAVTKTHTMLGTE EEKL…	Murine WASH (475AA) NP_081109.1
MTPVKTQCSLAGQLYAVPLIQPDLRTRGGNPASGRCPAVPTEHLWRHLQQ	#19 Mutant allele 1/2
MTPVKTQCSLAGQLYAVPLIQPDLRTRGGNPASGRCPAVPTEHLWRHLQQ MTPVKTQCSLAGQLYAVPLIQPDLRRQSSKWQMPCSTYRTSLETSSA	#20 Mutant allele 1 #20 Mutant allele 2
MTPVKTQCSLAGQLYAVPLIQPDLRTRGGNPASGRCPAVPTEHLWRHLQQ MTPVKTQCSLAGQLYAVPLIQPDLRERRQSSKWQMPCSTYRTSLETSSA	#22 Mutant allele 1 #22 Mutant allele 2

Figure 6.4: Protein alignments of NIH/3T3 WT and WASH KO cells. In this study, I established NIH/3T3 deficient in *wash*. Three clonal cell lines were generated by using one sgRNA targeting the coding region of *wash*, which produced *indels* that abolished WASH protein expression. Amino acids labeled in red indicate positions that differ from the WT sequence.

Protein sequence of murine JMY WT (**black**) or mutation-derived (red)	GB Acc and Clone numbers
MSFALEETLESDWVAVRPHVFDEREKHKFVFIVAWNEIEGKFAITCHNRTA QRQRSGSREQAGTPASDGSRGPGSPAARGRSEAAASATAALRSPGPRK SQAWAEGGSPRSARSLKGDPPRGPAGRGPESPLRSPARAKASPLRRSA ESRDATASATPAPPAPPVPPVSSVRVVSASGAVSEEIEVLEMVRED...	Murine JMY (983AA) NP_067285
MSFALEETLESLGGGAAPRIRRAREAQVCVHCGLERDRRQVCYNLSQPD GPETEERFPGTGGDARV* MSFALEETLGGAAPRIRRAREAQVCVHCGLERDRRQVCYNLSQPDGPET EERFPGTGGDARV*	#2 Mutant allele 1 #2 Mutant allele 2
MSFALEETLESVGGGAAPRIRRAREAQVCVHCGLERDRRQVCYNLSQPD GPETEERFPGTGGDARV* MSFALEETLESLGGGAAPRIRRAREAQVCVHCGLERDRRQVCYNLSQPD GPETEERFPGTGGDARV*	#5 Mutant allele 1 #5 Mutant allele 2
CRSRWRRHSSPDWVAVRPHVFDEREKHKFVFIVAWNEIEGKFAITCHNRT AQRQRSGSREQAGTPASDGSRGPGSPAARGRSEAAASATAALRSPGPR KSQAWAEGGSPRSARSLKGDPPRGPAGRGPESPLRSPARAKASPLRRS AESRDATASATPAPPAPPVPPVSSVRVVSASGAVSEEIEVLEMVRED	#10 Mutant allele 1
MSFALEETLES-WVAVRPHVFDEREKHKFVFIVAWNEIEGKFAITCHNRTA QRQRSGSREQAGTPASDGSRGPGSPAARGRSEAAASATAALRSPGPRK SQAWAEGGSPRSARSLKGDPPRGPAGRGPESPLRSPARAKASPLRRSA ESRDATASATPAPPAPPVPPVSSVRVVSASGAVSEEIEVLEMVRED	#10 Mutant allele 2
VVRAGGDTRVDWVAVRPHVFDEREKHKFVFIVAWNEIEGKFAITCHNRTA QRQRSGSREQAGTPASDGSRGPGSPAARGRSEAAASATAALRSPGPRK SQAWAEGGSPRSARSLKGDPPRGPAGRGPESPLRSPARAKASPLRRSA ESRDATASATPAPPAPPVPPVSSVRVVSASGAVSEEIEVLEMVRED	#10 Mutant allele 3

Figure 6.5: Protein alignments of NIH/3T3 WT deficient in *jmy*. In this study, I established NIH/3T3 deficient in *jmy*. Three clonal cell lines were generated by using one sgRNA targeting the coding region of *jmy*, which produced *indels* that abolished JMY protein expression. Amino acids labeled in red indicate positions that differ from the WT sequence. Horizontal dash indicates missing amino acid(s). Protein sequence alignments show positions of premature stop codons (designated by stars) due to the introduced frameshifts.

6.1.2 Cell size and actin pattern in WHAMM KO cells

Immunofluorescence stainings of NIH/3T3 WHAMM KOs are displayed in Figure 6.6, A. DAPI staining (blue) was used as a cellular nucleus marker. F-actin (red) was stained by fluorescent phalloidin. Note that KO cells appeared larger in comparison to WT cells. Additionally, the cell area was examined 5 h after cell seeding (Figure 6.6, B). These data show that WHAMM KO causes cell enlargement and consequently confirm previous experiments shown in Figure 4.5.

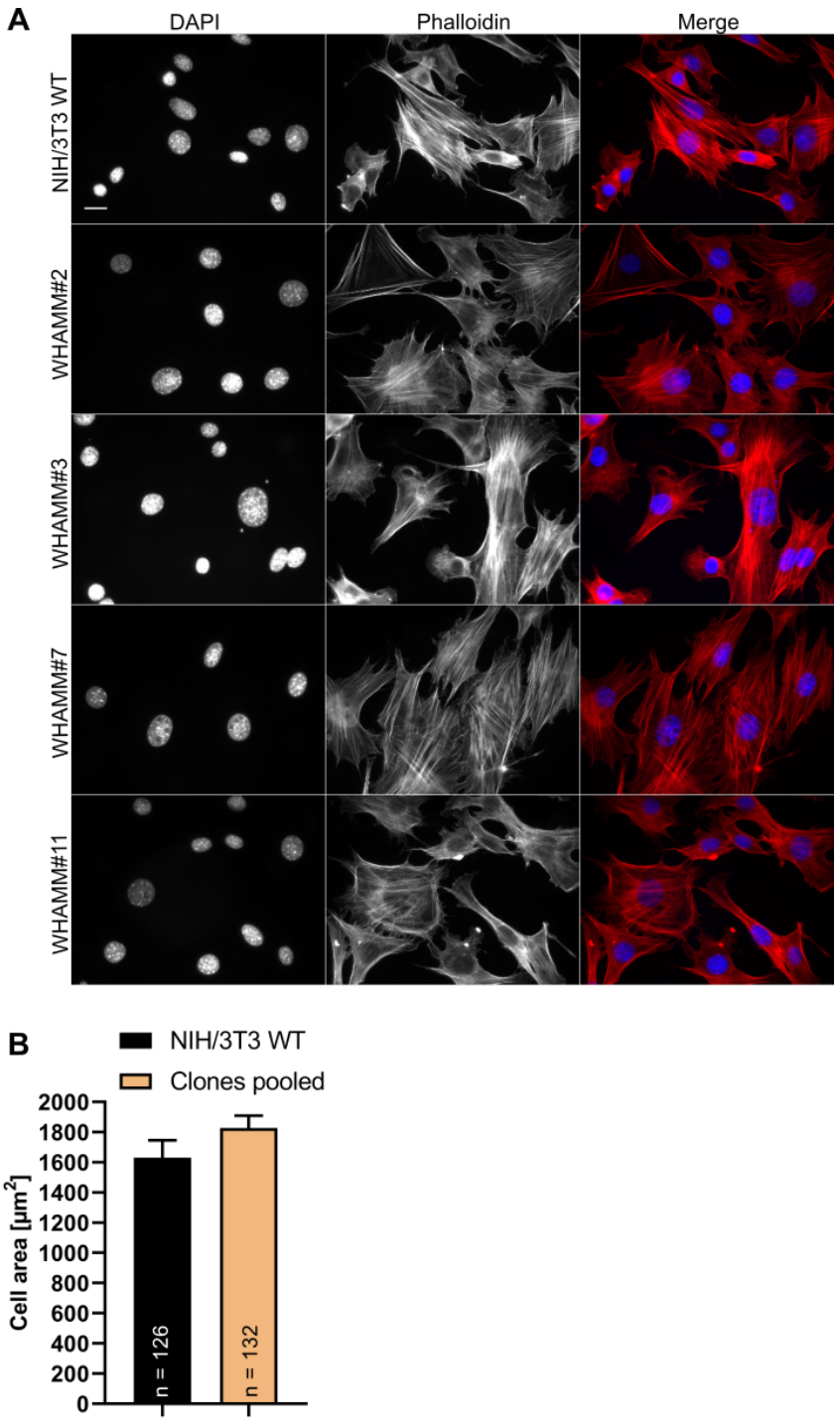

Figure 6.6: NIH/3T3 cells deficient in WHAMM expression display unaltered stress fibers but are larger in size. (A) DAPI staining (blue) was used as a cellular nucleus marker. F-actin (red) was stained by fluorescent phalloidin. Scale bar: 20 µm. (B) Cells were stained with CellTracker, seeded onto fibronectin-coated coverslips and fixed after 5 h. Quantitative analysis of WT and WHAMM KO cells confirms an impact of *whamm* deletion on cell area. Data are representative of two independent experiments. n = number of cells analyzed. Error bars represent SEM.

6.1.3 Granularity in WHAMM KO cells

Cells were analyzed by flow cytometry with the help of Stephanie Stahnke (HZI, Braunschweig) to assess their cellular volume (Figure 6.7, A). Cells were grouped into four categories, depending on cell size and cell granularity. For this measurement, sideward scatter SSC and forward scatter FSC are plotted and gates are set to WT parameters. The results show that loss of WHAMM results in a shift from smaller to larger cell populations as well as to big granular cells (Figure 6.7, B-C).

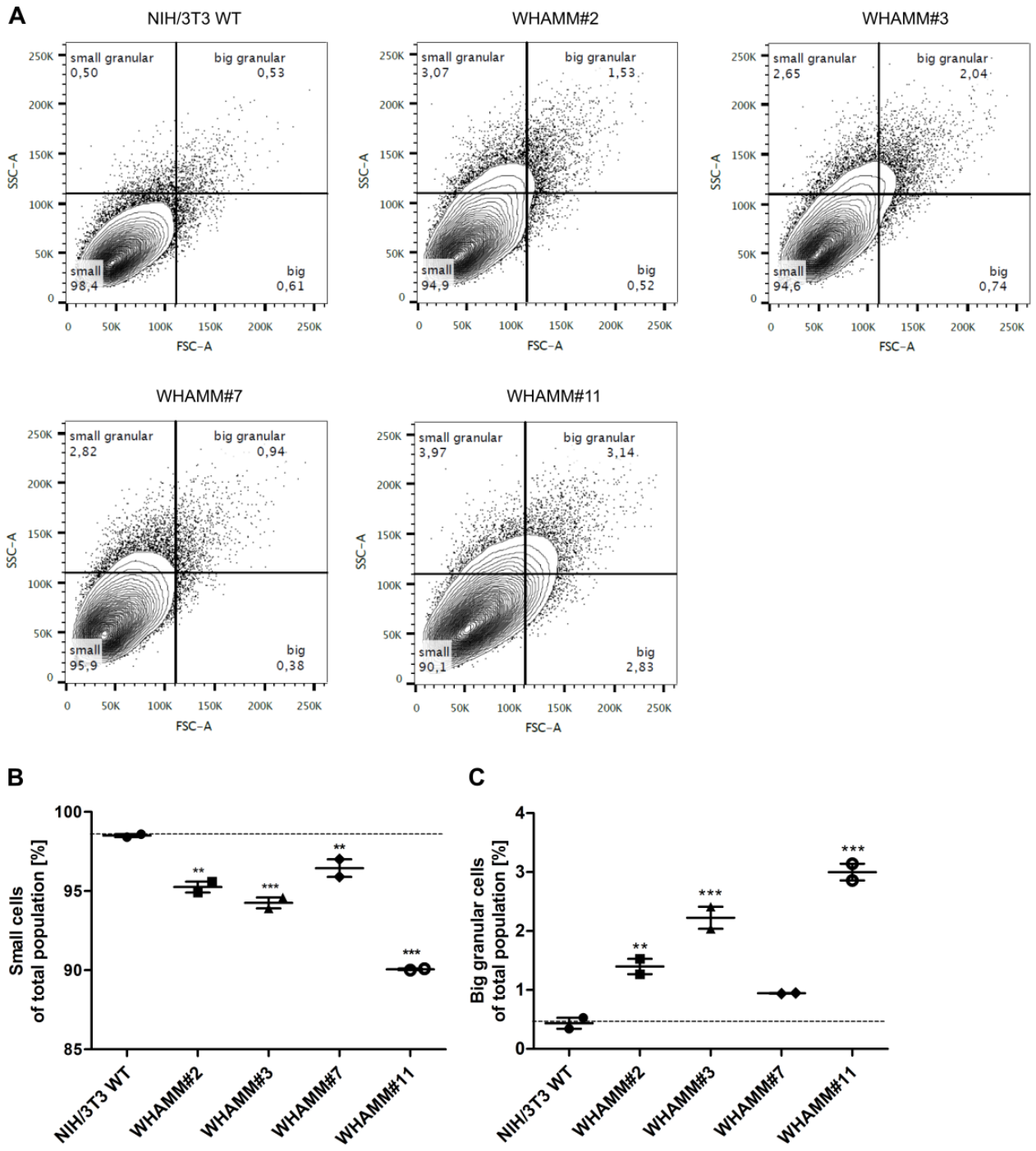

Figure 6.7: Effect of WHAMM KO on cell size and granularity. (A) Cell size and cell granularity were analyzed by flow cytometry. Quadrant gates split the population into four adjacent, discrete subpopulations. (B-C) Quantitative analysis of WT cells versus WHAMM KO clones confirms a shift in cell population from smaller to large cells in KO cells as well as a higher number of big granular cells. Data are representative of two independent experiments. **P $\leq$ 0.005, ***P $\leq$ 0.0001, One-way ANOVA. Error bars represent SEM.

6.1.4 ER and ERGIC pattern in WHAMM KO cells

Immunofluorescence stainings of NIH/3T3 WHAMM KO cells are displayed in Figures 6.8 and 6.9. F-actin filaments were visualized with phalloidin, ER was uncovered with GFP-tagged VAP-A, and ERGIC was targeted with EGFP-ERGIC.

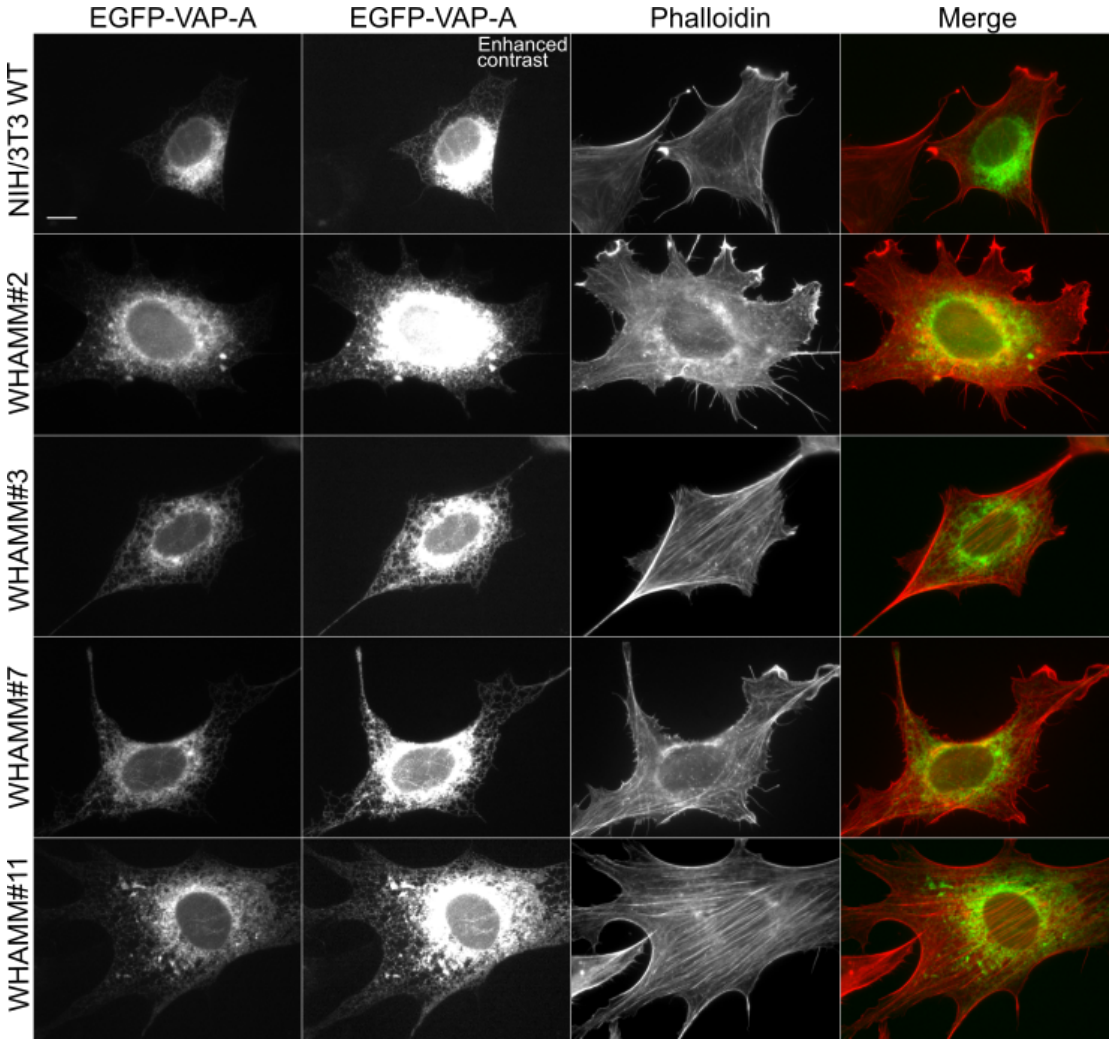

Figure 6.8: Subcellular localization of VAP-A in WT and WHAMM KO cells. Representative immunofluorescence images of WT and WHAMM KO cells. EGFP-VAP-A (green) was used to label the position of ER. F-actin (red) was stained by fluorescent phalloidin. Enhanced contrast was utilized to improve visualization of the ER. Scale bar: 10 µm. Data are derived from one experiment.

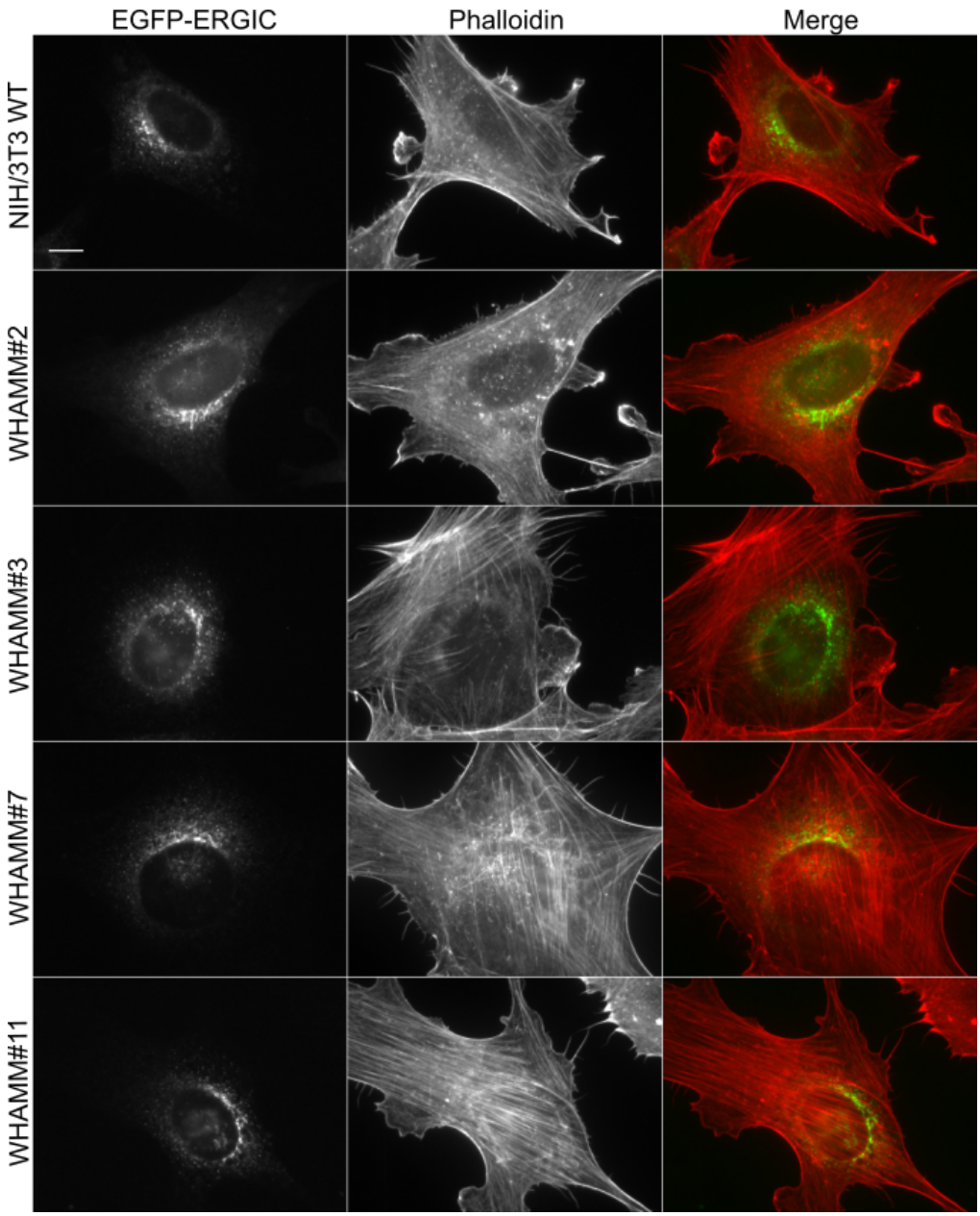

Figure 6.9: ERGIC staining in WT and WHAMM KO cells. Representative immunofluorescence images of WT and WHAMM KO cells. EGFP-ERGIC (green) was used to label the position of ERGIC elements. F-actin (red) was stained by fluorescent phalloidin. Scale bar: 10 µm. Data are derived from one experiment.

6.1.5 Golgi pattern in WHAMM KO cells

Immunofluorescence stainings of NIH/3T3 WHAMM KO cells are displayed in Figures 6.10. Golgi apparatus was visualized with Giantin and DAPI was used to visualize nuclear DNA.

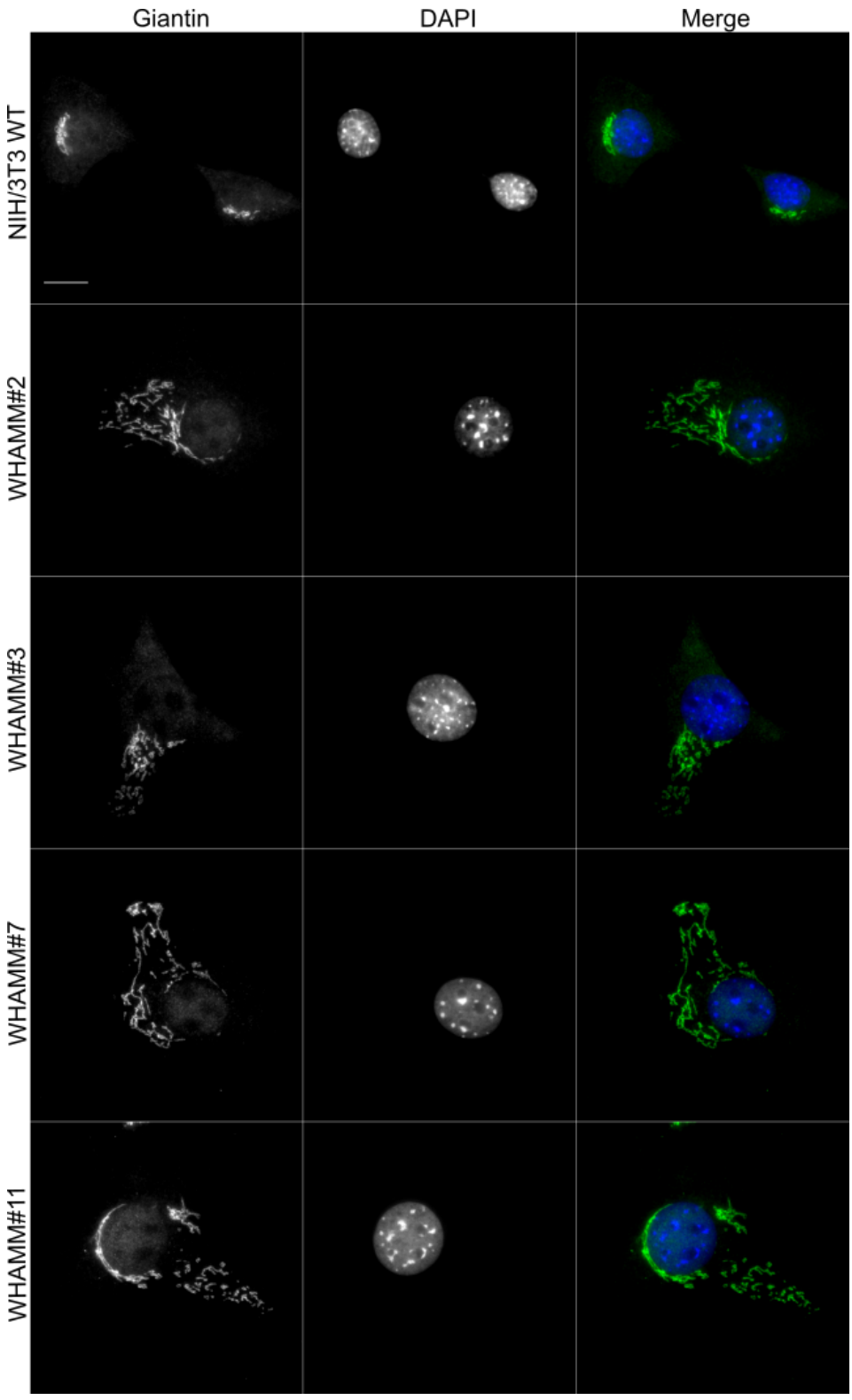

Figure 6.10: Effect of WHAMM KO on Golgi apparatus in NIH/3T3 cells. Representative immunofluorescence images of WT and WHAMM KO cells. The majority of cells deficient for WHAMM expression show a disseminated Golgi complex. Giantin staining (green) was used to label the position of Golgi. DAPI staining (blue) was used as a cellular nucleus marker. Scale bar: 20 µm.

6.1.6 WHAMM KO affects autophagy

Early autophagy was investigated with EGFP-DFCP1. Figure 6.11 displays EGFP-DFCP1-coated omegasomes under basal conditions.

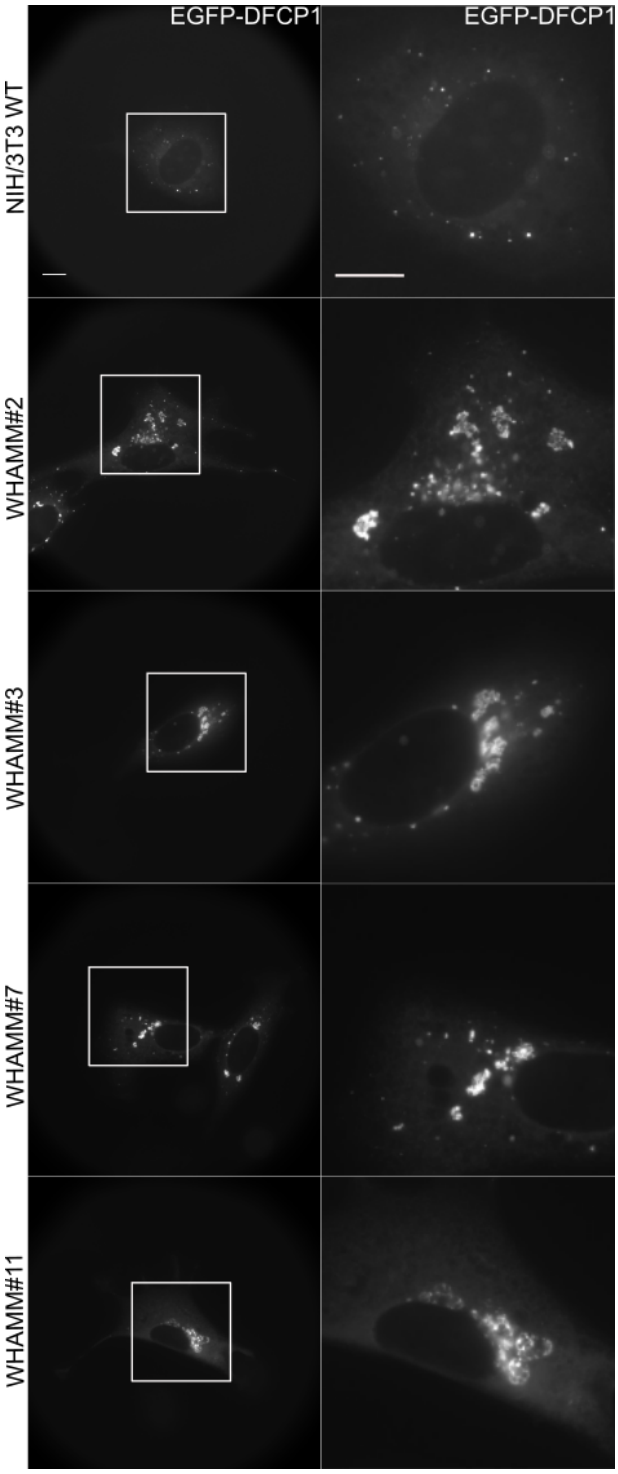

Figure 6.11: WHAMM KO leads to an accumulation of omegasomes. Representative immunofluorescence images of WT and WHAMM KO cells. EGFP-DFCP1 was used to label the position of omegasomes. WHAMM KOs in general exhibited an accumulation of DFCP1-positive structures under fed conditions. Scale bar: 10 µm.

Autophagy was induced in both WT and WHAMM KO cells by HBSS treatment. Moreover, the autophagic flux was further examined by HBSS and/or BafA1 treatment. Level of autophagy was monitored and measured by LC3 and p62 westerm blot analyses as well as immunofluorescence stainings. A representative image of LC3-I and LC3-II detection in WT and two WHAMM KO cells starved with HBSS is shown in Figure 6.12. Immunofluorescence stainings of NIH/3T3 WT and WHAMM KO cells treated with HBSS are displayed in Figures 6.13 and 6.14. Immunofluorescence stainings of NIH/3T3 WT and WHAMM KO cells treated with HBSS and/or BafA1 are displayed in Figures 6.15 and 6.16.

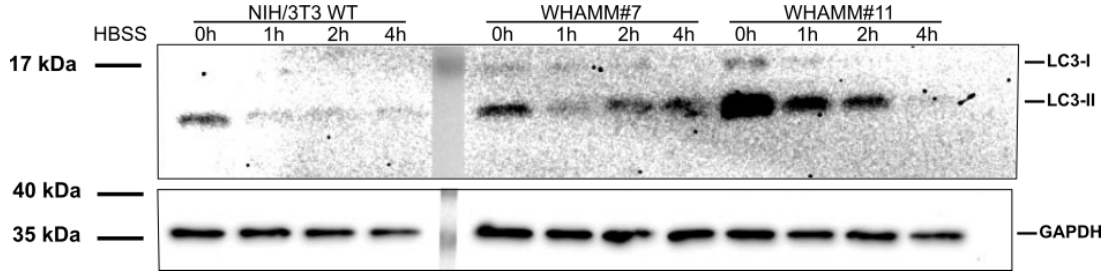

Figure 6.12: Western blot analysis of LC3-I and LC3-II after HBSS treatment. Representative image of western blots. Cells were seeded and starved with HBSS for the indicated time points. Lysates of WT and WHAMM KO cells were separated on a SDS gel. Membrane was blotted for LC3-I and LC3-II as well as GAPDH was used as loading control. Western blot analysis revealed a diffuse or weak antibody staining, especially for LC3-I detection. Data are representative of at least three independent experiments.

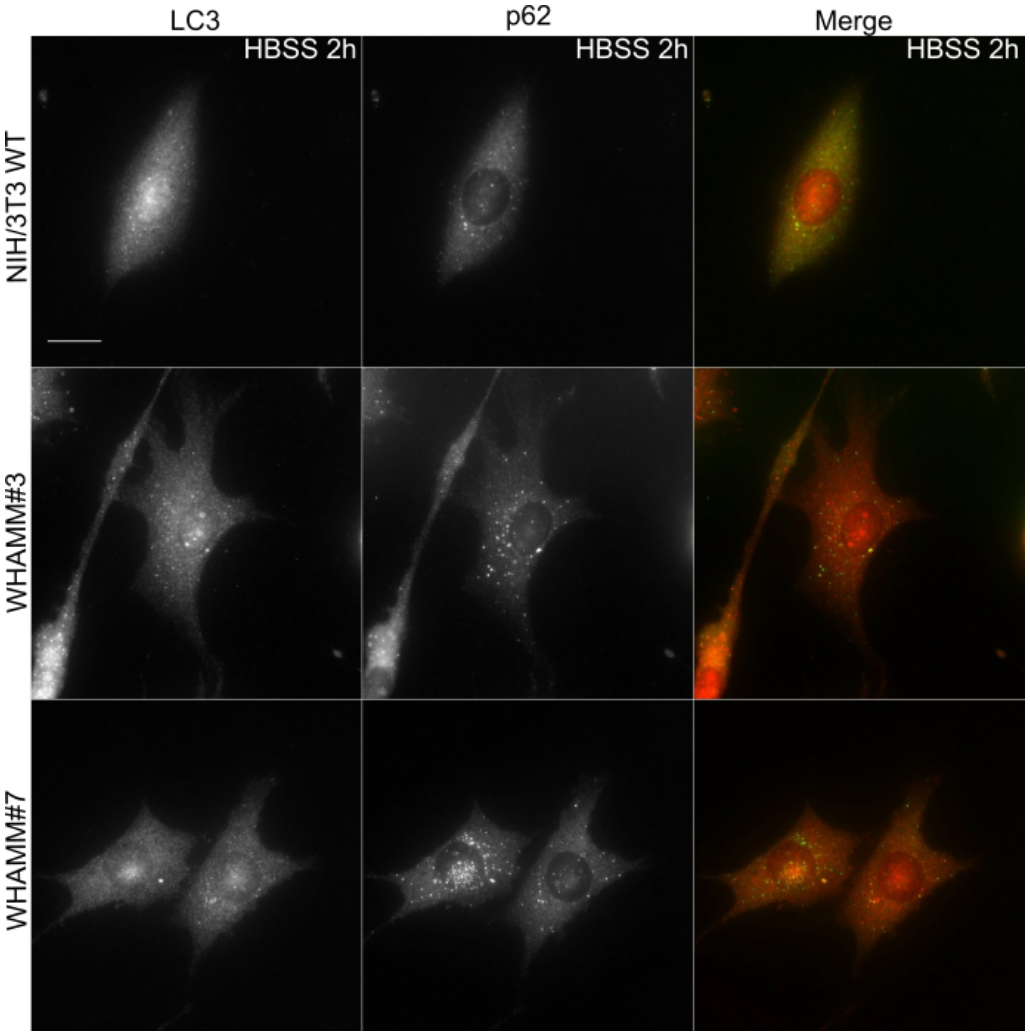

Figure 6.13: Loss of WHAMM does affect autophagy. Autophagy was induced by HBSS treatment and studied with autophagy markers LC3 (red) and p62 (green). Scale bar: 20 µm.

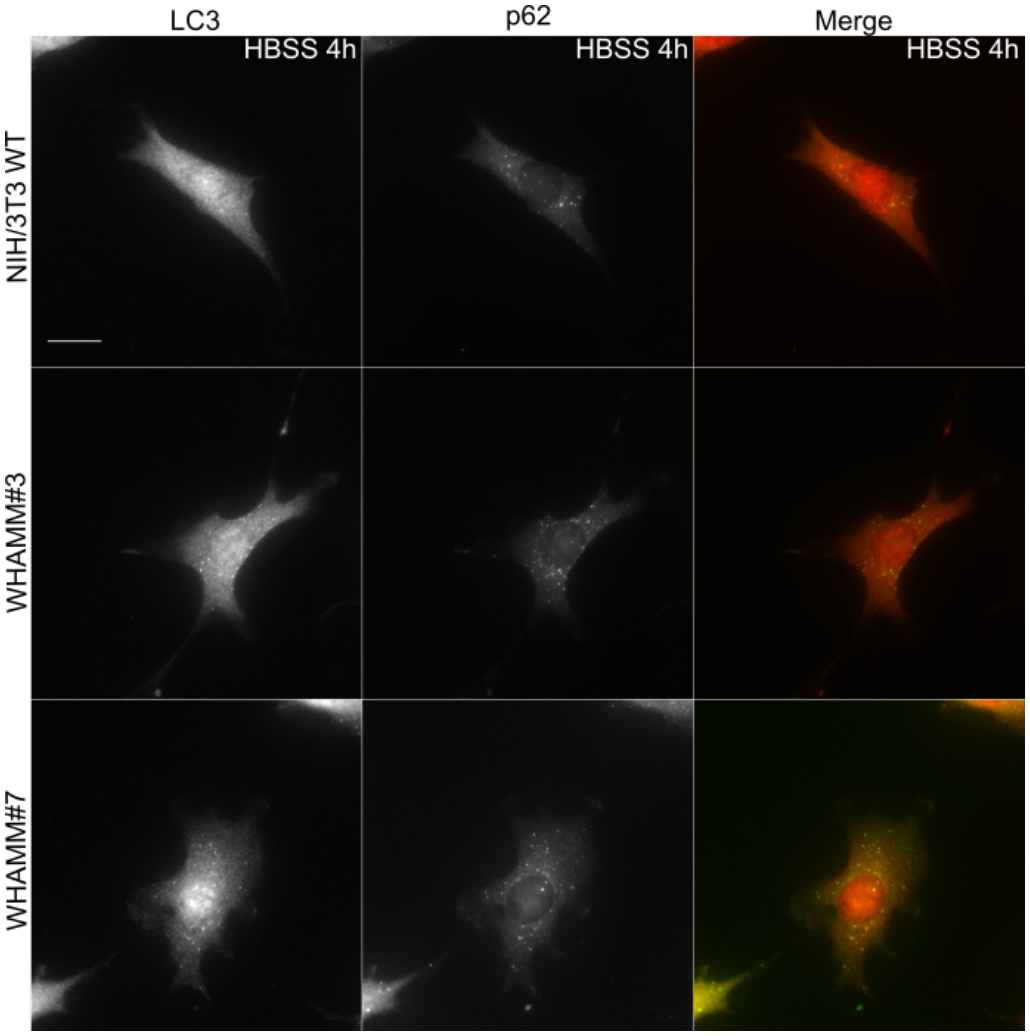

Figure 6.14: Loss of WHAMM does affect autophagy. Autophagy was induced by HBSS treatment and studied with autophagy markers LC3 (red) and p62 (green). Scale bar: 20 µm.

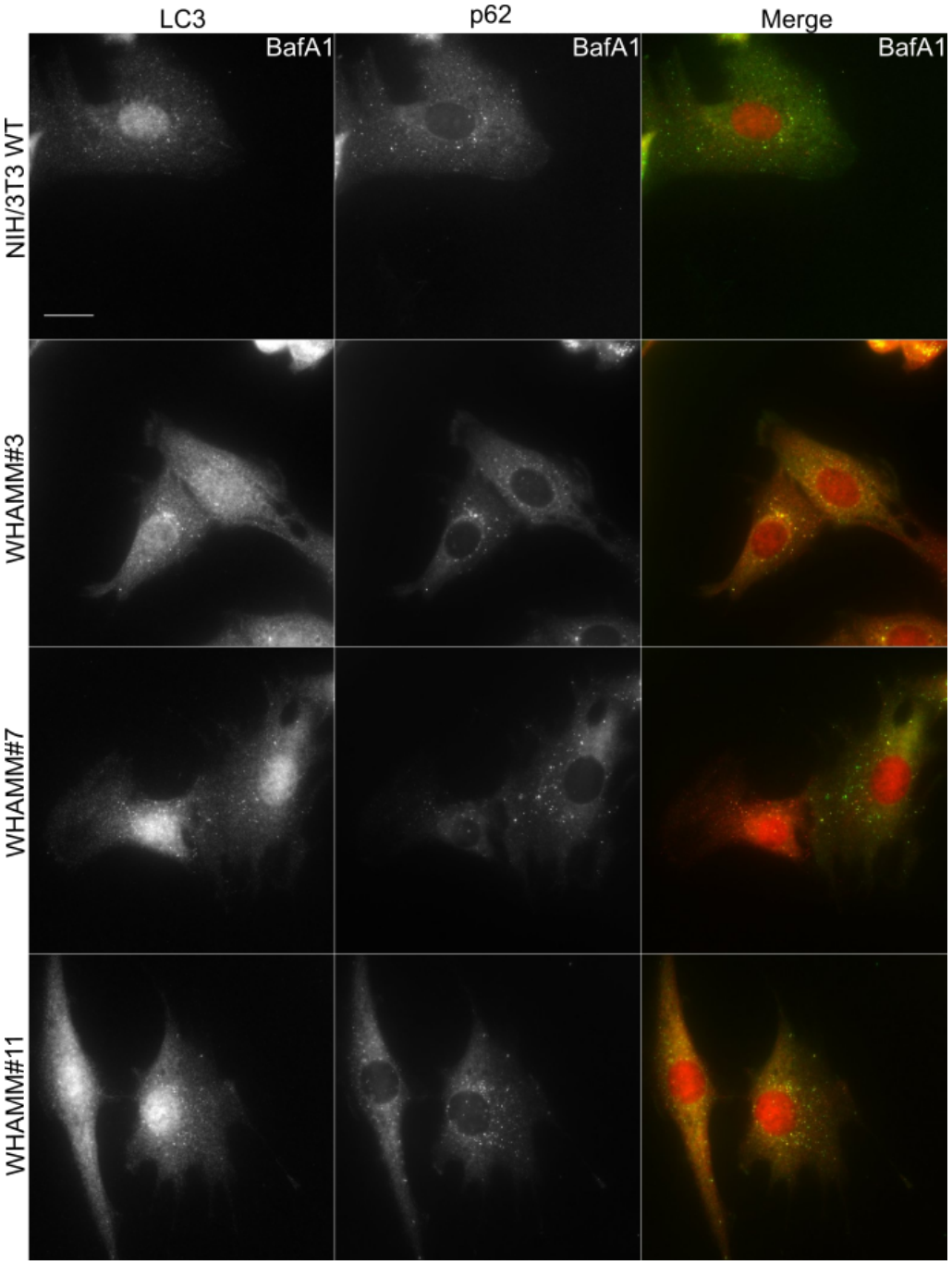

Figure 6.15: Loss of WHAMM does affect autophagy. The autophagic flux was further investigated by BafA1 treatment and studied with autophagy markers LC3 (red) and p62 (green). Scale bar: 20 µm.

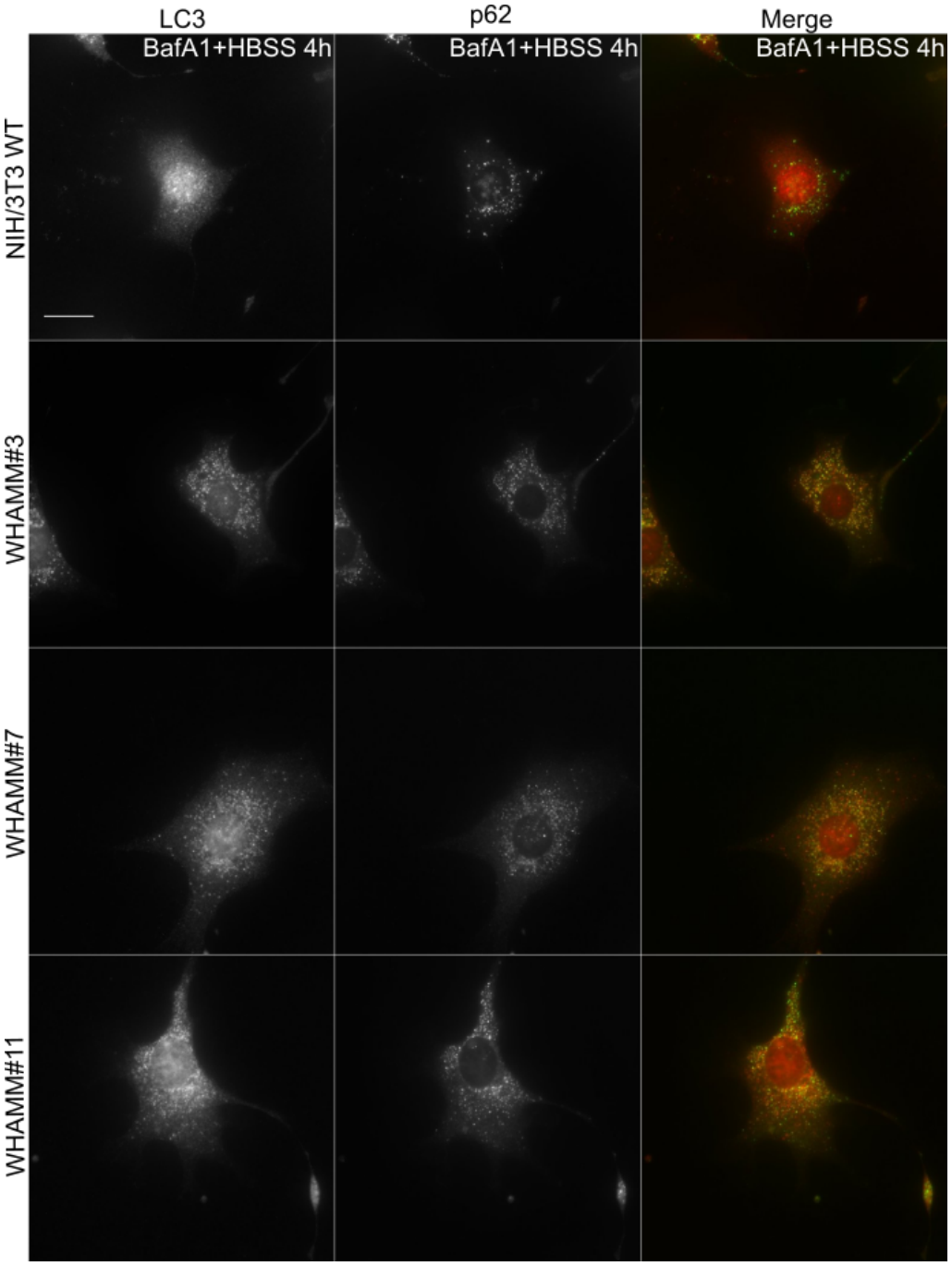

Figure 6.16: Loss of WHAMM does affect autophagy. The autophagic flux was further investigated by HBSS treatment in the presence of BafA1 and studied with autophagy markers LC3 (red) and p62 (green). Scale bar: 20 µm.

A flow cytometry-based assay was applied as further method to analyze and quantify the amount of LC3 in WHAMM KO cells. Cells were untreated or treated with HBSS for the indicated time points followed by flow cytometry analysis. Representative flow cytometry gating plots of untreated cells are depicted in Figure 6.17, A. Quantification of fluorescence intensity in WT and WHAMM KO cells is shown in Figure 6.17, B. Calculations are based on population 3 (P3).

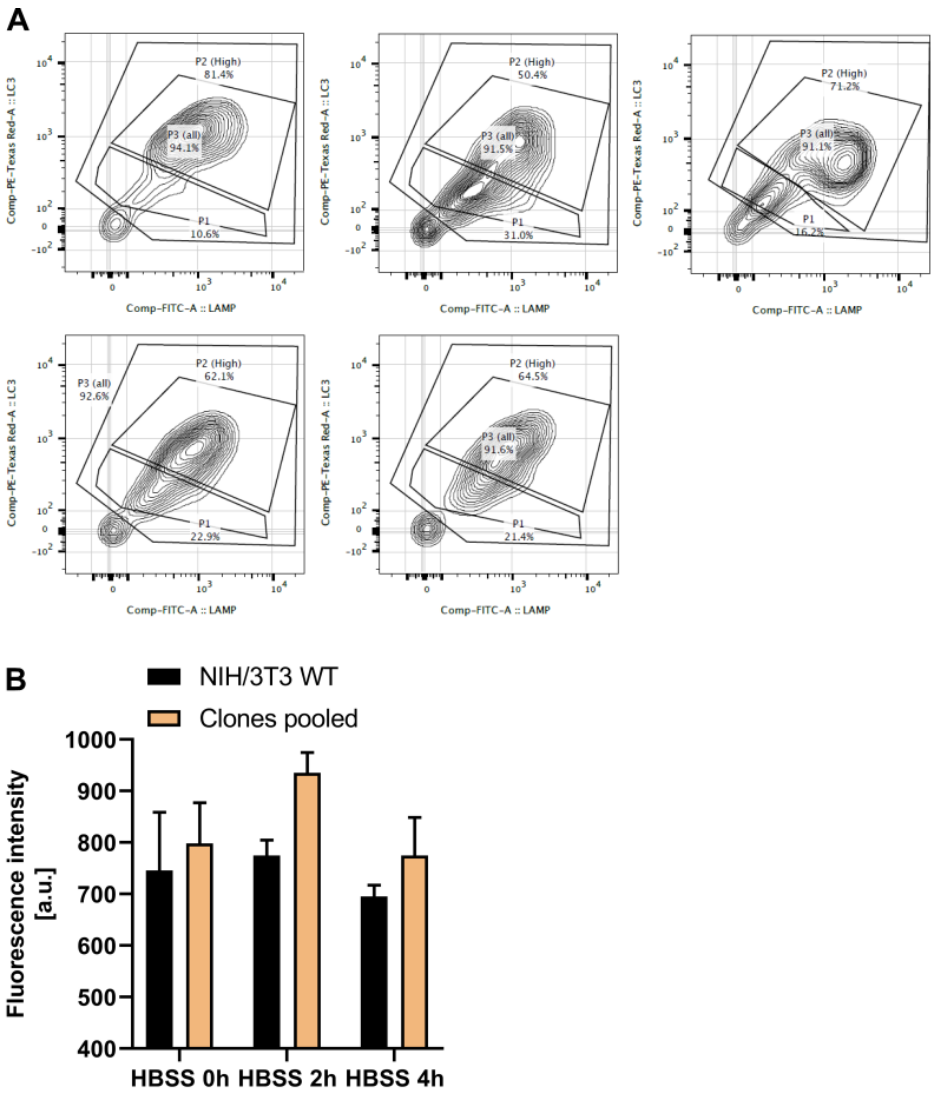

Figure 6.17: Quantification of LC3 by flow cytometry. (A) Representative flow cytometry plots of untreated cells. Texas Red A (LC3) vs. FITC A (LAMP1) channels are plotted. Cells were split into three populations (P3 consists of P1 and P2). (B) Preliminary results confirm a higher fluorescence intensity in WHAMM KO cells under basal and starvation condition. Data are derived from one experiment. Error bars represent SEM.

Flow cytometry has also been applied to quantify the amount of LAMP1 present in WHAMM KO cells. Cells were untreated or treated with HBSS for the indicated time points followed by flow cytometry analysis. Representative flow cytometry gating plots of untreated cells are depicted in Figure 6.17, A. Quantification of fluorescence intensity in WT and WHAMM KO cells is shown in Figure 6.18. Calculations are based on population 3 (P3).

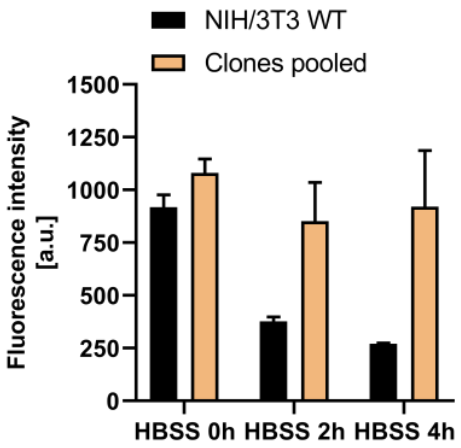

Figure 6.18: Quantification of LAMP1 by flow cytometry. Preliminary results confirm a higher fluorescence intensity in WHAMM KO cells under basal and starvation condition. Data are derived from one experiment. Error bars represent SEM.

6.1.7 Gene regulation in WHAMM KO cells

Microarray analysis of WHAMM KO cells was performed with the help of Robert Geffers (HZI, Braunschweig). Top 50 genes are shown in Table 6.1. Note that the first genes (*acadsb* - *6430550D23Rik*) are downregulated, whereas all others are upregulated in comparison to WT cells. Expression patterns of several ATGs were analyzed and are depicted in Figure 6.19.

Table 6.1: Top 50 genes

Gene	Function
Acadsb	Catalyze dehydrogenation of acyl-CoA derivatives in the metabolism of fatty acids or branch chained amino acids
Acat2	Plays a role in lipoprotein assembly and dietary cholesterol absorption Acyltransferase and ligase activity
Acly	ATP-citrate synthase Synthesis of cytosolic acetyl-CoA Central role in *de novo* lipid synthesis
Aldh4a1	Dehydrogenase Conversion of delta-1-pyrroline-5-carboxylate to glutamate

Aox3	Oxidizes aromatic azaheterocycles, aldehydes Involved in the regulation of reactive oxygen species homeostasis Catalyzes nitric oxide production
Ap3s1 ps1/ps2	Part of AP-3 complex that facilitates the budding of vesicles from the Golgi May be directly involved in trafficking to lysosomes
Bmf	May play a role in apoptosis
Ccr7	Receptor for MIP-3-beta chemokine
Cebpd	Transcription activator regulating the expression of genes involved in immune and inflammatory responses
Cped1	Cadherin Like And PC-Esterase Domain Containing 1
Cyba	Critical component of membrane-bound oxidase of phagocytes Superoxide generation
Dact1	Plays a role in canonical and/or non-canonical Wnt signaling
Galnt15	Catalyzes initial reaction in O-linked oligosaccharide biosynthesis
Gas1	Growth arrest protein involved in growth suppression Blocks entry to S phase
Gdpd2	Glycerophosphoinositol inositolphosphodiesterase activity Hydrolyzes glycerophosphoinositol Remodeling of the actin cytoskeleton
Gmpr	Catalyzes the irreversible NADPH-dependent deamination of GMP Functions in the conversion of nucleobase, nucleoside and nucleotide derivatives of G to A nucleotides,

	and in maintaining the intracellular balance of A and G nucleotides
Gm12060	Involved in ER-associated degradation of misfolded, glycosylated proteins Has a role in the protection of cells from ER stress-induced apoptosis
Gxylt2	Glycosyltransferase, elongates O-linked glucose attached to EGF-like repeats by catalyzing the addition of xylose
Ifi27l2a	Localizes at the inner nuclear membrane in transfected cell lines, inhibits function of the NR4A1 nuclear receptor, downregulated NR4A1-target genes Mitochondrial protein
Limd2	Cell motility
Lrrk2	Positively regulator of autophagy Activation of CaMKK/AMPK signaling pathway Plays a role in retrograde trafficking pathway for recycling proteins
Lurap1	Activates NF-kappa-B pathway Drives production of proinflammatory cytokines Involved cell protrusion and migration
Mgp	Associates with the organic matrix of bone and cartilage Acts as an inhibitor of bone formation
Nfil3	Transcriptional regulator
Nr4a2	Transcriptional regulator Iimportant for differentiation and maintenance of meso-diencephalic dopaminergic neurons
Osmr	Cytokine binding

	Cytokine receptor activity Growth factor binding Oncostatin-M receptor activity
Pde8b	Hydrolyzes second messenger cAMP Regulator of many important physiological processes
Pdzk1ip1	Scaffold protein that connects plasma membrane proteins and regulatory components May be involved in the coordination of a diverse range of regulatory processes for ion transport and second messenger cascades Plays a role in maintaining normal plasma cholesterol levels
Pmvk	Involved in mevalonate pathway
Ptgir	Prostacyclin receptor
Rassf2	Potential tumor suppressor Acts as a KRAS-specific effector protein May promote apoptosis and cell cycle arrest
Rbbp9	May play a role in the transformation process
Scd1	ER enzyme Catalyzes rate-limiting step in formation of monounsaturated fatty acids
Slc25a35	Transmembrane transporter activity
Stat3	Transcription factor involved in interleukin 6 signaling
Tm7sf2	Involved in cholesterol biosynthesis
6430550D23Rik	-
A930033H14Rik	-

Apobec1	Essential component of the apolipoprotein B mRNA editing enzyme complex
Cav1	Mediates entry of calcium ions Involved in calcium-dependent processes (e.g. muscle contraction, cell motility, cell division and cell death)
Isoc1	Catalytic activity
Slc25a22	Involved in transport of glutamate across the inner mitochondrial membrane
Zfpm1	Transcription regulator Plays a role in erythroid and megakaryocytic cell differentiation

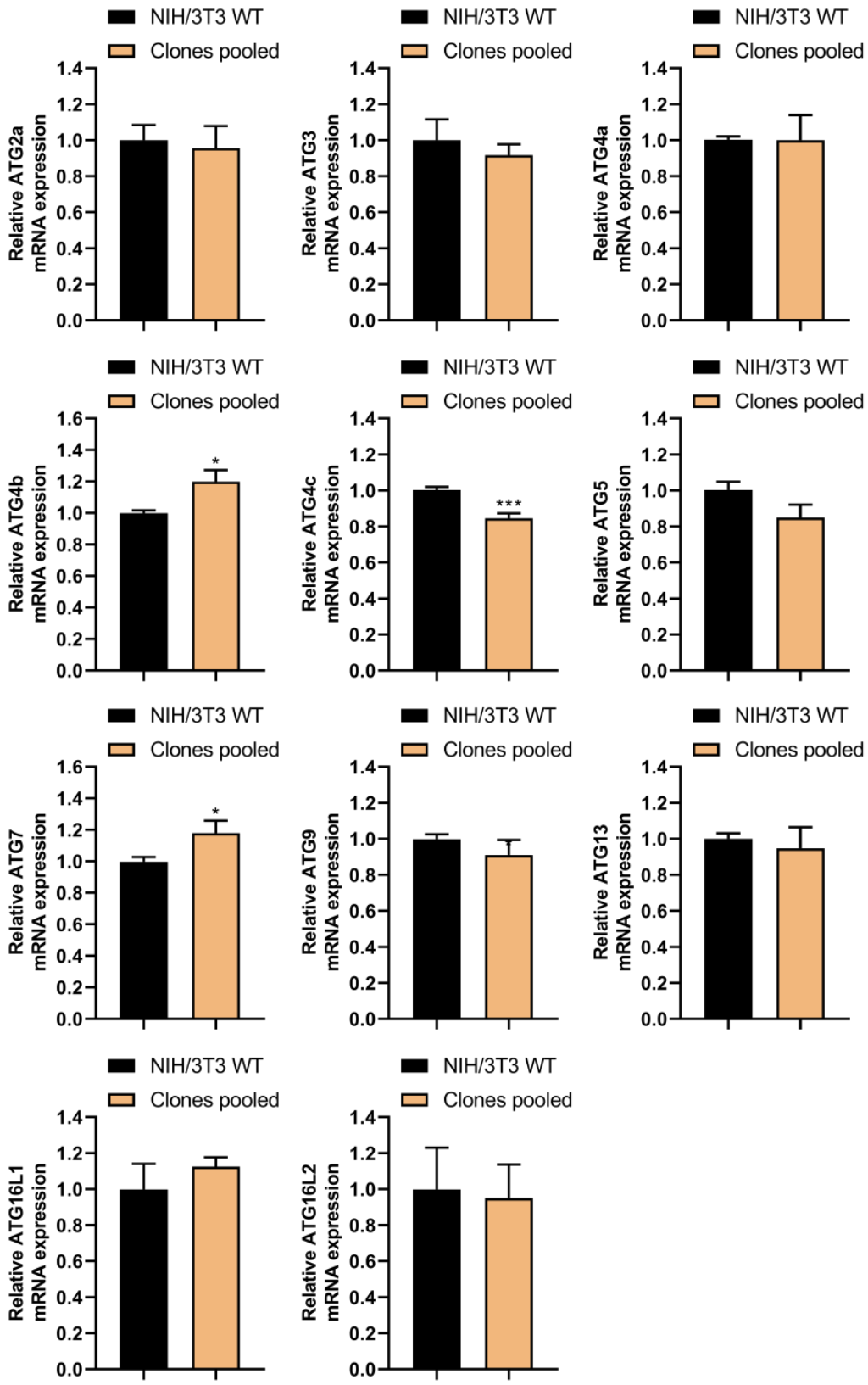

Figure 6.19: mRNA levels of various ATGs. Relative mRNA expression of ATG2a, ATG3, ATG4a, ATG4b, ATG4c, ATG5, ATG7, ATG9, ATG13, ATG16L1, and ATG16L2 in WT and WHAMM KO cells. Gene expression was assessed by microarray analysis and normalized to WT levels. Data are derived from one experiment. *P $\leq$ 0.05, ***P $\leq$ 0.001, Student's t-test. Error bars represent SEM.

DHCR7 and SOAT1 transcript levels in WHAMM KO cells were additionally determined by qPCR and are shown in Figure 6.20. qPCR was conducted with the help of Silvia Prettin (HZI, Braunschweig).

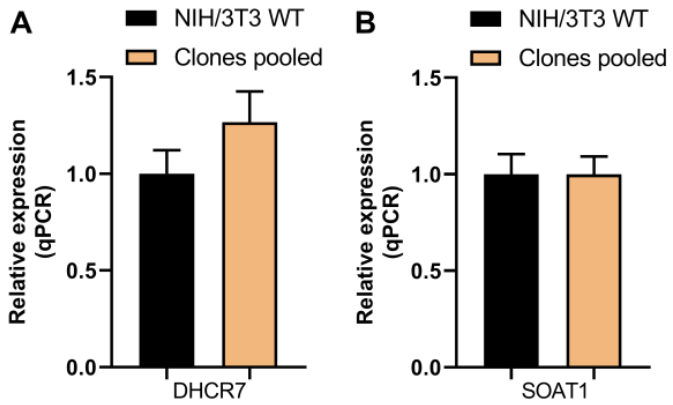

Figure 6.20: Transcription levels of *dhcr7* and *soat1* quantified by qPCR. (A-B) Target genes expressed in WT and WHAMM KO cells. The relative expression levels were normalized to the expression levels of *rps9*. Data are representative of three independent experiment. Error bars represent SEM.

KEGG pathway diagrams represent the relationships of genes or gene products in the pathway of steriod biosynthesis (Figure 6.21) and adhesion signaling (Figure 6.22).

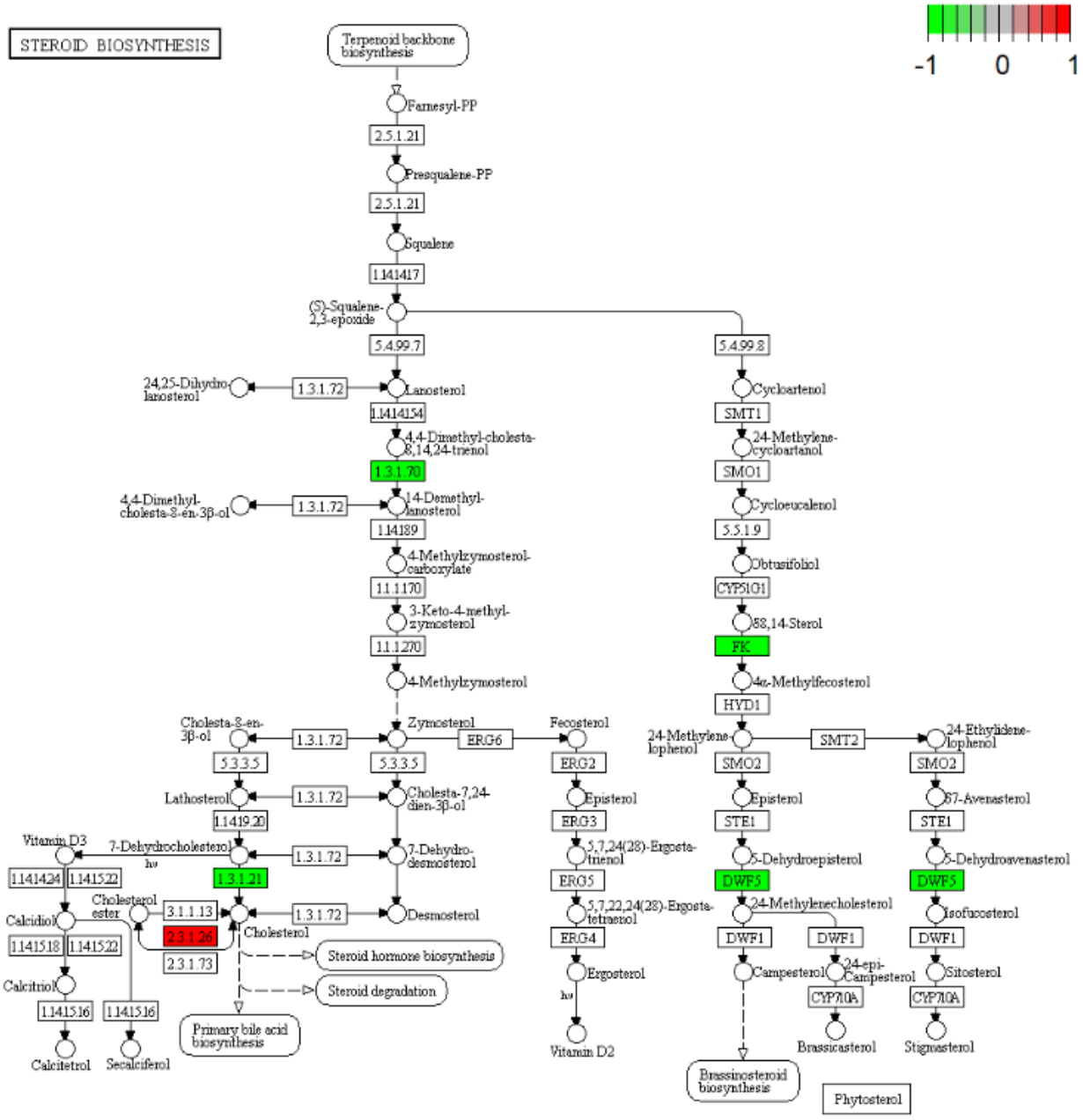

Figure 6.21: Impact of WHAMM KO on steriod biosynthesis. The pathway model was obtained from KEGG pathway. Red boxes indicate upregulated, whereas green boxes downregulated genes.

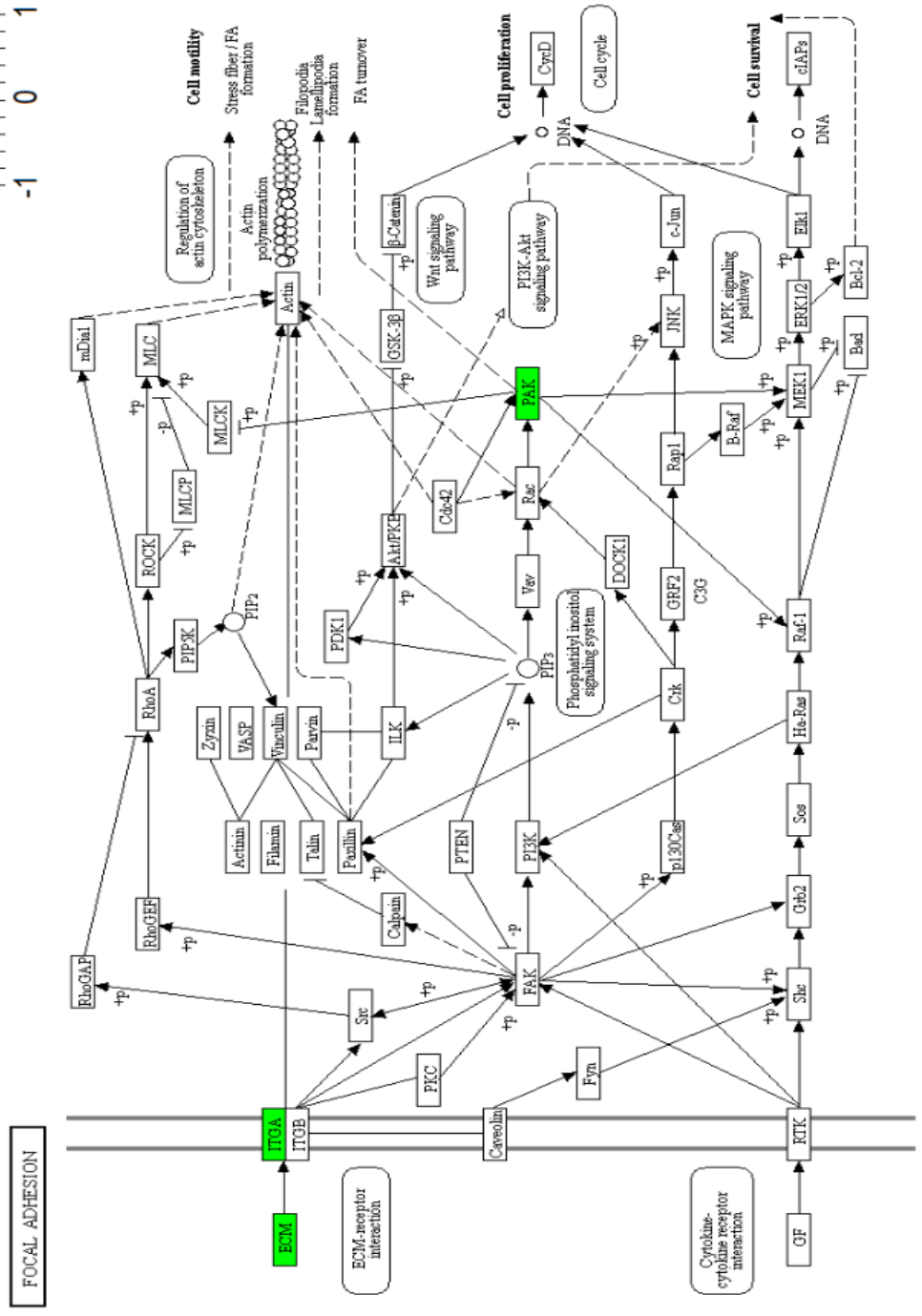

Figure 6.22: Impact of WHAMM KO on adhesion signaling. The pathway model was obtained from KEGG pathway. Green boxes indicate downregulated genes.

6.1.8 VSV and HSV-1 infection in WHAMM KO cells

Flow cytometry was utilized to assess the number of infected WT cells and one WHAMM KO clone. A GFP reporter was used to provide information about noninfected *versus* infected cells. Preliminary data showed that WHAMM#3 tends to be less susceptible to both VSV and HSV-1 compared to WT cells (Figures 6.23 and 6.24).

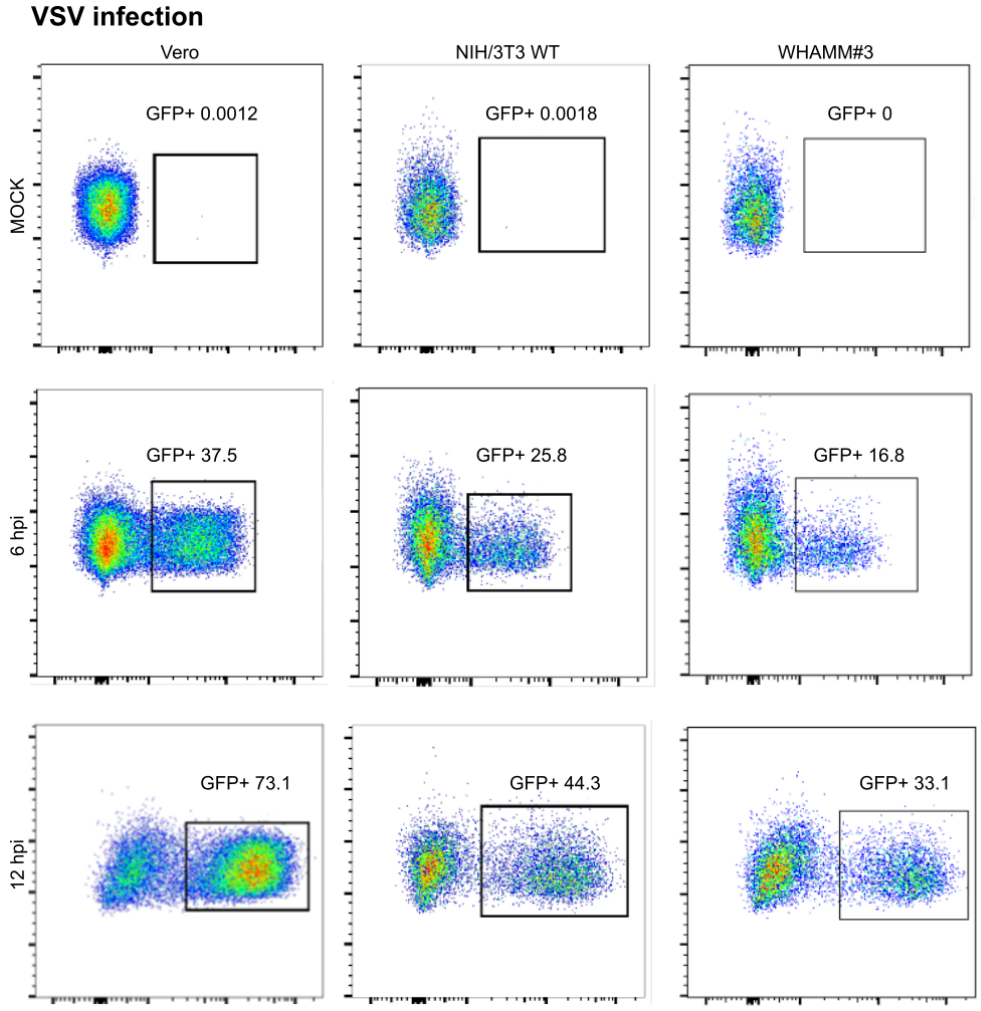

Figure 6.23: Flow cytometry analysis of WHAMM KO cells after VSV infection. Cells were seeded, infected with VSV and inspected after 6 and 12 hpi. GFP fluorescence provided a sensitive and accurate measure of the proportions of infected cells. The amount of cells infected is expressed as percentage. Mock infection was used as negative control. Vero cell line was utilized as infection control. Data are derived from one experiment.

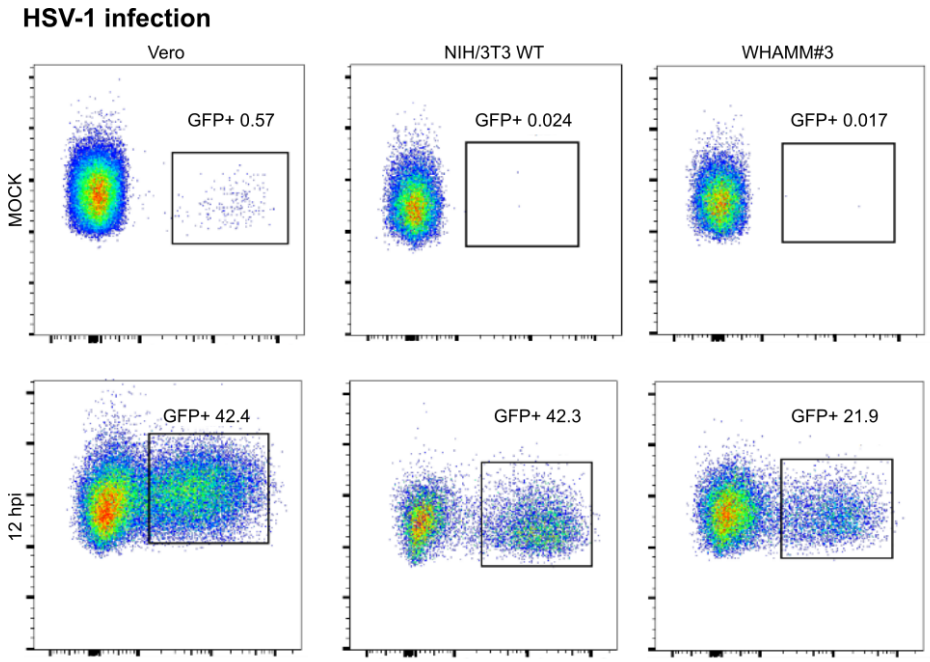

Figure 6.24: Flow cytometry analysis of WHAMM KO cells HSV-1 infection Cells were seeded, infected with HSV-1 and inspected after 12 hpi. GFP fluorescence provided a sensitive and accurate measure of the proportions of infected cells. The amount of cells infected is expressed as percentage. Mock infection was used as negative control. Vero cell line was utilized as infection control. Data are derived from one experiment.

References

[1] Julian Lewis Martin Raff Keith Roberts Bruce Alberts, Alexander Johnson and Peter Walter. *Molecular Biology of the Cell. 4th edition*. Garland Science, 2002.

[2] Markus Ladwein and Klemens Rottner. On the rho'd: The regulation of membrane protrusions by rho-GTPases. *FEBS Letters*, 582(14):2066–2074, apr 2008.

[3] M Welch E Goley. The arp2/3 complex: an actin nucleator comes of age. *Nature reviews. Molecular cell biology*, 2006.

[4] S. Dramsi and P. Cossart. Intracellular pathogens and the actin cytoskeleton. *Annual Review of Cell and Developmental Biology*, 14(1):137–166, nov 1998.

[5] W Gebhard W Kabsch KC Holmes, D Popp. Atomic model of the actin filament. *Nature*, 1990.

[6] M Hertzog E Frittoli Klemens Rottner G Scita A Disanza, Anika Steffen. Actin polymerization machinery: the finish line of signaling networks, the starting point of cellular movement. *Cell Mol Life Sci 62, 955-70*, 2005.

[7] S Lawrence Zipursky Paul Matsudaira David Baltimore James Darnell Harvey Lodish, Arnold Berk. *Molecular Cell Biology*. W. H. Freeman, 2000.

[8] Emile L. Boulpaep Walter F. Boron. *Medical Physiology*. Elsevier LTD, Oxford, 2016.

[9] A Wegner. Head to tail polymerization of actin. *J Mol Biol.*, 1976.

[10] Gary G Borisy Thomas D Pollard. Cellular motility driven by assembly and disassembly of actin filaments. *Cell*, 2003.

[11] L. Weston, A. S. Coutts, and N. B. La Thangue. Actin nucleators in the nucleus: an emerging theme. *Journal of Cell Science*, 125(15):3519–3527, aug 2012.

[12] Melissa A Chesarone and Bruce L Goode. Actin nucleation and elongation factors: mechanisms and interplay. *Current Opinion in Cell Biology*, 21(1):28–37, feb 2009.

[13] Michelle Peckham Anne Ridley and Peter Clark. *Cell Motility: From Molecules to Organisms (Life Sciences)*. Wiley, 2004.

[14] Dennis Breitsprecher and Bruce L. Goode. Formins at a glance. *Journal of Cell Science*, 126(1):1–7, jan 2013.

[15] Actin and actin-binding proteins. In *Cell Biology*, pages 575–591. Elsevier, 2017.

[16] Frieda Kage, Moritz Winterhoff, Vanessa Dimchev, Jan Mueller, Tobias Thalheim, Anika Freise, Stefan Brühmann, Jana Kollasser, Jennifer Block, Georgi Dimchev, Matthias Geyer, Hans-Joachim Schnittler, Cord Brakebusch, Theresia E. B. Stradal, Marie-France Carlier, Michael Sixt, Josef Käs, Jan Faix, and Klemens Rottner. FMNL formins boost lamellipodial force generation. *Nature Communications*, 8:14832, mar 2017.

[17] Roberto Dominguez. The WH2 domain and actin nucleation: Necessary but insufficient. *Trends in Biochemical Sciences*, 41(6):478–490, jun 2016.

[18] Klemens Rottner, Jan Hänisch, and Kenneth G. Campellone. WASH, WHAMM and JMY: regulation of arp2/3 complex and beyond. *Trends in Cell Biology*, 20(11):650–661, nov 2010.

[19] Olga Alekhina, Ezra Burstein, and Daniel D. Billadeau. Cellular functions of WASP family proteins at a glance. *Journal of Cell Science*, 130(14):2235–2241, jun 2017.

[20] Kenneth G. Campellone, Neil J. Webb, Elizabeth A. Znameroski, and Matthew D. Welch. WHAMM is an arp2/3 complex activator that binds microtubules and functions in ER to golgi transport. *Cell*, 134(1):148–161, jul 2008.

[21] Elena V. Linardopoulou, Sean S. Parghi, Cynthia Friedman, Gregory E. Osborn, Susan M. Parkhurst, and Barbara J. Trask. Human subtelomeric WASH genes encode a new subclass of the WASP family. *PLoS Genetics*, 3(12):e237, 2007.

[22] D. Jia, T. S. Gomez, Z. Metlagel, J. Umetani, Z. Otwinowski, M. K. Rosen, and D. D. Billadeau. WASH and WAVE actin regulators of the wiskott-aldrich syndrome protein (WASP) family are controlled by analogous structurally related complexes. *Proceedings of the National Academy of Sciences*, 107(23):10442–10447, may 2010.

[23] R. Liu, M. T. Abreu-Blanco, K. C. Barry, E. V. Linardopoulou, G. E. Osborn, and S. M. Parkhurst. Wash functions downstream of rho and links linear and branched actin nucleation factors. *Development*, 136(16):2849–2860, jul 2009.

[24] Timothy S. Gomez, Jacquelyn A. Gorman, Amaia Artal-Martinez de Narvajas, Alexander O. Koenig, and Daniel D. Billadeau. Trafficking defects in WASH-knockout fibroblasts originate from collapsed endosomal and lysosomal networks. *Molecular Biology of the Cell*, 23(16):3215–3228, aug 2012.

[25] Pengyan Xia, Shuo Wang, Ying Du, Zhenao Zhao, Lei Shi, Lei Sun, Guanling Huang, Buqing Ye, Chong Li, Zhonghua Dai, Ning Hou, Xuan Cheng, Qingyuan Sun, Lei Li, Xiao Yang, and Zusen Fan. WASH inhibits autophagy through suppression of beclin 1 ubiquitination. *The EMBO Journal*, 32(20):2685–2696, aug 2013.

[26] Benedikt M. Nagel, Meike Bechtold, Luis Garcia Rodriguez, and Sven Bogdan. DrosophilaWASH is required for integrin-mediated cell adhesion, cell motility and lysosomal neutralization. *Journal of Cell Science*, 130(2):344–359, nov 2016.

[27] Alison M Elliott, Louise R Simard, Gail Coghlan, Albert E Chudley, Bernard N Chodirker, Cheryl R Greenberg, Tanya Burch, Valentina Ly, Grant M Hatch, and Teresa Zelinski. A novel mutation inKIAA0196: identification of a gene involved in ritscher–schinzel/3c syndrome in a first nations cohort. *Journal of Medical Genetics*, 50(12):819–822, sep 2013.

[28] F. Ropers, E. Derivery, H. Hu, M. Garshasbi, M. Karbasiyan, M. Herold, G. Nurnberg, R. Ullmann, A. Gautreau, K. Sperling, R. Varon, and A. Rajab. Identification of a novel candidate gene for non-syndromic autosomal recessive intellectual disability: the WASH complex member SWIP. *Human Molecular Genetics*, 20(13):2585–2590, apr 2011.

[29] Paul N. Valdmanis, Inge A. Meijer, Annie Reynolds, Adrienne Lei, Patrick MacLeod, David Schlesinger, Mayana Zatz, Evan Reid, Patrick A. Dion, Pierre Drapeau, and Guy A. Rouleau. Mutations in the KIAA0196 gene at the SPG8 locus cause hereditary spastic paraplegia. *The American Journal of Human Genetics*, 80(1):152–161, jan 2007.

[30] Emmanuel Derivery, Carla Sousa, Jérémie J. Gautier, Bérangère Lombard, Damarys Loew, and Alexis Gautreau. The arp2/3 activator WASH controls the fission of endosomes through a large multiprotein complex. *Developmental Cell*, 17(5):712–723, nov 2009.

[31] Steve N. Duleh and Matthew D. Welch. WASH and the arp2/3 complex regulate endosome shape and trafficking. *Cytoskeleton*, pages NA–NA, 2010.

[32] Michael Carnell, Tobias Zech, Simon D. Calaminus, Seiji Ura, Monica Hagedorn, Simon A. Johnston, Robin C. May, Thierry Soldati, Laura M. Machesky, and Robert H. Insall. Actin polymerization driven by WASH causes v-ATPase retrieval and vesicle neutralization before exocytosis. *The Journal of Cell Biology*, 193(5):831–839, may 2011.

[33] Catherine M. Buckley, Navin Gopaldass, Cristina Bosmani, Simon A. Johnston, Thierry Soldati, Robert H. Insall, and Jason S. King. WASH drives early recycling from macropinosomes and phagosomes to maintain surface phagocytic receptors. *Proceedings of the National Academy of Sciences*, 113(40):E5906–E5915, sep 2016.

[34] Da Jia, Timothy S. Gomez, Daniel D. Billadeau, and Michael K. Rosen. Multiple repeat elements within the FAM21 tail link the WASH actin regulatory complex to the retromer. *Molecular Biology of the Cell*, 23(12):2352–2361, jun 2012.

[35] Ian J. McGough, Florian Steinberg, Da Jia, Peter A. Barbuti, Kirsty J. McMillan, Kate J. Heesom, Alan L. Whone, Maeve A. Caldwell, Daniel D. Billadeau, Michael K. Rosen, and Peter J. Cullen. Retromer binding to FAM21 and the WASH complex is perturbed by the parkinson disease-linked VPS35(d620n) mutation. *Current Biology*, 24(14):1670–1676, jul 2014.

[36] Eszter Zavodszky, Matthew N.J. Seaman, Kevin Moreau, Maria Jimenez-Sanchez, Sophia Y. Breusegem, Michael E. Harbour, and David C. Rubinsztein. Mutation in VPS35 associated with parkinson's disease impairs WASH complex association and inhibits autophagy. *Nature Communications*, 5(1), may 2014.

[37] Valentina Marchesin, Antonio Castro-Castro, Catalina Lodillinsky, Alessia Castagnino, Joanna Cyrta, Hélène Bonsang-Kitzis, Laetitia Fuhrmann, Marie Irondelle, Elvira Infante, Guillaume Montagnac, Fabien Reyal, Anne Vincent-Salomon, and Philippe Chavrier. ARF6–JIP3/4 regulate endosomal tubules for MT1-MMP exocytosis in cancer invasion. *The Journal of Cell Biology*, 211(2):339–358, oct 2015.

[38] Ashley A. Rowland, Patrick J. Chitwood, Melissa J. Phillips, and Gia K. Voeltz. ER contact sites define the position and timing of endosome fission. *Cell*, 159(5):1027–1041, nov 2014.

[39] Rui Dong, Yasunori Saheki, Sharan Swarup, Louise Lucast, J. Wade Harper, and Pietro De Camilli. Endosome-ER contacts control actin nucleation and retromer

function through VAP-dependent regulation of PI4p. *Cell*, 166(2):408–423, jul 2016.

[40] Rachel Allison, James R. Edgar, Guy Pearson, Tania Rizo, Timothy Newton, Sven Günther, Fiamma Berner, Jennifer Hague, James W. Connell, Jürgen Winkler, Jennifer Lippincott-Schwartz, Christian Beetz, Beate Winner, and Evan Reid. Defects in ER–endosome contacts impact lysosome function in hereditary spastic paraplegia. *The Journal of Cell Biology*, 216(5):1337–1355, apr 2017.

[41] Annica K. B. Gad, Vishal Nehru, Aino Ruusala, and Pontus Aspenström. RhoD regulates cytoskeletal dynamics via the actin nucleation–promoting factor WASp homologue associated with actin golgi membranes and microtubules. *Molecular Biology of the Cell*, 23(24):4807–4819, dec 2012.

[42] Ashley J. Russo, Alyssa J. Mathiowetz, Steven Hong, Matthew D. Welch, and Kenneth G. Campellone. Rab1 recruits WHAMM during membrane remodeling but limits actin nucleation. *Molecular Biology of the Cell*, 27(6):967–978, mar 2016.

[43] Qing-Tao Shen, Peter P. Hsiue, Charles V. Sindelar, Matthew D. Welch, Kenneth G. Campellone, and Hong-Wei Wang. Structural insights into WHAMM-mediated cytoskeletal coordination during membrane remodeling. *The Journal of Cell Biology*, 199(1):111–124, oct 2012.

[44] David J. Kast, Allison L. Zajac, Erika L.F. Holzbaur, E. Michael Ostap, and Roberto Dominguez. WHAMM directs the arp2/3 complex to the ER for autophagosome biogenesis through an actin comet tail mechanism. *Current Biology*, 25(13):1791–1797, jun 2015.

[45] Alyssa J. Mathiowetz, Emma Baple, Ashley J. Russo, Alyssa M. Coulter, Eric Carrano, Judith D. Brown, Robert N. Jinks, Andrew H. Crosby, and Kenneth G. Campellone. An amish founder mutation disrupts a PI(3)p-WHAMM-arp2/3 complex–driven autophagosomal remodeling pathway. *Molecular Biology of the Cell*, 28(19):2492–2507, sep 2017.

[46] J. Bradley Zuchero, Amanda S. Coutts, Margot E. Quinlan, Nicholas B. La Thangue, and R. Dyche Mullins. p53-cofactor JMY is a multifunctional actin nucleation factor. *Nature Cell Biology*, 11(4):451–459, mar 2009.

[47] Kai Schlüter, Dieter Waschbüsch, Moritz Anft, Debbie Hügging, Sabine Kind, Jan Hänisch, Goran Lakisic, Alexis Gautreau, Angelika Barnekow, and Theresia E.B. Stradal. JMY is involved in anterograde vesicle trafficking from the trans-golgi network. *European Journal of Cell Biology*, 93(5-6):194–204, may 2014.

[48] Noriko Shikama, Chang-Woo Lee, Stephen France, Laurent Delavaine, Jonathan Lyon, Marija Krstic-Demonacos, and Nicholas B La Thangue. A novel cofactor for p300 that regulates the p53 response. *Molecular Cell*, 4(3):365–376, sep 1999.

[49] A. S. Coutts, L. Weston, and N. B. La Thangue. A transcription co-factor integrates cell adhesion and motility with the p53 response. *Proceedings of the National Academy of Sciences*, 106(47):19872–19877, nov 2009.

[50] J. Bradley Zuchero, Brittany Belin, and R. Dyche Mullins. Actin binding to WH2 domains regulates nuclear import of the multifunctional actin regulator JMY. *Molecular Biology of the Cell*, 23(5):853–863, mar 2012.

[51] Punsiri M. Colonne, Caylin G. Winchell, and Daniel E. Voth. Hijacking host cell highways: Manipulation of the host actin cytoskeleton by obligate intracellular bacterial pathogens. *Frontiers in Cellular and Infection Microbiology*, 6, sep 2016.

[52] Klemens Rottner, Theresia E.B. Stradal, and Juergen Wehland. Bacteria-host-cell interactions at the plasma membrane: Stories on actin cytoskeleton subversion. *Developmental Cell*, 9(1):3–17, jul 2005.

[53] Theresia E.B. Stradal, Klemens Rottner, Andrea Disanza, Stefano Confalonieri, Metello Innocenti, and Giorgio Scita. Regulation of actin dynamics by WASP and WAVE family proteins. *Trends in Cell Biology*, 14(6):303–311, jun 2004.

[54] Cristián A Quintero, Julián Gambarte Tudela, and María T Damiani. Rho GTPases as pathogen targets: Focus on curable sexually transmitted infections. *Small GTPases*, 6(2):108–118, apr 2015.

[55] Joana N. Bugalhão, Luís Jaime Mota, and Irina S. Franco. Bacterial nucleators: actin' on actin. *Pathogens and Disease*, 73(9):ftv078, sep 2015.

[56] Marlies Galle, Isabelle Carpentier, and Rudi Beyaert. Structure and function of the type III secretion system of pseudomonas aeruginosa. *Current Protein and Peptide Science*, 13(8):831–842, dec 2012.

[57] C. V. Srikanth, Regino Mercado-Lubo, Kelly Hallstrom, and Beth A. McCormick. Salmonella effector proteins and host-cell responses. *Cellular and Molecular Life Sciences*, 68(22):3687–3697, oct 2011.

[58] Fernando Navarro-Garcia, Antonio Serapio-Palacios, Paul Ugalde-Silva, Gabriela Tapia-Pastrana, and Lucia Chavez-Dueñas. Actin cytoskeleton manipulation by effector proteins secreted by DiarrheagenicEscherichia coliPathotypes. *BioMed Research International*, 2013:1–22, 2013.

[59] Matthew P. Taylor, Orkide O. Koyuncu, and Lynn W. Enquist. Subversion of the actin cytoskeleton during viral infection. *Nature Reviews Microbiology*, 9(6):427–439, apr 2011.

[60] Erwin Fleissner and Ellen Tress. Chromatographic and electrophoretic analysis of viral proteins from hamster and chicken cells transformed by rous sarcoma virus. *Journal of Virology*, 1973.

[61] N. S. McNutt. Contact-inhibited revertant cell lines isolated from sv 40-transformed cells. iv. microfilament distribution and cell shape in untransformed, transformed, and revertant balb-c 3t3 cells. *The Journal of Cell Biology*, 56(2):412–428, feb 1973.

[62] R. D. Goldman, C. Chang, and J. F. Williams. Properties and behavior of hamster embryo cells transformed by human adenovirus type 5. *Cold Spring Harbor Symposia on Quantitative Biology*, 39(0):601–614, jan 1974.

[63] Shadi Shahriari, James Gordon, and Reena Ghildyal. Host cytoskeleton in respiratory syncytial virus assembly and budding. *Virology Journal*, 13(1), sep 2016.

[64] V. Nunbhakdi-Craig, L. Craig, T. Machleidt, and E. Sontag. Simian virus 40 small tumor antigen induces deregulation of the actin cytoskeleton and tight junctions in kidney epithelial cells. *Journal of Virology*, 77(5):2807–2818, mar 2003.

[65] M. G. Lyman and L. W. Enquist. Herpesvirus interactions with the host cytoskeleton. *Journal of Virology*, 83(5):2058–2066, oct 2008.

[66] Danielle Glick, Sandra Barth, and Kay F. Macleod. Autophagy: cellular and molecular mechanisms. *The Journal of Pathology*, 221(1):3–12, feb 2010.

[67] B. Ravikumar, M. Futter, L. Jahreiss, V. I. Korolchuk, M. Lichtenberg, S. Luo, D. C. O. Massey, F. M. Menzies, U. Narayanan, M. Renna, M. Jimenez-Sanchez, S. Sarkar, B. Underwood, A. Winslow, and D. C. Rubinsztein. Mammalian macroautophagy at a glance. *Journal of Cell Science*, 122(11):1707–1711, may 2009.

[68] Katherine R. Parzych and Daniel J. Klionsky. An overview of autophagy: Morphology, mechanism, and regulation. *Antioxidants & Redox Signaling*, 20(3):460–473, jan 2014.

[69] Yuchen Feng, Ding He, Zhiyuan Yao, and Daniel J Klionsky. The machinery of macroautophagy. *Cell Research*, 24(1):24–41, dec 2013.

[70] Maryam Mehrpour, Audrey Esclatine, Isabelle Beau, and Patrice Codogno. Overview of macroautophagy regulation in mammalian cells. *Cell Research*, 20(7):748–762, jun 2010.

[71] E. Bejarano and A. M. Cuervo. Chaperone-mediated autophagy. *Proceedings of the American Thoracic Society*, 7(1):29–39, feb 2010.

[72] Kadija Abounit, Tiziano M Scarabelli, and Roy B McCauley. Autophagy in mammalian cells. *World Journal of Biological Chemistry*, 3(1):1, 2012.

[73] Eisuke Itakura, Chieko Kishi, Kinji Inoue, and Noboru Mizushima. Beclin 1 forms two distinct phosphatidylinositol 3-kinase complexes with mammalian atg14 and UVRAG. *Molecular Biology of the Cell*, 19(12):5360–5372, dec 2008.

[74] Mitsuko Hayashi-Nishino, Naonobu Fujita, Takeshi Noda, Akihito Yamaguchi, Tamotsu Yoshimori, and Akitsugu Yamamoto. A subdomain of the endoplasmic reticulum forms a cradle for autophagosome formation. *Nature Cell Biology*, 11(12):1433–1437, nov 2009.

[75] Simon McGurk. The molecular biology of cancer: A bridge from bench to bedside – second edition the molecular biology of cancer: A bridge from bench to bedside – second edition. *Nursing Standard*, 28(1):30–30, sep 2013.

[76] David J. Kast and Roberto Dominguez. The cytoskeleton–autophagy connection. *Current Biology*, 27(8):R318–R326, apr 2017.

[77] Carol A. Mercer, Alagammai Kaliappan, and Patrick B. Dennis. A novel, human atg13 binding protein, atg101, interacts with ULK1 and is essential for macroautophagy. *Autophagy*, 5(5):649–662, jul 2009.

[78] Hong-Gang Wang, editor. *Autophagy and Cancer*. Springer New York, 2013.

[79] N. Jaber, Z. Dou, J.-S. Chen, J. Catanzaro, Y.-P. Jiang, L. M. Ballou, E. Selinger, X. Ouyang, R. Z. Lin, J. Zhang, and W.-X. Zong. Class III PI3k vps34 plays an essential role in autophagy and in heart and liver function. *Proceedings of the National Academy of Sciences*, 109(6):2003–2008, jan 2012.

[80] You-Kyung Lee and Jin-A Lee. Role of the mammalian ATG8/LC3 family in autophagy: differential and compensatory roles in the spatiotemporal regulation of autophagy. *BMB Reports*, 49(8):424–430, aug 2016.

[81] Yuchen Feng and Daniel J Klionsky. Autophagic membrane delivery through ATG9. *Cell Research*, 27(2):161–162, jan 2017.

[82] A. R. J. Young. Starvation and ULK1-dependent cycling of mammalian atg9 between the TGN and endosomes. *Journal of Cell Science*, 119(18):3888–3900, aug 2006.

[83] Milton Osmar Aguilera, Walter Berón, and María Isabel Colombo. The actin cytoskeleton participates in the early events of autophagosome formation upon starvation induced autophagy. *Autophagy*, 8(11):1590–1603, nov 2012.

[84] Pengyan Xia, Shuo Wang, Guanling Huang, Ying Du, Pingping Zhu, Man Li, and Zusen Fan. RNF2 is recruited by WASH to ubiquitinate AMBRA1 leading to downregulation of autophagy. *Cell Research*, 24(8):943–958, jul 2014.

[85] Amanda S. Coutts and Nicholas B. La Thangue. Actin nucleation by WH2 domains at the autophagosome. *Nature Communications*, 6(1), jul 2015.

[86] Anna Chiara Nascimbeni, Patrice Codogno, and Etienne Morel. Phosphatidylinositol-3-phosphate in the regulation of autophagy membrane dynamics. *The FEBS Journal*, 284(9):1267–1278, jan 2017.

[87] Devashish Rath, Lina Amlinger, Archana Rath, and Magnus Lundgren. The CRISPR-cas immune system: Biology, mechanisms and applications. *Biochimie*, 117:119–128, oct 2015.

[88] Rodolphe Barrangou and Luciano A. Marraffini. CRISPR-cas systems: Prokaryotes upgrade to adaptive immunity. *Molecular Cell*, 54(2):234–244, apr 2014.

[89] F Ann Ran, Patrick D Hsu, Jason Wright, Vineeta Agarwala, David A Scott, and Feng Zhang. Genome engineering using the CRISPR-cas9 system. *Nature Protocols*, 8(11):2281–2308, oct 2013.

[90] Joseph Sambrook Tom Maniatis, E. F. Fritsch. *Molecular Cloning: A Laboratory Manual*. Cold Spring Harbor Laboratory, 1982.

[91] Elizabeth L. Axe, Simon A. Walker, Maria Manifava, Priya Chandra, H. Llewelyn Roderick, Anja Habermann, Gareth Griffiths, and Nicholas T. Ktistakis. Autophagosome formation from membrane compartments enriched in phosphatidylinositol 3-phosphate and dynamically connected to the endoplasmic reticulum. *The Journal of Cell Biology*, 182(4):685–701, aug 2008.

[92] H. Ben-Tekaya. Live imaging of bidirectional traffic from the ERGIC. *Journal of Cell Science*, 118(2):357–367, jan 2005.

[93] Kai Er Eng, Marc D. Panas, Gunilla B. Karlsson Hedestam, and Gerald M. McInerney. A novel quantitative flow cytometry-based assay for autophagy. *Autophagy*, 6(5):634–641, jul 2010.

[94] Pascale Cossart. Actin-based motility of pathogens: the arp2/3 complex is a central player. microreview. *Cellular Microbiology*, 2(3):195–205, jun 2000.

[95] Ju Huang and John H. Brumell. Bacteria–autophagy interplay: a battle for survival. *Nature Reviews Microbiology*, 12(2):101–114, jan 2014.

[96] G. Galea, M. G. Bexiga, A. Panarella, E. D. O'Neill, and J. C. Simpson. A high-content screening microscopy approach to dissect the role of rab proteins in golgi-to-ER retrograde trafficking. *Journal of Cell Science*, 128(13):2339–2349, may 2015.

[97] Iryna Monastyrska and Daniel J. Klionsky. Autophagy in organelle homeostasis: Peroxisome turnover. *Molecular Aspects of Medicine*, 27(5-6):483–494, oct 2006.

[98] Fulvio Reggiori and Sharon A. Tooze. Autophagy regulation through atg9 traffic: Figure 1. *The Journal of Cell Biology*, 198(2):151–153, jul 2012.

[99] Noboru Mizushima, Tamotsu Yoshimori, and Beth Levine. Methods in mammalian autophagy research. *Cell*, 140(3):313–326, feb 2010.

[100] Tor Erik Rusten and Harald Stenmark. p62, an autophagy hero or culprit? *Nature Cell Biology*, 12(3):207–209, mar 2010.

[101] Victoria Cohen-Kaplan, Aaron Ciechanover, and Ido Livneh. p62 at the crossroad of the ubiquitin-proteasome system and autophagy. *Oncotarget*, 7(51), dec 2016.

[102] Geir Bjørkøy, Trond Lamark, Serhiy Pankiv, Aud Øvervatn, Andreas Brech, and Terje Johansen. Chapter 12 monitoring autophagic degradation of p62/SQSTM1. In *Methods in Enzymology*, pages 181–197. Elsevier, 2009.

[103] Zhonghua Gao, Noor Gammoh, Pui-Mun Wong, Hediye Erdjument-Bromage, Paul Tempst, and Xuejun Jiang. Processing of autophagic protein LC3 by the 20s proteasome. *Autophagy*, 6(1):126–137, jan 2010.

[104] M. L. Seibenhener, J. R. Babu, T. Geetha, H. C. Wong, N. R. Krishna, and M. W. Wooten. Sequestosome 1/p62 is a polyubiquitin chain binding protein involved in ubiquitin proteasome degradation. *Molecular and Cellular Biology*, 24(18):8055–8068, aug 2004.

[105] Nina Raben, Lauren Shea, Victoria Hill, and Paul Plotz. Chapter 21 monitoring autophagy in lysosomal storage disorders. In *Autophagy in Disease and Clinical Applications, Part C*, pages 417–449. Elsevier, 2009.

[106] O. G. Ramprasad, G. Srinivas, K. Sridhar Rao, Powrnima Joshi, Jean Paul Thiery, Sylvie Dufour, and Gopal Pande. Changes in cholesterol levels in the plasma membrane modulate cell signaling and regulate cell adhesion and migration on fibronectin. *Cell Motility and the Cytoskeleton*, 64(3):199–216, mar 2007.

[107] T. S. van Zanten, A. Cambi, M. Koopman, B. Joosten, C. G. Figdor, and M. F. Garcia-Parajo. Hotspots of GPI-anchored proteins and integrin nanoclusters function as nucleation sites for cell adhesion. *Proceedings of the National Academy of Sciences*, 106(44):18557–18562, oct 2009.

[108] Bharat Jaishy and E. Dale Abel. Lipids, lysosomes, and autophagy. *Journal of Lipid Research*, 57(9):1619–1635, jun 2016.

[109] Claudia Dall'Armi, Kelly A. Devereaux, and Gilbert Di Paolo. The role of lipids in the control of autophagy. *Current Biology*, 23(1):R33–R45, jan 2013.

[110] Elina Ikonen. Cellular cholesterol trafficking and compartmentalization. *Nature Reviews Molecular Cell Biology*, 9(2):125–138, feb 2008.

[111] Jinglei Cheng, Yuki Ohsaki, Kumi Tauchi-Sato, Akikazu Fujita, and Toyoshi Fujimoto. Cholesterol depletion induces autophagy. *Biochemical and Biophysical Research Communications*, 351(1):246–252, dec 2006.

[112] Mireille Ouimet, Vivian Franklin, Esther Mak, Xianghai Liao, Ira Tabas, and Yves L. Marcel. Autophagy regulates cholesterol efflux from macrophage foam cells via lysosomal acid lipase. *Cell Metabolism*, 13(6):655–667, jun 2011.

[113] Ismail Sergin and Babak Razani. Self-eating in the plaque: what macrophage autophagy reveals about atherosclerosis. *Trends in Endocrinology & Metabolism*, 25(5):225–234, may 2014.

[114] Frederick R. Maxfield and Daniel Wüstner. Analysis of cholesterol trafficking with fluorescent probes. In *Methods in Cell Biology*, pages 367–393. Elsevier, 2012.

[115] Mark Spear and Yuntao Wu. Viral exploitation of actin: force-generation and scaffolding functions in viral infection. *Virologica Sinica*, 29(3):139–147, jun 2014.

[116] David K. Cureton, Ramiro H. Massol, Saveez Saffarian, Tomas L. Kirchhausen, and Sean P. J. Whelan. Vesicular stomatitis virus enters cells through vesicles incompletely coated with clathrin that depend upon actin for internalization. *PLoS Pathogens*, 5(4):e1000394, apr 2009.

[117] Xiaohua Hu and R. Dyche Mullins. LC3 and STRAP regulate actin filament assembly by JMY during autophagosome formation. *The Journal of Cell Biology*, page jcb.201802157, nov 2018.

[118] A Janssen and R H Medema. Genetic instability: tipping the balance. *Oncogene*, 32(38):4459–4470, dec 2012.

[119] Pingsu Mao, Jingfan Liu, Zepeng Zhang, Hong Zhang, Haiying Liu, Song Gao, Yikang S. Rong, and Yong Zhao. Homologous recombination-dependent repair of telomeric DSBs in proliferating human cells. *Nature Communications*, 7(1), jul 2016.

[120] María A. Blasco. The epigenetic regulation of mammalian telomeres. *Nature Reviews Genetics*, 8(4):299–309, apr 2007.

[121] Sebald AN Verkuijl and Marianne G Rots. The influence of eukaryotic chromatin state on CRISPR–cas9 editing efficiencies. *Current Opinion in Biotechnology*, 55:68–73, feb 2019.

[122] Deepa Jaganathan, Karthikeyan Ramasamy, Gothandapani Sellamuthu, Shilpha Jayabalan, and Gayatri Venkataraman. CRISPR for crop improvement: An update review. *Frontiers in Plant Science*, 9, jul 2018.

[123] Prashant Mali, John Aach, P Benjamin Stranges, Kevin M Esvelt, Mark Moosburner, Sriram Kosuri, Luhan Yang, and George M Church. CAS9 transcriptional activators for target specificity screening and paired nickases for cooperative genome engineering. *Nature Biotechnology*, 31(9):833–838, aug 2013.

[124] John P Guilinger, David B Thompson, and David R Liu. Fusion of catalytically inactive cas9 to FokI nuclease improves the specificity of genome modification. *Nature Biotechnology*, 32(6):577–582, apr 2014.

[125] Ciaran M Lee, Thomas J Cradick, and Gang Bao. The neisseria meningitidis CRISPR-cas9 system enables specific genome editing in mammalian cells. *Molecular Therapy*, 24(3):645–654, mar 2016.

[126] Atsushi Satomura, Ryosuke Nishioka, Hitoshi Mori, Kosuke Sato, Kouichi Kuroda, and Mitsuyoshi Ueda. Precise genome-wide base editing by the CRISPR nickase system in yeast. *Scientific Reports*, 7(1), may 2017.

[127] Dmitry Y. Guschin, Adam J. Waite, George E. Katibah, Jeffrey C. Miller, Michael C. Holmes, and Edward J. Rebar. A rapid and general assay for monitoring endogenous gene modification. In *Methods in Molecular Biology*, pages 247–256. Humana Press, 2010.

[128] F. Ann Ran, Patrick D. Hsu, Chie-Yu Lin, Jonathan S. Gootenberg, Silvana Konermann, Alexandro E. Trevino, David A. Scott, Azusa Inoue, Shogo Matoba, Yi Zhang, and Feng Zhang. Double nicking by RNA-guided CRISPR cas9 for enhanced genome editing specificity. *Cell*, 154(6):1380–1389, sep 2013.

[129] Haoyi Wang, Hui Yang, Chikdu S. Shivalila, Meelad M. Dawlaty, Albert W. Cheng, Feng Zhang, and Rudolf Jaenisch. One-step generation of mice carrying mutations in multiple genes by CRISPR/cas-mediated genome engineering. *Cell*, 153(4):910–918, may 2013.

[130] Peter Qiu, Harini Shandilya, James M. D'Alessio, Kevin O'Connor, Jeffrey Durocher, and Gary F. Gerard. Mutation detection using surveyor™ nuclease. *BioTechniques*, 36(4):702–707, apr 2004.

[131] T. CAVALIER-SMITH. Economy, speed and size matter: Evolutionary forces driving nuclear genome miniaturization and expansion. *Annals of Botany*, 95(1):147–175, jan 2005.

[132] T.R. Gregory. Genome size evolution in animals. *The Evolution of the Genome*, 2005.

[133] Frank R. Neumann and Paul Nurse. Nuclear size control in fission yeast. *The Journal of Cell Biology*, 179(4):593–600, nov 2007.

[134] J. Curlej and P. Chrenek. Evaluation of chromosomal aneuploidy in mouse fibroblasts of two different cell lines cd1 and nih-3t3. *Slovak Journal of Animal Science, Vol 45 No 3*, 2012.

[135] M. Webster, K. L. Witkin, and O. Cohen-Fix. Sizing up the nucleus: nuclear shape, size and nuclear-envelope assembly. *Journal of Cell Science*, 122(10):1477–1486, may 2009.

[136] Jeffrey M. Verboon, Hector Rincon-Arano, Timothy R. Werwie, Jeffrey J. Delrow, David Scalzo, Vivek Nandakumar, Mark Groudine, and Susan M. Parkhurst. Wash interacts with lamin and affects global nuclear organization. *Current Biology*, 25(6):804–810, mar 2015.

[137] Zi Li LIN, Xiang-Shun CUI, Suk NAMGOONG, and Nam-Hyung KIM. Junction-mediating and regulatory protein (JMY) is essential for early porcine embryonic development. *Journal of Reproduction and Development*, 61(5):361–367, 2015.

[138] Jakub Cibulka, Martin Fraiberk, and Jitka Forstova. Nuclear actin and lamins in viral infections. *Viruses*, 4(3):325–347, feb 2012.

[139] Karen Tumaneng, Ryan C. Russell, and Kun-Liang Guan. Organ size control by hippo and TOR pathways. *Current Biology*, 22(9):R368–R379, may 2012.

[140] Étienne Audet-Walsh, Catherine R. Dufour, Tracey Yee, Fatima Z. Zouanat, Ming Yan, Georges Kalloghlian, Mathieu Vernier, Maxime Caron, Guillaume Bourque, Eleonora Scarlata, Lucie Hamel, Fadi Brimo, Armen G. Aprikian, Jacques Lapointe, Simone Chevalier, and Vincent Giguère. Nuclear mTOR acts as a transcriptional integrator of the androgen signaling pathway in prostate cancer. *Genes & Development*, 31(12):1228–1242, jun 2017.

[141] D. C. Fingar. Mammalian cell size is controlled by mTOR and its downstream targets s6k1 and 4ebp1/eIF4e. *Genes & Development*, 16(12):1472–1487, jun 2002.

[142] Amal Houssaini, Marielle Breau, Kanny Kebe, Shariq Abid, Elisabeth Marcos, Larissa Lipskaia, Dominique Rideau, Aurelien Parpaleix, Jin Huang, Valerie Amsellem, Nora Vienney, Pierre Validire, Bernard Maitre, Aya Attwe, Christina Lukas, David Vindrieux, Jorge Boczkowski, Genevieve Derumeaux, Mario Pende, David Bernard, Silke Meiners, and Serge Adnot. mTOR pathway activation drives lung cell senescence and emphysema. *JCI Insight*, 3(3), feb 2018.

[143] Damien Cuvelier, Manuel Théry, Yeh-Shiu Chu, Sylvie Dufour, Jean-Paul Thiéry, Michel Bornens, Pierre Nassoy, and L. Mahadevan. The universal dynamics of cell spreading. *Current Biology*, 17(8):694–699, apr 2007.

[144] Elisabetta Ada Cavalcanti-Adam, Tova Volberg, Alexandre Micoulet, Horst Kessler, Benjamin Geiger, and Joachim Pius Spatz. Cell spreading and focal adhesion dynamics are regulated by spacing of integrin ligands. *Biophysical Journal*, 92(8):2964–2974, apr 2007.

[145] Benjamin Geiger, Joachim P. Spatz, and Alexander D. Bershadsky. Environmental sensing through focal adhesions. *Nature Reviews Molecular Cell Biology*, 10(1):21–33, jan 2009.

[146] Michele A Wozniak, Katarzyna Modzelewska, Lina Kwong, and Patricia J Keely. Focal adhesion regulation of cell behavior. *Biochimica et Biophysica Acta (BBA) - Molecular Cell Research*, 1692(2-3):103–119, jul 2004.

[147] Ziheng Xu and Daniel J. Klionsky. Autophagy promotes cell motility by driving focal adhesion turnover. *Autophagy*, 12(10):1685–1686, aug 2016.

[148] Karo Gosselin, Emeric Deruy, Sébastien Martien, Chantal Vercamer, Fatima Bouali, Thibault Dujardin, Christian Slomianny, Ludivine Houel-Renault, Fazia Chelli, Yvan De Launoit, and Corinne Abbadie. Senescent keratinocytes die by autophagic programmed cell death. *The American Journal of Pathology*, 174(2):423–435, feb 2009.

[149] Anna Shteingauz, Yaara Porat, Tali Voloshin, Rosa S. Schneiderman, Mijal Munster, Einav Zeevi, Noa Kaynan, Karnit Gotlib, Moshe Giladi, Eilon D. Kirson, Uri Weinberg, Adrian Kinzel, and Yoram Palti. AMPK-dependent autophagy

upregulation serves as a survival mechanism in response to tumor treating fields (TTFields). *Cell Death & Disease*, 9(11), oct 2018.

[150] Geoffrey Cooper. *The Cell: A Molecular Approach*. Sinauer Associates Inc, 2000.

[151] Ludger Johannes and Vincent Popoff. Tracing the retrograde route in protein trafficking. *Cell*, 135(7):1175–1187, dec 2008.

[152] Jeremy C. Simpson, Tommy Nilsson, and Rainer Pepperkok. Biogenesis of tubular ER-to-golgi transport intermediates. *Molecular Biology of the Cell*, 17(2):723–737, feb 2006.

[153] Kevin T. Vaughan. Microtubule plus ends, motors, and traffic of golgi membranes. *Biochimica et Biophysica Acta (BBA) - Molecular Cell Research*, 1744(3):316–324, jul 2005.

[154] Takeshi Noda. Autophagy in the context of the cellular membrane-trafficking system: the enigma of atg9 vesicles. *Biochemical Society Transactions*, 45(6):1323–1331, nov 2017.

[155] Kristiane Søreng, Thomas P. Neufeld, and Anne Simonsen. Membrane trafficking in autophagy. In *International Review of Cell and Molecular Biology*, pages 1–92. Elsevier, 2018.

[156] S. R. Carlsson and A. Simonsen. Membrane dynamics in autophagosome biogenesis. *Journal of Cell Science*, 128(2):193–205, jan 2015.

[157] Fulvio Reggiori, Iryna Monastyrska, Takahiro Shintani, and Daniel J. Klionsky. The actin cytoskeleton is required for selective types of autophagy, but not nonspecific autophagy, in the yeast saccharomyces cerevisiae. *Molecular Biology of the Cell*, 16(12):5843–5856, dec 2005.

[158] Cuiqin Zhuo, Yuhua Ji, Zhenping Chen, Kaio Kitazato, Yangfei Xiang, Meigong Zhong, Qiaoli Wang, Ying Pei, Huaiqiang Ju, and Yifei Wang. Proteomics analysis of autophagy-deficient atg7-/- MEFs reveals a close relationship between f-actin and autophagy. *Biochemical and Biophysical Research Communications*, 437(3):482–488, aug 2013.

[159] Shanshan He, Duojiao Ni, Binyun Ma, Joo-Hyung Lee, Tian Zhang, Irene Ghozalli, Sara Dolatshahi Pirooz, Zhen Zhao, Nagakumar Bharatham, Baihong Li,

Soohwan Oh, Wen-Hwa Lee, Yoshinori Takahashi, Hong-Gang Wang, Arlet Minassian, Pinghui Feng, Vojo Deretic, Rainer Pepperkok, Mitsuo Tagaya, Ho Sup Yoon, and Chengyu Liang. PtdIns(3)p-bound UVRAG coordinates golgi–ER retrograde and atg9 transport by differential interactions with the ER tether and the beclin 1 complex. *Nature Cell Biology*, 15(10):1206–1219, sep 2013.

[160] S. Alers, A. S. Loffler, S. Wesselborg, and B. Stork. Role of AMPK-mTOR-ulk1/2 in the regulation of autophagy: Cross talk, shortcuts, and feedbacks. *Molecular and Cellular Biology*, 32(1):2–11, oct 2011.

[161] E. Karanasios, E. Stapleton, M. Manifava, T. Kaizuka, N. Mizushima, S. A. Walker, and N. T. Ktistakis. Dynamic association of the ULK1 complex with omegasomes during autophagy induction. *Journal of Cell Science*, 126(22):5224–5238, sep 2013.

[162] Liang Ge, David Melville, Min Zhang, and Randy Schekman. The ER–golgi intermediate compartment is a key membrane source for the LC3 lipidation step of autophagosome biogenesis. *eLife*, 2, aug 2013.

[163] Maho Hamasaki, Nobumichi Furuta, Atsushi Matsuda, Akiko Nezu, Akitsugu Yamamoto, Naonobu Fujita, Hiroko Oomori, Takeshi Noda, Tokuko Haraguchi, Yasushi Hiraoka, Atsuo Amano, and Tamotsu Yoshimori. Autophagosomes form at ER–mitochondria contact sites. *Nature*, 495(7441):389–393, mar 2013.

[164] Elena Marcassa, Marzia Raimondi, Tahira Anwar, Eeva-Liisa Eskelinen, Michael P. Myers, Gianluca Triolo, Claudio Schneider, and Francesca Demarchi. Calpain mobilizes atg9/bif-1 vesicles from golgi stacks upon autophagy induction by thapsigargin. *Biology Open*, 6(5):551–562, mar 2017.

[165] T. Saitoh, N. Fujita, T. Hayashi, K. Takahara, T. Satoh, H. Lee, K. Matsunaga, S. Kageyama, H. Omori, T. Noda, N. Yamamoto, T. Kawai, K. Ishii, O. Takeuchi, T. Yoshimori, and S. Akira. Atg9a controls dsDNA-driven dynamic translocation of STING and the innate immune response. *Proceedings of the National Academy of Sciences*, 106(49):20842–20846, nov 2009.

[166] Saori R. Yoshii and Noboru Mizushima. Monitoring and measuring autophagy. *International Journal of Molecular Sciences*, 18(9):1865, aug 2017.

[167] Noboru Mizushima and Tamotsu Yoshimori. How to interpret LC3 immunoblotting. *Autophagy*, 3(6):542–545, nov 2007.

[168] Peidu Jiang and Noboru Mizushima. LC3- and p62-based biochemical methods for the analysis of autophagy progression in mammalian cells. *Methods*, 75:13–18, mar 2015.

[169] I.F. Sbalzarini and P. Koumoutsakos. Feature point tracking and trajectory analysis for video imaging in cell biology. *Journal of Structural Biology*, 151(2):182–195, aug 2005.

[170] J.A. Helmuth, C.J. Burckhardt, U.F. Greber, and I.F. Sbalzarini. Shape reconstruction of subcellular structures from live cell fluorescence microscopy images. *Journal of Structural Biology*, 167(1):1–10, jul 2009.

[171] Á González-Rodríguez, R Mayoral, N Agra, M P Valdecantos, V Pardo, M E Miquilena-Colina, J Vargas-Castrillón, O Lo Iacono, M Corazzari, G M Fimia, M Piacentini, J Muntané, L Boscá, C García-Monzón, P Martín-Sanz, and Á M Valverde. Impaired autophagic flux is associated with increased endoplasmic reticulum stress during the development of NAFLD. *Cell Death & Disease*, 5(4):e1179–e1179, apr 2014.

[172] Angeles Duran, Ramars Amanchy, Juan F. Linares, Jayashree Joshi, Shadi Abu-Baker, Aleksey Porollo, Malene Hansen, Jorge Moscat, and Maria T. Diaz-Meco. p62 is a key regulator of nutrient sensing in the mTORC1 pathway. *Molecular Cell*, 44(1):134–146, oct 2011.

[173] Takeshi Kaizuka, Hideaki Morishita, Yutaro Hama, Satoshi Tsukamoto, Takahide Matsui, Yuichiro Toyota, Akihiko Kodama, Tomoaki Ishihara, Tohru Mizushima, and Noboru Mizushima. An autophagic flux probe that releases an internal control. *Molecular Cell*, 64(4):835–849, nov 2016.

[174] Franziska Kriegenburg, Christian Ungermann, and Fulvio Reggiori. Coordination of autophagosome–lysosome fusion by atg8 family members. *Current Biology*, 28(8):R512–R518, apr 2018.

[175] Nina Durchfort, Shane Verhoef, Michael B. Vaughn, Rishna Shrestha, Dieter Adam, Jerry Kaplan, and Diane McVey Ward. The enlarged lysosomes in beigej cells result from decreased lysosome fission and not increased lysosome fusion. *Traffic*, 13(1):108–119, nov 2011.

[176] Carl Ward, Nuria Martinez-Lopez, Elsje G. Otten, Bernadette Carroll, Dorothea Maetzel, Rajat Singh, Sovan Sarkar, and Viktor I. Korolchuk. Autophagy,

lipophagy and lysosomal lipid storage disorders. *Biochimica et Biophysica Acta (BBA) - Molecular and Cell Biology of Lipids*, 1861(4):269–284, apr 2016.

[177] Christophe Viret and Mathias Faure. Regulation of syntaxin 17 during autophagosome maturation. *Trends in Cell Biology*, 29(1):1–3, jan 2019.

[178] Huimei Ren, Fabian Elgner, Bingfu Jiang, Kiyoshi Himmelsbach, Regina Medvedev, Daniela Ploen, and Eberhard Hildt. The autophagosomal SNARE protein syntaxin 17 is an essential factor for the hepatitis c virus life cycle. *Journal of Virology*, 90(13):5989–6000, apr 2016.

[179] Adi L. Tarca, Roberto Romero, and Sorin Draghici. Analysis of microarray experiments of gene expression profiling. *American Journal of Obstetrics and Gynecology*, 195(2):373–388, aug 2006.

[180] Roman Jaksik, Marta Iwanaszko, Joanna Rzeszowska-Wolny, and Marek Kimmel. Microarray experiments and factors which affect their reliability. *Biology Direct*, 10(1), sep 2015.

[181] Mohamed A. El-Brolosy and Didier Y. R. Stainier. Genetic compensation: A phenomenon in search of mechanisms. *PLOS Genetics*, 13(7):e1006780, jul 2017.

[182] Christine Vogel and Edward M. Marcotte. Insights into the regulation of protein abundance from proteomic and transcriptomic analyses. *Nature Reviews Genetics*, 13(4):227–232, mar 2012.

[183] Raquel de Sousa Abreu, Luiz O. Penalva, Edward M. Marcotte, and Christine Vogel. Global signatures of protein and mRNA expression levels. *Molecular BioSystems*, 2009.

[184] Matthew D. Welch and Michael Way. Arp2/3-mediated actin-based motility: A tail of pathogen abuse. *Cell Host & Microbe*, 14(3):242–255, sep 2013.

[185] Theresia E. B. Stradal and Mario Schelhaas. Actin dynamics in host-pathogen interaction. *FEBS Letters*, 592(22):3658–3669, jul 2018.

[186] David K. Cureton, Ramiro H. Massol, Sean P. J. Whelan, and Tomas Kirchhausen. The length of vesicular stomatitis virus particles dictates a need for actin assembly during clathrin-dependent endocytosis. *PLoS Pathogens*, 6(9):e1001127, sep 2010.

[187] Shalane K. Yacovone, Amanda M. Smelser, Jed C. Macosko, George Holzwarth, David A. Ornelles, and Douglas S. Lyles. Migration of nucleocapsids in vesicular stomatitis virus-infected cells is dependent on both microtubules and actin filaments. *Journal of Virology*, 90(13):6159–6170, apr 2016.

[188] Bettina Stolp and Oliver T. Fackler. How HIV takes advantage of the cytoskeleton in entry and replication. *Viruses*, 3(4):293–311, mar 2011.

[189] Alicia Irurzun, Luis Pérez, and Luis Carrasco. Brefeldin a blocks protein glycosylation and RNA replication of vesicular stomatitis virus. *FEBS Letters*, 336(3):496–500, dec 1993.

[190] M Schmelz, B Sodeik, M Ericsson, E J Wolffe, H Shida, G Hiller, and G Griffiths. Assembly of vaccinia virus: the second wrapping cisterna is derived from the trans golgi network. *Journal of Virology*, 68(1):130–147, 1994.

[191] Annalucia Serafino, Maria Beatrice Valli, Federica Andreola, Annalisa Crema, Giampietro Ravagnan, Luisa Bertolini, and Guido Carloni. Suggested role of the golgi apparatus and endoplasmic reticulum for crucial sites of hepatitis c virus replication in human lymphoblastoid cells infected in vitro. *Journal of Medical Virology*, 70(1):31–41, mar 2003.

[192] Robert Wang, Yu-Jen Wu, Han-Shan Chen, and Chih-Jung Chen. A KDEL retrieval system for ER-golgi transport of japanese encephalitis viral particles. *Viruses*, 8(2):44, feb 2016.

[193] Jan HÃ¤nisch, Julia Ehinger, Markus Ladwein, Manfred Rohde, Emmanuel Derivery, Tanja Bosse, Anika Steffen, Dirk Bumann, Benjamin Misselwitz, Wolf-Dietrich Hardt, Alexis Gautreau, Theresia E. B. Stradal, and Klemens Rottner. Molecular dissection ofSalmonella-induced membrane ruffling versus invasion. *Cellular Microbiology*, 12(1):84–98, jan 2010.

[194] Asghar Abdoli, Mehrdad Alirezaei, Parvaneh Mehrbod, and Faezeh Forouzanfar. Autophagy: The multi-purpose bridge in viral infections and host cells. *Reviews in Medical Virology*, 28(4):e1973, apr 2018.

[195] Christophe Viret, Aurore Rozières, and Mathias Faure. Autophagy during early virus–host cell interactions. *Journal of Molecular Biology*, 430(12):1696–1713, jun 2018.

[196] K O Smith and W Kennell. Differentiation of members of the human herpesviridae family by radioimmunoassay. *Infection and Immunity*, 33(2):491–497, 1981.

[197] Qiming Liang, Gil Ju Seo, Youn Jung Choi, Mi-Jeong Kwak, Jianning Ge, Mary A. Rodgers, Mude Shi, Benjamin J. Leslie, Karl-Peter Hopfner, Taekjip Ha, Byung-Ha Oh, and Jae U. Jung. Crosstalk between the cGAS DNA sensor and beclin-1 autophagy protein shapes innate antimicrobial immune responses. *Cell Host & Microbe*, 15(2):228–238, feb 2014.

[198] Simon B. Rasmussen, Kristy A. Horan, Christian K. Holm, Amanda J. Stranks, Thomas C. Mettenleiter, A. Katharina Simon, Søren B. Jensen, Frazer J. Rixon, Bin He, and Søren R. Paludan. Activation of autophagy by α-herpesviruses in myeloid cells is mediated by cytoplasmic viral DNA through a mechanism dependent on stimulator of IFN genes. *The Journal of Immunology*, 187(10):5268–5276, oct 2011.

[199] Marion Lussignol and Audrey Esclatine. Herpesvirus and autophagy: "all right, everybody be cool, this is a robbery!". *Viruses*, 9(12), 2017.

[200] D. E. Alexander, S. L. Ward, N. Mizushima, B. Levine, and D. A. Leib. Analysis of the role of autophagy in replication of herpes simplex virus in cell culture. *Journal of Virology*, 81(22):12128–12134, sep 2007.

[201] Brian Yordy, Norifumi Iijima, Anita Huttner, David Leib, and Akiko Iwasaki. A neuron-specific role for autophagy in antiviral defense against herpes simplex virus. *Cell Host & Microbe*, 12(3):334–345, sep 2012.

[202] A. C. Haugo, M. L. Szpara, L. Parsons, L. W. Enquist, and R. J. Roller. Herpes simplex virus 1 pUL34 plays a critical role in cell-to-cell spread of virus in addition to its role in virus replication. *Journal of Virology*, 85(14):7203–7215, may 2011.

[203] Leonid A. Serebryannyy, Michaela Yuen, Megan Parilla, Sandra T. Cooper, and Primal de Lanerolle. The effects of disease models of nuclear actin polymerization on the nucleus. *Frontiers in Physiology*, 7, oct 2016.

[204] Amanda S. Coutts and Nicholas B. La Thangue. Regulation of actin nucleation and autophagosome formation. *Cellular and Molecular Life Sciences*, 73(17):3249–3263, may 2016.

[205] A S Coutts, I M Pires, L Weston, F M Buffa, M Milani, J-L Li, A L Harris, E M Hammond, and N B La Thangue. Hypoxia-driven cell motility reflects the interplay between JMY and HIF-1α. *Oncogene*, 30(48):4835–4842, may 2011.

[206] Fyza Y Shaikh and James E Crowe Jr. Molecular mechanisms driving respiratory syncytial virus assembly. *Future Microbiology*, 8(1):123–131, jan 2013.

Publications

Kage F, Winterhoff M, Haas V, Müller JM, Thalheim T, Freise A, Brühmann S, **Kollasser J**, Block J, Dimchev G, Geyer M, Schnittler HJ, Brakebusch CH, Stradal TE, Carlier MF, Sixt M, Käs J, Faix J, Rottner K. FMNL formins boost lamellipodial force generation. (2017) Nature Communication, 8:14832

Halfen J, **Kollasser J**, Gröbe L, Hagendorff P, Geffers R, Steffen A, Brakebusch CH, Rottner K, Stradal TE. Dissecting the role of RhoA, -B and -C during host pathogen interaction. (2016) Mol. Biol. Cell 27, 3947 [Abstract #P93 (Poster)]

Kage F, Winterhoff M, Haas V, Müller JM, Thalheim T, Freise A, Brühmann S, **Kollasser J**, Block J, Dimchev G, Geyer M, Brakebusch CH, Stradal TE, Carlier M, Sixt M, Käs J, Faix J, Rottner K. FMNL formins are required for lamellipodia force generation. (2016) Mol. Biol. Cell 27, 3947 [Abstract #P286 (Poster)]

Kollasser J, Stahnke S, Kirchenwitz M, Otto A, Rottner K, Stradal TE. WHAMM- and Arp2/3-complex driven endomembrane trafficking during infection. (2016) Mol. Biol. Cell 27, 3947 [Abstract #P984 (Poster)]

Danksagung

Ich danke herzlich Prof. Dr. Theresia Stradal für das Offert sowie die Umsetzung meines Projektes. Besonderer Dank auch für das große Verständnis, vor allem in den letzten Monaten. Das war nicht selbstverständlich. Zudem bin ich sehr dankbar für die sehr gute Infrastruktur in der Abteilung ZBIO bzw. am gesamten HZI Campus und die Möglichkeit, sich wissenschaftlich mit anderen Gruppen austauschen zu können. Im Rahmen dessen konnte ich mehrmals über den Tellerrand hinausschauen, was mir Mut und Motivation für mein Projekt gab, als auch mich menschlich prägte und mir neue Richtungen aufzeigte.

Desweiteren danke ich Prof. Dr. Reinhard Köster für die Übernahme des Zweigutachtens sowie Prof. Dr. Michael Steinert für die Bereitschaft, den Prüfungsvorsitz zu übernehmen. Zudem danke ich Prof. Dr. Klemens Rottner und Prof. Dr. Melanie Brinkmann für die zahlreichen, konstruktiven Ideen, Ansätze und Vorschläge im Rahmen meines Thesis Committee´s. Besonderer Dank geht auch an unsere Kooperationspartner für die stets reibungslose und sehr nette Zusammenarbeit und der Erkenntnis, dass Lernen etwas Großartiges ist, was einen voranbringt und positiv stimmt. Ein Dank für die wertvollen und spannenden Daten geht an: Dr. Lothar Gröbe, Dr. Robert Geffers, Pia Brinkert bzw. Prof. Dr. Mario Schelhaas, Dr. Mathias Müsken sowie Luca Ghita bzw. Prof. Dr. Ulrich Kalinke. Vielen Dank auch an die HZI Grad School für die hilfreichen, angebotenen Workshops sowie die Organisation von Symposien und Retreats.

Ganz besonderer Dank richtet sich an alle Verrückten der Gruppe ZBIO, denen ich in den letzten vier Jahren begegnen durfte: Danke an Anika, Annette, Astrid, Charlotte, Frieda, Jan H., Jan W., Janne, Jessica, Jonas, Julia H., Julia M., Laura, Leonie, Marco, Marcus, Monique, Nadiia, Silvia, Steffi und alle anderen Studenten, Azubis und Hiwis, die ich an dieser Stelle nicht namentlich genannt habe. Die Zusammenarbeit war mir eine große Ehre sowie Freude, denn es gab viele Tage, da wurde "Spaß" wirklich sehr groß geschrieben. Hervorheben möchte ich hierbei drei ganz besondere Kollegen oder vielmehr, Freunde. Danke Annette, dass du so bist wie du bist, für die morgendlichen Gespräche, für deine schlauen Ideen und die schnelle Umsetzung solcher. Danke Jessica, dass du plus bist und ich minus oder *vice versa*, ganz wie du magst. Danke Marco, dass ich dich treffen durfte und du bei uns geblieben bist. Danke für euer konsequentes Nachfragen, euer Zuhören, euren Zuspruch. Ein riesiger Dank geht an Anika, Elsi, Julia, Katja und Steffi für die Korrektur meiner Arbeit und die

vielen Ideen und Hilfestellungen zu jeder Zeit. Danke Anika, dass deine Tür immer offen stand und du mir viele kleine, große Tipps mit auf meinen Weg gegeben hast. Ich habe mir oft gewünscht, einen Tag du zu sein, dann wäre wohl einiges leichter von der Hand gefallen. Danke für den Hinweis, dass Pfannkuchen auch Berliner sein können und viertel vier in eurer Welt viertel nach vier ist und nicht wie eigentlich, viertel nach drei. Ein riesiger Dank an Silvia für die Unterstützung bei den spontanen Experimenten in den letzten Monaten und die angebotene Hilfe in schweren Momenten. Danke außerdem an Astrid für die Hilfe bei jeglicher Bürokratie und der Organisation der Dienstreisen.

Danke für eure Toleranz, Offenheit und Neugier. Das ist nicht selbstverständlich und ich war immer sehr stolz darauf, in so einer Umgebung arbeiten zu dürfen.

Und ohne wen wäre das alles hier nicht möglich gewesen? Wenn man sehr viel Glück hat im Leben, bekommt man die Gelegenheit auf Menschen zu treffen, die einfach nur zu hören, die geduldig sind, einen respektieren und akzeptieren ohne dass man irgendetwas dafür tun muss. Danke an die besten Freunde überhaupt, die mir in den letzten Jahren mehr als einmal die Hand gehalten haben und mich vor allem in den vergangenen Monaten maximal unterstützt haben, wenngleich ich nicht immer einfach war. Danke Anne, danke Elsi, danke Erik, danke Katja, danke Maria, danke Nicole, danke Robert, danke Robert + Familie. Mir fallen eigentlich nur noch folgende Worte ein: "If you wanna be my lover, you gotta get with my friends. Make it last forever, friendship never ends".

Last but not least, auch wenn diese Floskel furchtbar klingt, aber unendlicher Dank geht an meine Eltern und meinen Bruder. Seitdem ich denken kann, habe ich alle Möglichkeiten dieser Welt, durfte immer ich sein und mich durchsetzen - nicht immer gut und von Vorteil, aber es hat mich zu dem Menschen gemacht, der ich heute bin. Danke für die Unterstützung und das Realisieren, studieren zu können und dafür, dass ihr auf meinen Skippy immer so gut aufgepasst habt. Dir, kleiner Kerl, gebührt der größte Dank. Dafür, dass du ich bist und ich du. Dafür, dass du mich auf deine ganz besondere Art liebst. Danke für die Momente, die ich niemals vergessen werde, die mich geprägt und glücklich gemacht haben. Danke, dass ich dir begegnen durfte. Danke mein Herz.